JACC
Basic to Translational Science

A Journal of the American College of Cardiology

JACC
Basic to Translational Science

A Journal of the American College of Cardiology

CORRESPONDENCE FOR AMERICAN COLLEGE OF CARDIOLOGY

All correspondence for the College, other than that related to *JACC: Basic to Translational Science* should be sent to Resource Center, American College of Cardiology, 2400 N Street, NW, Washington, DC 20037

JACC: BASIC TO TRANSLATIONAL SCIENCE VOL. 4, NO. 8, 2019

PRECLINICAL RESEARCH

A Novel Biological Strategy for Myocardial Protection by Intracoronary Delivery of Mitochondria: Safety and Efficacy

Borami Shin, MD,[a,b] Mossab Y. Saeed, MD,[a,b] Jesse J. Esch, MD,[b,c] Alvise Guariento, MD,[a,b] David Blitzer, MD,[a,b] Kamila Moskowitzova, MD,[a,b] Giovanna Ramirez-Barbieri, MD,[a,b] Arzoo Orfany, MD,[a,b] Jerusha K. Thedsanamoorthy, BA,[b,d] Douglas B. Cowan, PhD,[b,d] James A. Inkster, PhD,[b,e] Erin R. Snay, BRS,[e] Steven J. Staffa, MS,[b,d] Alan B. Packard, PhD,[b,d] David Zurakowski, PhD,[b,d] Pedro J. del Nido, MD,[a,b] James D. McCully, PhD[a,b]

VISUAL ABSTRACT

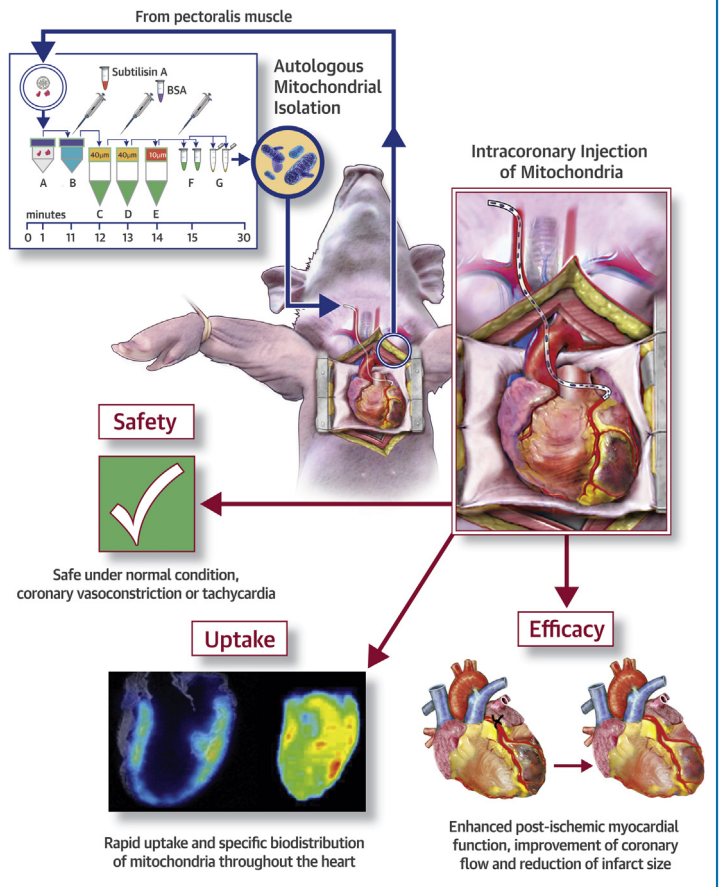

Shin, B. et al. J Am Coll Cardiol Basic Trans Science. 2019;4(8):871–88.

ISSN 2452-302X https://doi.org/10.1016/j.jacbts.2019.08.007

ABBREVIATIONS AND ACRONYMS

ADH = antidiuretic hormone

ATP = adenosine triphosphate

AUC = area under the curve

CBF = coronary blood flow

K^+ = potassium ion

K_{ATP} = ATP-sensitive potassium channel

K_{IR} = Inwardly rectifying potassium channel

LCA = left coronary artery

LV = left ventricular

HIGHLIGHTS

- **Mitochondrial transplantation uses mitochondria isolated from the patient's own body to replace or augment native mitochondria damaged by ischemia reperfusion injury.**
- **The transplanted mitochondria can be delivered to the myocardium by intra-coronary injection.**
- **Intracoronary injection of mitochondria is safe and has no effect on coronary patency.**
- **Intracoronary injection of mitochondria provides for the rapid uptake and specific biodistribution of mitochondria throughout the heart.**
- **Intracoronary mitochondrial transplantation is efficacious and provides for enhanced post-ischemic myocardial function, improved coronary blood flow and reduction of infarct size.**

SUMMARY

Mitochondrial dysfunction is the determinant insult of ischemia-reperfusion injury. Autologous mitochondrial transplantation involves supplying one's healthy mitochondria to the ischemic region harboring damaged mitochondria. The authors used in vivo swine to show that mitochondrial transplantation in the heart by intracoronary delivery is safe, with specific distribution to the heart, and results in significant increase in coronary blood flow, which requires intact mitochondrial viability, adenosine triphosphate production, and, in part, the activation of vascular K_{IR} channels. Intracoronary mitochondrial delivery after temporary regional ischemia significantly improved myocardial function, perfusion, and infarct size. The authors concluded that intracoronary delivery of mitochondria is safe and efficacious therapy for myocardial ischemia-reperfusion injury.

Ischemic heart disease is one of the leading causes of global morbidity and mortality (1). Mitochondrial damage is the principal pathogenesis of myocardial ischemia-reperfusion injury leading to cardiomyocyte death and contractile failure (2–7).

We have previously developed a novel therapy, autologous mitochondrial transplantation, in which viable, respiration-competent mitochondria from nonischemic tissue from the patient's own body are isolated and then transplanted into the ischemic myocardium to ameliorate the effects of mitochondrial damage experienced by the ischemic region. The therapeutic efficacy of mitochondrial transplantation was demonstrated in a series of animal studies (8–14) and showed promise in a recent human application (15). In both animals and humans, post-ischemic transplantation of healthy mitochondria by direct injection into the myocardium results in significant improvements of contractile function and tissue viability of the injured myocardium.

The transplanted mitochondria are readily internalized by cardiac cells (11) by actin-dependent endocytosis (12), with rapid cytosolic transition and fusion with the endogenous mitochondrial network (13). The transplanted mitochondria act to increase myocardial adenosine triphosphate (ATP) levels, upregulate proteomic pathways for mitochondrial function, upregulate myoprotective cytokines, and replace damaged mitochondrial deoxyribonucleic acid (8–10).

From the [a]Department of Cardiac Surgery, Boston Children's Hospital, Boston, Massachusetts; [b]Harvard Medical School, Boston, Massachusetts; [c]Department of Cardiology, Boston Children's Hospital, Boston, Massachusetts; [d]Department of Anesthesiology, Perioperative and Pain Medicine, Boston Children's Hospital, Boston, Massachusetts; and the [e]Division of Nuclear Medicine and Molecular Imaging, Department of Radiology, Boston Children's Hospital, Boston, Massachusetts. This study was supported by the Richard A. and Susan F. Smith President's Innovation Award, The Sidman Family Foundation, The Michael B. Rukin Charitable Foundation, The Kenneth C. Griffin Charitable Research Fund, and The Boston Investment Conference. Dr. Shen was supported by National Institutes of Health (NIH) grant 5T32HL007734. The synthesis of ^{18}F-rhodamine-6G was supported by NIH grant 5 RO1 HL108107. Drs. del Nido and McCully have patents pending for the isolation and usage of mitochondria. The authors have reported that that they have no relationships relevant to the contents of this paper to disclose.
The authors attest they are in compliance with human studies committees and animal welfare regulations of the authors' institutions and Food and Drug Administration guidelines, including patient consent where appropriate. For more information, visit the *JACC: Basic to Translational Science* author instructions page.

Manuscript received May 9, 2019; revised manuscript received August 20, 2019, accepted August 24, 2019.

Although mitochondrial transplantation by direct tissue injection of donor mitochondria is therapeutically effective, it harbors limitations in that multiple injections and physical manipulations of the heart are necessary for adequate distribution of mitochondria throughout the heart. Open access to the heart is also required, which significantly limits the potential patient population who could undergo mitochondrial transplantation.

Minimally invasive, intracoronary delivery of mitochondria can avoid these drawbacks and disseminate mitochondria to the entire region that was infused, allowing an entry for whole-organ mitochondrial therapy. Previous studies using an isolated perfused heart model have demonstrated that intracoronary delivery of mitochondria results in rapid uptake and global distribution of the transplanted mitochondria (11). However, preclinical in vivo evaluation of the biodistribution, safety, and efficacy of intracoronary delivery of mitochondria is imperative for clinical translation and the expansion of therapeutic applications.

In the present report, we investigated the biodistribution and the safety of a catheter-based, intracoronary mitochondrial transplantation and evaluated the therapeutic efficacy in treating regional myocardial ischemia-reperfusion injury in the clinically relevant in vivo swine model.

SEE PAGE 889

METHODS

All procedures conformed to institutional guidelines for the care and use of laboratory animals and were approved by the Institutional Animal Care and Use Committee of Boston Children's Hospital.

EXPERIMENTAL DESIGN. A total of 57 adult female Yorkshire swine (45.0 ± 5.5 kg) were used. This study was conducted in 3 phases. In the first phase, the safety profile and biodistribution of mitochondria by intracoronary delivery was determined in the nonischemic swine. In the second phase, based on the first-phase finding of the increase in coronary blood flow (CBF) from intracoronary infusion of mitochondria, the mechanism of mitochondria-induced increase in CBF was investigated. Finally, in the third phase, the efficacy of intracoronary mitochondrial transplantation in providing cardioprotection after regional myocardial ischemia was evaluated.

SURGICAL PREPARATION AND MITOCHONDRIAL ISOLATION. Animals were sedated with Telazol (Zoetis, Parsippany, New Jersey) (2.2–4.4 mg/kg)/xylazine (Anased, Greeley, Colorado) (1–2 mg/kg) and intubated. General anesthesia was maintained with a 0.5% to 2% isoflurane-oxygen mixture. Ventilation was adjusted to maintain pH 7.35 to 7.45, P_{CO_2} 30 to 40 mm Hg, and P_{O_2} 85 to 100 mm Hg. Core temperatures were maintained at >36°C. Median sternotomy was performed, and the heart was suspended in a pericardial cradle. Then, angiographic access to the left coronary artery (LCA) was established by floating a 5-F JR angiography catheter (Merit Medical Systems, Inc., South Jordan, Utah) through the right carotid artery (5-F sheath) to the left coronary ostium under fluoroscopy. The coronary tree was visualized by injection of 5 ml of contrast solution (74% Ioversol Optiray-350, Mallinckrodt, Inc., St. Louis, Missouri) during 5 s, followed by a 5-ml saline flush. Two pieces of muscle were harvested from the pectoralis major muscle of each animal with a 6-mm biopsy punch and immediately used for mitochondrial isolation. Autologous mitochondria were isolated and mitochondrial ATP content was measured as previously described (8,9,16).

PHASE I: SAFETY OF INTRACORONARY DELIVERY OF MITOCHONDRIA AND BIODISTRIBUTION IN THE NONISCHEMIC HEART. A total of 20 animals were used in phase 1. There were no animal losses in phase 1 studies. Myocardial uptake and biodistribution of mitochondria by intracoronary delivery were evaluated in 3 animals. Next, 6 animals were used to evaluate the concentration tolerance of intracoronary injection of mitochondria by angiographic injection of 5 mitochondrial concentrations into the LCA. Intracoronary injection of 1 optimum mitochondrial concentration was then tested under normal conditions and in the presence of myocardial stressors, including coronary vasoconstriction, tachycardia, and increased afterload (n = 6). The safety of repeated injections of mitochondria was evaluated (n = 5). Coronary patency, CBF, hemodynamics, and regional and global left ventricular (LV) functions were evaluated.

Mitochondrial biodistribution and cellular uptake. To evaluate myocardial uptake and biodistribution of mitochondria, autologous mitochondria were labeled with ^{18}F-rhodamine-6G (11,17). To increase detection sensitivity, mitochondria were delivered at a concentration 6-fold greater (6×10^9) than the therapeutic dosage used in our previous studies (1×10^9). Mitochondria were injected serially in 6 5-s boluses, each bolus containing 1×10^9 mitochondria in 5 ml of vehicle (300 mM sucrose, 10 mM K^+ 4-(2-hydroxyethyl)-1-piperazineethanesulfonic acid pH 7.2, and 1 mM K^+ ethylene glycol-bis(β-aminoethyl ether)-*N*,*N*,*N*′*N*′-tetraacetic acid, pH 8.0; Sigma Aldrich, St. Louis, Missouri). After 10 min of circulation, a timeframe long enough for the blood to circulate through the entire body approximately 10 times (18), the animal

was euthanized and imaged by whole-body positron emission tomography (Siemens, Munich, Germany) (n = 2). In a separate animal, cellular uptake of mitochondria was evaluated by intracoronary injection of xenogeneic mitochondria isolated from human cardiac fibroblasts and labeled with iron (II, III) oxide nanoparticles. The use of human mitochondria allows differentiation of the transplanted mitochondria from the native swine cardiac mitochondria by immunohistochemistry. Transplanted mitochondria were detected by Prussian blue staining for iron-labeled mitochondria and immunohistochemistry as previously described (9,11) (n = 1).

Safety of intracoronary injection of mitochondria. Five concentrations of mitochondria (1×10^3, 1×10^5, 1×10^7, 1×10^9, and 1×10^{11}) were each suspended in 5 ml of vehicle. Each concentration was injected into the LCA as a 5-s bolus followed by a 5-ml saline flush in the order of increasing concentration (n = 6).

To evaluate the safety of intracoronary injection of mitochondria in the presence of increased myocardial demand, coronary vasoconstriction or tachycardia with increased afterload was individually induced in 6 animals. Coronary vasoconstriction was induced by intracoronary injection of antidiuretic hormone (ADH) (Par Pharmaceutical, Woodcliff Lake, New Jersey; and Sigma Aldrich) (1.75 nmol in 5 ml of saline). Tachycardia with increased afterload was induced with epinephrine (0.5 μmol in 5 ml of saline) (Patterson Veterinary, Devens, Massachusetts; and Sigma Aldrich). On confirmation of the intended effects, 1×10^9 mitochondria were provided as boluses into the LCA (n = 6). Then, in 5 animals, the safety of repeated injection of mitochondria was assessed by 10 serial intracoronary injections of 1×10^9 mitochondria in 5 ml of vehicle into the LCA in 5-s boluses every 5 min.

Assessment of coronary patency, coronary blood flow, and cardiac function. Coronary patency was evaluated by angiography immediately after and 5 min after intracoronary mitochondrial injections. Angiographic analysis was performed by the Cardiology Department of Boston Children's Hospital. CBF was continuously measured by placing an ultrasonic flow probe (3R1334, Transonic Systems Inc, Ithaca, New York) circumferentially around a 5-mm to 7-mm segment of the left anterior descending artery distal to the first diagonal branch and recorded via a Transonic T206 blood-flowmeter. Global LV function was evaluated by a 7F-VSL transonic pressure-volume conductance catheter inserted into the LV cavity through the LV apex. Measurements were analyzed with LabChart 7 acquisition software (AD Instruments, Sydney, Australia). Regional myocardial function was evaluated by sonomicrometry of the LV free wall and analyzed with SonoView post-processing software SonoLabD53 (Sonometrics Corp., London, United Kingdom) (19).

PHASE 2: EVALUATION OF MITOCHONDRIA-INDUCED INCREASE IN CORONARY BLOOD FLOW. A total of 21 animals were used in phase 2. There were no animal losses in phase 2 studies. We first evaluated whether the increase in CBF resulting from intracoronary injection of mitochondria was the result of increased myocardial oxygen consumption by the introduction of large amounts of mitochondria into the vasculature. This was done by 2 methods: first, by measuring the CBF in response to direct myocardial injection of mitochondria at 10 locations (1×10^8 each in 0.1 mL of vehicle) in close proximity to the left anterior descending artery, using a tuberculin syringe (n = 3); and second, by the measurement of coronary sinus proportion venous oxygen saturation at baseline, immediately after (at peak of increase in CBF) and 10 min after intracoronary injection of mitochondria (n = 4).

Intracoronary injection of devitalized mitochondria, HeLa and HeLa p^0 cell mitochondria. To investigate the role of mitochondrial viability and respiration competence in mitochondria-induced increase in CBF, mitochondria were devitalized (9) and injected into the LCA (n = 4). Next, mitochondria (1×10^9) isolated from HeLa- and HeLa-p^0 cells, which differ in their ability to perform oxidative phosphorylation (12), were injected separately into the left anterior descending artery (n = 6). CBF was compared. HeLa cells (CRM-CCL-2, American Type Culture Collection, Manassas, Virginia) and HeLa-p^0 cells were cultured as previously described (9,12).

Inhibition of coronary vasodilatory pathways. To determine the biochemical pathway(s) involved in mitochondria-induced increase in CBF, potential key mediators of coronary vasodilation were investigated in vivo, including endothelium-mediated nitric oxide synthase (20), cyclooxygenase (20) and vascular smooth muscle (SM) mediated adenosine receptors (21), ATP-sensitive potassium (K_{ATP}) channels (22), and inwardly rectifying potassium (K_{IR}) channels (23). CBF in response to intracoronary injection of 1×10^9 mitochondria was compared in the presence and absence of each pathway inhibition. Activators of each pathway were used as positive controls.

Animals were pre-treated separately by slow intracoronary infusion of increasing concentrations of the pedigreed blocker of each vasodilatory pathway (n = 4): nitromonomethyl L-arginine (0-100 μM; nitric oxide synthase blocker) (Sigma Aldrich) (20), indomethacin (0-100 mM; cyclooxygenase blocker) (Sigma Aldrich) (20), 8-*p*-sulfophenyl

theophylline (0–1 mM; adenosine receptor blocker) (Sigma Aldrich) (21), glibenclamide (0–2 mM; K_{ATP} channel blocker) (Sigma Aldrich) (22), and barium chloride (0 to 100 μM; K_{IR} channel blocker) (23). Nitromonomethyl L-arginine, 8-*p*-sulfophenyl theophylline, and barium chloride (Sigma Aldrich) were dissolved separately in 60 ml of saline. Stock solutions of glibenclamide and indomethacin were made in 1 ml of dimethyl sulfoxide (Sigma Aldrich) and slowly dissolved in 60 ml of warmed saline. A blocker was infused into the LCA during 20 min. Five min after completion of blocker treatment, pathway inhibition was confirmed by intracoronary injection of a known activator of the tested pathway. Bradykinin (0.01 nmol) (Sigma Aldrich) was used as cyclooxygenase and nitromonomethyl L-arginine pathway activator (24), nicorandil (50 μmol) (Sigma Aldrich) was used as K_{ATP}-channel activator (25), and ATP (30 μM) was used as K_{IR}-channel pathway activator (23). After confirmation of inhibition of the pathway in question, 1×10^9 mitochondria were injected into the LCA and CBF was measured. All blockers and activators were purchased from Sigma-Aldrich, St. Louis, Missouri).

PHASE 3: EFFICACY OF INTRACORONARY DELIVERY OF MITOCHONDRIA IN REGIONAL ISCHEMIA-REPERFUSION INJURY. A total of 16 animals were used in phase 3. There was 1 animal loss in the vehicle group. Animals were subjected to 30 min of regional myocardial ischemia by temporary snaring of the mid left anterior descending artery just distal to the second diagonal branch. The snare was released, and immediately on reperfusion, animals received either an intracoronary bolus of 1×10^9 mitochondria in 5 ml of vehicle (n = 8) or 5 ml of vehicle alone (n = 8). Hemodynamics, regional and global LV function, and CBF were continuously acquired. After 120 min of reperfusion, animals were euthanized, and the hearts were analyzed for area at risk and infarct size.

ECHOCARDIOGRAPHY. Echocardiography was acquired with a Philips iE33 machine (Philips Medical Systems, Andover, Massachusetts) with an X7-2 (7-2 MHz) transducer at pre-ischemia, at 30 min of ischemia, and after 1 and 2 h of reperfusion. Short-axis view and M-mode tracings at the midpapillary level were analyzed with a RadiAnt DICOM Viewer 5.02 (Medixant, Poznan, Poland) according to the American Society of Echocardiography standards (26).

EUTHANASIA. Animals were euthanized by intravenous injection of Fatal-Plus (50 μg/kg).

AREA AT RISK AND INFARCT SIZE. Area at risk and infarct size were determined with tetrazolium chloride staining and planimetry analysis (7–9).

STATISTICAL ANALYSIS. Statistical analyses were performed with Stata software version 11.0 (StataCorp, College Station, Texas). All data are expressed as mean ± SE of the mean. Blinding was not adopted for data collection and analysis of different injectates. Continuous data (CBF, hemodynamics, and regional and global LV contractility) were compared between groups with 2-way repeated-measures analysis of variance. When the overall difference across groups was significantly different, a Bonferroni-adjusted post hoc analysis was used for pairwise comparisons of interest. For CBF, comparisons were made between each point and baseline CBF at time zero within each group. Area under the curve (AUC) was compared between groups with a 1-way analysis of variance, and results are presented as mean ± SE of the mean with 95% confidence interval. A 1-way analysis of variance was also used for echocardiographic analyses, area at risk, and infarct size. Statistical significance was claimed at a 2-sided $p < 0.05$.

RESULTS

PHASE 1: SAFETY AND BIODISTRIBUTION OF INTRACORONARY DELIVERY OF MITOCHONDRIA. Myocardial uptake and biodistribution of mitochondria. Myocardial uptake and biodistribution of mitochondria were evaluated by intracoronary injection of ^{18}F-rhodamine-6G–labeled mitochondria (6×10^9) in the LCA (n = 2). Whole-body positron emission tomographic scan images showed that the transplanted mitochondria were located specifically in the left ventricle (**Figures 1A to 1C**). ^{18}F-tracer signals were also present in the arterial sheath and in the right carotid artery where the coronary catheter was placed, and a small amount of tracer was detected in the descending aorta (**Figures 1A to 1C**). There was no evidence of significant tracer accumulation in any other organs.

Myocardial cellular uptake of mitochondria was demonstrated in a separate animal by intracoronary injection of iron (II, III) oxide–labeled human cardiac fibroblast mitochondria into the swine LCA (n = 1). Serial section immunohistochemistry and Prussian blue costaining of the swine heart confirmed the presence of human mitochondria in the heart tissue within cardiomyocytes, interstitial spaces, and the vascular walls (**Figures 1D to 1G**).

Intracoronary injection of mitochondria and myocardial function. There were no statistical differences between intracoronary injection of vehicle and baseline values for any of the hemodynamic parameters. Intracoronary injection of mitochondria did not affect heart rate, mean arterial pressure, or

FIGURE 1 Biodistribution and Myocardial Uptake of Autologous Mitochondria by Intracoronary Delivery

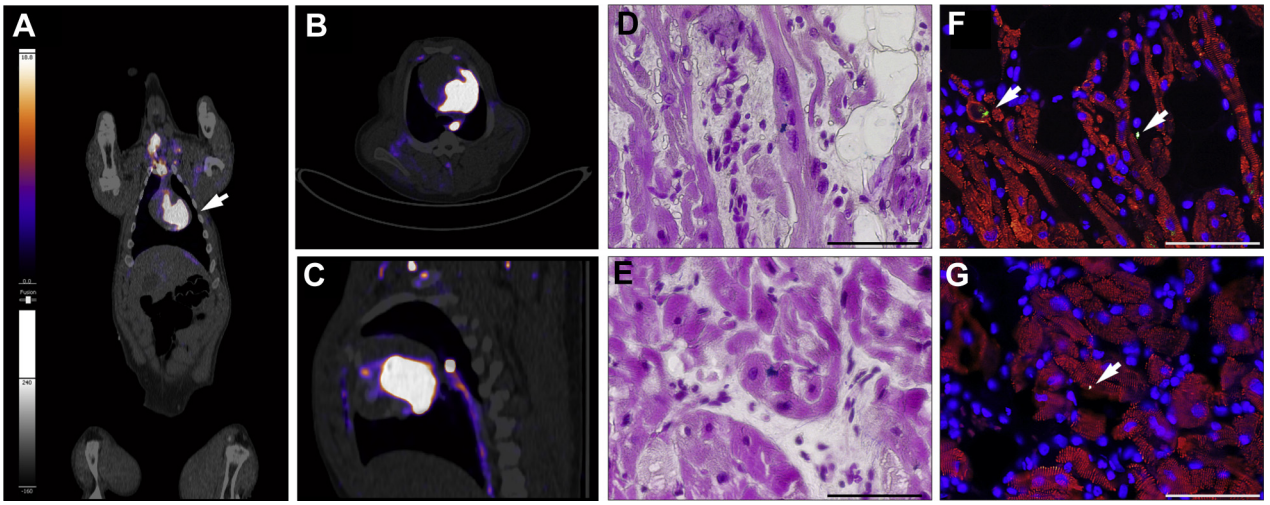

(A, B, and C) Representative positron emission tomography (PET) images 10 min after intracoronary injection of ^{18}F-rhodamine-6G iron (II, III) oxide nanoparticle-labeled mitochondria. Tracer accumulation is observed in the left ventricle **(arrow)** and along the coronary angiography catheter present through the right carotid arterial access **(arrow)**. **(D and E)** Prussian blue stain of iron oxide–labeled human mitochondria transplanted into a swine myocardium. **(F and G)** Fluorescence immunohistochemistry of the transplanted mitochondria in consecutive slices of **(D)** and **(E) (arrows)**. **Green**: antihuman mitochondria (MTCO2); **red**: antisarcomeric α-actinin; **blue** (4′,6-diamidino-2-phenylindol [DAPI]): nuclei. Scale bars = 100 μm.

cardiac rhythm at any concentration of mitochondria tested compared with baseline or vehicle (Figure 2A). Higher concentrations of mitochondria (1×10^9 and 1×10^{11}) significantly enhanced regional and global LV function, as observed by increases in the proportion of LV free-wall segmental shortening (1×10^9 $p = 0.016$ vs. baseline and $p = 0.015$ vs. vehicle; 1×10^{11} $p = 0.013$ vs. baseline and $p = 0.014$ vs. vehicle) and +max dP/dt (1×10^9 $p = 0.026$ vs. baseline and $p = 0.024$ vs. vehicle; 1×10^{11} $p < 0.001$ vs. baseline and $p < 0.001$ vs. vehicle), and by peak LV developed pressure (1×10^9 $p = 0.034$ vs. baseline and $p = 0.029$ vs. vehicle; 1×10^{11} $p = 0.035$ vs. baseline and $p = 0.028$ vs. vehicle) (Figures 2B to 2E).

Intracoronary injection of mitochondria and CBF. Angiographic analyses showed patent coronary arteries with no detectable lesions or blockages (Figures 3A and 3B, Videos 1 and 2). Mean CBF before mitochondrial injection was 20.5 ± 1.3 ml/min (Figure 3C). Intracoronary injection of mitochondria increased CBF in a concentration-dependent manner (Figures 3C and 3D). Analysis of the AUC for CBF showed significant increases in CBF at mitochondrial concentrations of 1×10^7 (10,001.7 ± 914.3 ml/min × s; $p = 0.032$), 1×10^9 (19,843.7 ± 1,208.4 ml/min × s; $p < 0.001$), and 1×10^{11} (18,262.3 ± 2,131.6 ml/min × s; $p < 0.001$) compared with vehicle alone (7,242.9 ± 624.7 ml/min × s) (Figure 3D). Maximum CBF was observed at a mitochondrial concentration of 1×10^9, a 325% increase compared with baseline CBF ($p < 0.001$). Increase in CBF was sustained for 6.5 ± 0.6 min. No differences were observed in peak CBF ($p = 0.842$) or in the duration of increase ($p = 0.304$) between 1×10^9 and 1×10^{11} mitochondria (Figures 3C and 3D). The response of CBF was reproducible with repeated injections of mitochondria (1×10^9), every 5 min for 10 repetitions (Figure 3E). There were no effects on heart rate or mean arterial pressure with either single or serial injections of mitochondria (Figure 3F).

Intracoronary injection of mitochondria during increased myocardial demand. Intracoronary injection of ADH resulted in coronary vasoconstriction, leading to a significant decrease in CBF ($p < 0.001$) (Figures 4A and 4B). Intracoronary injection of mitochondria in the ADH-treated coronary artery significantly increased CBF ($p < 0.001$) (Figure 4B). No changes in heart rate, mean arterial pressure (Figure 4A), or cardiac rhythm were observed (Figures 4A, 4C, and 4D) and no differences in global LV function were detected (Figures 4E and 4F). There was a trend toward improved +dP/dt max and LV peak developed pressure when mitochondria were added to ADH compared with ADH alone; however, they did not reach statistical significance. Regional LV function, as measured by the proportion of segmental

FIGURE 2 Hemodynamics and Left Ventricular Function After Intracoronary Injection of Mitochondria

A

	Baseline	Vehicle	10^3 Mitochondria	10^5 Mitochondria	10^7 Mitochondria	10^9 Mitochondria	10^{11} Mitochondria
HR (beats/min)	81.1 ± 9.3	78.7 ± 4.9	78.6 ± 7.9	78.7 ± 8.6	78.5 ± 8.4	78.9 ± 8.3	79.4 ± 7.8
MAP (mmHg)	69.9 ± 2.5	72.1 ± 4.3	68.9 ± 1.9	70.8 ± 2.3	70.1 ± 1.8	71.2 ± 1.8	71.9 ± 2.4

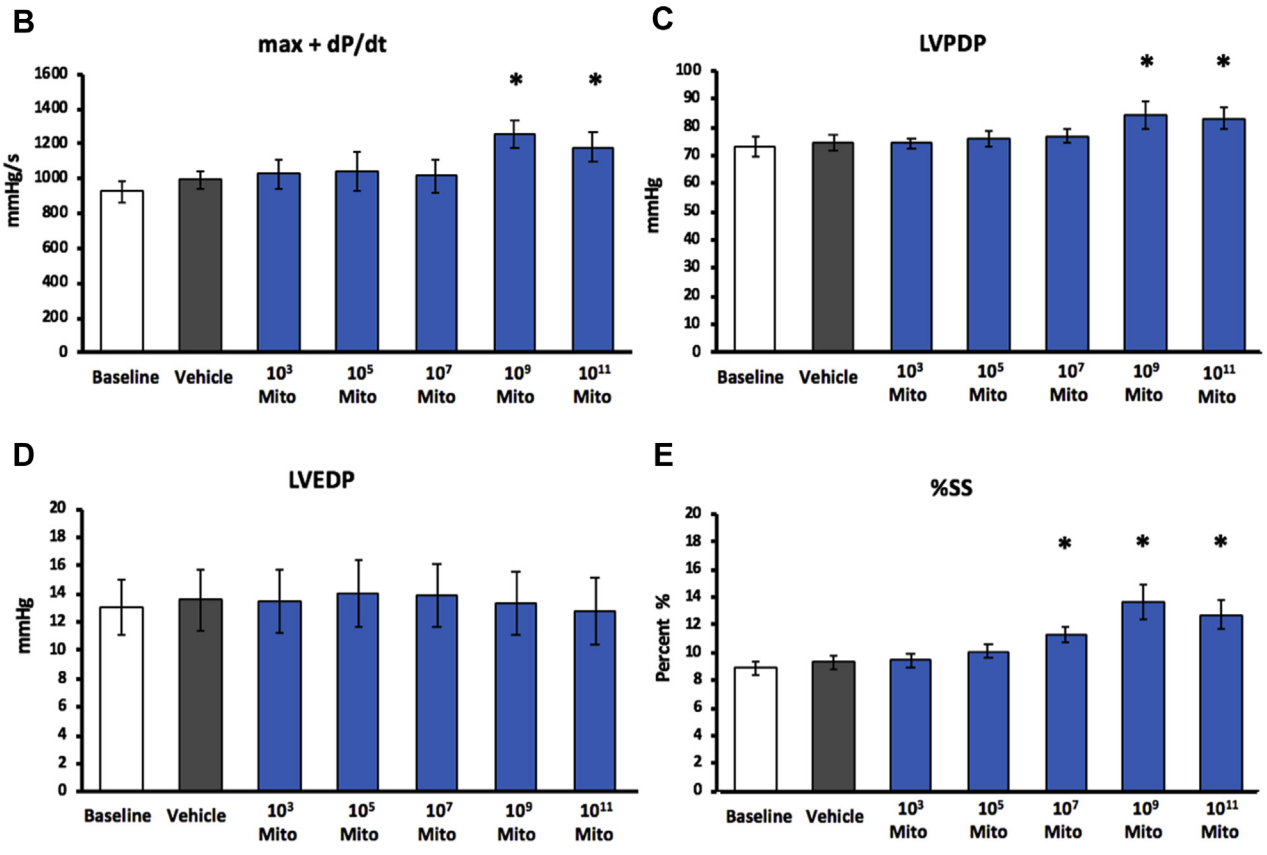

(A) Heart rate (HR) and mean arterial pressure (MAP) at baseline, after intracoronary injection of vehicle and different concentrations of mitochondria (n = 6). **(B, C, and D)** Global functional assessments of the left ventricle after intracoronary injection of mitochondria at different mitochondrial concentrations. Left ventricular peak developed pressure (LVPDP), maximal rate of increase of left ventricular pressure (maximal proportion dP/dt), and left ventricular end-diastolic pressure (LVEDP) (n = 6). **(E)** Regional left ventricular contractile assessment by proportion segmental shortening (%SS) (n = 6). All values are mean ± SEM, averaged during 60 cardiac cycles immediately after intracoronary injections. *p < 0.05 versus vehicle. Mito = mitochondria.

shortening, showed a modest increase on injection of mitochondria into the vasoconstricted LCA (11.3% ± 1.5% vs. 8.5% ± 0.8%; p = 0.017) (Figure 4G).

Intracoronary injection of epinephrine produced significant tachycardia and systemic hypertension (Figure 4A). Mitochondrial injection in the epinephrine-treated coronary artery produced no changes in heart rate, mean arterial pressure, cardiac rhythm, or regional or global LV function (Figures 4A to 4G). Evaluation of CBF in response to epinephrine with mitochondria was excluded from the analysis because the significant tachycardia and hypertension created by epinephrine causes a secondary increase in CBF and confounds the primary changes in CBF by mitochondria.

To provide a positive control, a separate study was performed in which polystyrene microbeads (3, 10, and 150 μm, 1 × 10^9 each) were injected separately

FIGURE 3 Coronary Patency and Coronary Blood Flow

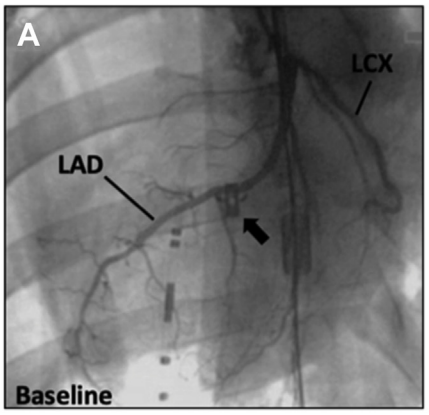

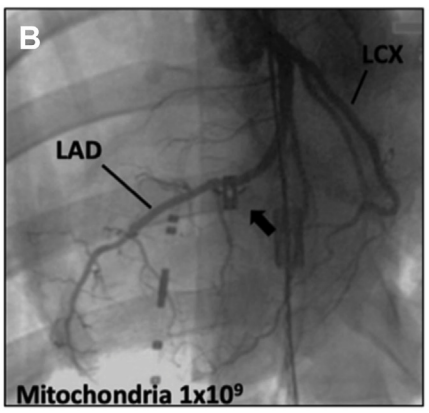

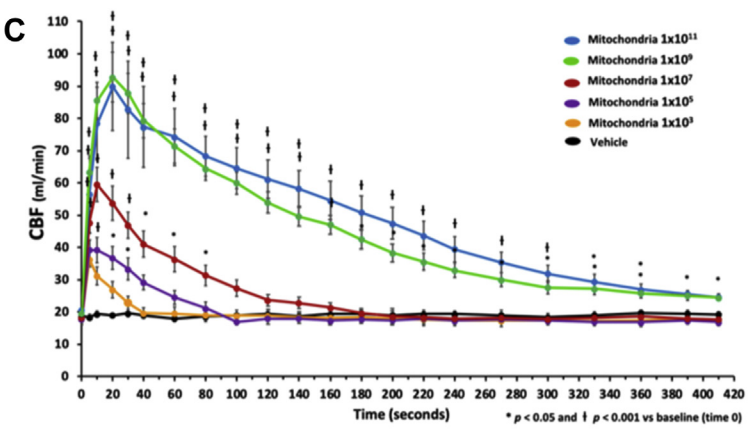

D

Group	AUC	SE	95% CI	P (vs. Vehicle)
Mitochondria 1 x 10^{11}	18,262.3	2,131.6	(14,084.4, 22,440.2)	< 0.001
Mitochondria 1 x 10^{9}	19,843.7	1,208.5	(17,475.3, 22,212.0)	< 0.001
Mitochondria 1 x 10^{7}	10,001.7	914.3	(8,209.7, 11,793.6)	0.032
Mitochondria 1 x 10^{5}	8,154.6	647.5	(6,885.4, 9,423.7)	0.335
Mitochondria 1 x 10^{3}	7,718.3	695.0	(6,356.1, 9,080.6)	0.622
Vehicle	7,242.9	624.7	(6,018.6, 8,467.3)	Reference

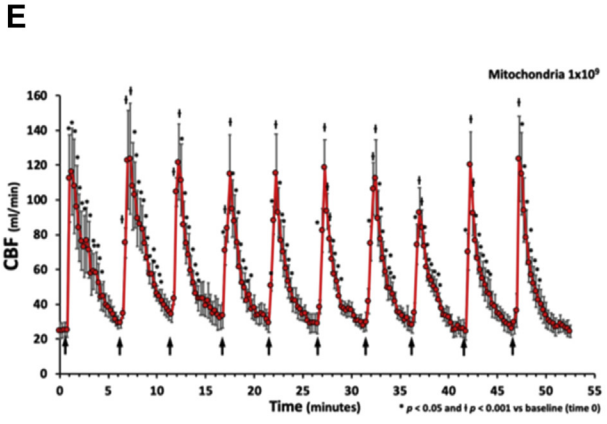

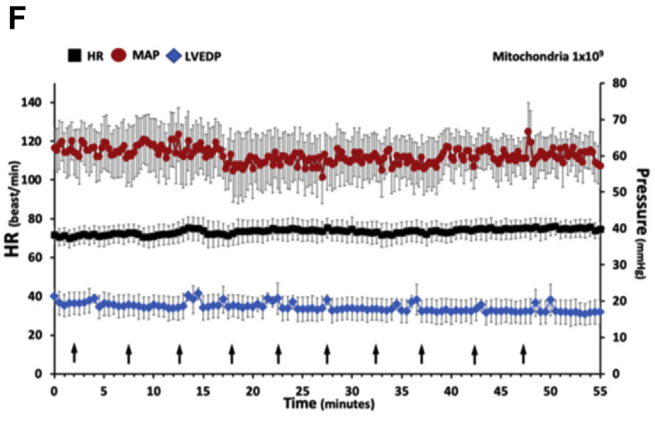

(A) Representative coronary angiography of swine under baseline condition (Video 1) and **(B)** immediately after intracoronary injection of 1×10^9 mitochondria (Video 2). Transonic flow probe **(arrows)**. **(C)** Continuous coronary blood flow (CBF) at the mid left anterior descending artery on intracoronary injection of vehicle and different concentrations of mitochondria (n = 6). **(D)** Comparisons of the area under the curve (AUC) of graph **(C)** using the trapezoidal rule from time 0 to 410 s, in milliliters per min × s. **(E)** CBF and **(F)** heart rate, mean arterial pressure, and left ventricular end-diastolic pressure on serial, intracoronary injections of mitochondria (1×10^9) every 5 min, 10 times. **Arrows** denote the times of mitochondrial injection. Values are mean ± SEM. * $p < 0.05$ and † $p < 0.001$ versus baseline (time 0) (n = 5). LAD = left anterior descending artery; LCX = left circumflex artery. Abbreviations as in Figure 2.

FIGURE 4 Intracoronary Injection of Mitochondria During Coronary Vasoconstriction and Tachycardia

A

	Baseline	Vehicle	Mitochondria	ADH	Epinephrine	ADH + Mitochondria	Epinephrine + Mitochondria
HR (beats/min)	78.2 ± 4.3	68.7 ± 4.9	80.0 ± 3.6	68.7 ± 8.1	152.1 ± 7 †	74.6 ± 6.7	159.1 ± 12.3 †
MAP (mmHg)	65.6 ± 2.7	72.1 ± 4.3	65.3 ± 2.7	75.4 ± 3.6	91.0 ± 3.2 †	75.3 ± 3.1	92.9 ± 4.2 †

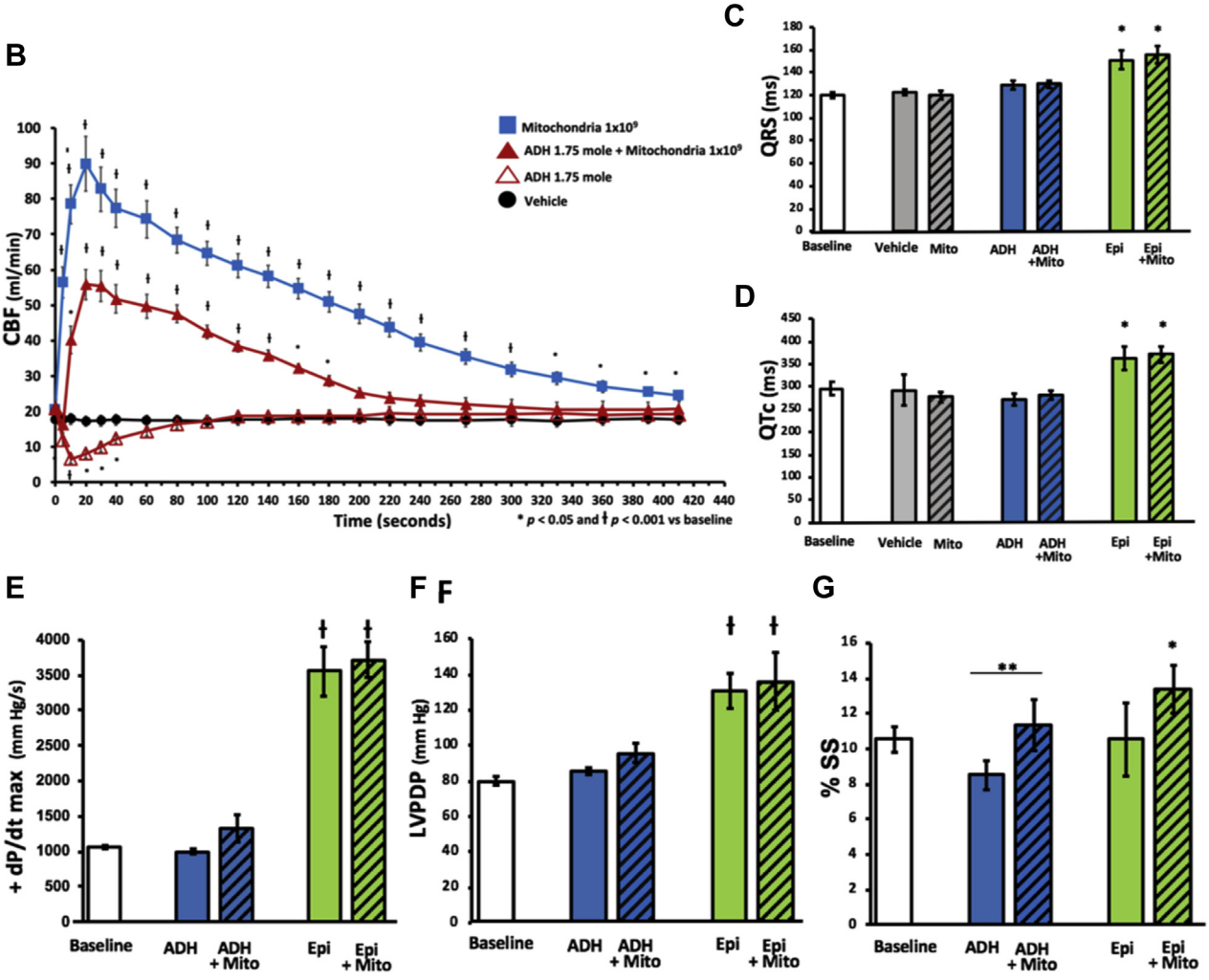

(A) Heart rate and mean arterial pressure after intracoronary injection of mitochondria (1×10^9) at normal condition (baseline) and during coronary vasoconstriction induced by antidiuretic hormone (ADH; 1.75 nmol) and tachycardia induced by epinephrine (Epi; 0.5 μmol). † $p < 0.001$ versus baseline ($n = 6$). **(B)** Coronary blood flow after intracoronary injection of mitochondria (1×10^9), vehicle, ADH, and ADH + mitochondria (1×10^9). * $p < 0.05$ and † $p < 0.001$ versus baseline (time 0) ($n = 6$). **(C and D)** Lengths of QRS complex and corrected QT intervals (QTc) after intracoronary injection of mitochondria (1×10^9), vehicle, ADH, ADH + mitochondria, epinephrine, and epinephrine + mitochondria. **(E, F, and G)** Left ventricular contractile assessment after intracoronary injection of the designated agents. *$p < 0.05$ versus baseline, †$p < 0.001$ versus baseline, and **$p < 0.05$ between groups designated by bars ($n = 6$). Values are mean ± SEM, averaged during 60 cardiac cycles after intracoronary injections of designated agents. Abbreviations as in Figures 2 and 3.

into the LCA ($n = 5$). The sizes of the microbeads were chosen to exceed the size ranges of mitochondria (0.5-1.0 μm) (Supplemental Figure S1). Intracoronary injection of 3-μm microbeads had no effect on hemodynamics or LV function (Supplemental Figure S2). In contrast, 10- and 150-μm microbeads, which significantly exceed the size of the injected mitochondria, resulted in significant coronary

FIGURE 5 Coronary Blood Flow and Mitochondrial Respiration Capacity

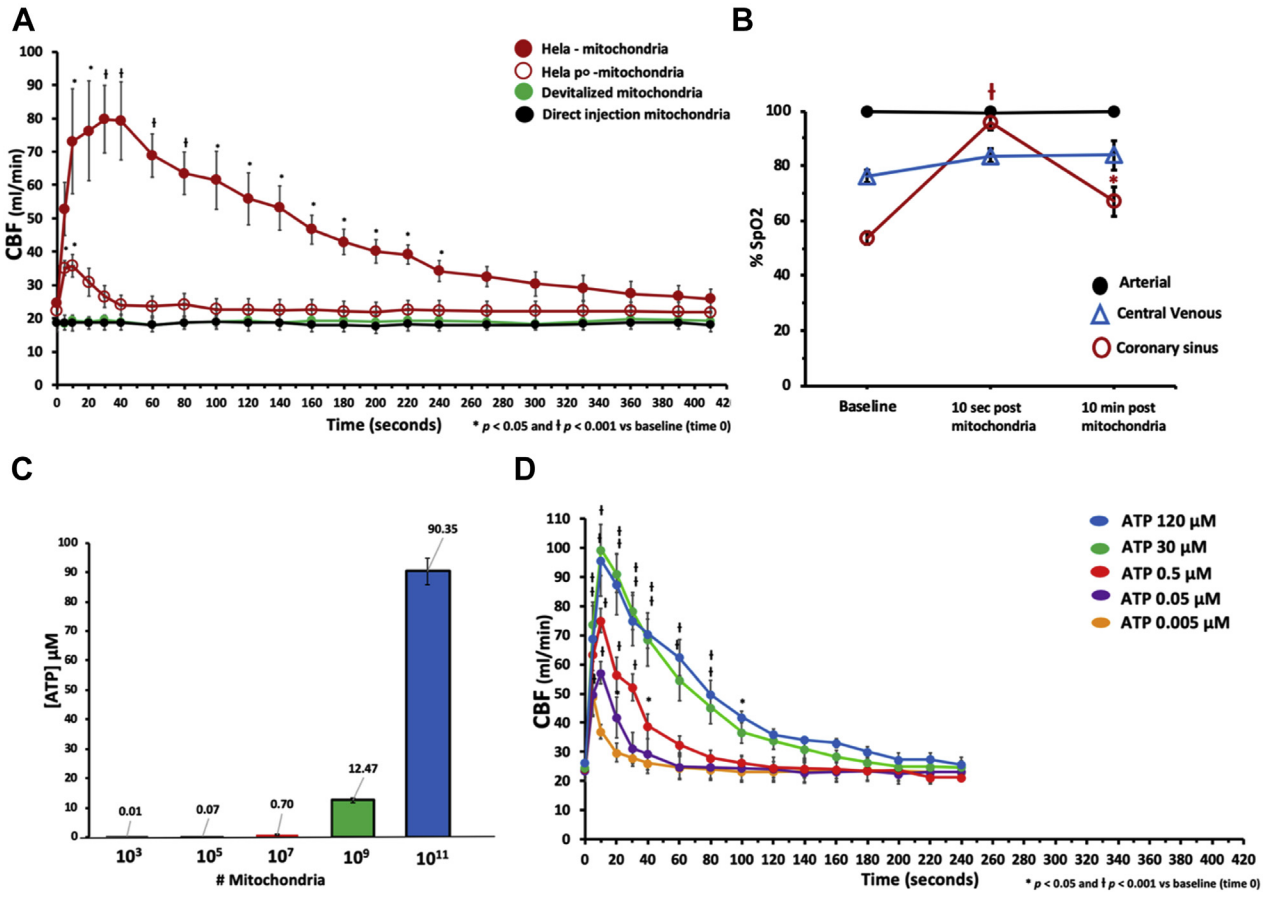

(A) Coronary blood flow on direct myocardial injection of mitochondria at 10 different sites in close proximity to the left anterior descending artery (1×10^9 total; n = 3), intracoronary injection of devitalized mitochondria (1×10^9; n = 4), and mitochondria isolated from HeLa cells and from HeLa-p^o cells (n = 6). * p < 0.05 and †p < 0.001 versus baseline (time 0). **(B)** Percentage oxygen saturation (%Spo_2) of blood from the carotid artery (arterial), superior vena cava (central venous), and coronary sinus collected 10 s (during peak increase in coronary blood flow) and 10 min after intracoronary injection of mitochondria (n = 4). Values are mean ± SEM. *p < 0.05 and †p < 0.001 versus baseline %Spo_2 within each group. **(C)** ATP content present in various concentrations of mitochondria. **(D)** Coronary blood flow on intracoronary injection of ATP alone, as measured in the various concentrations of mitochondria. *p < 0.05 and †p < 0.001 versus baseline (time 0) (n = 4). ATP = adenosine triphosphate; other abbreviations as in Figure 3.

occlusions and myocardial contractile failure (Supplemental Figure S2).

PHASE 2: EVALUATION OF INCREASE IN CORONARY BLOOD FLOW. The role of mitochondrial viability and respiration competence. In contrast to intracoronary injection of mitochondria, there was no change in CBF associated with direct injection of mitochondria to the myocardium (Figure 5A) (n = 3). If myocardial oxygen consumption increased, it would also be reflected by the decrease of coronary sinus proportion venous oxygen saturation associated with a compensatory increase in CBF (27). On the contrary, coronary sinus proportion venous oxygen saturation increased to near arterial levels immediately on intracoronary delivery of mitochondria, from 53.7% ± 2.4% to 96.1% ± 1.3% (n = 4; p < 0.001), concomitant with the increase in CBF (Figure 5B).

The role of mitochondrial viability and respiration competence in mitochondria-induced coronary vasodilation was investigated by intracoronary injection of devitalized mitochondria, HeLa and HeLa-p^o mitochondria. Intracoronary injection of devitalized mitochondria (1×10^9) did not alter CBF (n = 4) (Figure 5A). Intracoronary injection of HeLa mitochondria, which are capable of oxidative phosphorylation, increased CBF from 24.6 ± 2.9 ml/min to 79.7 ± 8.1 ml/min (n = 6; p < 0.001) (Figure 5A). In

contrast, intracoronary injection of HeLa-ρ^0 mitochondria, which are not capable of oxidative phosphorylation, had no effect on CBF (n = 6) (HeLa AUC 18,416.5 ± 2,204.4 vs. HeLa-ρ^0 AUC 9,524.27 ± 1,230.1 ml/min × s; p = 0.005) (Figure 5A).

The role of ATP. To investigate the role of mitochondrial energy synthesis in coronary vasodilation, ATP content in the previously tested mitochondrial concentrations (1×10^3, 1×10^5, 1×10^7, 1×10^9, and 1×10^{11}) was determined and the corresponding doses of ATP alone were injected into the LCA (n = 4) (Figure 5C). Intracoronary injection of ATP in the absence of mitochondria increased CBF similarly to the corresponding concentration of mitochondria (Figure 5D). However, the duration of hyperemia was significantly shorter than that observed from intracoronary injection of mitochondria. For instance, the injection of 1×10^9 mitochondria provided 6.5 ± 0.6 min of increase in CBF versus 3.3 ± 0.2 min when 30 μM of ATP (amount found in 1×10^9 mitochondria) was injected alone (p < 0.001).

Signaling pathways of coronary vasodilation. Mitochondria-induced increase in CBF was unaffected by the inhibition of endothelium-derived pathways of coronary vasodilation (nitric oxide synthase and cyclooxygenase) (Figures 6A and 6B) (n = 4 each). Inhibition of the adenosine receptors and inhibition of K_{ATP} channels also had no effect on mitochondria-induced increase in CBF (Figures 6C and 6E) (n = 4 each). In contrast, inhibition of K_{IR} channels significantly attenuated mitochondria-induced increase in CBF from 97.8 ± 11.9 ml/min to 60.1 ± 8.4 ml/min (p = 0.018) and to 50.2 ± 7.6 ml/min (p = 0.012) at barium chloride concentrations 10 and 100 μM, respectively (Figure 6E) (n = 4).

PHASE 3: CARDIOPROTECTIVE EFFICACY OF MITOCHONDRIAL TRANSPLANTATION BY INTRACORONARY DELIVERY IN ISCHEMIA-REPERFUSION INJURY. Animals. There was no significant difference in animal body weight between the mitochondria group and the vehicle-only group (p = 0.133). One animal in the vehicle group died of refractory ventricular fibrillation at the onset of reperfusion.

Post-ischemic myocardial function. There were no differences in the pre-ischemic vital signs or LV contractility between the 2 groups (Figures 7A to 7G). With the onset of regional ischemia, significant depressions in LV contractility were observed in both the mitochondria group (n = 8) and vehicle-only group (n = 7) (Figures 7C to 7G), but no differences were observed between the groups. During reperfusion, all contractile measures were significantly higher in the mitochondria group (Figures 7C to 7G) and returned to pre-ischemic levels by the end of the reperfusion period. Similarly, echocardiographic analyses showed superior LV function in the mitochondria group as measured by proportion of LV fractional shortening (23.8% ± 2.8% vs. 13.9% ± 1.2%; p = 0.004), proportion LV fractional area change (41.8% ± 2.9% vs. 28.6% ± 2.3%; p = 0.003), and proportion ejection fraction (EF) (47.9% ± 4.6% vs. 30.2% ± 2.3%; p = 0.003) at 2 h of reperfusion (Figures 8B to 8D, Videos 3 and 4).

Post-ischemic coronary blood flow. The mitochondria group exhibited significantly higher CBF throughout the reperfusion period compared with the vehicle-only group. Pre-ischemic CBF was 13.4 ± 1.9 ml/min and 11.1 ± 2.5 ml/min in the mitochondria group and vehicle-only group, respectively (Figure 8A) (p = 0.462). With the onset of ischemia, CBF decreased to near 0 ml/min in both groups. Immediately on reperfusion, reactive hyperemia was observed in both groups to peak at CBF levels of 76.0 ± 4.5 ml/min in the mitochondria group and 67.4 ± 16.5 ml/min in the vehicle-only group. However, 19.2 min post-reperfusion, mean CBF remained significantly higher in the mitochondria group, and this increase was present until the end of the 120-min reperfusion period (AUC 1,329.5 ± 277.9 vs. 550.2 ± 119.1 ml/min × s; p = 0.042) (Figure 8A).

Infarct size. There was no difference in the mean area at risk (proportion of LV mass) between the mitochondria group and the vehicle-only group (37.4 ± 1.9 vs. 35.4 ± 2.7; p = 0.343). Infarct size (proportion of area at risk) was significantly reduced in the mitochondria group (7.3% ± 1.1% vs. 38.6% ± 2.7%; p < 0.001) (Figures 8E and 8F).

DISCUSSION

In our previous studies, transplantation of mitochondria was performed by direct tissue injection with a 28-gauge-needle syringe (6,8–10,14,15). This technique allows specific delivery of the donor mitochondria to a localized area of the myocardium. Although effective, it requires open-heart access, potential manipulation of the heart, and multiple injections. We have previously reported the histologic quantification of radioactive, iron oxide-labeled, human mitochondria transplanted to isolated perfused rabbit hearts through intracoronary delivery (11). Similar to our present findings, positron emission tomographic imaging of these isolated hearts showed global distribution of radioactive signal throughout the entire organ, whereas histologic analysis showed mitochondria within blood vessels (25.7%), cardiomyocytes (23.6%), and the

FIGURE 6 Mechanism of Mitochondria-Induced Coronary Vasodilation

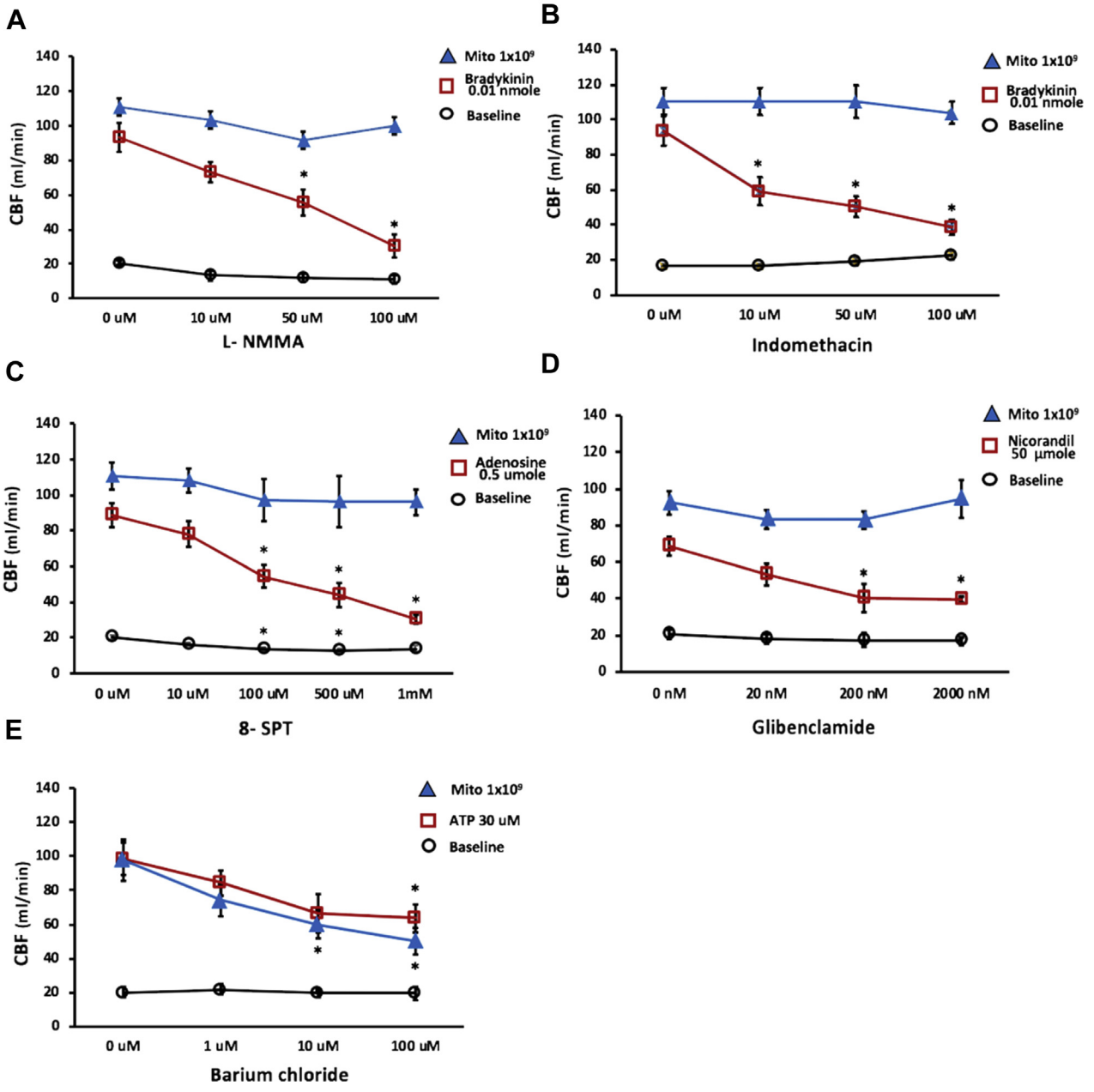

(A) CBF on intracoronary injection of mitochondria (1×10^9) after pretreatment with increasing concentrations of nitric oxide synthase inhibitor nitro-monomethyl L-arginine (L-NMMA). CBF after bradykinin injection (nitric oxide synthase activator, 0.01 nmol) shows positive inhibition of nitric oxide synthase ($n = 4$). Baseline indicates CBF after 20 min of pretreatment with L-NMMA before intracoronary injection of mitochondria or bradykinin. **(B)** CBF on intracoronary injection of mitochondria after pretreatment with increasing concentrations of cyclooxygenase inhibitor indomethacin. CBF after bradykinin injection (cyclooxygenase activator, 0.01 nmol) shows positive inhibition of cyclooxygenase ($n = 4$). **(C)** CBF on intracoronary injection of mitochondria after pretreatment with increasing concentrations of adenosine receptor inhibitor 8-*p*-sulfophenyl theophylline (8-SPT). CBF after adenosine (0.5 µmol) injection shows positive inhibition of adenosine receptor ($n = 4$). **(D)** CBF on intracoronary injection of mitochondria after pretreatment with increasing concentrations of K_{ATP}-channel inhibitor glibenclamide. CBF after nicorandil injection (K_{ATP}-channel activator, 50 µmol) shows positive inhibition of K_{ATP} channels ($n = 4$). **(E)** CBF on intracoronary injection of mitochondria after pretreatment with increasing concentrations of K_{IR}-channel inhibitor barium chloride. CBF after ATP injection (K_{IR}-channel activator, 30 µM) shows positive inhibition of K_{IR} channels ($n = 4$). Values are ± SEM; * $p < 0.05$ versus CBF in the absence of inhibitor within the same group. Abbreviations as in Figures 3 and 5.

FIGURE 7 Myocardial Function After Intracoronary Mitochondrial Transplantation in Regional Myocardial Ischemia-Reperfusion Injury

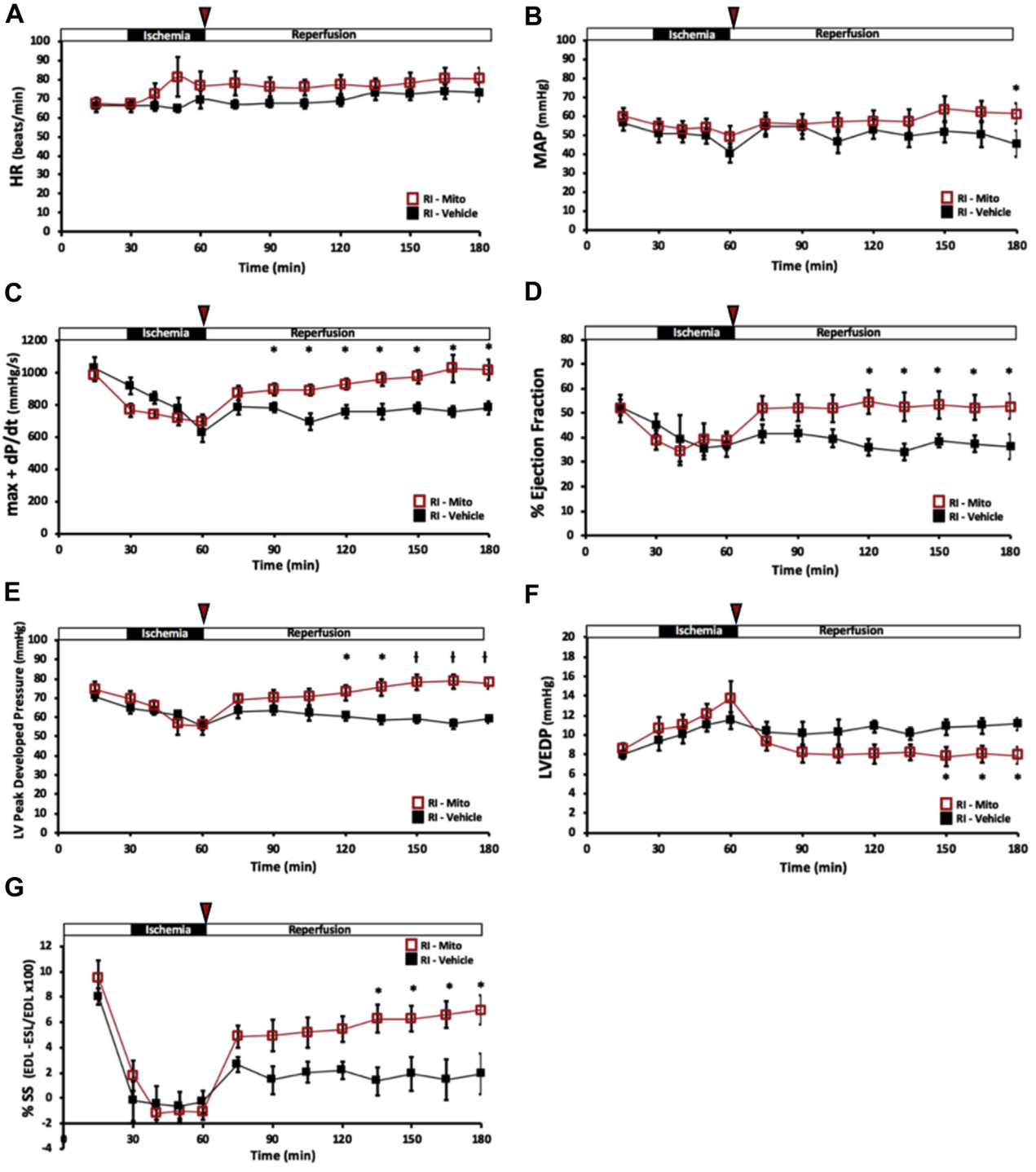

(A) Heart rate, **(B)** mean arterial pressure, **(C)** max + dP/dt (mm Hg), **(D)** proportion ejection fraction, **(E)** left ventricular peak developed pressure (mm Hg), **(F)** left ventricular end-diastolic pressure (mm Hg), and **(G)** proportion segmental shortening at the end of systole in the vehicle-only group (RI-Vehicle) and mitochondria group (RI-Mito) at pre-ischemia, during 30 min of regional ischemia and 120 min of reperfusion. **Arrowheads** denote the time of intracoronary injection of either vehicle or mitochondria. * $p < 0.05$ and † $p < 0.001$ between the 2 groups. Abbreviations as in Figure 2.

FIGURE 8 Coronary Blood Flow and Tissue Survival After Intracoronary Mitochondrial Transplantation in Regional Ischemia-Reperfusion Injury

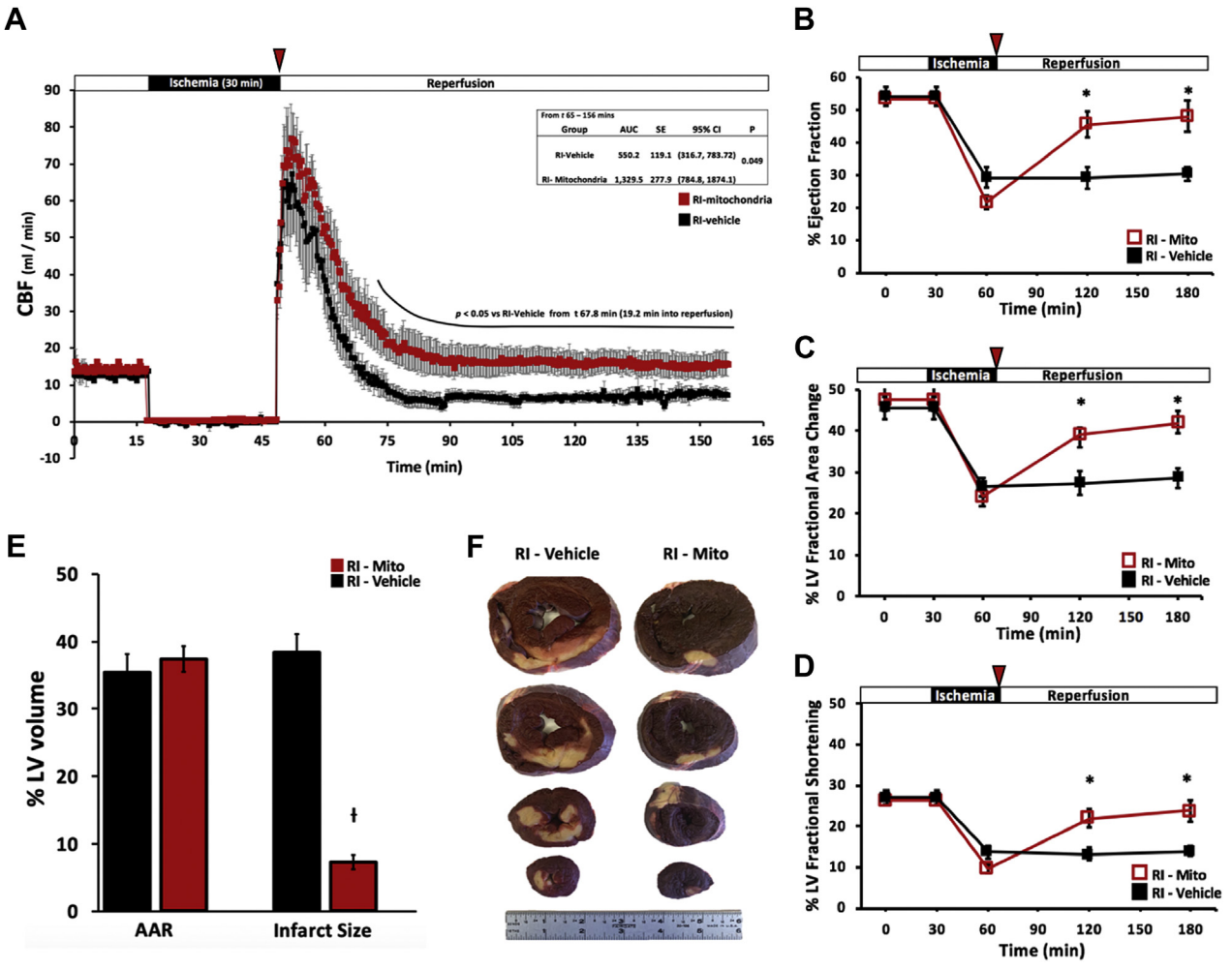

(A) CBF at the left anterior descending artery distal to temporary occlusion in the vehicle group (RI-Vehicle) and mitochondria group (RI-Mito). $p < 0.05$ between 2 groups from 67.8 min (19.2 min into reperfusion) to the end of reperfusion (120 min). Areas under the curve are compared between the 2 groups from 65 min after reactive hyperemia, in which mean CBF exhibited a statistically significant difference. **(B, C, and D)** Echocardiographic analysis of left ventricular (LV) function analyzed from short-axis view and M-mode tracings at the midpapillary level. Values are mean ± SEM; *$p < 0.05$ versus RI-Vehicle (Videos 3 and 4). **(E)** Area at risk (proportion LV volume) and infarct size proportion of area at risk) after 120 min of reperfusion. †$p < 0.001$ versus RI-Vehicle. **Arrowheads** denote the time of intracoronary injection of either vehicle or mitochondria. **(F)** Representative photograph of hearts stained with triphenyl tetrazolium, showing infarct sizes in RI-Vehicle and RI-Mitochondria groups. Abbreviations as in Figure 3.

interstitium (11). Distribution of mitochondria appeared scattered but uniform, consistent with global dispersal by intravascular delivery, as opposed to clustered appearance when delivered via localized direct injections into the myocardium (11). Our previous studies also suggest that the number of mitochondria needed for cardioprotection is not a function of the absolute number of mitochondria transplanted; for example, 2×10^5 to 2×10^8 mitochondria per gram of tissue had the same extent of improvements in infarct sizes, regional segmental shortening, and increased total tissue ATP content in the area at risk (6,8,9).

In the present study, we focused our attention on demonstrating the systemic distribution of mitochondria when delivered via the coronary arteries. We first evaluated the uptake and biodistribution of mitochondria by intracoronary delivery, using ^{18}F-rhodamine-6G, which specifically labels actively respiring mitochondria (16). Positron emission tomographic imaging demonstrated that intracoronary delivery distributed mitochondria specific to the

vascular supply of LCA. Minor signal was detected in the descending aorta, likely because of forward flow of blood from the ascending aorta as mitochondria were injected into the LCA. The tracer signal was not detected in other organs despite the injection of much higher concentrations of mitochondria than the therapeutic dosage. We did not demonstrate long-term viability of the donor mitochondria in this nonsurvival study. We have previously demonstrated the presence of transplanted mitochondria in the area at risk in swine hearts 28 days after injection of vehicle containing mitochondria (10). These regions displayed higher total tissue ATP content than the experimental control area at risk that received vehicle-only injections (10).

The mechanisms of vascular extravasation of mitochondria are beyond the scope of the current investigation and remain to be fully elucidated. However, the rapidity of mitochondria transport to cardiac cells is likely to involve mechanisms similar to those involved in bacterial or viral uptake (28–30). Support for such pathways may be seen in our studies showing the rapid uptake of mitochondria, using ^{18}F-rhodamine-6G-labeled mitochondria (11), and that reported by Bomberger et al. (31) demonstrating the rapid cellular uptake of rhodamine-R18-labeled outer membrane vesicles, as well as those by others showing rapid uptake of intact extracellular vesicles (28,29). Moreover, numerous studies demonstrating cellular transformations of exogenous mitochondria suggest that the process requires both the physical and functional integrity of mitochondria. We previously showed that only intact, respiration-competent mitochondria are taken up by cardiac cells (11,12). Kesner et al. (29) also reported that cellular uptake of exogenous mitochondria is inhibited by disruptions in the mitochondrial outer membrane. These results correlate with our previous findings demonstrating the inability of nonviable mitochondria, mitochondrial fractions, mitochondrial deoxyribonucleic acid, ribonucleic acid, and exogenous adenosine diphosphate and ATP to provide protection to the ischemic heart (8,14).

A major safety concern of intracoronary injection of particles is the risk of microvascular obstruction. Concerns in regard to intracoronary infusion of particles >10 μm in diameter have been raised (32), whereas others have reported various degrees of safety with larger agents such as mesenchymal stem cells (≈20 μm) which may exceed the diameter of some resistance arterioles (33–35). In contrast, mitochondria are 0.3 ± 0.1 μm in diameter (Supplemental Figure S1) in both swine and in humans (11,13), which is smaller than the diameter of the smallest capillaries present in human and swine hearts (5–10 μm) (35). According to our results, intracoronary injection of mitochondria at concentrations of 1×10^3 to 1×10^{11} has no adverse effects on coronary patency or cardiac function. Mitochondria were also safely injected into severely constricted coronary arteries as well as under hemodynamic stresses of significant tachycardia and hypertension, all of which often accompany various pathologic conditions of the heart. The safety of intracoronary infusion of mitochondria is further corroborated by adverse response to intracoronary injection of microbeads (10 and 150 μm) that are larger than the diameters of the small and midsize coronary arterioles of swine (36), resulting in significant coronary occlusion, arrhythmia, and contractile failure, none of which were observed with intracoronary injections of mitochondria.

To our knowledge, this is the first study to provide evidence that intracoronary infusion of mitochondria significantly increases CBF. This effect on CBF was immediate and concentration dependent, with maximal hyperemia achieved by intracoronary injection of 1×10^9 mitochondria. The duration of hyperemia by mitochondria (6.5 ± 0.6 min) is significantly higher than that of many of the mainstream pharmacologic coronary vasodilators such as papaverine (≈50 s) and adenosine (≈20 s) (37), and the hyperemia was safely extendable by serial injections. Furthermore, intracoronary injection of mitochondria was able to entirely reverse the vasoconstrictions induced by a potent coronary vasoconstrictor.

Our results suggest that ATP is at least partly responsible for mitochondria-induced hyperemia because the increase in CBF was achievable only through the delivery of intact, respiration-competent mitochondria. ATP has been reported to be a potent dilator of coronary circulation (38–40). This is further corroborated by our finding that mitochondria-induced hyperemia was attenuated only by the inhibition of the K_{IR} channels and unaffected by the inhibition of nitric oxide synthase, cyclooxygenase, or adenosine receptor. These findings are consistent with previous reports that ATP-mediated coronary vasodilation is largely independent of endothelium-derived pathways or the breakdown of ATP to adenosine (40), and that K_{IR} channel is involved in ATP-mediated vasodilation (23,41). The inhibition of K_{IR} channels only partly abolished the vasodilatory effect by mitochondria, suggesting the presence of additional and yet-unidentified mechanisms.

CBF in response to intracoronary injection of ATP alone paralleled that of the corresponding mitochondrial concentrations in the magnitude of increase in CBF; however, the durations of hyperemia

were significantly shorter. One possible explanation for these findings may be related to the short half-life of exogenous ATP in blood (0.5 to 1.5 s) (42), rendering it undesirable for clinical application (43). Intact mitochondria with active electron transport chain and ATP synthesis may continuously renew ATP as they are infused in the coronary arteries, leading to the prolongation of the vasodilatory effect of ATP. Support for such a mechanism comes from our previous studies demonstrating increased cellular ATP content and ATP synthesis after mitochondrial transplantation (9,11–13). Although further studies are required to delineate the full mechanism, our results implicate the sustained production of ATP as a key mediator and the activation of K_{IR} channels as a downstream pathway of mitochondria-induced coronary vasodilation.

Our results demonstrate strong cardioprotective efficacy of intracoronary mitochondrial transplantation in myocardial ischemia-reperfusion injury by improving post-ischemic function, perfusion, and infarct size. We used a model of temporary coronary occlusion followed by mitochondrial injection at reperfusion because, in current practice, most patients with acute myocardial ischemia undergo reperfusion by emergency coronary catheterization, which would also be an opportune time to administer mitochondria.

Our results also show that the increase in post-ischemic CBF was sustained throughout the 120 min of reperfusion in the mitochondria hearts compared with vehicle hearts. The increase in CBF is an advantageous phenomenon unique to intracoronary injection and absent when mitochondria are directly injected into the heart muscle. Although the improvement of CBF is therapeutically beneficial, our previous studies have shown that direct injection and intravascular delivery provide similar improvements in post-ischemic functional recovery and infarct size (8,9,11). This indicates the presence of a primary cardioprotective process at the level of the tissue that is separate and successive to the improved CBF after intracoronary infusion of mitochondria. At present, our studies have found that direct injections of mitochondria lead to increase in the ATP content of the recipient tissue, upregulation of proteomic pathways for the mitochondrion and precursor metabolites, reduction of inflammatory mediators, upregulation of antiapoptotic markers, and replenishment of damaged mitochondrial deoxyribonucleic acid (8–10). It is therefore reasonable to suspect, at least at the tissue level, that intracoronary delivery of mitochondria leads to the same changes as direct muscle injection once they have reached the tissue. Nevertheless, other investigations have shown benefits of coronary vasodilators in improving microvascular dysfunction and impaired perfusion that are present in ischemic injury (44,45). In the setting of ischemia-reperfusion, mitochondria resulted in a post-peak CBF that was higher throughout the entire reperfusion period compared with a transient effect of approximately 7 min in the nonischemic hearts. Although the full mechanism remains to be elucidated, the biochemical milieu of the ischemic heart is markedly different from that of the normal heart. We speculate that intracoronary delivery of mitochondria may offer the dual benefit of counteracting impaired tissue perfusion at the level of the coronary arteries and rescuing metabolic and inflammatory pathways at the tissue level. The rescue of cardiomyocytes from both approaches may further reduce the production of various vasoconstrictive signals (8,9), producing a synergistic and cascading improvement to CBF, myocardial function, and infarct size.

Intracoronary use of mitochondria provides a variety of possible applications for both angiographic and surgical therapies by exploiting its multifactorial rescue of myocellular damage (9,14), coronary vasodilation, and the versatility of the minimally invasive catheter-based delivery. Mitochondria can be effectively delivered by bolus injections to the heart by rapid continuous-flow infusions rather than by the stop-reflow technique, which involves the temporal coronary occlusions used during certain cell therapies such as mesenchymal stem cells, which carry the risk of arrhythmia and myocardial injury (46). Mitochondria may also serve as an adjunct to percutaneous coronary intervention treatments for acute myocardial ischemia, in place of current vasodilatory drugs investigated for the prevention and treatment of post-ischemic microvascular dysfunction (“no reflow”), including adenosine (47), nitroprusside (48), verapamil (49), and nicorandil (50), without the risks of the pharmacologic adverse effects. Although validation in humans is required, mitochondria may offer a safer profile while providing near-maximum vasodilatory capacity of the coronary vasculature (51). Mitochondria may also be used during coronary catheterization in subacute settings such as myocardial stunning or hibernation because contractile improvements have been shown from transplantations 2 to 15 days after ischemic injury in humans (15).

STUDY LIMITATIONS. Certain limitations of our study must be considered when these results are interpreted. First, in our investigation of safety, we used only healthy adult swine. Although we have attempted to mimic pathologic cardiac physiology with vasoactive drugs, our use of healthy subjects

may underestimate potential complications associated with additional cardiopulmonary dysfunction such as heart failure, respiratory distress, and/or other organ dysfunction. We have also not yet obtained analyses of additional organ function (e.g., kidneys, liver) after intracoronary injection of mitochondria. Although previous animal and human data have not detected changes in systemic inflammatory markers, or respiratory or renal function, randomized controlled clinical trials addressing short-term and long-term outcomes are required.

CONCLUSIONS

In conclusion, mitochondrial transplantation by intracoronary delivery to the myocardium is safe and efficacious, with strong vasodilatory capacity, which translates to significant therapeutic efficacy in treating myocardial ischemia-reperfusion injury. The capacities of metabolic restoration, cardiomyocyte salvage, and coronary vasodilation may be harnessed to produce therapeutic synergy, with the present findings serving as a preclinical platform to help optimize human application across the clinical spectrum of ischemic heart disease and coronary regulation.

ADDRESS FOR CORRESPONDENCE: Dr. James D. McCully, Department of Cardiac Surgery, Boston Children's Hospital, 300 Longwood Avenue, Enders-407, Boston, Massachusetts 02115. E-mail: james.mccully@childrens.harvard.edu.

PERSPECTIVES

COMPETENCY IN MEDICAL KNOWLEDGE: The use of healthy mitochondria to treat ischemia-reperfusion injury has been successfully applied in various animal models in the heart, kidneys, liver, lung, and brain. The therapeutic benefit of mitochondrial transplantation in humans was recently described in pediatric cardiac ischemia-reperfusion patients, using direct myocardial injection into the myocardium.

TRANSLATIONAL OUTLOOK: This study supplies the preclinical validation of safety and efficacy of intracoronary delivery of mitochondria, which significantly widens the application and potential usage of mitochondrial transplantation. Controlled, multicenter, prospective studies are warranted in pediatric and adult cardiac patients to confirm safety and efficacy.

REFERENCES

1. Benjamin EJ, Blaha MJ, Chiuve SE, et al., American Heart Association Statistics Committee and Stroke Statistics Subcommittee. Heart disease and stroke statistics–2017 update: a report from the American Heart Association. Circulation 2017;135:e146–603.

2. Lesnefsky EJ, Chen Q, Slabe TJ, et al. Ischemia, rather than reperfusion, inhibits respiration through cytochrome oxidase in the isolated, perfused rabbit heart: role of cardiolipin. Am J Physiol Heart Circ Physiol 2004;287:H258–67.

3. McCully JD, Wakiyama H, Cowan DB, Federman M, Parker RA, Levitsky S. Diazoxide amelioration of myocardial injury and mitochondrial damage during cardiac surgery. Ann Thorac Surg 2002;74:2138–45.

4. Levitsky S, Laurikka J, Stewart RD, Campos CT, Lahey SJ, McCully JD. Mitochondrial DNA deletions in coronary artery bypass grafting patients. Eur J Cardiothorac Surg 2003;24:777–84.

5. Hsieh YJ, Wakiyama H, Levitsky S, McCully JD. Cardioplegia and diazoxide modulates STAT3 activation and DNA binding. Ann Thorac Surg 2007;84:1272–8.

6. McCully JD, Levitsky S, Del Nido PJ, Cowan DB. Mitochondrial transplantation for therapeutic use. Clin Transl Med 2016;5:16.

7. Rousou AJ, Ericsson M, Federman M, Levitsky S, McCully JD. Opening of mitochondrial K_{ATP} channels enhances cardioprotection through the modulation of mitochondrial matrix volume, calcium accumulation, and respiration. Am J Physiol Heart Circ Physiol 2004;287:H1967–76.

8. McCully JD, Cowan DB, Pacak CA, Toumpoulis IK, Dayalan H, Levitsky S. Injection of isolated mitochondria during early reperfusion for cardioprotection. Am J Physiol Heart Circ Physiol 2009;296:H94–105.

9. Masuzawa A, Black KM, Pacak CA, et al. Transplantation of autologously derived mitochondria protects the heart from ischemia-reperfusion injury. Am J Physiol Heart Circ Physiol 2013;304:H966–82.

10. Kaza AK, Wamala I, Friehs I, et al. Myocardial rescue with autologous mitochondrial transplantation in a porcine model of ischemia/reperfusion. J Thorac Cardiovasc Surg 2017;153:934–43.

11. Cowan DB, Yao R, Akurathi V, et al. Intracoronary delivery of mitochondria to the ischemic heart for cardioprotection. PLoS One 2016;11:e0160889.

12. Pacak AC, Preble JM, Kondo H, et al. Actin-dependent mitochondrial internalization in cardiomyocytes: evidence for rescue of mitochondrial function. Biol Open 2015;4:622–6.

13. Cowan DB, Yao R, Thedsanamoorthy JK, Zurakowski D, Del Nido PJ, McCully JD. Transit and integration of extracellular mitochondria in human heart cells. Sci Rep 2017;7:17450.

14. McCully JD, Cowan DB, Emani SM, Del Nido PJ. Mitochondrial transplantation: from animal models to clinical use in humans. Mitochondrion 2017;34:127–34.

15. Emani SM, Piekarski BL, Harrild D, Del Nido PJ, McCully JD. Autologous mitochondrial transplantation for dysfunction after ischemia-reperfusion injury. J Thorac Cardiovasc Surg 2017;154:286–9.

16. Preble JM, Pacak CA, Kondo H, MacKay AA, Cowan DB, McCully JD. Rapid isolation and purification of mitochondria for transplantation by tissue dissociation and differential filtration. J Vis Exp 2014;91:e51682.

17. Bartholomä MD, Zhang S, Akurathi V, et al. (18) F-labeled rhodamines as potential myocardial perfusion agents: comparison of pharmacokinetic properties of several rhodamines. Nucl Med Biol 2015;42:796–803.

18. Hannon JP, Bossone CA, Wade CE. Normal physiological values for conscious pigs used in biomedical research. Lab Anim Sci 1990;40:293–8.

19. Toyoda Y, Di Gregorio V, Parker RA, Levitsky S, McCully JD. Anti-stunning and anti-infarct effects of adenosine-enhanced ischemic preconditioning. Circulation 2000;102:III326–31.

20. Muller JM, Myers PR, Laughlin MH. Vasodilator response of coronary resistance arteries of exercise-trained pigs. Circulation 1994;89:2308–14.

21. Long W, Mokelke EA, Neeb ZP, Alloosh M, Edwards JM, Sturek M. Adenosine receptor regulation of coronary blood flow in Ossabaw miniature swine. J Pharmacol Exp Ther 2010;335:781–7.

22. McCully JD, Levitsky S. Mitochondrial ATP-sensitive potassium channels in surgical

cardioprotection. Arch Biochem Biophys 2003;420:237–45.

23. Crecelius AR, Kirby BS, Luckasen GJ, Larson DG, Dinenno FA. ATP-mediated vasodilation occurs via activation of inwardly rectifying potassium channels in humans. J Physiol 2012;590:5349–59.

24. Su JB, Hoüel R, Héloire F, et al. Stimulation of bradykinin B_1 receptors induces vasodilation in conductance and resistance coronary vessels in conscious dogs: comparison with B_2 receptor stimulation. Circulation 2000;101:1848–53.

25. Quayle JM, Nelson MT, Standen NB. ATP-sensitive and inwardly rectifying potassium channels in smooth muscle. Physiol Rev 1997;77:1165–232.

26. Lang RM, Badano LP, Mor-Avi V, et al. Recommendations for cardiac chamber quantification by echocardiography in adults: an update from the American Society of Echocardiography and the European Association of Cardiovascular Imaging. J Am Soc Echocardiogr 2015;28:1–39.

27. Yasuda T, Sawa S, Ishikawa N, Tanaka N. Simultaneous measurement of coronary sinus oxygen saturation and blood flow during terminal warm blood cardioplegia in coronary artery bypass grafting. Ann Thorac Cardiovasc Surg 1998;4:271–4.

28. Jäger J, Keese S, Roessle M, Steinert M, Schromm AB. Fusion of *Legionella pneumophila* outer membrane vesicles with eukaryotic membrane systems is a mechanism to deliver pathogen factors to host cell membranes. Cell Microbiol 2015;5:607–20.

29. Kesner EE, Saada-Reich A, Lorberboum-Galski H. Characteristics of mitochondrial transformation into human cells. Sci Rep 2016;6:26057.

30. O'Donoghue EJ, Krachler AM. Mechanisms of outer membrane vesicle entry into host cells. Cell Microbiol 2016;11:1508–17.

31. Bomberger JM, Maceachran DP, Coutermarsh BA, Ye S, O'Toole GA, Stanton BA. Long-distance delivery of bacterial virulence factors by *Pseudomonas aeruginosa* outer membrane vesicles. PLoS Pathogens 2009;5:e1000382.

32. Bolli R, Tang XL, Sanganalmath SK, et al. Intracoronary delivery of autologous cardiac stem cells improves cardiac function in a porcine model of chronic ischemic cardiomyopathy. Circulation 2013;128:122–31.

33. Wehman B, Siddiqui O, Jack G, et al. Intracoronary stem cell delivery to the right ventricle: a preclinical study. Semin Thorac Cardiovasc Surg 2016;28:817–24.

34. Keith MC, Tokita Y, Tang XL, et al. Effect of the stop-flow technique on cardiac retention of c-kit positive human cardiac stem cells after intracoronary infusion in a porcine model of chronic ischemic cardiomyopathy. Basic Res Cardiol 2015;110:503.

35. Potter RF, Groom AC. Capillary diameter and geometry in cardiac and skeletal muscle studies by means of corrosion casts. Microvasc Res 1983;25:68–84.

36. Kassab GS, Rider CA, Tang NJ, Fung YC. Morphometry of pig coronary arterial trees. Am J Physiol 1993;265:H350–65.

37. Layland J, Carrick D, Lee M, Oldroyd K, Berry C. Adenosine: physiology, pharmacology, and clinical applications. J Am Coll Cardiol Intv 2014;6:581–91.

38. Farias M, Gorman MW, Savage MV, Feigl EO. Plasma ATP during exercise: possible role in regulation of coronary blood flow. Am J Physiol Heart Circ Physiol 2005;288:H1586–90.

39. Horiuchi T, Dietrich HH, Hongo K, Dacey RG Jr. Comparison of P2 receptor subtypes producing dilation in rat intracerebral arterioles. Stroke 2003;34:1473–8.

40. Brown IP, Thompson CI, Belloni FL. Mechanisms of coronary vasodilation produced by ATP in guinea-pig isolated perfused heart. Br J Pharmacol 1992;105:211–5.

41. Smith PD, Brett SE, Luykenaar KD, et al. KIR channels function as electrical amplifiers in rat vascular smooth muscle. J Physiol 2008;586:1147–60.

42. Shapiro MJ, Jellinek M, Pyrros D, Sundine M, Baue AE. Clearance and maintenance of blood nucleotide levels with adenosine triphosphate-magnesium chloride injection. Circ Shock 1992;36:62–7.

43. Skrabanja AT, Bouman EA, Dagnelie PC. Potential value of adenosine 5′-triphosphate (ATP) and adenosine in anesthesia and intensive care medicine. Br J Anaesth 2005;94:556–62.

44. Matsumura K, Jeremy RW, Schaper J, Becker LC. Progression of myocardial necrosis during reperfusion of ischemic myocardium. Circulation 1998;97:795–804.

45. Gao Q, Yang B, Guo Y, Zheng F. Efficacy of adenosine in patients with acute myocardial infarction undergoing primary percutaneous coronary intervention: a PRISMA-compliant meta-analysis. Medicine (Baltimore) 2015;94:e1279.

46. Grieve SM, Bhindi R, Seow J, et al. Microvascular obstruction by intracoronary delivery of mesenchymal stem cells and quantification of resulting myocardial infarction by cardiac magnetic resonance. Circ Heart Fail 2010;3:e5–6.

47. Mahaffey KW, Puma JA, Barbagelata NA, et al. Adenosine as an adjunct to thrombolytic therapy for acute myocardial infarction: results of a multicenter, randomized, placebo-controlled trial: the Acute Myocardial Infarction Study of Adenosine (AMISTAD) trial. J Am Coll Cardiol 1999;34:1711–20.

48. Barcin C, Denktas AE, Lennon RJ, et al. Comparison of combination therapy of adenosine and nitroprusside with adenosine alone in the treatment of angiographic no-reflow phenomenon. Catheter Cardiovasc Interv 2004;61:484–91.

49. Hang CL, Wang CP, Yip HK, et al. Early administration of intracoronary verapamil improves myocardial perfusion during percutaneous coronary interventions for acute myocardial infarction. Chest 2005;128:2593–8.

50. Ishii H, Ichimiya S, Kanashiro SM, et al. Impact of a single intravenous administration of nicorandil before reperfusion in patients with ST-segment-elevation myocardial infarction. Circulation 2005;112:1284–8.

51. Schelbert HR. Anatomy and physiology of coronary blood flow. J Nucl Cardiol 2010;17:545–54.

KEY WORDS ischemia-reperfusion injury, mitochondria, mitochondrial transplantation, myocardial protection

APPENDIX For supplemental figures and videos please see the online version of this paper.

JACC: BASIC TO TRANSLATIONAL SCIENCE VOL. 4, NO. 8, 2019

EDITORIAL COMMENT

The New Promise of Mitochondrial Transplantation for Myocardial Recovery*

W.H. Wilson Tang, MD

"There are times when a critic truly risks something, and that is in the discovery and defense of the new. The world is often unkind to new talent, new creations. The new needs friends."
—Anton Ego, in *Ratatoulle* (2007) (1)

Mitochondria are fascinating bacteria-like cellular organelles primarily located within subsarcolemmal, perinuclear, and intrafibrillar regions of the cardiomyocytes that regulate multiple cell processes, including calcium signaling, apoptosis, and cell metabolism in their hosts. We are just beginning to understand that these processes may be caused by altered expression of proteins that regulate mitochondrial dynamics in the form of fission, fusion, and autophagy, which are essential for energy production and structural integrity of the organelles (2). Indeed, altered mitochondrial biogenesis, fragmentation, and hyperplasia have long been observed in the failing myocardium, leading to the decreased capacity to oxidize fatty acid substrates seen in heart failure (3). Mitochondria contain their own circular genome encoding selected subunits of the oxidative phosphorylation complexes, and often leverage their host cells to generate the majority of their own protein components. Recent findings have revealed that mitochondria can even traverse cell boundaries, and can thereby horizontally transferred between cells. This has raised the possibility that transplantation of viable mitochondria into the injured tissues would replace or augment damaged mitochondria, allowing the potential "rescue" of a variety of cells (4). The hypothesis implies that autologous healthier mitochondria may "engraft" into the myocardium, or like mesenchymal stem cells, they might have paracrine effects that would benefit myocardial function. Even though earlier studies on this topic have provided much-needed proof of concept, logistics of direct tissue injection may be impractical beyond surgical approaches (5).

SEE PAGE 871

In this issue of *JACC: Basic to Translational Science*, Shin et al. (6) extend their prior research in autologous mitochondrial transplant to direct myocardial injection and demonstrate that autologous mitochondrial transplantation with intracoronary delivery can potentially preserve myocardial blood flow in a swine ischemia-reperfusion model. Shin et al. (6) describe 3 sets of experiments and demonstrate that: 1) intracoronary autologous mitochondria can be safely administered and are taken up by the myocardium without hemodynamic consequences; 2) compared with nonviable or other cell types, autologous mitochondria transplantation leads to an increase in coronary blood flow, likely via inwardly rectifying potassium channels; and 3) autologous mitochondrial transplantation leads to a reduction in infarct size and cardiac remodeling in an ischemia-reperfusion model. The findings are indeed intriguing, although the proposed mechanistic benefits still need to explain the physiologic outcome differences, as the observed number of mitochondria taken up seemed relatively sparse. It would be helpful to better understand "uptake" dynamics and

*Editorials published in *JACC: Basic to Translational Science* reflect the views of the authors and do not necessarily represent the views of *JACC: Basic to Translational Science* or the American College of Cardiology.

From the Kaufman Center for Heart Failure and Recovery, Heart and Vascular Institute, Cleveland Clinic, Cleveland, Ohio. Dr. Tang has reported that he has no relationships relevant to the contents of this paper to disclose.

The author attests they are in compliance with human studies committees and animal welfare regulations of the authors' institutions and Food and Drug Administration guidelines, including patient consent where appropriate. For more information, visit the *JACC: Basic to Translational Science* author instructions page.

ISSN 2452-302X https://doi.org/10.1016/j.jacbts.2019.11.009

affinity of transplanted mitochondria toward the failing myocardium via this approach. Furthermore, it is not entirely clear how to reconcile the time course of the changes in the coronary blood flow, with transient effects seen in the nonischemic hearts versus sustained improvements observed in ischemia-reperfusion hearts. The premise would have stronger support if the effects of autologous mitochondrial transplant on coronary blood flow may somehow be negated with direct inwardly rectifying potassium channel inhibition. The lack of blinding of the measurements and the lack of randomization may have limited the confidence of the findings, and such observations would require independent external validation. Nevertheless, these intriguing findings have provided promise for mitochondrial transplantation as means for promoting myocardial recovery.

The potential for metabolic modulation and myocardial salvage with intracoronary injections in the setting of cardiogenic shock is not entirely new, as the impact of impaired myocardial energetics in the failing heart has been explored for over half a century. However, the prospects of autologous mitochondrial transplantation will likely be disruptive. It may create a unique opportunity to preserve or restore myocardial function via metabolic modulation with infusion of intact organelles, a concept that has largely been focused on modulating substrate availability and therapeutic targeting of myocardial energetic processes with small molecules. First, the opportunity to perform autologous transplantation of organelles to restore solid organ function captivates the potential of a therapeutic approach in the setting of cardiogenic shock that mirrors bone marrow transplantation in hematologic malignancies even in the acute setting. Second, there are potential applications in donor organ preservation with this approach, whereby donor mitochondria can be applied either in vivo (or potentially even ex vivo after harvest within portal organ perfusion systems) to reduce ischemic organ damage or even revive those that are otherwise unsuitable for transplantation. With improved myocardial viability, the potential for extending donor organ transfer ranges and cold-time durations may be expanded. Third, it is conceivable with multiple functions of mitochondria in the myocardium that replenishment of healthier mitochondria can be leveraged in various cardiotoxic settings besides ischemia-reperfusion injuries.

We have a lot to learn from understanding which patients may be benefit from such approaches, how many mitochondria are needed and whether they behave similarly in different conditions or settings, and how to maximize the uptake into myocytes and whether they can even be administered intravenously rather than through intracoronary approaches. The beneficial effects of autologous mitochondrial transplantation still demand rigorous human clinical investigations, including prospective randomization between treatment and placebo intracoronary infusions, and the need for stringent double-blind, multicenter study designs. Also, the validation process will demand replication of similar findings from other laboratories. Although it is tempting to follow the testimonies of promising observations such as those reported in this exciting report, we are reminded of the treacherous journeys of stem cell research that have taught us the importance balance of cautious optimism and careful scrutiny in clinical therapeutics development, especially for innovative new ideas such as this. The new does need friends.

ADDRESS FOR CORRESPONDENCE: Dr. W.H. Wilson Tang, Kaufman Center for Heart Failure and Recovery, Heart and Vascular Institute, Cleveland Clinic, 9500 Euclid Avenue, Desk J3-4, Cleveland, Ohio 44195. E-mail: tangw@ccf.org.

REFERENCES

1. Wikipedia. Ratatouille Wikipedia page. Available at: https://en.wikiquote.org/wiki/Ratatouille. Accessed November 24, 2019.

2. Zhou B, Tian R. Mitochondrial dysfunction in pathophysiology of heart failure. J Clin Invest 2018;128:3716–26.

3. Brown DA, Perry JB, Allen ME, et al. Expert consensus document: Mitochondrial function as a therapeutic target in heart failure. Nat Rev Cardiol 2017;14:238–50.

4. McCully JD, Levitsky S, Del Nido PJ, Cowan DB. Mitochondrial transplantation for therapeutic use. Clin Transl Med 2016;5:16.

5. Emani SM, Piekarski BL, Harrild D, Del Nido PJ, McCully JD. Autologous mitochondrial transplantation for dysfunction after ischemia-reperfusion injury. J Thorac Cardiovasc Surg 2017;154:286–9.

6. Shin B, Saeed MY, Esch JJ, et al. A novel biological strategy for myocardial protection by intracoronary delivery of mitochondria: safety and efficacy. J Am Coll Cardiol Basic Trans Sci 2019;4:871–88.

KEY WORDS coronary blood flow, heart failure, ischemic-reperfusion, mitochondrial transplant

JACC: BASIC TO TRANSLATIONAL SCIENCE VOL. 4, NO. 8, 2019

PRECLINICAL RESEARCH

Associations of Interleukin-5 With Plaque Development and Cardiovascular Events

Anki Knutsson, PhD,[a] Harry Björkbacka, PhD,[b] Pontus Dunér, PhD,[b] Gunnar Engström, MD, PhD,[b] Christoph J. Binder, MD, PhD,[c] Anna Hultgårdh Nilsson, PhD,[a] Jan Nilsson, MD, PhD[b]

VISUAL ABSTRACT

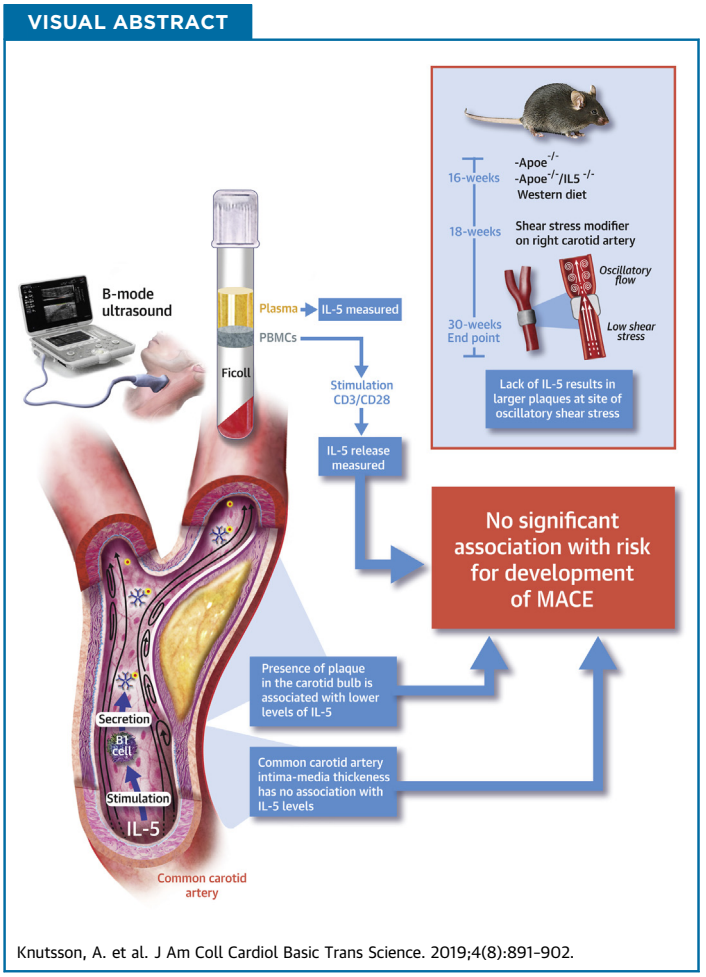

Knutsson, A. et al. J Am Coll Cardiol Basic Trans Science. 2019;4(8):891-902.

HIGHLIGHTS

- **There is strong experimental evidence that IL-5 has a protective role in atherosclerosis but the clinical importance of this remains poorly studied.**
- **In a prospective study involving 696 subjects with a follow-up of close to 17 years we show that baseline plasma levels of IL-5 do not predict risk for coronary events and stroke.**
- **However, subjects with high levels of IL-5 were less likely to have a carotid plaque at the baseline investigation.**
- **Experimental studies using a shear stress-modifying cast to the carotid artery of *Apoe*$^{-/-}$ mice deficient for IL-5 showed that lack of IL-5 was associated with increased plaque formation at sites of oscillatory blood flow.**
- **The findings are in line with previous experimental observations of an atheroprotective role of IL-5 but do not support the use of IL-5 measurement in cardiovascular risk prediction.**

ISSN 2452-302X https://doi.org/10.1016/j.jacbts.2019.07.002

JACC: BASIC TO TRANSLATIONAL SCIENCE VOL. 4, NO. 8, 2019
DECEMBER 2019:891–902

ABBREVIATIONS AND ACRONYMS

ApoE = apolipoprotein E

CVD = cardiovascular disease

HR = hazard ratio

IL-5 = interleukin-5

ILC2 = type 2 innate lymphoid cells

MACE = major adverse cardiac events

OR = odds ratio

SUMMARY

Experimental studies have suggested an atheroprotective role of interleukin (IL)-5 through the stimulation of natural immunoglobulin M antibody expression. In the present study we show that there are no associations between baseline levels of IL-5 and risk for development of coronary events or stroke during a 15.7 ± 6.3 years follow-up of 696 subjects randomly sampled from the Malmö Diet and Cancer study. However, presence of a plaque at the carotid bifurcation was associated with lower IL-5 and IL-5 deficiency resulted in increased plaque development at sites of oscillatory blood flow in *Apoe*$^{-/-}$ mice suggesting a protective role for IL-5 in plaque development. (J Am Coll Cardiol Basic Trans Science 2019;4:891–902)

Aggregation and oxidation of low-density lipoprotein (LDL) particles in the arterial intima initiates a complex array of innate and adaptive immune responses that play important roles in the development of atherosclerosis (1–3). Many of these responses are pro-inflammatory and contribute to plaque growth and de-stabilization, but a number of atheroprotective immune responses have also been identified. Antibodies reacting with danger-associated molecular patterns represent one of the best-characterized atheroprotective immune responses (4,5). These are typically immunoglobulin M (IgM) antibodies that react with oxidation-specific epitopes on damaged cells and lipoproteins and are referred to as natural antibodies because they are germline encoded. Natural antibodies play important housekeeping functions by facilitating the removal of potentially toxic structures thus limiting inflammation and injury to the tissue (6). They are produced by a relatively small subset of B cells called B1 cells that primarily resides in the spleen and the peritoneum (7). The notion that B1 cells and natural antibodies have atheroprotective functions has gained support from experimental studies showing that transfer of B1 cells in particular reverses the proatherogenic effect of splenectomy and that this effect is dependent on the ability of B1 cells to secrete IgM antibodies (8–10). The mechanisms regulating the expression of danger-associated molecular pattern-specific IgM antibodies by B1 cells remains to be fully characterized (11), but interleukin (IL)-5 released from type 2 innate lymphoid cells (ILC2) has been identified as one important stimuli (11). The observation that deletion of ILC2 in hypercholesterolemic mice accelerates atherosclerosis adds further support to the notion of an atheroprotective role of natural antibodies produced through activation of the ILC2/B1 immune pathway (12). There is also evidence from experimental studies that IL-5 plays a critical role in this atheroprotective immune pathway. Selective genetic ablation of ILC2 in LDL receptor-deficient mice accelerates the development of atherosclerosis, which is prevented by reconstitution with wild-type but not *IL5*$^{-/-}$ ILC2 (12). Similar observations were made following reconstitution of irradiated LDL receptor-deficient mice with wild-type, but not IL-5 deficient, bone marrow (13). Moreover, Zhao et al. (14) found that a macrophage overexpression of IL-5 was associated with increased plasma levels of natural antibodies and attenuation of atherosclerosis. Despite the strong experimental evidence of an atheroprotective role of IL-5, little is known about its possible importance for development of cardiovascular disease (CVD) in man. In a case-control study comparing 931 subjects with prevalent coronary heart disease and 974 controls, Clarke et al. (15) found that those in the highest tertile of plasma IL-5 had a 50% higher risk for coronary heart disease. This

From the [a]Department of Experimental Medical Science, Lund University, Lund, Sweden; the [b]Department of Clinical Sciences Malmö, Lund University, Lund, Sweden; and the [c]Department of Laboratory Medicine, Medical University of Vienna, Vienna, Austria. This study was supported by grants from the Swedish Medical Research Council, the Swedish Heart-Lung foundation, Swedish Foundation for Strategic Research, and the European Union's Seventh Framework Program (FP7/2007-2013) under grant agreement VIA n°603131. The authors have reported that they have no relationships relevant to the contents of this paper to disclose.

The authors attest they are in compliance with human studies committees and animal welfare regulations of the authors' institutions and US Food and Drug Administration guidelines, including patient consent where appropriate. For more information, visit the *JACC: Basic to Translational Science* author instructions page.

Manuscript received April 2, 2019; revised manuscript received July 9, 2019, accepted July 10, 2019.

observation is in apparent contrast to the atheroprotective role of IL-5 suggested by experimental studies but could possibly represent activation of protective responses in subjects with prevalent CVD. To resolve this issue, we studied the association between baseline levels of IL-5 (both in plasma and the release from activated leukocytes) and the risk for development of cardiovascular events during a follow-up period of more than 15 years. We also studied the association between IL-5 and carotid atherosclerosis in the study cohort as well as the development of carotid plaques at sites of artificially modified shear stress in *Apoe*$^{-/-}$mice with or without IL-5 deficiency.

SEE PAGE 903

METHODS

STUDY POPULATION. The study population consisted of a random sample (n = 700) recruited from the cardiovascular arm of the Malmö Diet and Cancer study (16) as previously described (17). Data regarding the incidence of major coronary events (fatal and nonfatal myocardial infarction, coronary artery by-pass grafting, and percutaneous coronary intervention) and stroke between the baseline investigation from 1991 to 1994 and December 31, 2014, were obtained from the Swedish Discharge Registry and the Cause of Death Registry of Sweden. Based on coronary event rate of 14% in the original cohort (n = 6,102), it was calculated that a subsample of 700 subjects would allow identification of a 5% difference in any given biomarker between incident coronary cases and controls with an alpha value of 0.01 and a power of 0.80. The random subsampling of 700 subjects was performed by an investigator not otherwise involved in the present study. Blood pressure, body mass index, cholesterol, smoking, and lipid levels were determined as previously described (18). Four subjects were excluded due to incomplete data. The study was approved by the Ethics Committee of Lund University and was conducted in accordance with the Helsinki Declaration. All subjects gave written informed consent.

B-MODE ULTRASOUND. Analysis of common carotid intima-media thickness (IMT) and carotid bulb plaque thickness were performed at the baseline investigation using an Acuson 128 CT system (Siemens AG, Erlangen, Germany) with a 7-MHz transducer as described previously (18). Images of IMT and plaque thickness were obtained in the longitudinal projection showing the thickest intima-media complex. Plaque was defined as a focal thickening of the IMT exceeding 1.2 mm and a plaque area >10 mm^2 (19).

ISOLATION OF MONONUCLEAR LEUKOCYTES. Blood was collected in heparin-containing BD Vacutainer tubes, (Becton Dickinson, Franklin Lakes, New Jersey) and mononuclear leukocytes isolated with FicollPaque Plus (GE Healthcare, Waukesha, Wisconsin) density gradient centrifugation according to the instructions of the manufacturer. The isolated cells were then suspended in 500 μl autologous serum with 500 μl 20% cold dimethyl sulfoxide in Roswell Park Memorial Institute (RPMI) 1640 medium, transferred into cryofreezing containers, and then frozen at −80°C for at least 1 h or overnight. The tubes were then transferred to −140°C and stored until analysis. At the time of analysis, cells were thawed, washed with phosphate-buffered saline supplemented with 1% human serum, and centrifuged at 330*g* for 10 min at room temperature. The cells were then resuspended in RPMI 1640 media containing 10% human serum (Gibco, Life Technologies, Bleiswijk, the Netherlands) and different T cell subsets ($CD4^+$ T cells, $CD4^+$/interferon-γ^+ Th1 cells, $CD4^+$/IL-4^+ Th2 cells, $CD4^+$/$FoxP3^+$ regulatory T cells, and $CD8^+$ T cells) were analyzed by flow cytometry as previously described (17,20,21).

IL-5 ANALYSIS. To determine the release of activated mononuclear leukocytes, 4×10^5 cells were cultured in complete RPMI and stimulated with CD3/CD28 beads (MiltenyiBiotec, Bergisch Gladbach, Germany) for 72 h at 37°C in a cell incubator (5% CO_2). Thereafter, the cell supernatants were stored at −80°C until analysis. The concentration of IL-5 in plasma and conditioned leukocyte cell culture medium were determined by multiplex technology (MesoScale Discovery, Gaithersburg, Maryland).

EXPERIMENTAL ANIMAL STUDY. Apolipoprotein E-deficient (*Apoe*$^{-/-}$) mice (B6.129P2-Apoetm1Unc/J, The Jackson Laboratory) and IL-5-deficient mice (C57BL/6-Il5tm1Kopf/J, The Jackson Laboratory) were crossed. *Il5*$^{-/-}$*Apoe*$^{-/-}$ mice were used in experiments with *Apoe*$^{-/-}$ mice as controls. Starting at the age of 16-weeks, the mice were fed an atherogenic 0.15% cholesterol-containing Western diet (WD; R638, Lantmännen, Sweden). At 18-weeks, a perivascular shear stress modifier (referred to as a cast) was placed around the right common carotid artery to generate atherosclerotic plaques by altering the pattern of hemodynamic flow, as described by Cheng et al. (22). In short, the surgery was performed under anesthesia with oxygen-carried isoflurane. Buprenorphine was administered subcutaneously at 0.1 mg/kg before and after surgery. The mice were euthanized at 30 weeks of age. Blood was collected by cardiac puncture and placed into ethylenediaminetetraacetic acid-coated tubes. Plasma was retrieved by centrifugation at

3,000 rpm for 15 min at 4 °C. The colorimetric assay Infinity Total Cholesterol (Thermo Scientific, Liverpool, United Kingdom) was used to quantify total plasma cholesterol and triglycerides and the Bio-Plex Pro Mouse Cytokine Assay (BIO-RAD) was used to quantify plasma cytokine concentrations of with IL-2, IL-4, IL-5, IL-6, IL-10, IL-12p70, IL-13, IL-17A, and tumor necrosis factor-α. Both analyses were performed according to instructions from the manufacturer. Sera were diluted between 1:100 and 1:500 and IgM antibodies to copper-oxidized LDL, malondialdehyde modified (MDA)-LDL, and phosphoryl choline-bovine serum albumin (PC-BSA) were measured by chemiluminescent enzyme-linked immunosorbent assay as previously described (23). The animal studies were approved by the Malmoe/Lund regional ethical committee (Sweden).

SAMPLE PREPARATION AND HISTOLOGIC ANALYSES. The carotid arteries were fixed in Histochoice (Amresco), embedded in paraffin, and sectioned at 5 μm. Carotid artery sections were stained with Accustain trichrome (Masson) (Sigma-Aldrich) according to the manufacturer's instructions to determine collagen content. Carotid artery sections were immunohistochemically stained using antibodies against Mac-2 (Cedarlane; Burlington, Ontario, Canada) and IgM (Vector Laboratories, Cat. No: BA-2020). Sections were deparaffinized and rehydrated in xylene and a graded series of alcohols before heat-induced antigen epitope retrieval was performed (pH 6.0, 20 min). The ImmPRESS HRP anti-rat (mouse absorbed) polymer detection kit (Vector Laboratories, MP-7444) was used for the MAC-2 staining procedure according to the manufacturer's instructions. The Vectastain ABC-kit (Vector Laboratories, PK-6100) was used for the IgM staining procedure according to the manufacturer's instructions. To detect apoptosis in the plaques, the terminal deoxynucleotidyl transferase deoxyuridine triphosphate nick-end labelling (TUNEL) assay kit—HRP-DAB (Abcam, ab206386)—was used according to the manufacturer's instructions, with the exception of interchanging the counterstain methyl green with Meyer's hematoxylin. Flat preparations of descending aortas were stained with 0.3% Oil Red O for 50 min and mounted with Mountquick (Daido Sangyo Co. LTD, Tokyo, Japan). Immunohistochemically stained sections and flat preparations were scanned and digitalized using an Aperio ScanScope digital slide scanner (Scanscope Console v8.2.0.1263, Aperio Technologies, Vista, California). Image analysis was performed using BioPix iQ software (BioPixAB, Gothenburg, Sweden). The atherosclerotic carotid lesion size is expressed as absolute area.

STATISTICS. Values are given as mean ± SD for variables with normal distribution and as median and interquartile 25th and 75th percentiles for skewed variables. Statistical comparisons of baseline variables between cases and controls were performed using univariable Cox proportional hazards regression models. In the experimental studies Student's *t*-test or the Mann-Whitney U test were used for statistical comparison between groups as appropriate. The Spearman rank test was used to calculate correlation coefficients. Kaplan-Meier plots and log rank test were used to analyze associations of IL-5 tertiles and IL-5 categories with coronary events and stroke. Cox proportional hazards regression models adjusting for the pre-specified covariates age, sex, current smoking, body mass index (BMI), diabetes, LDL, and high-density lipoprotein (HDL) cholesterol, triglycerides, systolic blood pressure, and high-sensitivity C-reactive protein (hsCRP) was used to investigate the possible influence of other risk factors on the associations of IL-5 tertiles and IL-5 categories with coronary events and stroke. The proportional hazards assumption was confirmed by visual inspection of the survival plots. In a sensitivity analysis we excluded 24 prevalent cases of major adverse cardiac events (MACE) to only study incident cases. Competing risk regression according to Fine and Gray (with deaths from causes unrelated to MACE or stroke as competing events) was used to examine the association between plasma IL-5/leukocyte IL-5 and incidence of MACE/stroke. Sub-hazard ratios (HRs) were obtained with the adjustment for potential confounding factors. Logistic regression models for used to adjust for the influence of conventional risk factors on the association between IL-5 and presence of a carotid plaque and the results presented as odds ratios (ORs) with 95% confidence interval (CI). IBM SPSS statistics version 22 was used for analyses of the clinical data and GraphPad Prism version 7 for the experimental data. A p value < 0.05 was considered statistically significant.

RESULTS

ASSOCIATIONS OF IL-5 WITH RISK FOR DEVELOPMENT OF MACE AND STROKE. Among the 696 study subjects, a total of 142 MACE (fatal and nonfatal myocardial infarction, coronary artery by-pass grafting, and percutaneous coronary interventions) were identified in national registers during a mean follow-up time of 15.7 ± 6.3 years. Subjects with MACE were more often males and suffered from diabetes (Table 1). They also had higher baseline fasting glucose, hsCRP, and systolic blood pressure as well as lower HDL cholesterol.

TABLE 1 Baseline Clinical Characteristics and Interleukin 5 Levels in Subjects With or Without a Major Adverse Cardiac Event or Stroke During Follow-Up

	MACE				Stroke			
	No (n = 553)	Yes (n = 143)	HR (95% CI)	p Value	No (n = 574)	Yes (n = 122)	HR (95% CI)	p Value
Age, yrs	65.6 ± 1.1	65.7 ± 1.2	1.13 (0.97-1.31)	ns	65.6 ± 1.1	65.6 ± 1.2	1.00 (0.85-1.18)	ns
Males, %	36.7	52.4	1.78 (1.29-2.45)	<0.001	40.1	48.4	1.54 (1.08-2.20)	ns
Current smokers, %	17.4	20.1	1.46 (0.97-2.21)	ns	17.8	18.6	1.54 (0.97-2.46)	ns
Diabetes, %	11.5	23.7	2.35 (1.59-3.47)	<0.001	13.3	17.2	1.53 (0.94-2.48)	ns
BMI, kg/m^2	26.3 ± 4.0	26.7 ± 3.9	1.03 (0.99-1.07)	ns	26.3 ± 4.0	26.3 ± 3.8	1.00 (0.96-1.05)	ns
f-glucose, mmol/l	5.3 ± 1.4	5.6 ± 2.0	1.13 (0.97-1.31)	<0.001	5.3 ± 1.4	5.6 ± 1.8	1.15 (1.04-1.28)	0.009
LDL, mmol/l	4.4 ± 1.0	4.4 ± 1.0	0.99 (0.84-1.17)	ns	4.5 ± 1.0	4.2 ± 1.1	0.80 (0.66-0.98)	0.028
HDL, mmol/l	1.4 ± 0.4	1.3 ± 0.4	0.41 (0.24-0.69)	0.001	1.4 ± 0.4	1.3 ± 0.4	0.67 (0.39-1.16)	ns
Triglycerides, mmol/l	1.3 (0.9-1.8)	1.3 (1.0-1.8)	1.16 (0.95-1.41)	ns	1.3 (0.9-1.8)	1.3 (1.0-1.8)	1.17 (0.95-1.45)	ns
Systolic BP, mm Hg	150 ± 19	155 ± 20	1.02 (1.01-1.02)	<0.001	151 ± 20	152 ± 19	1.01 (1.00-1.02)	ns
hsCRP, mg/l	1.6 (0.8-3.10)	1.7 (0.7-1.1)	1.04 (1.01-1.07)	0.005	1.6 (0.8-3.6)	1.5 (0.6-3.1)	1.03 (1.00-1.07)	ns
Plasma IL-5, pg/ml	0.73 (0.50-1.36)	0.70 (0.47-1.14)	1.00 (1.00-1.01)	ns	0.75 (0.50-1.34)	0.65 (0.47-1.26)	1.00 (1.00-1.01)	ns
Leukocyte IL-5 release, pg/ml	3.8 (0-58.1)	4.6 (0-84.1)	1.00 (1.00-1.00)	ns	4.40 (0-59.0)	3.1 (0-62.9)	1.00 (1.00-1.00)	ns

Values are mean ± SD or median (interquartile range). Statistical comparisons between cases and controls were done using univariable Cox proportional hazards regression models.

BMI = body mass index; BP = blood pressure; CI = confidence interval; HDL = high-density lipoprotein; HR = hazard ratio; hsCRP = high-sensitivity C-reactive protein; IL = interleukin; LDL = low-density lipoprotein; MACE = major adverse cardiac event.

There was no difference in plasma levels of IL-5 between those with and without MACE (Table 1). To further investigate a possible association between IL-5 and risk of MACE, we analyzed the release of IL-5 from activated peripheral blood mononuclear cells (PBMCs). These PBMCs were isolated at the baseline investigation and stored at -140°C with more than 95% of the cells remaining viable when thawed 20 years later (24). The cells were activated by exposure to CD3/CD28 beads for 72 h followed by analysis of IL-5 in the cell culture medium. Again, we found no difference between those with or without MACE (Table 1). Because IL-5 levels both in plasma and cell medium were skewed, we categorized IL-5 levels into low, medium, and high using the intervals 0 to 0.50, 0.51 to 1.00, and >1.00 pg/ml, respectively, for plasma and 0, 0.1 to 20.0, and >20.0 pg/ml, respectively, for cell-conditioned medium; these IL-5 categories lacked association with risk of MACE (Figures 1A and 1B). Controlling for age, sex, current smoking, BMI, diabetes, LDL and HDL cholesterol, triglycerides, systolic blood pressure, and hsCRP in Cox proportional hazards regression models, there were still no significant associations between IL-5 categories and risk of MACE (HR: 0.74; 95% CI: 0.46 to 1.17; and HR: 1.30; 95% CI: 0.87 to 2.10) for the highest versus the lowest category for plasma and leukocyte release of IL-5, respectively. There were 24 cases of prevalent MACE at baseline. Excluding those did not change the lack of association between IL-5 categories and risk of MACE (HR: 0.69; 95% CI: 0.42 to 1.12 and HR: 1.39; 95% CI: 0.92 to 2.12) for the highest versus the lowest category for plasma and leukocyte release of IL-5, respectively, using the same covariates in Cox regression models as above. Adjusting plasma IL-5 levels for total circulating numbers of CD4$^+$ T cells (10^6 cells/ml of blood) did not affect the lack of association between IL-5 and MACE (data not shown). The adjusted sub-HR, taking into account deaths from other causes unrelated to MACE, remained nonsignificant.

There were 122 cases of incident stroke during the follow-up period. There was no difference in plasma levels of IL-5, or the release of IL-5 from activated PBMCs, between those with and without incident stroke (Table 1). There were also no associations between IL-5 categories and risk for development of stroke (Figures 1C and 1D), and this remained the same when controlling for the same covariates as above in Cox proportional hazards regression models. The adjusted sub-HR, taking into account deaths from other causes unrelated to stroke, also remained nonsignificant.

LOW PLASMA LEVELS OF IL-5 IS ASSOCIATED WITH PRESENCE OF CAROTID PLAQUES. To study the possible association of IL-5 with atherosclerosis severity, we determined how the presence of a plaque in the right carotid bifurcation at baseline related to plasma levels and PBMC release of IL-5. A plaque was defined as a focal thickening of the intima-media layer >1.2 mm and a plaque area >10 mm^2. Subjects with carotid plaques (n = 324) had higher plasma levels of IL-5, whereas there was no significant difference for the release of IL-5 from activated PBMC between those with and without a carotid plaque (Table 2). Similar findings were made when adjusting

FIGURE 1 Kaplan-Meier Plots

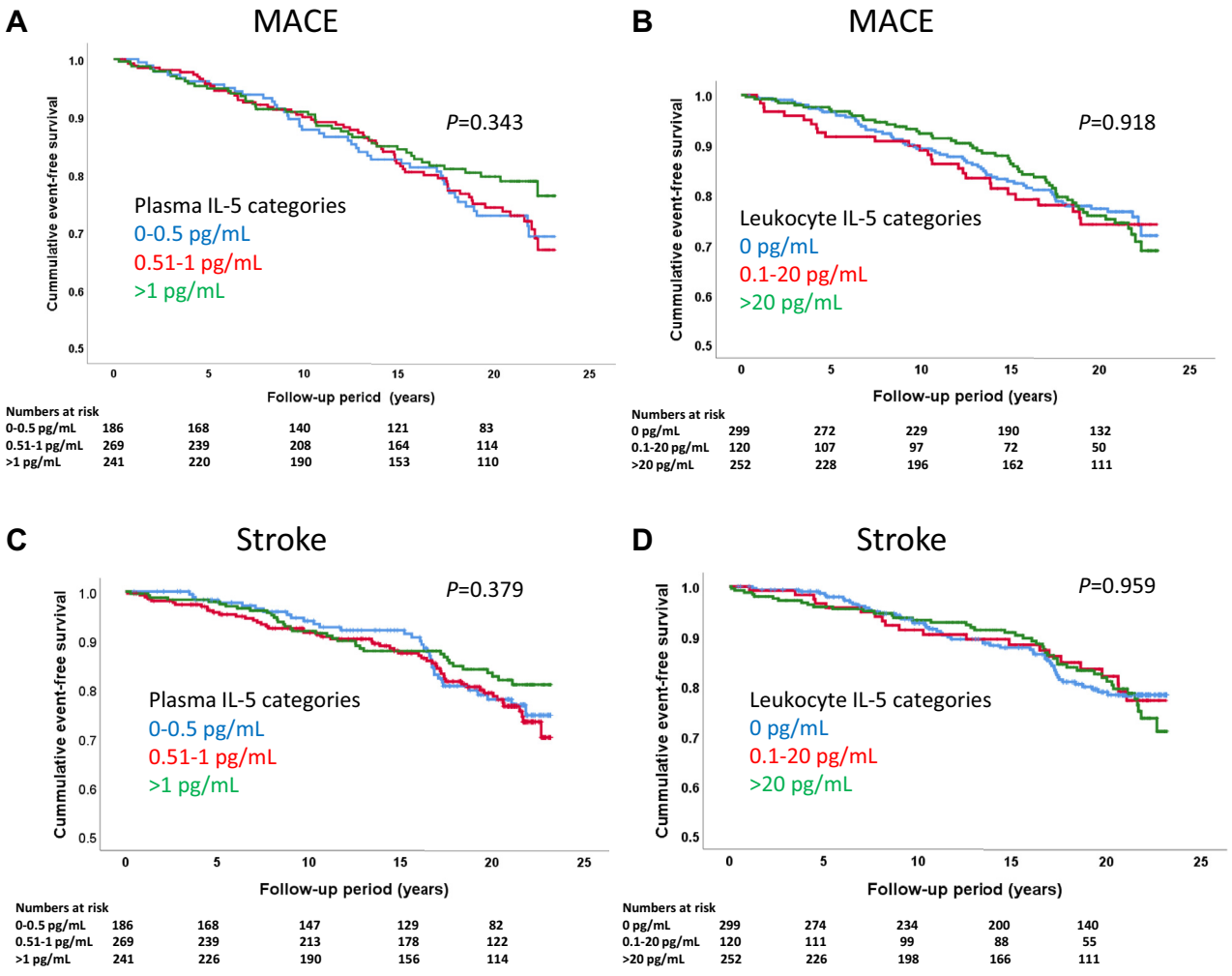

Kaplan-Meier plots showing the associations of intervals of **(A)** plasma interleukin (IL)-5 and **(B)** IL-5 released from activated leukocytes and major adverse cardiac events (MACE) as well as the associations of intervals of **(C)** plasma IL-5 and **(D)** IL-5 released from activated leukocytes and stroke. No significant associations were identified using the log rank test.

plasma IL-5 levels for total circulating numbers of $CD4^+$ T cells (Table 2). When adjusting for age and sex in a logistic regression model, those in the highest plasma IL-5 category (>1.0 pg/ml) had a decreased OR for the presence of carotid plaque of 0.63 (95% CI: 0.42 to 0.94; p = 0.023). However, this association became of borderline significance when also including current smoking, diabetes, LDL cholesterol, HDL cholesterol, and systolic blood pressure in the model (OR: 0.65; 95% CI: 0.42 to 1.00; p = 0.05). There was no significant association between plasma IL-5 and the IMT of the common carotid artery (r = -0.06, p = 0.124). The plasma levels of IL-5 decreased with age and correlated with hsCRP, but otherwise the IL-5 levels did not correlate significantly with cardiovascular risk factors (Table 3).

Plasma levels of IL-5 were inversely related to the number of $CD8^+$ T cells in the blood, but there were no significant associations with other T cell subsets including the number of Th2 ($IL\text{-}4^+/CD4^+$) cells (Table 3). When comparing the release of IL-5 from activated leukocytes, we instead found significant positive associations with both the number of $CD4^+$ and $CD8^+$ T cells in the blood (Table 2). Finally, we determined the association between IL-5 and 2 different oxidized LDL-specific IgM antibodies and found a weak significant association between IL-5 released from activated leukocytes and IgM against

the MDA modified p45 sequence (amino acids 661-680) of apolipoprotein B-100 (Table 2). There was no significant association between the release of IL-5 from activated leukocytes and IL-5 in plasma ($r = 0.01$; $p = 0.845$).

IL-5 DEFICIENCY IS ASSOCIATED WITH INCREASED FORMATION OF PLAQUES AT SITES OF OSCILLATORY STRESS IN APOE$^{-/-}$ MICE. The clinical observations described above imply an association between IL-5 and atherosclerotic plaque formation at sites of oscillatory blood flow (carotid bifurcation), but not at sites with laminar flow (common carotid artery). To investigate the possible interaction between blood flow patterns, IL-5, and plaque formation, we generated *IL5*$^{-/-}$*Apoe*$^{-/-}$ mice and applied a cast to the right carotid artery that generates a laminar, low shear stress proximal to the cast, and an oscillatory flow distal to the cast. This model generates lipid-rich, inflammatory plaques at the proximal site, whereas plaques at the distal site become more fibrous (Figure 2A). *IL5*$^{-/-}$*Apoe*$^{-/-}$ mice developed larger plaques at the site with oscillatory flow than *Apoe*$^{-/-}$ mice with intact IL-5 expression. There were no differences in plaque size at the site with low shear, laminar flow (Figure 2B). IL-5 deficiency did not affect the macrophage and collagen content in plaques at either site (Figures 2C and 2D). Atherosclerosis in the descending aorta, a site where blood flow also is predominantly laminar with high shear stress, was assessed by en face staining with Oil Red O. Again, we found no difference between *IL5*$^{-/-}$*Apoe*$^{-/-}$ *and* *Apoe*$^{-/-}$ mice (Figure 2E). IL-5 deficiency did not affect plasma levels of IL-6, monocyte chemotactic protein-1, tumor necrosis factor-α, IL-10, IL-13, and IL-17, suggesting that the IL-5-deficiency has no effect on systemic inflammation (data not shown). It also was without effect on plasma cholesterol and triglyceride levels (Figures 3A and 3B). IL-5 is known to stimulate the synthesis of the natural, germline-encoded IgM antibodies that facilitates the removal of certain micro-organisms, apoptotic cells, and oxidized LDL. In accordance, IL-5-deficient mice had lower levels of IgM against oxidized LDL, whereas there were no differences in IgM against phosphoryl choline or MDA (Figures 3C to 3E). The lower levels of IgM against oxidized LDL in IL-5-deficient mice were not associated with reduced accumulation of IgM or an increased presence of apoptotic cells in carotid plaques (Figures 4A and 4B).

TABLE 2 Baseline Clinical Characteristics and Interleukin 5 Levels in Subjects With or Without a Plaque in the Carotid Bifurcation at Baseline

	Carotid Plaque		
	No (n = 339)	Yes (n = 324)	p Value
Age, yrs	65.7 ± 1.1	65.5 ± 1.2	ns
Males, %	38.9	43.5	ns
Current smokers, %	12.0	24.3	<0.001
Diabetes, %	12.4	15.6	ns
BMI, kg/m^2	26.5 ± 3.8	25.8 ± 3.7	<0.018
f-glucose, mmol/l	5.28 ± 1.28	5.46 ± 1.72	ns
LDL, mmol/l	4.34 ± 0.98	4.47 ± 1.05	ns
HDL, mmol/l	1.37 ± 0.36	1.37 ± 0.38	ns
Triglycerides, mmol/l	1.21 (0.90-1.75)	1.31 (0.95-1.81)	ns
Systolic BP, mm Hg	149 ± 20	153 ± 20	<0.009
hsCRP, mg/l	1.60 (0.80-3.10)	1.60 (0.70-3.10)	ns
Plasma IL-5, pg/ml	0.81 (0.50-1.43)	0.67 (0.49-1.13)	<0.037
Plasma IL-5/10^6 CD4$^+$ T cells	1.65 (0.96-3.19)	1.35 (0.77-2.80)	<0.046
Leukocyte IL-5 Release, pg/ml	3.47 (0-42.2)	4.58 (0-103.1)	ns

Values are mean ± SD or median (interquartile range). Student's *t*-test or the Mann-Whitney U test was used statistical comparison as appropriate.
Abbreviations as in Table 1.

DISCUSSION

In the present study, we found no association between plasma levels of IL-5 at baseline and the risk for development of coronary events during a follow-up period of more than 15 years. There was also no association between the release of IL-5 from activated leukocytes and the risk of coronary events. Accordingly, IL-5 is likely not a clinically useful marker of

TABLE 3 Associations of Interleukin 5 With Cardiovascular Risk Factors and T Cell Subsets

	Plasma IL-5	p Value	PBMC IL-5 Release	p Value
Risk factors				
Age	−0.07	ns	−0.11	0.006
BMI	0.03	ns	0.01	ns
f-glucose	0.00	ns	0.05	ns
LDL	0.00	ns	0.04	ns
HDL	−0.05	ns	−0.07	ns
Triglycerides	−0.05	ns	0.04	ns
hsCRP	0.10	0.015	0.04	ns
T cell subtypes				
CD4$^+$ T cells	−0.07	ns	0.13	0.001
Th1 T cells	−0.02	ns	0.13	0.001
Th2 T cells	0.04	ns	0.05	ns
Regulatory T cells	−0.03	ns	−0.03	ns
CD8$^+$ T cells	−0.13	0.001	0.13	0.001
Oxidized LDL IgM				
MDA-p45	0.06	ns	0.09	0.036
MDA-p210	0.01	ns	−0.04	ns

Correlations are shown as Spearman rank correlation coefficients. The values for T cell subsets used in the analyses are the total numbers of each subset per milliliter of blood.
PBMC = peripheral blood mononuclear cell; other abbreviations as in Table 1.

FIGURE 2 Effect of Interleukin 5 Deficiency on Atherosclerotic Plaque Formation in *Apoe*$^{-/-}$ Mice

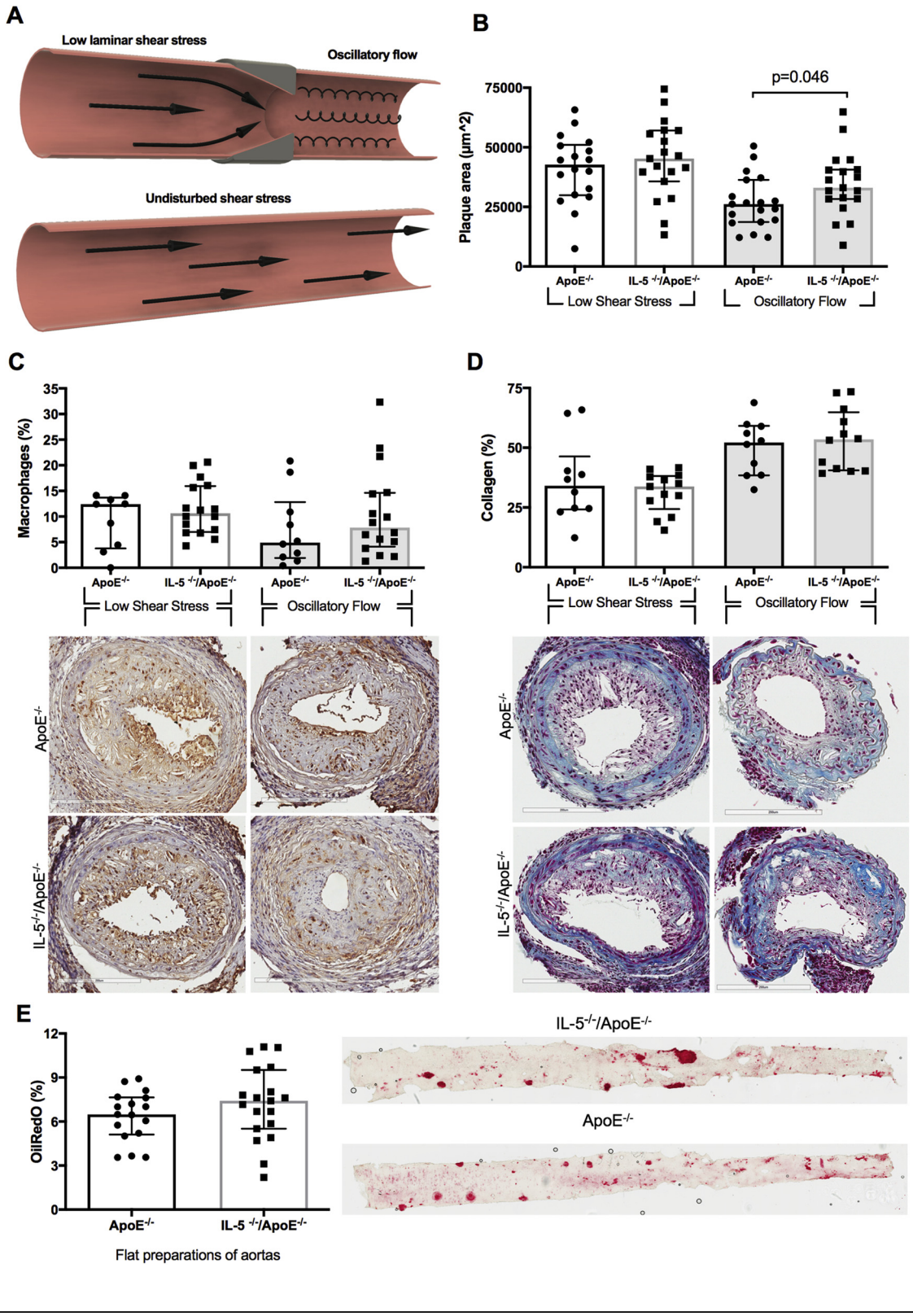

Continued on the next page

FIGURE 3 Effect of Interleukin 5 Deficiency on Plasma Lipids and Low-Density Lipoprotein–Associated Autoantibodies

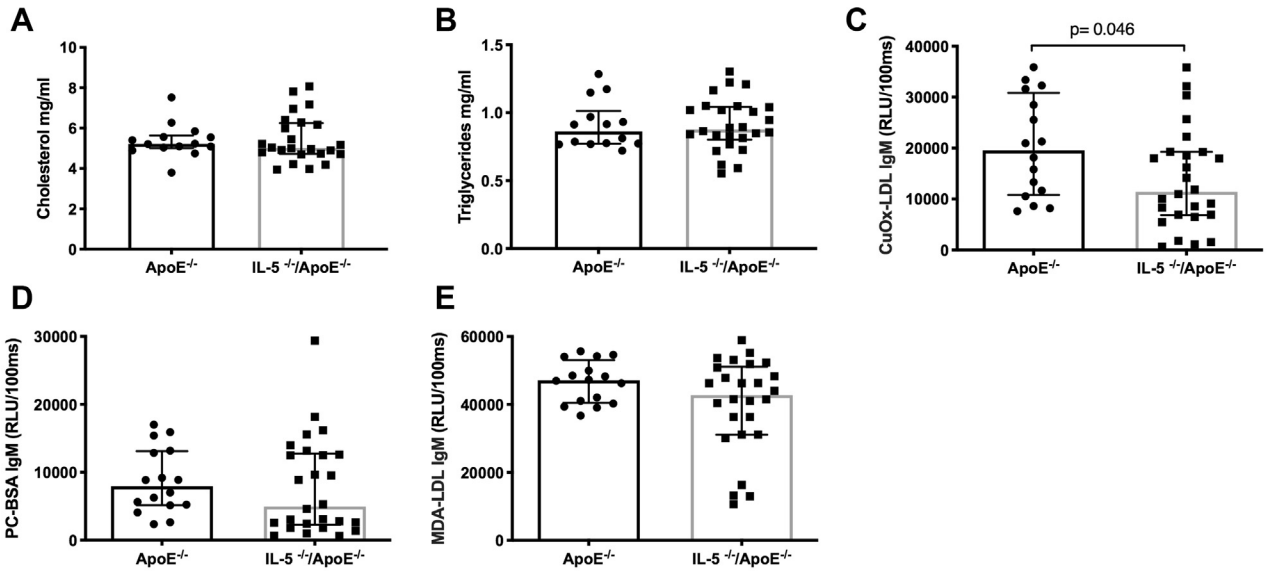

Effect of interleukin 5 (IL-5) deficiency on plasma lipids and low-density lipoprotein (LDL)–associated autoantibodies in *Apoe*$^{-/-}$ mice **(A,B).** *Apoe*$^{-/-}$ and *IL5*$^{-/-}$*/Apoe*$^{-/-}$ mice had similar levels of cholesterol and triglycerides. **(C to E)** IL-5 is known to stimulate in the expression of the natural immunoglobulin M (IgM) antibodies. In accordance, IL-5–deficient mice had lower levels of IgM against copper oxidized LDL, whereas there were no differences in IgM against phosphoryl choline and malondialdehyde. Graphs are plotted as median with interquartile range. The p values were calculated using the Mann-Whitney *U* test. BSA = bovine serum albumin; PC = phosphoryl choline; RLU = relative luminescence intensities.

cardiovascular risk. Although the present observational studies do not allow any conclusions regarding causal relationships to be made, our findings do not support an important protective role of IL-5 in CVD. They are also not in line with the observations from the PROCARDIS (Precocious Coronary Artery Disease) study in which subjects with prevalent CVD had higher IL-5 levels indicating a potential harmful role of IL-5 (15). Possible explanations to the finding of higher plasma levels of IL-5 in subjects with prevalent coronary heart disease could be that protective IL-5 responses are activated as a result of a more severe atherosclerosis in these subjects or that they have a general activation of immunity. However, the present observation that subjects with a plaque in the carotid bulb have lower plasma levels of IL-5 argue against this possibility. In a study, involving 1,011 middle-aged Finnish subjects Sämpi et al. (25) also found that high plasma levels of IL-5 were associated with a smaller IMT in carotid bulb but not in the common carotid artery. Accordingly, both this and our study found that high levels of IL-5 is associated with less atherosclerosis in the carotid bulb, observations which are more in accordance with the atheroprotective effects of IL-5 found in experimental studies (12–14). In both studies, the inverse association between IL-5 and atherosclerosis was only observed in the carotid bulb, but not in the common carotid artery, suggesting that it may be dependent on the pattern of blood flow. Blood flow in the common carotid artery is laminar, producing a high shear stress that is anti-inflammatory and has an anti-atherogenic

FIGURE 2 Continued

(A) To induce plaque formation in *Apoe*$^{-/-}$ and *IL5*$^{-/-}$*Apoe*$^{-/-}$ mice a cast with a fixed geometry was applied to the right carotid artery generating a laminar, low shear stress proximal to the cast and an oscillatory flow distal to the cast. **(B)** *IL5*$^{-/-}$*Apoe*$^{-/-}$ mice developed larger plaques at the site with oscillatory flow than *Apoe*$^{-/-}$ mice with intact interleukin 5 (IL-5) expression. There were no differences in plaque size at the site with low shear, laminar flow. **(C, D)** IL-5 deficiency did not affect the macrophage or collagen content in plaques at either site. **(E)** Atherosclerosis in the descending aorta, a site where blood flow also is predominantly laminar, was assessed by en face staining with Oil Red O. No difference was found between *IL5*$^{-/-}$*Apoe*$^{-/-}$ *and* *Apoe*$^{-/-}$ mice. Graphs are plotted as median with interquartile range. The p values were calculated using the Mann-Whitney *U* test.

FIGURE 4 Effect of Interleukin 5 Deficiency on Immunoglobulin M Accumulation and Apoptosis

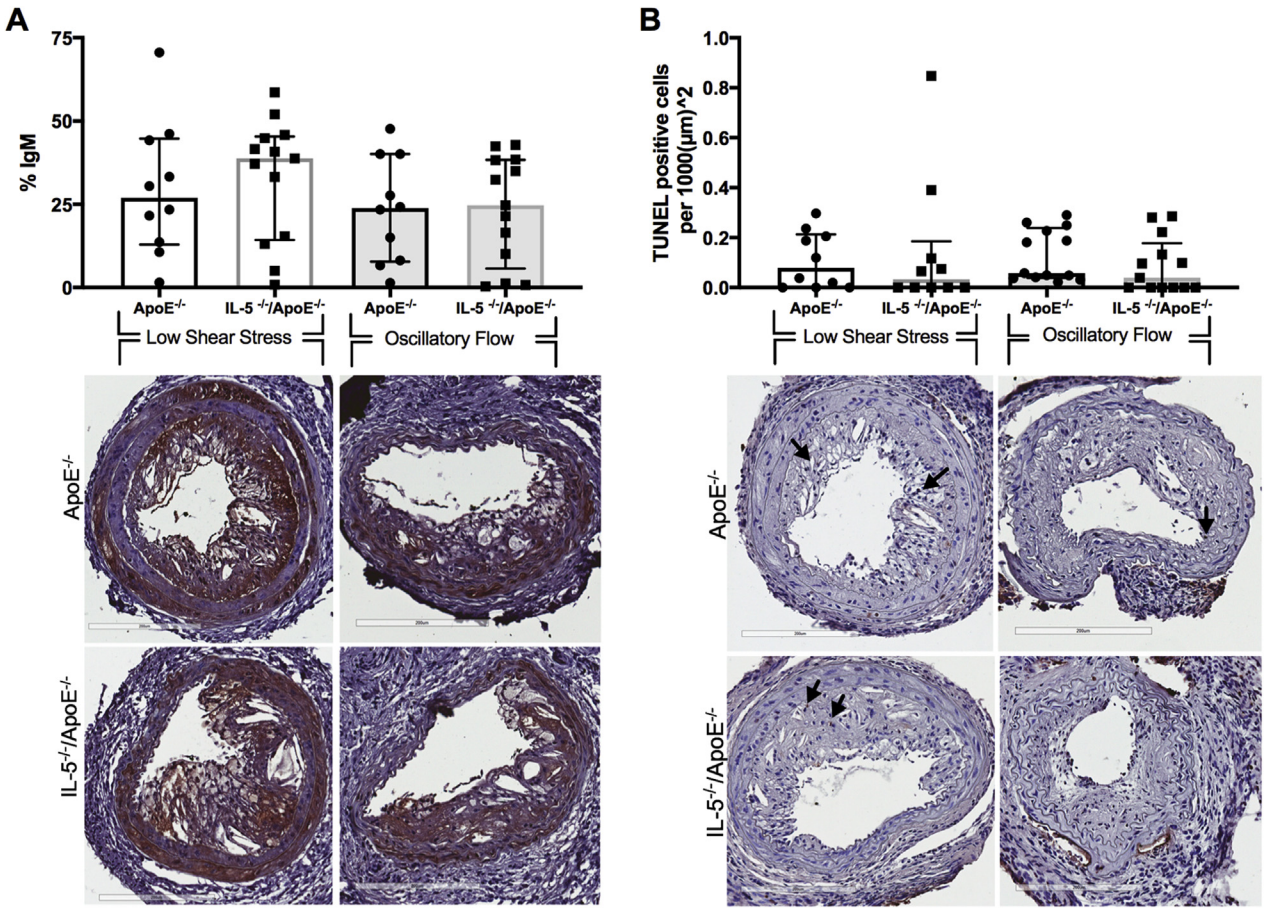

Effect of interleukin 5 (IL-5) deficiency on immunoglobulin M (IgM) accumulation and apoptosis in plaques of *Apoe*$^{-/-}$ mice IL-5 deficiency did not affect **(A)** the IgM content or **(B)** amount of terminal deoxynucleotidyl transferase deoxyuridine triphosphatase nick end labeling (TUNEL)–positive cells in plaques from low shear stress sites or in the oscillatory flow sites. Representative images of the IgM stain and TUNEL stain are shown under the respective graphs. IgM is shown in **brown** and TUNEL positive cells are shown with **black arrows**. Graphs are plotted as median with interquartile range. p values were calculated using the Mann-Whitney *U* test.

effect. In contrast, the arterial bifurcation in the carotid bulb results in an oscillatory flow and reduced shear stress that is known to activate inflammatory responses and promote atherogenesis (22,26,27). To further investigate how blood flow patterns and shear stress influence the effect of IL-5 on plaque development, we generated *IL5*$^{-/-}$*Apoe*$^{-/-}$ mice and induced different shear stress patterns by implanting a shear stress modifier cast around 1 of the carotid arteries. At the distal site of the cast, where an oscillatory blood flow results in formation of predominantly fibrous lesions, there was increased plaque development in *IL5*$^{-/-}$*Apoe*$^{-/-}$ mice as compared to IL-5 competent *Apoe*$^{-/-}$ mice. Proximal to the cast, where a laminar but low shear stress flow accelerates the formation of lesions rich in lipid and inflammatory cells, IL-5 deficiency did not affect plaque development. This observation suggests that the atheroprotective effect of IL-5 primarily is effective at sites with oscillatory blood flow. This is also well in line with the clinical observations of an inverse association between IL-5 and atherosclerosis in carotid bulb but not in the common carotid artery. It should be kept in mind that the low shear stress created by the carotid cast in the mouse model primarily is representative of the flow pattern proximal to a large plaque significantly reducing the blood flow in humans and did thus not correspond to the carotid blood flow patterns in our clinical study. The site-specificity of the atheroprotective effect of IL-5 is intriguing. Because there is no evidence that IL-5 in itself has direct influence on plaque development, it can be assumed that IL-5 is

atheroprotective through stimulation of the expression of natural antibodies. Arterial bifurcations generate oscillatory blood flow resulting in impaired endothelial ability to exclude lipoprotein infiltration (28). As a result, there is commonly subendothelial aggregation and oxidation lipoproteins at such sites. It is possible that natural antibodies are particularly important for the clearance of such lipoproteins. We did not find evidence for reduced accumulation of total IgM in the plaque of $IL5^{-/-}Apoe^{-/-}$ mice, but this does not exclude reduced accumulation of certain subtypes of IgM such as natural antibodies.

Several experimental studies have shown a functional role for IL-5 in the expression of natural antibodies binding to oxidized LDL (5,29). The present observation of reduced levels of IgM recognizing oxidized LDL in $IL5^{-/-}Apoe^{-/-}$ mice add further support to this notion. The relative importance of this pathway for expression of natural antibodies in humans is less well characterized. Sämpi et al. (25) found a correlation between plasma IL-5 and IgM against both oxidized and MDA-modified LDL in middle-aged Finnish cohort. In the present study, we observed an association between IgM reacting with the MDA-modified p45 amino acid sequence of apolipoprotein B-100. We have previously shown that low levels of this autoantibody is associated with an increased risk for myocardial infarction (30). This could represent a possible mechanism through which IL-5 could be atheroprotective in man, but this notion remains speculative.

There are some limitations of the present study that should be considered. In the clinical study, we only had access to IL-5 values from a single time point (e.g., the baseline investigation). There is no published data on how the plasma level of IL-5 varies over time in the same individual. A study where blood samples were repeatedly drawn from healthy volunteers during a 2-month period found correlations coefficients ranging from 0.6 to 0.9 for IL-1β, IL-6, and IL-8 suggesting that plasma cytokine levels in healthy individuals are relatively stable (31). Furthermore, it cannot be excluded that the long storage period affected the possibility to correctly analyze plasma IL-5. Finally, the cohort used in the present study may have been too small for identification of associations between IL-5 and cardiovascular risk.

In conclusion, we applied a translational approach to study the role of IL-5 in CVD. We found evidence for a protective role of IL-5 in the development of atherosclerotic plaques at sites of oscillatory blood flow but found no evidence that this was associated with a reduced risk of cardiovascular events.

ACKNOWLEDGMENTS The authors thank Maria Ozsvar Kozma for excellent technical assistance, and Yan Borné for statistical advice.

ADDRESS FOR CORRESPONDENCE: Dr. Jan Nilsson, Department of Clinical Sciences, Jan Waldenströms gata 35, 20502 Malmö, Sweden. E-mail: jan.nilsson@med.lu.se.

PERSPECTIVES

COMPETENCY IN MEDICAL KNOWLEDGE: Despite experimental data of an atheroprotective role of IL-5, plasma analysis of this cytokine does not help to identify subjects at risk of cardiovascular events.

TRANSLATIONAL OUTLOOK: Low levels of IL-5 are associated in presence of plaques in the carotid bifurcation, an observation that can be replicated in experimental studies.

REFERENCES

1. Hansson GK, Hermansson A. The immune system in atherosclerosis. Nat Immunol 2011;12:204–12.

2. Lichtman AH, Binder CJ, Tsimikas S, Witztum JL. Adaptive immunity in atherogenesis: new insights and therapeutic approaches. J Clin Invest 2013;123:27–36.

3. Libby P, Lichtman AH, Hansson GK. Immune effector mechanisms implicated in atherosclerosis: from mice to humans. Immunity 2013;38:1092–104.

4. Binder CJ, Shaw PX, Chang MK, et al. The role of natural antibodies in atherogenesis. J Lipid Res 2005;46:1353–63.

5. Tsiantoulas D, Diehl CJ, Witztum JL, Binder CJ. B cells and humoral immunity in atherosclerosis. Circ Res 2014;114:1743–56.

6. Shaw PX, Horkko S, Chang MK, et al. Natural antibodies with the T15 idiotype may act in atherosclerosis, apoptotic clearance, and protective immunity. J Clin Invest 2000;105:1731–40.

7. Baumgarth N. The double life of a B-1 cell: self-reactivity selects for protective effector functions. Nat Rev Immunol 2011;11:34–46.

8. Caligiuri G, Nicoletti A, Poirier B, Hansson GK. Protective immunity against atherosclerosis carried by B cells of hypercholesterolemic mice. J Clin Invest 2002;109:745–53.

9. Kyaw T, Tay C, Krishnamurthi S, et al. B1a B lymphocytes are atheroprotective by secreting natural IgM that increases IgM deposits and reduces necrotic cores in atherosclerotic lesions. Circ Res 2011;109:830–40.

10. Ait-Oufella H, Herbin O, Bouaziz JD, et al. B cell depletion reduces the development of atherosclerosis in mice. J Exp Med 2010;207:1579–87.

11. Baumgarth N. B-1 Cell Heterogeneity and the regulation of natural and antigen-induced IgM production. Front Immunol 2016;7:324.

12. Newland SA, Mohanta S, Clement M, et al. Type-2 innate lymphoid cells control the

development of atherosclerosis in mice. Nat Commun 2017;8:15781.

13. Binder CJ, Hartvigsen K, Chang MK, et al. IL-5 links adaptive and natural immunity specific for epitopes of oxidized LDL and protects from atherosclerosis. J Clin Invest 2004;114:427–37.

14. Zhao W, Lei T, Li H, et al. Macrophage-specific overexpression of interleukin-5 attenuates atherosclerosis in LDL receptor-deficient mice. Gene Ther 2015;22:645–52.

15. Clarke R, Valdes-Marquez E, Hill M, et al. Plasma cytokines and risk of coronary heart disease in the PROCARDIS study. Open Heart 2018;5: e000807.

16. Berglund G, Elmstahl S, Janzon L, Larsson SA. The Malmo Diet and Cancer Study. Design and feasibility. J Intern Med 1993;233:45–51.

17. Wigren M, Bjorkbacka H, Andersson L, et al. Low levels of circulating CD4+FoxP3+ T cells are associated with an increased risk for development of myocardial infarction but not for stroke. Arterioscler Thromb Vasc Biol 2012;32:2000–4.

18. Hedblad B, Nilsson P, Janzon L, Berglund G. Relation between insulin resistance and carotid intima-media thickness and stenosis in non-diabetic subjects. Results from a cross-sectional study in Malmo, Sweden. Diabet Med 2000;17:299–307.

19. Li C, Engstrom G, Berglund G, Janzon L, Hedblad B. Incidence of ischemic stroke in relation to asymptomatic carotid artery atherosclerosis in subjects with normal blood pressure. A prospective cohort study. Cerebrovasc Dis 2008;26: 297–303.

20. Engelbertsen D, Andersson L, Ljungcrantz I, et al. T-helper 2 immunity is associated with reduced risk of myocardial infarction and stroke. Arterioscler Thromb Vasc Biol 2013;33: 637–44.

21. Kolbus D, Ljungcrantz I, Andersson L, et al. Association between CD8+ T-cell subsets and cardiovascular disease. J Intern Med 2013;274: 41–51.

22. Cheng C, Tempel D, van Haperen R, et al. Atherosclerotic lesion size and vulnerability are determined by patterns of fluid shear stress. Circulation 2006;113:2744–53.

23. Binder CJ, Horkko S, Dewan A, et al. Pneumococcal vaccination decreases atherosclerotic lesion formation: molecular mimicry between Streptococcus pneumoniae and oxidized LDL. Nat Med 2003;9:736–43.

24. Berg KE, Ljungcrantz I, Andersson L, et al. Elevated CD14++CD16- monocytes predict cardiovascular events. Circ Cardiovasc Genet 2012;5:122–31.

25. Sampi M, Ukkola O, Paivansalo M, Kesaniemi YA, Binder CJ, Horkko S. Plasma interleukin-5 levels are related to antibodies binding to oxidized low-density lipoprotein and to decreased subclinical atherosclerosis. J Am Coll Cardiol 2008;52:1370–8.

26. Gimbrone MA Jr., Garcia-Cardena G. Vascular endothelium, hemodynamics, and the pathobiology of atherosclerosis. Cardiovasc Pathol 2013; 22:9–15.

27. Brown AJ, Teng Z, Evans PC, Gillard JH, Samady H, Bennett MR. Role of biomechanical forces in the natural history of coronary atherosclerosis. Nat Rev Cardiol 2016;13:210–20.

28. Tabas I, Williams KJ, Boren J. Subendothelial lipoprotein retention as the initiating process in atherosclerosis: update and therapeutic implications. Circulation 2007;116:1832–44.

29. Mantani PT, Duner P, Bengtsson E, et al. IL-25 inhibits atherosclerosis development in apolipoprotein E deficient mice. PLoS ONE 2015;10: e0117255.

30. Bjorkbacka H, Alm R, Persson M, Hedblad B, Nilsson J, Fredrikson GN. Low Levels of apolipoprotein B-100 autoantibodies are associated with increased risk of coronary events. Arterioscler Thromb Vasc Biol 2016; 36:765–71.

31. Alves Dias J, Hellstrand S, Ericson U, et al. Plasma variation and reproducibility of oxidized LDL-cholesterol and low-grade inflammation biomarkers among participants of the Malmo Diet and Cancer cohort. Biomarkers 2016:1–10.

KEY WORDS interleukin 5, atherosclerosis, myocardial infarction, stroke

JACC: BASIC TO TRANSLATIONAL SCIENCE VOL. 4, NO. 8, 2019

EDITORIAL COMMENT

Interleukin 5 Contributes to Human Atherosclerosis Development But not to Thrombotic Complications*

Hafid Ait-Oufella, MD, PhD,[a,b] Soraya Taleb, PhD,[a] Alain Tedgui, PhD[a]

Atherosclerosis is a complex disease that develops in medium and large arteries in response to lipoprotein retention and oxidation in the subendothelial space. Because of compensatory enlargement as lesion area increases, a process first described by Seymour Glagov in human coronary arteries more than 30 years ago, functional impairment of blood flow is delayed until an advanced stage when lumen stenosis becomes significant. Acute ischemia observed during stroke and myocardial infarction is mainly due to thrombotic complications of atherosclerosis that suddenly narrow the artery lumen and compromise blood flow and peripheral oxygen delivery. The use of genetically engineered atheroprone mice has been instrumental in understanding the major role for both innate and adaptive immunity in atherosclerotic plaque formation and growth; however, unfortunately, animal experiments were less helpful in deciphering the mechanisms of plaque rupture and subsequent occlusive thrombosis. Murine atherosclerotic plaques share common features with human lesions but do not display fibrous cap rupture even at advanced stages.

Interleukin 5 (IL-5) is a cytokine produced by eosinophils, mast cells, macrophages, $CD4^+$ T, and type 2-innate lymphoid cells (ILC2). Its expression is regulated by several transcription factors including GATA3. In atherosclerotic animal models, seminal studies from Witztum's laboratory (1) have shown that IL-5 production by $CD4^+$ T cells drives B1 cell activation and production of protective natural immunoglobulin M (IgM) antibodies against oxidation-specific epitopes, including oxidized low-density lipoprotein (oxLDL). Anti-oxLDL IgM are able to bind to oxidized phospholipid-rich apoptotic cells and block their pro-inflammatory properties. In addition, anti-oxLDL IgM promote the clearance of apoptotic cells that accumulate within advanced atherosclerotic lesions and participate to the growth of the necrotic core (1). Hematopoietic *Il-5* inactivation was found to decrease plasma levels of IgM levels and to accelerate atherosclerosis (1). In addition, IL-5 might also be involved in the atheroprotective function of ILC2, independently of humoral B1 responses (2). Yet, the clinical relevance of these experimental findings remained unclear.

SEE PAGE 891

In this issue of *JACC: Basic to Translational Science*, Knutsson et al. (3) investigated the role of IL-5 in atherothrombotic cardiac events in a prospective cohort of adults from the Malmö Diet and Cancer study (N = 696) with a 15-year follow-up, by analyzing the relationship between IL-5 plasma levels and either the presence of atherosclerotic plaque in the carotid artery or the occurrence of major adverse cardiac events (e.g., fatal and nonfatal myocardial infarction, coronary artery bypass grafting, and percutaneous coronary interventions). In univariate analysis, they found significantly lower plasma levels of IL-5 in patients with carotid atherosclerotic

*Editorials published in *JACC: Basic to Translational Science* reflect the views of the authors and do not necessarily represent the views of *JACC: Basic to Translational Science* or the American College of Cardiology.

From the [a]Université de Paris, Paris Cardiovascular Research Center - PARCC, Paris, France; and the [b]Service de Médecine Intensive-Réanimation, Hôpital Saint-Antoine, Assistance Publique-Hôpitaux de Paris, Sorbonne-Université Paris, Paris, France. This work was supported by Institut National de la Santé et de la Recherche Médicale (INSERM). The authors have reported that they have no relationships relevant to the contents of this paper to disclose.

The authors attest they are in compliance with human studies committees and animal welfare regulations of the authors' institutions and Food and Drug Administration guidelines, including patient consent where appropriate. For more information, visit the *JACC: Basic to Translational Science* author instructions page.

ISSN 2452-302X https://doi.org/10.1016/j.jacbts.2019.11.005

plaques measured by ultrasound, as compared with subjects without arterial lesions. Such an association remained significant after adjustment on sex, age, and cardiovascular risk factors. In a large European prospective cohort study of high-risk individuals (N = 3,534) free of clinically overt cardiovascular disease at enrollment, IL-5 plasma concentrations was previously shown to be significantly inversely correlated with changes in carotid intima-media thickness over a period of 30 months (4). Moreover, in diabetic patients, variants coding for *Il-5* receptor were found to be independently associated with ischemic stroke. A Finnish prospective observational study had shown previously that plasma IL-5 levels were significantly associated with antibody titers to copper oxLDL and IgM to malondialdehyde-modified LDL (5), and high levels of IgM autoantibodies to oxLDL have been reported to be predictive of better cardiovascular outcomes. However, in this study, Knutsson et al. (3) did not find any association between IL-5 plasma levels and IgM against oxidation-specific epitopes. They only found a weak significant association between IL-5 released from activated leukocytes and IgM against a malondialdehyde modified sequence of apo B-100. Therefore, although experimental and human evidence strongly suggest an atheroprotective role of IL-5, the mechanisms of vascular protection remain unclear, and might not be related to its effects on the modulation of natural IgM humoral responses.

Recently, Newland et al. (2) reported that ILC2 is a major source of IL-5. ILC2 deficiency leads to a 50% decrease of IL-5 plasma levels in an $Ldlr^{-/-}$ chimeric mouse model and reduces atherosclerosis development. ILC2 deficiency had a significant but modest effect on B1 population in the spleen and the mesenteric lymph nodes but did not alter anti-oxLDL antibody titers suggesting that IL-5–related vascular protection was unlikely to be driven by humoral B1 cell activation (2). IL-5 modulated macrophage function within atherosclerotic lesions. In mice lacking ILC2, macrophage phenotype was switched toward pro-inflammatory M1, associated with higher content of $iNOS^{+}F4/80^{+}$macrophages and less $Arg1^{+}F4/80^{+}$ macrophages.

Knutsson et al. (3) speculated that the effects of IL-5 on atherosclerosis development vary according to hemodynamic parameters because they observed a significant relationship between IL-5 plasma levels and the presence of atherosclerotic plaque in the carotid bulb, a low shear stress region, but no association with atherosclerosis in the common carotid artery, where blood flow is laminar and shear stress high. To mimic such conditions, the authors applied a cast to the right carotid artery to generate a laminar low flow proximal to the cast and an oscillatory flow distal to the cast. After 14 weeks of fat diet, atherosclerosis was significantly increased in the distal oscillatory flow region in $Apoe^{-/-}Il\text{-}5^{-/-}$ mice, as compared to control $Apoe^{-/-}Il\text{-}5^{+/+}$ mice, but no difference was observed in the proximal laminar low shear stress area, in agreement with ultrasonographic observations in humans. This result suggests that IL-5 might directly target endothelial cells that are very sensitive to blood flow and shear stress variations. A recent in vitro study reported that IL-5 per se is able to modulate endothelial cell phenotype and activity. Further investigations are required to understand the mechanisms accounting for the direct effects of IL-5 on endothelial biology.

The translational study by Knutsson et al. (3) supports the protective role of IL-5 on atherosclerosis plaque growth. As monoclonal antibody targeting IL-5 are currently being developed to treat patients with severe asthma, cardiovascular side effects should be carefully recorded, especially in adult patients with cardiovascular risk factors. Such prospective epidemiologic monitoring should provide unique opportunity to decipher the role of IL-5 in human atherosclerotic plaque stability (6).

ADDRESS FOR CORRESPONDENCE: Dr. Hafid Ait-Oufella, UMR-S 970 Paris Cardiovascular Research Center - PARCC, 56 rue Leblanc, 75015 Paris, France. E-mail: hafid.aitoufella@inserm.fr.

REFERENCES

1. Binder CJ, Papac-Milicevic N, Witztum JL. Innate sensing of oxidation-specific epitopes in health and disease. Nat Rev Immunol 2016;16:485–97.

2. Newland SA, Mohanta S, Clement M, et al. Type-2 innate lymphoid cells control the development of atherosclerosis in mice. Nat Commun 2017;8:15781.

3. Knutsson A, Björkbacka H, Dunér P, et al. Associations of interleukin-5 with plaque development and cardiovascular events. J Am Coll Cardiol Basic Trans Science 2019;4:891–902.

4. Silveira A, McLeod O, Strawbridge RJ, et al. Plasma IL-5 concentration and subclinical carotid atherosclerosis. Atherosclerosis 2015;239:125–30.

5. Sampi M, Ukkola O, Paivansalo M, Kesaniemi YA, Binder CJ, Horkko S. Plasma interleukin-5 levels are related to antibodies binding to oxidized low-density lipoprotein and to decreased subclinical atherosclerosis. J Am Coll Cardiol 2008;52:1370–8.

6. Ait-Oufella H, Libby P, Tedgui A. Anticytokine immune therapy and atherothrombotic cardiovascular risk. Arterioscler Thromb Vasc Biol 2019;39:1510–9.

KEY WORDS atherosclerosis, interleukin 5, myocardial infarction, stroke

JACC: BASIC TO TRANSLATIONAL SCIENCE VOL. 4, NO. 8, 2019

PRECLINICAL RESEARCH

Preservation of Post-Infarction Cardiac Structure and Function via Long-Term Oral Formyl Peptide Receptor Agonist Treatment

Ricardo A. García, PhD,[a,b] Bruce R. Ito, PhD,[b] John A. Lupisella, MSc,[a] Nancy A. Carson, BSc,[a] Mei-Yin Hsu, MSc,[a] Gayani Fernando, MSc,[a] Madeleine Heroux, PhD,[c] Michel Bouvier, PhD,[c] Elizabeth Dierks, PhD,[a] Ellen K. Kick, PhD,[a] David A. Gordon, PhD,[a] Jian Chen, PhD,[a] Gabe Mintier, BSc,[a] Marilyn Carrier, PhD,[c] Stéphane St-Onge, MSc,[c] Himanshu Shah, MSc,[a] Jordan Towne, BSc,[b] Marcela Sotelo Bucardo, BSc,[b] Xiuying Ma, PhD,[a] Carol S. Ryan, BSc,[a] Nicholas R. Wurtz, PhD,[a] Jacek Ostrowski, PhD,[a] Francisco J. Villarreal, MD, PhD[b]

VISUAL ABSTRACT

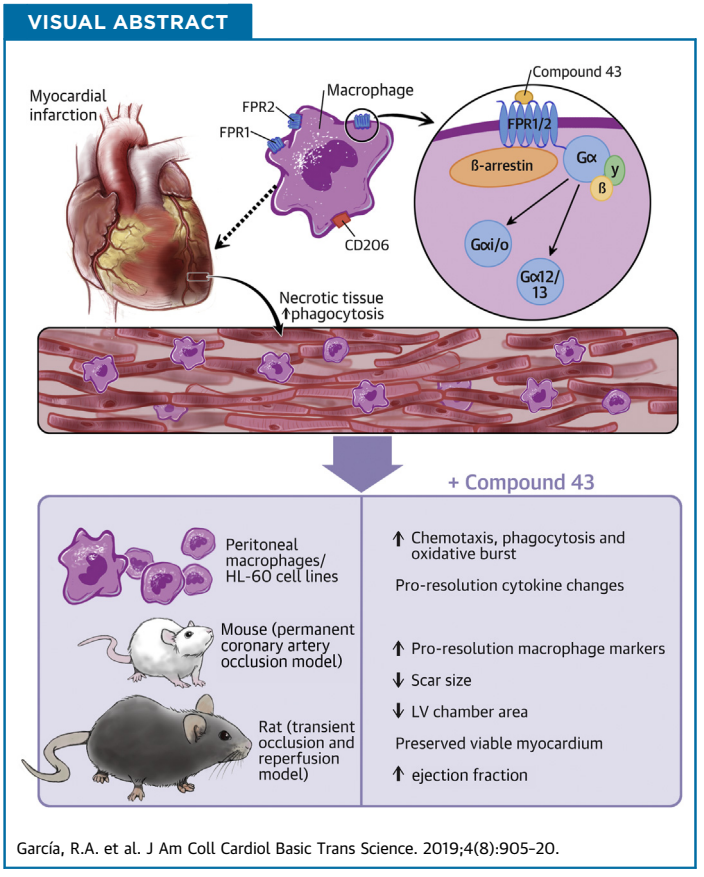

García, R.A. et al. J Am Coll Cardiol Basic Trans Science. 2019;4(8):905-20.

HIGHLIGHTS

- **Myocardial infarction leads to recruitment of monocyte/macrophages to the injured myocardium to drive infarct healing.**
- **Activation of formyl peptide receptors (FPR1 and FPR2) present on macrophages contributes to key cellular activities that can potentiate wound healing.**
- **Myocardial infarction was induced in rodents to study the effects of long-term treatment with Compound 43, a small molecule agonist of FPR1 and FPR2.**

ISSN 2452-302X https://doi.org/10.1016/j.jacbts.2019.07.005

JACC: BASIC TO TRANSLATIONAL SCIENCE VOL. 4, NO. 8, 2019
DECEMBER 2019:905–20

ABBREVIATIONS AND ACRONYMS

Cmpd43 = Compound 43
FPR = formyl peptide receptor
HF = heart failure
IL = interleukin
IR = ischemia-reperfusion
KO = knockout
LAD = left anterior descending
LV = left ventricular
MI = myocardial infarction
PV = pressure-volume
SAA = serum amyloid A
WT = wild-type

- **Main findings: Compound 43 stimulated proresolution macrophage activities, improved left ventricle and infarct structure, and preserved cardiac function post-myocardial infarction.**
- **The results suggest that stimulation of proresolution activities of FPRs can favorably alter post-myocardial infarction pathophysiology that leads to heart failure.**

SUMMARY

Dysregulated inflammation following myocardial infarction (MI) promotes left ventricular (LV) remodeling and loss of function. Targeting inflammation resolution by activating formyl peptide receptors (FPRs) may limit adverse remodeling and progression towards heart failure. This study characterized the cellular and signaling properties of Compound 43 (Cmpd43), a dual FPR1/FPR2 agonist, and examined whether Cmpd43 treatment improves LV and infarct remodeling in rodent MI models. Cmpd43 stimulated FPR1/2-mediated signaling, enhanced proresolution cellular function, and modulated cytokines. Cmpd43 increased LV function and reduced chamber remodeling while increasing proresolution macrophage markers. The findings demonstrate that FPR agonism improves cardiac structure and function post-MI.

Heart failure (HF) is a leading cause of morbidity and mortality in the United States, affecting up to 5.7 million people (1). Myocardial infarction (MI) remains a prevalent cause of HF, with up to 25% of patients with MI developing the disease. Despite advances in pharmacotherapy, HF-associated mortality remains high, and the development of new therapeutic approaches is needed.

The early sequelae of events following MI include a localized inflammatory response that resolves in a coordinated manner to enable myocardial healing and scar formation. Unresolved inflammation is responsible for the pathophysiology of multiple, diverse chronic diseases, such as atherosclerosis and HF (2). In the MI setting, persistent unresolved inflammation is a major contributor to the progressive development of adverse left ventricular (LV) remodeling and eventually HF. However, early attempts to mitigate inflammation following MI using relatively nonspecific agents, such as glucocorticoids (3,4) or cyclooxygenase-2 inhibitors (5,6), have been unsuccessful and led to major adverse events, including LV rupture. An alternative strategy to address post-MI inflammation involves the promotion of resolution to improve healing of the damaged myocardium and its restoration to homeostasis. The discovery of proresolving lipid mediators (e.g., lipoxins and resolvins) and their cognate receptors, including formyl peptide receptor (FPR) 2, has opened new opportunities for pharmacological treatment of unresolved inflammation (7).

FPRs are G–protein-coupled receptors that are prominently expressed by phagocytic leukocytes, including macrophages, and play important roles in the initiation and resolution of inflammation. FPR1 and FPR2 are the most characterized isoforms in the FPR family, and both bind structurally diverse ligands. The stimulation of FPR2 has been shown to modulate the post-MI healing response via the polarization of macrophages to a proresolution phenotype, sometimes referred to as “M2” (8,9). In

From the [a]Department of Cardiovascular and Fibrosis Drug Discovery, Bristol-Myers Squibb Company, Pennington, New Jersey; [b]Department of Medicine, University of California San Diego, San Diego, California; and the [c]Institute for Research in Immunology and Cancer, Université de Montréal, Montréal, Québec, Canada. This work was supported by Bristol-Myers Squibb (Princeton, NJ, USA). Bristol-Myers Squibb policy on data sharing may be found at https://www.bms.com/researchers-andpartners/independent-research/data-sharing-request-process.html. All other authors have reported that they have no relationships relevant to the contents of this paper to disclose.
The authors attest they are in compliance with human studies committees and animal welfare regulations of the authors’ institutions and Food and Drug Administration guidelines, including patient consent where appropriate. For more information, visit the *JACC: Basic to Translational Science* author instructions page.

Manuscript received February 22, 2019; revised manuscript received July 16, 2019, accepted July 17, 2019.

addition, treatment with the endogenous ligands resolvin D1 and 15-epi-lipoxin promotes inflammation resolution and limits early remodeling (8,9). Similar observations have been made with a synthetic FPR1/2-biased agonist that demonstrated cardioprotective properties when given at the time of myocardial injury (10).

SEE PAGE 921

To address the capacity of FPRs to provide long-term benefit after myocardial injury, a dual agonist of FPR1/2 identified as Compound 43 (Cmpd43) (11–13) was administered orally to evaluate relationships between heart structure and function after MI. In addition, the signaling and cellular response stimulated by Cmpd43 and regulation of key cytokines associated with proinflammatory and pro-resolution phases are described.

METHODS

For an expanded Methods section, please see the Online Appendix.

IN VITRO AND/OR CELLULAR ASSAYS. The dose-response activity of Cmpd43 on intracellular signaling and key inflammatory cell functions, including phagocytosis, oxidative burst, chemotaxis, and cytokine gene expression, was determined in peritoneal macrophages or established cell lines (HL-60 or HEK293).

The signaling profile of Cmpd43 was determined in HEK293 cells that transiently expressed either FPR1 or FPR2. Activation of G proteins (Gαi1, Gαi2, Gαi3, GαoA, GαoB, Gα12, and Gα13) and recruitment of β-arrestins (β-arrestin-1 and β-arrestin-2) were measured using bioluminescence resonance energy transfer–based biosensor assays (14).

Phagocytosis was evaluated using BioGel-elicited peritoneal macrophages from wild-type (WT) C57BL/6 mice and FPR1 and FPR2 knockout (KO) mice. The FPR2 KO was analogous to that reported by Dufton et al. (15), which was deficient in FPR2 and FPR3 (see Online Appendix). Macrophages were treated with Cmpd43 for 15 min and provided with opsonized fluorescein isothiocyanate-labeled zymosan (1:8 ratio of cells to zymosan) for 45 min at 37°C. Phagocytosis was quantified using a fluorescence plate reader.

Cellular oxidative burst, which occurs in phagocytes following zymosan uptake, was measured in differentiated HL-60 cells and engineered CRISPR KO HL-60 cells deficient in FPR1 or FPR2. Cells were incubated for 15 min in buffer containing 0.4 mM luminol and a concentration range of Cmpd43 before stimulation with 2 μg of opsonized zymosan. Bioluminescence was quantified immediately after stimulation using a plate reader.

Chemotaxis in HL-60 cells was assessed using Transwell plates. Migration was induced by placing Cmpd43 in the bottom chamber and HL-60 cells in the top. Cells were allowed to migrate into the lower chamber for 120 min and then quantified using a cell viability assay.

Regulation of cytokine gene expression in BioGel-elicited peritoneal macrophages was evaluated in the setting of proinflammatory stimulation using serum amyloid A (SAA). SAA is an acute-phase protein secreted during the early inflammatory response and is a ligand for various receptors, including FPR2 (16). Macrophages were pre-treated with Cmpd43 for 30 min followed by incubation for 5 h ± 600 nM SAA. Cells were lysed directly in Tri Reagent, and mRNA levels of inflammatory cytokines interleukin (IL)-10 and IL-6 were quantified by reverse transcription polymerase chain reaction.

ANIMAL STUDIES

Animal studies followed American Association for Accreditation of Laboratory Animal Care guidelines, and protocols were approved by Bristol-Myers Squibb and University of California San Diego Animal Care and Use committees. Adult male C57BL/6 mice (10 to 12 weeks old) and adult male Sprague-Dawley rats (6 to 7 weeks old) were purchased from the Jackson Laboratory (Bar Harbor, Maine) and Charles River Laboratories (Wilmington, Massachusetts), respectively.

Animals were anesthetized with an intraperitoneal injection of ketamine (100 mg/kg) and xylazine (8 mg/kg) followed by endotracheal intubation and mechanical ventilation with oxygen supplemented with isoflurane (2.0% to 2.5%). The heart was exposed surgically via a left thoracotomy. In mice, the left anterior descending (LAD) artery was permanently occluded by suture. In rats, ischemia-reperfusion (IR) was implemented by transiently occluding the LAD artery for 45 min. For sham animals, a suture was placed but not tightened. The chest was closed and appropriate analgesics administered. In the mouse MI study, the treatment groups were sham (n = 14), MI vehicle (0.5% carboxymethylcellulose) (n = 13), MI Cmpd43 (1 mg/kg) (n = 14), and MI Cmpd43 (10 mg/kg) (n = 14). Once-daily oral dosing by gavage was initiated 24 h post-MI and continued for 4 weeks. An independent set of treated mice (n = 4 to 8) were euthanized approximately 3 days post-MI, and hearts were harvested 2 h after dosing for macrophage marker assays as described in the following section. In the rat IR experiments, treatment groups were

FIGURE 1 Signaling Profile of Cmpd43 in HEK293 Cells Expressing Human FPR1 and FPR2

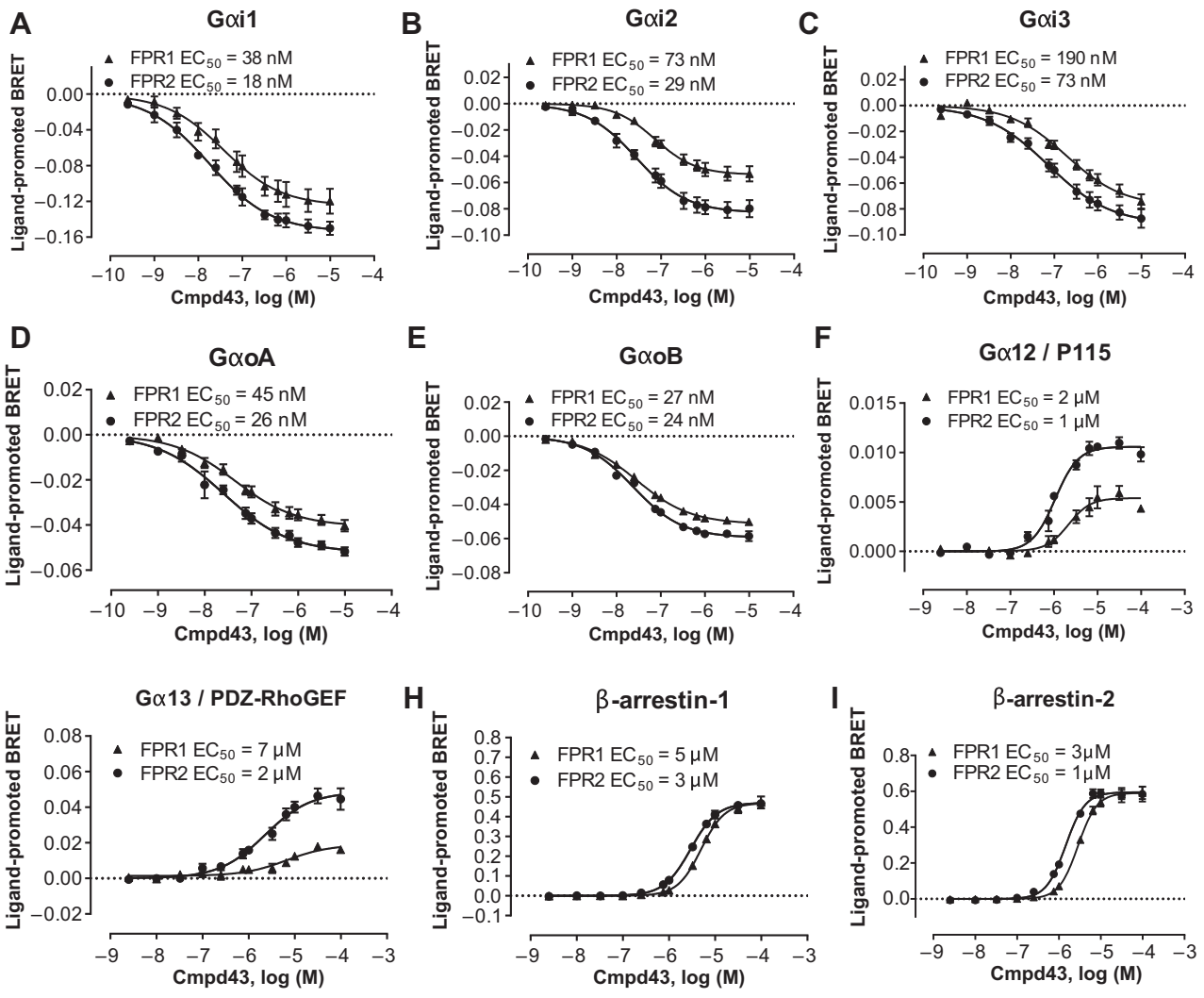

The ability of Compound 43 (Cmpd43) to engage different signaling pathways was assessed using bioluminescence resonance energy transfer (BRET) biosensors that detected the activation of **(A)** Gαi1, **(B)** Gαi2, **(C)** Gαi3, **(D)** GαoA, and **(E)** GαoB, the interaction of effectors with **(F)** Gα12 and **(G)** Gα13, as well as the recruitment of **(H)** β-arrestin-1 and **(I)** β-arrestin-2 to the plasma membrane. HEK293 cells expressing human formyl peptide receptor (FPR)-1 or FPR2 were stimulated with Cmpd43, and modulation of the BRET signals from the different biosensors was recorded. Data represent the mean ± SEM of 3 independent experiments. EC_{50} = concentration of Cmpd43 that gives half-maximal response.

sham (n = 10), MI vehicle (n = 17), and MI Cmpd43 (10 mg/kg) (n = 14). Once-daily oral dosing by gavage was initiated 48 h post-MI and continued for 6 weeks.

In terminal studies, LV pressure-volume (PV) relationships (mouse and rat) and passive 2-dimensional epicardial strains of the infarct scar (mouse) were measured ex vivo in diastolic-arrested and excised mouse and rat hearts. Using a Langendorff apparatus, the aorta was cannulated for perfusion with diastolic arrest buffer. A thin-walled balloon was placed into the LV cavity and connected to a pressure transducer and infusion pump. Epicardial surface markers were placed on the anterior epicardial wall. A digital camera was positioned to capture images of the scar or analogous region of sham hearts. LV inflation-deflation conditioning cycles were followed by 2 to 3 acquisition runs. Synchronized video images were obtained. Subsequently, hearts were perfusion fixed with 10% buffered formalin while maintaining LV balloon pressure at 10 to 15 mm Hg. Hearts were stored in formalin for histological processing. In the rat terminal

FIGURE 2 Regulation of Inflammatory Cell Function by Cmpd43

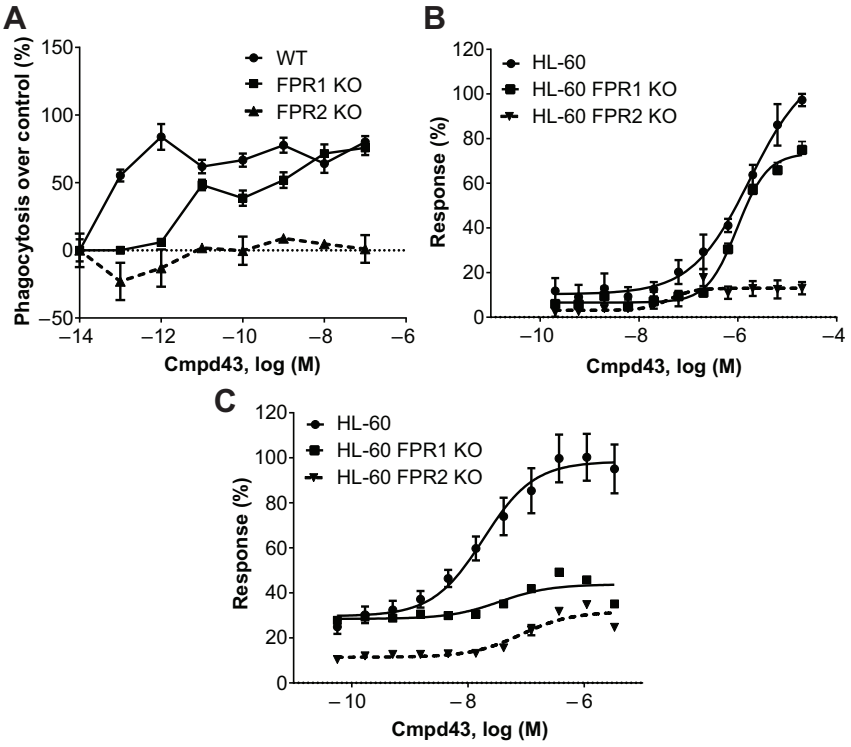

(A) Enhancement of zymosan phagocytosis by Cmpd43 was assessed in BioGel-elicited peritoneal macrophages from wild-type (WT), FPR1 knock out (KO), and FPR2 KO mice. **(B)** Stimulation of oxidative burst activity was evaluated in neutrophil-like HL-60, HL-60 FPR1 KO, and HL-60 FPR2 KO cell lines. **(C)** Chemotactic responses to Cmpd43 were evaluated in HL-60, HL-60 FPR1 KO, and HL-60 FPR2 KO cell lines. Other abbreviations as in Figure 1.

experiments at 6 weeks post-IR, animals were re-anesthetized with isoflurane, and a transducer-tipped conductance catheter (2.5-F; Millar, Inc., Houston, Texas) was inserted into the left ventricle via a right carotid cutdown. LV PV loop data were acquired and corrected for parallel conductance using the bolus intravenous saline injection method. Volume calibration was performed with rat blood against known volumes using standardized cuvettes. PV loop data were analyzed using LabChart software (AD Instruments, Inc., Colorado Springs, Colorado). Rat hearts were subsequently excised following diastolic arrest, and ex vivo passive PV curves were obtained as described previously for mice.

MACROPHAGE PHENOTYPING. Two h after the last Cmpd43 dose, mice were injected intraperitoneally with 100 U of heparin and then anesthetized with 5% isoflurane. Hearts were removed, minced into pieces, and digested with a mild collagenase cocktail for 35 min. The cell suspension was filtered to remove debris, and residual red blood cells were lysed. Samples (2×10^6 cells) were processed for flow cytometry using the following surface markers: CD45 [PerCP], Ly-6G[APC-Cy7], CD64[APC], and CD206[PE-Cy7]. Data were analyzed post hoc.

HISTOLOGY. Hearts were cut along the short axis at the midventricle and processed. Paraffin-embedded sections were cut and stained with trichrome or picrosirius red for collagen evaluation and analyzed by computer-assisted histomorphometry for quantitation of scar area and left ventricle cavity and myocardial wall dimensions. In situ hybridization experiments were carried out to detect arginase-1 and FPR2 mRNA levels in the peri-infarct border zone of mouse hearts. The target mRNAs were visualized using a standard bright field microscope and scanned at 20× using the Aperio eSlide Manager (Leica Biosystems Imaging, Inc., Vista, California) followed by quantitation.

DATA AND STATISTICAL ANALYSIS. Statistical significance was determined using a Student's *t*-test or analysis of variance followed by a Dunnett's post hoc

FIGURE 3 IL-10 and IL-6 Regulation by Cmpd43

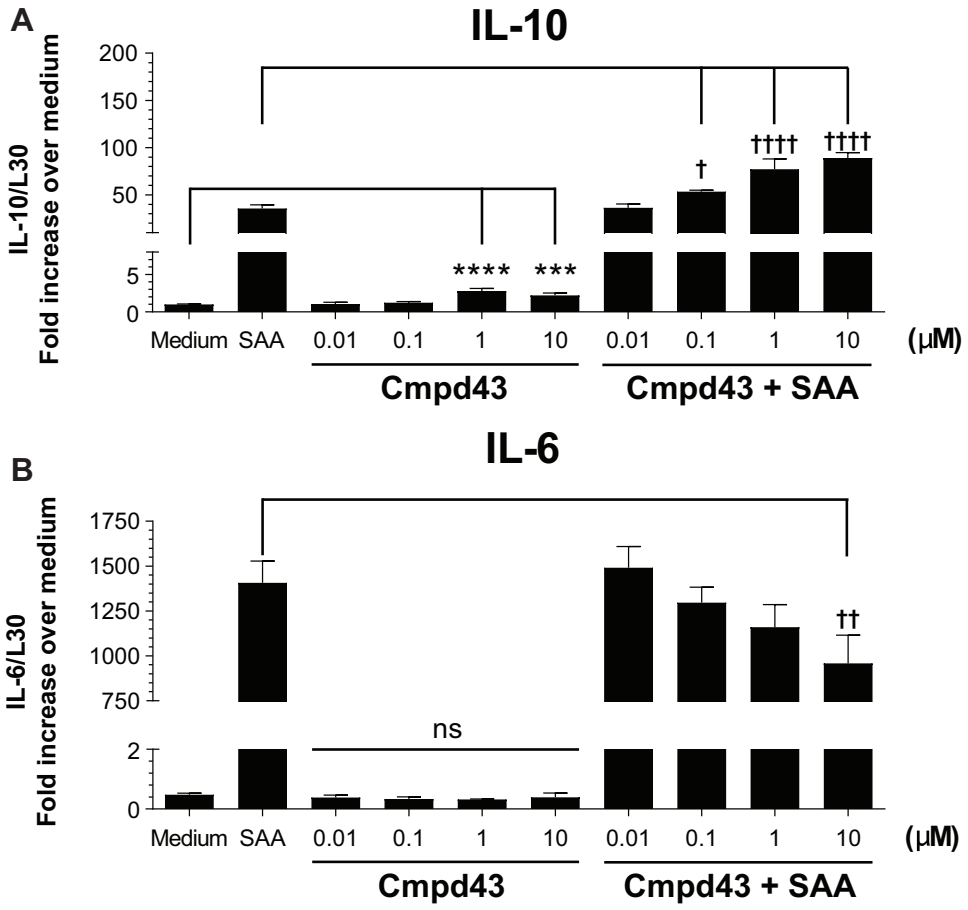

Concentration-dependent regulation of **(A)** interleukin (IL)-10 and **(B)** IL-6 mRNA levels by Cmpd43 in BioGel-elicited mouse peritoneal macrophages. Macrophages were pretreated with Cmpd43 for 30 min followed by incubation for 5 h ± 600 nM serum amyloid A (SAA). **(C)** IL-10 and **(D)** IL-6 mRNA modulation in peritoneal macrophages from WT and FPR2 KO mice are presented. Data represent the mean ± SEM. Dunnett's versus medium: **$p < 0.01$, ***$p < 0.001$, ****$p < 0.0001$. Dunnett's versus SAA: †$p < 0.05$, ††$p < 0.01$, †††$p < 0.001$, ††††$p < 0.0001$. Other abbreviations as in Figures 1 and 2.

Continued on the next page

test to compare specified treatments with a single control. Statistical analyses were conducted, and values for the concentration of Cmpd43 that gives half-maximal response (EC_{50}) were calculated using GraphPad Prism Version 7.03 (GraphPad Software, Inc., La Jolla, California). Unless otherwise noted, data are shown as mean ± SEM. Statistical significance was noted as $p < 0.05$, $p < 0.01$, $p < 0.001$, or $p < 0.0001$.

RESULTS

The first objective was to evaluate the cellular properties of Cmpd43. The signaling profile was examined in HEK293 cells that expressed human FPR1 or FPR2. Cmpd43 produced concentration-dependent modulation of bioluminescence resonance energy transfer signals for Gαi1, Gαi2, Gαi3, GαoA, and GαoB biosensors following FPR1 and FPR2 activation (EC_{50} shown in Figures 1A to 1E). The responses for the Gαi/o signaling pathways were consistent with FPR1 and FPR2 agonist-mediated reductions in cellular cyclic adenosine monophosphate (17,18). A response was also observed for Gα12 and Gα13 biosensors after stimulation of FPR1- or FPR2-expressing cells with Cmpd43 (Figures 1F and 1G), but not for Gαq, Gα11, or Gαs biosensors (Online Figure 1). This

FIGURE 3 Continued

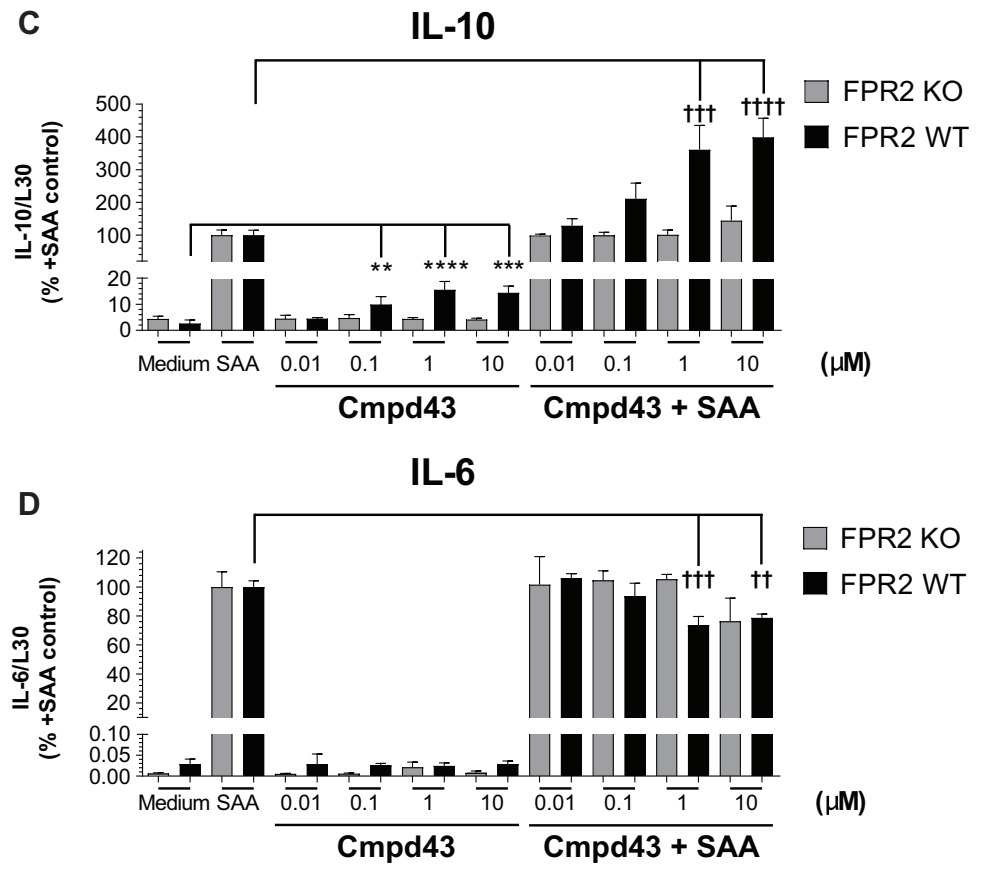

observation suggested that in addition to coupling to Gαi/o family members, FPR1 and FPR2 could also engage Gα12 and Gα13 proteins after stimulation with Cmpd43. Cmpd43 also promoted β-arrestin-1 and -2 recruitment to both FPR1 and FPR2 (**Figures 1H and 1I**). The potency values for β-arrestin-1 and -2 recruitment, as well as for Gα12 and Gα13 activation, were consistently reduced for both receptor subtypes compared with the Gαi/o signaling pathways, with EC_{50} values between 1 and 7 μM for the β-arrestins and Gα12/13 signaling pathways, as opposed to 18 to 190 nM for Gαi/o activation. Bioluminescence resonance energy transfer assays were also carried out using rat and mouse FPR2 receptors and confirmed activation of the Gi pathway as well as recruitment of β-arrestin-1 to rodent species with Cmpd43 (Online Figure 2). Overall, the signaling profile of Cmpd43 was conserved between FPR1 and FPR2, with both receptor subtypes leading to Gαi/o, Gα12/13, and β-arrestin-1 and -2 activation after Cmpd43 stimulation.

Zymosan phagocytosis was evaluated in peritoneal macrophages from WT, FPR1 KO, and FPR2 KO mice. As shown in **Figure 2A**, potent stimulation of phagocytosis with Cmpd43 occurred with WT-derived macrophages (EC_{50} ~0.1 pM) with an apparent plateau achieved at 1 pM. By contrast, FPR2 KO–derived macrophages did not respond to Cmpd43 stimulation above control. FPR1 KO–derived macrophages showed an intermediate response, which suggested a modest role of FPR1 in phagocytosis enhancement.

Phagocytes respond to chemotactic stimuli and degrade internalized particles and bacteria while undergoing an oxidative respiratory burst (19). The capacity of Cmpd43 to stimulate oxidative burst activity and chemotaxis was investigated using differentiated human promyelocytic leukemia HL-60 cells, which possess a neutrophil-like lineage (20). **Figure 2B** shows Cmpd43-stimulated oxidative burst activity in HL-60 (EC_{50} = 1.8 μM) and HL-60 FPR1 KO (EC_{50} = 1 μM) cells. Activity was essentially abolished in the HL-60 FPR2 KO line. Cmpd43 also stimulated

FIGURE 4 Arginase-1 and CD206 Levels Post-MI

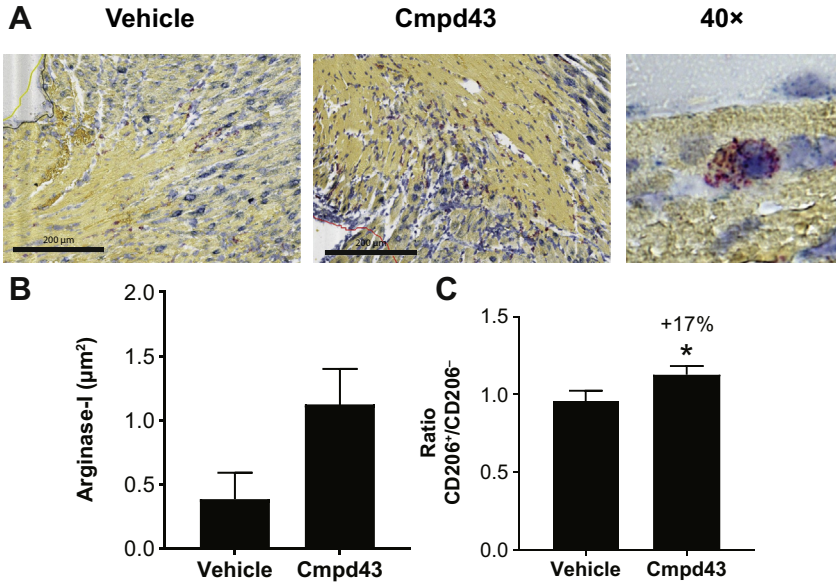

(A) Histologic images of arginase-1 by in situ hybridization 74 h following myocardial infarction (MI) via permanent left coronary artery ligation. Representative images of the peri-infarct zone from infarcted mice treated with vehicle or Cmpd43 (10 mg/kg) are shown. Arginase-1 mRNA is indicated in **red** and FPR2 mRNA is **blue**. A 40× image of a macrophage containing arginase-1 and FPR2 is shown on the **right**. **(B)** Quantification of arginase-1 mRNA levels for vehicle and Cmpd43 (10 mg/kg; n = 4 per group). **(C)** Ratio of $CD206^{+}/CD206^{-}$ macrophages from infarcted mice treated with vehicle (n = 9) or Cmpd43 (10 mg/kg; n = 10). Whole hearts were digested and cell homogenates were analyzed by flow cytometry. *t*-test: *$p < 0.05$. Other abbreviations as in Figures 1 and 2.

chemotaxis of differentiated HL-60 cells with an EC_{50} of 18 nM (Figure 2C). Absence of FPR1 and FPR2 severely impaired chemotactic responses, which suggested both isoforms were involved.

The cytokines IL-10 and IL-6 are induced during inflammation and resolution processes (21). As shown in Figure 3, Cmpd43 modulated the expression levels of these cytokines in peritoneal macrophages. In the absence of proinflammatory stimulation with SAA, Cmpd43 alone increased IL-10 gene expression approximately 2- to 3-fold at 1 and 10 μM relative to medium control ($p < 0.001$) (Figure 3A). When macrophages were treated with 600 nM SAA, IL-10 mRNA increased 35-fold versus medium. In the presence of Cmpd43, IL-10 levels were increased 1.5-, 2.2-, and 2.5-fold at 0.1, 1, and 10 μM relative to SAA control, respectively. In the same experiment, induction of IL-6 mRNA expression with SAA was significantly attenuated in the presence of Cmpd43 10 μM ($p < 0.05$) (Figure 3B). To confirm that the changes in expression of these cytokines were due, in part, to agonism of FPR2 with Cmpd43, a parallel experiment was conducted with peritoneal macrophages from FPR2 KO mice and WT littermates. In the absence of FPR2, no modulation of IL-10 or IL-6 mRNA expression was observed either with Cmpd43 alone or in the presence of SAA (Figures 3C and 3D).

To determine whether Cmpd43 activity on macrophage function observed in vitro would manifest under MI conditions in vivo, the early effects of Cmpd43 on macrophages were evaluated in mouse cardiac tissue after MI. Arginase-1, a canonical marker for M2 proresolution macrophages (22), was evaluated in a small cohort of mice (n = 4 per group) approximately on day 3 following MI (2 h after the third dose of Cmpd43). Histologic images showed increases in arginase-1 mRNA via in situ hybridization (Figure 4A). A trend toward increased levels of arginase-1 was observed with Cmpd43 relative to vehicle in the peri-infarct border zone (~4-fold vs. vehicle) (Figure 4B). No apparent difference in total macrophage content between treatment groups was observed (Online Figure 3). A comparative experiment with a larger cohort was conducted to detect global changes in proresolution markers in the whole heart. CD206 represents another classic marker of proresolution macrophages (22). Using the same in-life protocol, CD206 surface levels were assessed

FIGURE 5 Cmpd43 Effects on LV and Infarct Structure 28 Days Post-MI in Mice

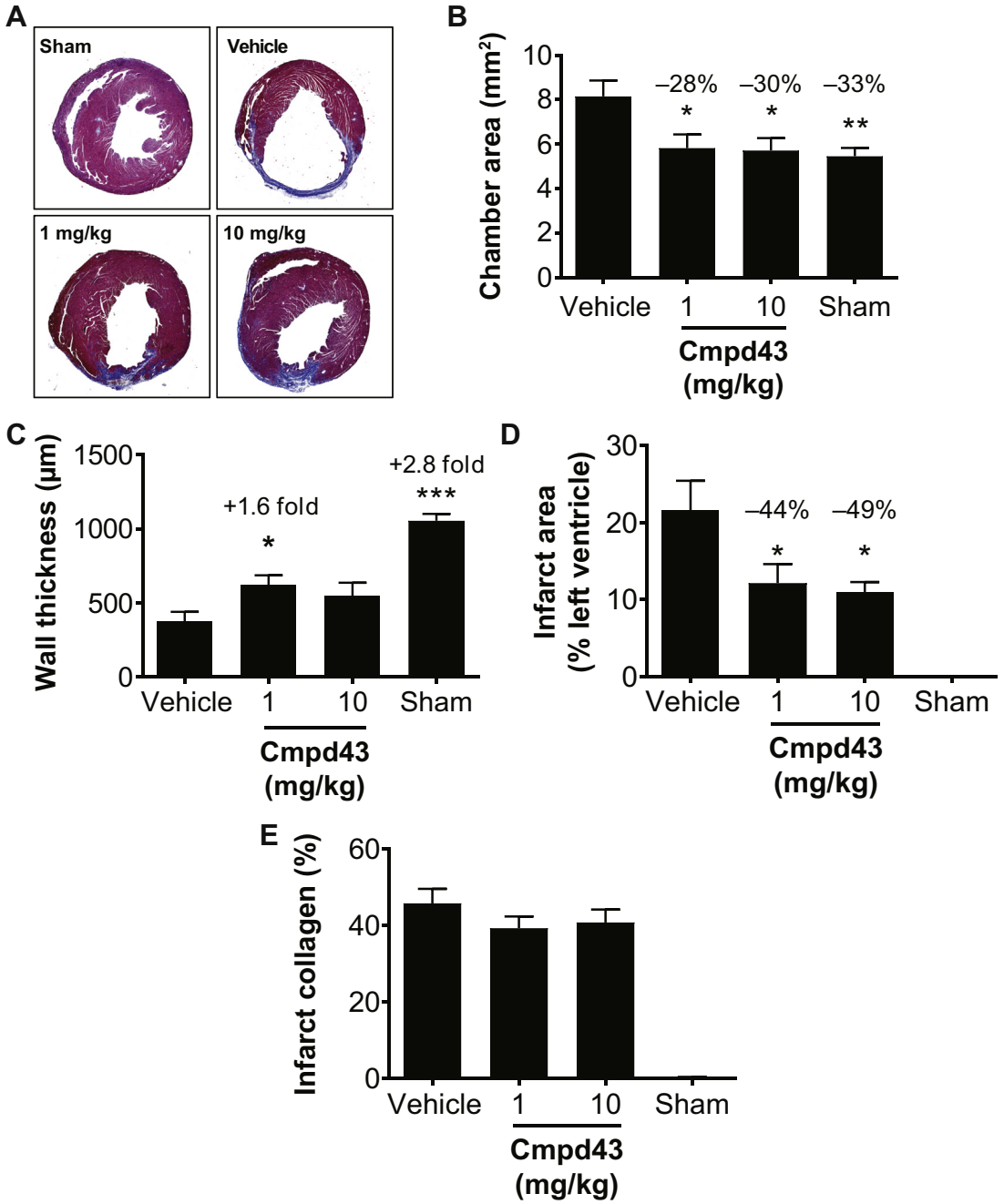

Treatments were initiated 24 h after MI and continued to 28 days. Treatments consisted of a suspension vehicle and Cmpd43 at either 1 mg/kg or 10 mg/kg. **(A)** Representative heart cross sections by histology depicting the degree of MI. Noninfarcted surgical sham animals are shown for comparison. Histomorphometric analysis of **(B)** chamber area, **(C)** infarct wall thickness, **(D)** infarct area, and **(E)** infarct collagen content 28 days after MI. Dunnett's versus vehicle: *$p < 0.05$, **$p < 0.01$, ***$p < 0.001$. Other abbreviations as in Figures 1, 2, and 4.

FIGURE 6 Mouse LV Passive Mechanics and 2-Dimensional Epicardial Scar Strains 28 Days Post-MI

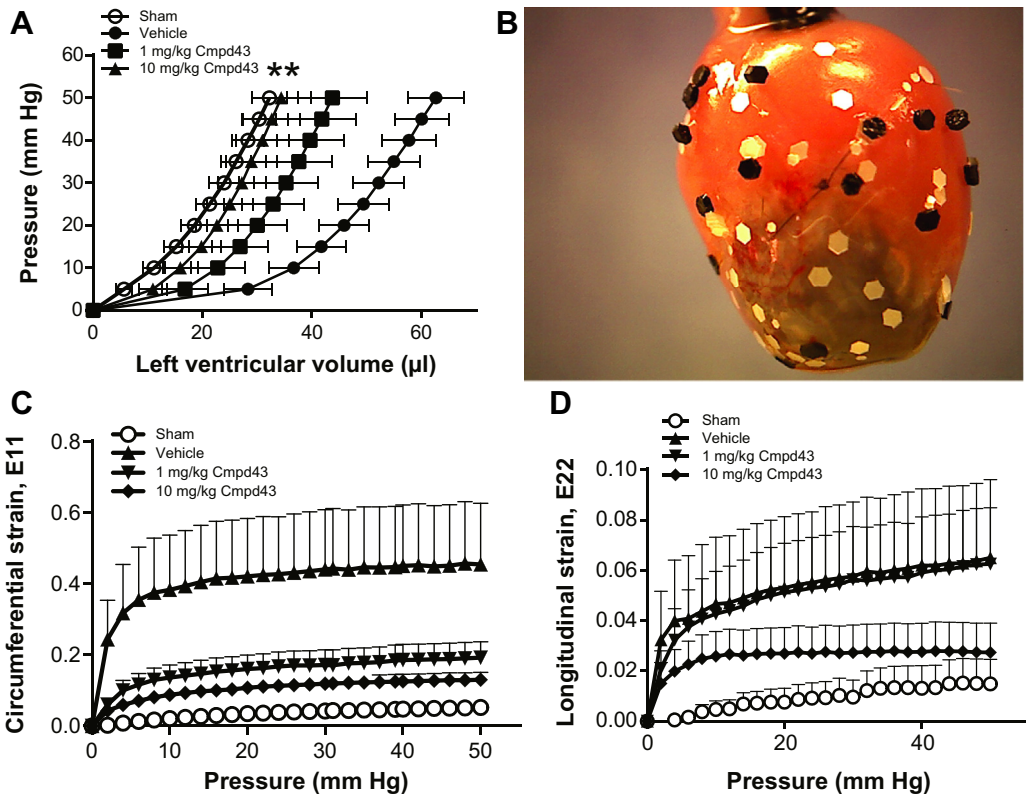

(A) LV pressure–volume curves. **(B)** Representative mouse heart preparation for epicardial scar strains analysis showing marker placement on the heart. **(C)** Circumferential (E_{11}) scar strains. **(D)** Longitudinal (E_{22}) scar strains. One-way analysis of variance (all pressures): **$p < 0.01$. Abbreviations as in Figures 1, 4, and 5.

in macrophages isolated from post-MI hearts following mild collagenase digestion and flow cytometry. The ratio of pro-resolution $CD206^+$ macrophages was increased 17% in mice treated with Cmpd43 versus vehicle ($p < 0.05$) (Figure 4C). No significant difference in $CD64^+$ macrophage content between treatment groups was detected (Online Figure 3).

The effects of a 28-day treatment with Cmpd43 (1 and 10 mg/kg QD, orally) on LV and infarct scar remodeling were evaluated in the mouse permanent coronary artery occlusion model. Cross sections of the heart were analyzed for histomorphometric assessments of LV chamber area, scar dimensions (size and wall thickness), and infarct collagen content. Figure 5A shows representative cross sections of trichrome-stained hearts for the various treatment groups and shams. The extent of chamber dilatation, wall thinning, and infarct scar in the treated groups was visually less than that in the vehicle group. Figure 5B shows the effects of treatments on chamber dilatation. Treatment with Cmpd43 attenuated chamber expansion at the 1 and 10 mg/kg doses (−28 and −30% vs. vehicle, respectively; $p < 0.05$). The chamber areas for Cmpd43-treated mice were similar in size to noninfarcted shams. Infarct wall thicknesses were measured for all groups (Figure 5C). The 1 mg/kg Cmpd43 dose yielded a 1.6-fold increase in wall thickness relative to vehicle ($p < 0.05$). A trend toward increased wall thickness was noted at the 10 mg/kg dose versus vehicle. In addition, there were no differences in contralateral wall thicknesses between treatment groups (Online Figure 4). Infarct scar area was measured and reported as a percentage of the total LV cross-sectional area. Cmpd43 reduced LV anterior wall infarct scar size at 1 and 10 mg/kg doses (44% and 49% relative reductions vs. vehicle, respectively; $p < 0.01$) (Figure 5D). Notably, no differences in infarct collagen content were observed between treatment groups (Figure 5E), indicating no

FIGURE 7 Cmpd43 Effects on Cardiac Structure/Function Following Ischemia–Reperfusion in the Rat

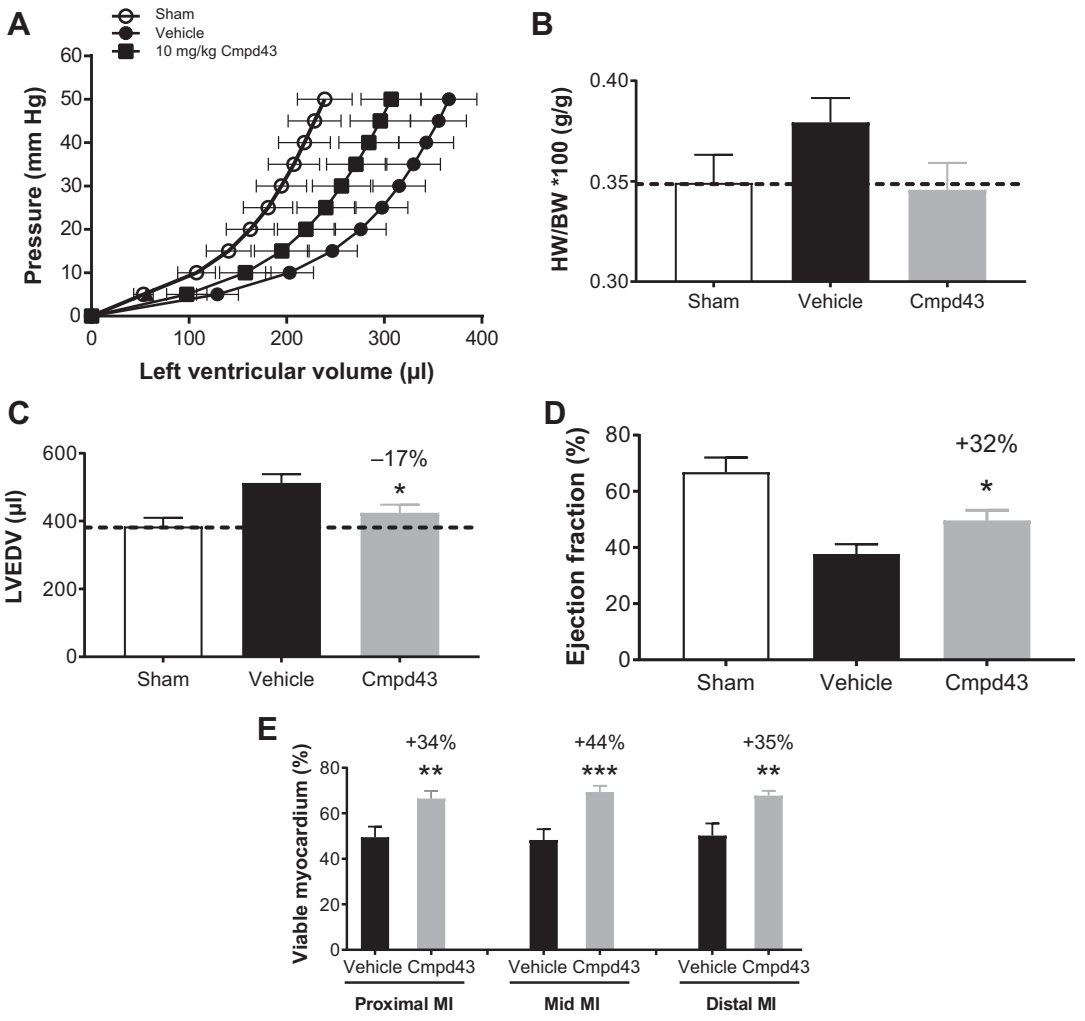

(A) LV pressure–volume curves, **(B)** heart weight (HW)/body weight (BW) ratio, **(C)** left ventricular end-diastolic volume (LVEDV), **(D)** ejection fraction, and **(E)** percent viable myocardium relative to infarct scar across the infarcted wall (epicardium to endocardium) at the proximal MI region near the ligature, at the mid-MI region, and at the distal MI region. Dunnett's versus vehicle: *$p < 0.05$, **$p < 0.01$, ***$p < 0.001$. Other abbreviations as in Figures 1, 4, and 5.

adverse impact on infarct collagen deposition and wound healing after MI.

The effect of Cmpd43 on ex vivo LV passive mechanics 28 days post-MI was consistent with the previously described histomorphometric data (Figure 6A). Compared with noninfarcted sham hearts, there was a pronounced rightward shift in the PV curve of the MI vehicle group. By contrast, PV curves obtained with Cmpd43 were left-shifted relative to vehicle ($p < 0.01$), which indicated smaller LV chamber volumes versus vehicle. At the 10 mg/kg dose, the PV curve was comparable to the sham PV curve. At the 1 mg/kg dose, the curve was left-shifted to an intermediate level between the sham and vehicle. Epicardial scar strains were measured for all groups (Figure 6B). Scar strain measurements along the short axis of the heart (circumferential E_{11} direction) are shown in Figure 6C. Sham hearts were analyzed in a region of the left ventricle where infarction was predicted to occur. For the sham group, E_{11} strains were small (i.e., stiff myocardium). By contrast, vehicle showed the highest scar strains in the E_{11} direction, which suggested an

TABLE 1 LV Hemodynamics Data 6 Weeks Post-Ischemia-Reperfusion Injury

	Sham	Vehicle	Cmpd43
Heart rate, beats/min	308.5 ± 7.6	316.0 ± 5.1	303.2 ± 8.1
Pao systolic, mm Hg	129.8 ± 5.5	125.1 ± 3.5	124.9 ± 4.6
Pao diastolic, mm Hg	93.0 ± 4.4	86.8 ± 3.1	88.5 ± 3.8
Pao mean, mm Hg	109.2 ± 4.8	104.2 ± 3.2	104.8 ± 3.9
Cardiac output, ml/min	73.8 ± 4.5	55.9 ± 3.8	59.8 ± 4.7
Stroke volume, μl	239.1 ± 14.4	176.9 ± 11.5	196.3 ± 13.7
End-diastolic volume, μl	384.4 ± 25.5	512.7 ± 25.7	424.8 ± 24.2*
End-systolic volume, μl	180.7 ± 25.4	328.7 ± 30.9	261.9 ± 24.3*
Ejection fraction, %	66.8 ± 5.2	37.7 ± 3.4	49.6 ± 3.6*
dV/dt max, ml/s	8.7 ± 0.6	7.4 ± 0.7	8.1 ± 0.5
LV volume at dP/dt max, μl	371.5 ± 25.8	464.3 ± 29.0	406.7 ± 25.0*
LV volume at dP/dt min, μl	173.8 ± 23.4	317.3 ± 30.4	250.0 ± 23.6*
ESPVR slope, mmHg/μl	0.51 ± 0.11	0.73 ± 0.19	0.62 ± 0.18
Tau, ms	10.8 ± 1.4	11.7 ± 1.4	12.8 ± 2.2

Values are mean ± SEM. Dunnett's versus vehicle: *$p < 0.05$.

Cmpd43 = Compound 43; ESPVR = end-systolic pressure-volume relationship; LV = left ventricular; Pao = aortic pressure.

increase in scar distension and compliance. E_{11} strains for the 1 mg/kg and 10 mg/kg Cmpd43 treatment groups approached levels achieved with sham hearts, indicating stiffer scarring in this direction. On average, smaller scar strains were obtained with 10 mg/kg Cmpd43 versus the 1 mg/kg treatment. As shown in **Figure 6D**, in the E_{22} direction (longitudinal axis), sham mice showed little change in strains (stiff myocardium), and vehicle showed the greatest increase in strains. Treatment with 1 mg/kg Cmpd43 produced a profile that closely resembled that of vehicle. At the 10 mg/kg dose, the profile showed an intermediate effect between sham and vehicle, suggesting an increase in infarct stiffness relative to vehicle.

The capacity of Cmpd43 to improve LV and infarct scar remodeling post-MI was also evaluated in the rat model. An IR design was used to reflect the clinical scenario because reperfusion strategies are used post-MI. LV PV curves (**Figure 7A**) obtained for the MI vehicle group showed an expected rightward shift compared with sham. The PV curve obtained with 10 mg/kg Cmpd43 was left-shifted relative to vehicle, indicating smaller chamber volumes. A trend toward a reduced heart weight/body weight ratio was observed with Cmpd43 treatment relative to the MI vehicle group and was comparable to the heart weight/body weight ratio of sham (**Figure 7B**). The MI vehicle group showed a 33% increase in mean LV end-diastolic volume relative to sham. Cmpd43 10 mg/kg decreased LV end-diastolic volume relative to vehicle by 17% (**Figure 7C**) ($p < 0.05$). As shown in **Figure 7D**, infarcted rats treated with vehicle showed a mean ejection fraction of 38%, whereas noninfarcted sham hearts had an ejection fraction average of 67%. Treatment with Cmpd43 yielded a statistically significant relative improvement in ejection fraction of 32% versus vehicle (12% absolute increase; $p < 0.05$). **Table 1** summarizes the various hemodynamic parameters measured in the study. Regional measurements of viable myocardium relative to infarct scar tissue were made transmurally across the infarct wall (i.e., from epicardium to endocardium) (**Figure 7E**). Preservation of myocardium was observed with Cmpd43 at the proximal MI region (nearest the ligature; 34% relative increase vs. vehicle; $p < 0.01$), at the mid-MI wall (44% relative increase vs. vehicle; $p < 0.001$), and at the distal MI region (35% relative increase vs. vehicle; $p < 0.01$). No statistically significant differences in wall thickness between vehicle- and Cmpd43-treated rats were observed in any region of the MI (Online Figure 5). Noninfarcted sham rats had 100% viable transmural walls (data not shown).

DISCUSSION

Activation of the acute inflammatory response following MI facilitates the onset of wound healing and scar formation in the heart. Dysregulation and/or prolongation of the inflammatory response can lead to additional tissue damage, worsened LV function, and eventual decompensation, leading to HF. In this regard, activation of the resolution process is critical for restoring damaged tissue to a non-inflamed healed state. Pharmacological strategies to stimulate inflammation resolution may thus speed healing and limit adverse post-MI changes in cardiac structure and function. Our findings demonstrated that targeted stimulation of FPR1/2 with Cmpd43 enhanced immune responses that drive inflammation resolution. In vivo, Cmpd43 protected the heart from ischemic injury and prevented the deterioration of cardiac function post-MI.

Macrophage phagocytosis of apoptotic and necrotic cells was shown to enable wound healing and to potentiate post-MI inflammation resolution (23,24). In WT mice, Cmpd43 stimulated robust phagocytosis of zymosan particles; the activity was largely attributed to FPR2, because no enhancement in zymosan clearance was observed in FPR2-deficient macrophages. These data are consistent with impairments in phagocytosis of peritoneal bacteria observed in a sepsis model that used FPR2-deficient mice (25). Interestingly, when phagocytosis experiments were carried out with FPR1-deficient macrophages, a decrease in potency was observed, which suggested

the partial involvement of FPR1 in phagocytosis. Activated phagocytes release reactive oxygen species (oxidative burst) into the ingested phagosome (19). Oxidative burst profiles obtained with parental HL-60 cells and those deficient in FPR1 or FPR2 revealed similar activity patterns after Cmpd43 exposure to those shown with peritoneal macrophages (i.e., no response with FPR2 deficiency and a slightly right-shifted response with FPR1 deficiency). Cmpd43 also readily stimulated HL-60 cell chemotaxis, whereas FPR1- and FPR2-deficient lines showed severely diminished responses. These results are in line with published reports that described the involvement of FPR1/2 in leukocyte chemotaxis (12,26,27).

The concentration-dependent effects of Cmpd43 on intracellular signaling of FPR1/2 via Gαi and Gαo proteins confirmed the known coupling of these receptors to the Gi family (10,28,29). Following activation of Gαi/o proteins, the dissociated Gβγ subunits engage downstream effectors, leading to release of calcium from intracellular stores and protein kinase C activation, a process believed to play a role in superoxide production and chemotaxis (30,31). Beyond the Gi family, engagement of Gα12 and Gα13 proteins was also observed upon stimulation with Cmpd43, for both FPR1 and FPR2. Such coupling of FPRs to Gα12 and Gα13 pathways was previously suggested based on the effect of Gα12/Gα13 dominant-negative constructs on cell polarity induced by stimulation of HL-60 cells with the FPR1 ligand fMLP (32). In addition to promoting activation of Gαi/o and Gα12/13 proteins, Cmpd43 stimulated FPR1/2-mediated recruitment of β-arrestins. A variety of FPR1/2 agonists are known to recruit β-arrestin (13,33). A noncanonical role for β-arrestin in leukocyte function, to include cell migration and infiltration, has been described and might be relevant to key functions attributed to FPR1/2 action (34). In human neutrophils, a selective FPR2 agonist with impaired β-arrestin recruitment properties was unable to stimulate chemotaxis (35). In HL-60 cells, targeted knockdown of β-arrestin-1 using short hairpin RNA-containing viral particles displayed a clear defect in chemotaxis towards fMLP (36). These observations demonstrate the importance of β-arrestin in leukocyte trafficking, in which impairments in this signaling pathway might disrupt important leukocyte responses during wound healing.

IL-10 has been described as a potent anti-inflammatory cytokine with clear links to the resolution of myocardial inflammation (37). In vitro treatment of SAA-activated peritoneal macrophages with Cmpd43 resulted in concentration-dependent increases in IL-10 mRNA levels, which were abolished in the absence of FPR2. Relevant to the present study, it has been reported that increases in IL-10 via short-term exogenous administration attenuated LV remodeling and infarct wall thinning post-MI (38). These improvements were preceded by early decreases in proinflammatory cytokines (IL-6, tumor necrosis factor-α, and others) in the myocardium. In the present study, Cmpd43 also reduced IL-6 mRNA in SAA-activated macrophages, which indicated a drive toward the resolution of inflammation. Collectively, these data support the concept that early macrophage FPR cytokine regulation, and, in particular, FPR2, achieved with Cmpd43 could lead to favorable effects on downstream LV remodeling post-MI. It was further demonstrated that early changes in macrophage phenotype could be evoked by Cmpd43 in post-MI cardiac tissue. An increase in proresolution $CD206^{+}$ macrophages was noted in the myocardium of mice assessed approximately 3 days post-MI. This was accompanied by increased expression of the proresolution marker, arginase-1, at the border zone of the infarct. These findings were consistent with the capacity of Cmpd43 via FPRs to stimulate proresolution macrophages during wound repair after MI. Importantly, enhanced expression of resolution markers achieved with endogenous ligands for FPR2 in the mouse heart has been reported to correlate with improved myocardial healing and LV function post-MI (8,9,39).

Long-term treatment with Cmpd43 improved cardiac structure and function relationships in both the mouse permanent coronary artery occlusion and rat IR MI models. In the mouse, Cmpd43 attenuated adverse LV remodeling following permanent LAD artery occlusion as indicated by reduced LV chamber areas and left-shifted PV curves. This was accompanied by a reduction in infarct scar size and preservation of infarct wall thickness compared with vehicle. In addition, passive 2-dimensional strains indicated increased scar stiffness with Cmpd43 treatment (E_{11} at all doses; E_{22} at high dose). Following IR injury in the rat, Cmpd43 attenuated LV chamber dilatation, improved systolic LV function, and increased viable myocardium levels across the infarct wall, which indicated that Cmpd43 was associated with the preservation of functional myocardium within the infarct scar. Considering these findings, the following observations merit attention. First, Cmpd43 treatment was started 24 to 48 h post-MI, which coincides with the peak of early

inflammation that involves neutrophils and proinflammatory monocytes (40). As such, the inflamed and ischemic tissue might represent an opportunistic site of action for FPR-targeted therapy. Second, the early increase in proresolution macrophages in the myocardium and infarct border zone suggested that macrophage polarization occurred with FPR1/2 agonism. These changes were predicted to increase wound healing activity early post-MI, leading to improved structure and/or function outcomes. As previously stated, early stimulation of a proresolution phenotype in the heart has been shown to diminish myocardial inflammation and reduce deterioration in LV function (8,9). The present study provided further direct evidence in support of proresolution strategies to treat post-MI injury and prevent HF development. Our studies were interventional in nature because treatment was given after MI. This was unique among the various reports that used FPR agonists to affect outcome post-MI (8-10,41,42). Although previous studies pre-treated with an agonist or provided it at the time of ischemic injury, our studies showed the impact of intervention within days following MI. The incorporation of an additional assessment of the impact of Cmpd43 treatment initiated in the first few hours post-MI would have been informative. The impact of timing of intervention post-MI, and, in particular, delayed intervention, on outcome remains to be addressed.

The effects of synthetic small molecule agonists of FPR1/2, including Cmpd43, on myocardial injury and infarction have been described (10). In a study by Qin et al. (10), mice subjected to IR were treated parenterally with Cmpd43 starting 24 h before ischemia and daily for 7 days thereafter. Cmpd43 was ineffective in reducing early cardiac necrosis and inflammation, and was unable to attenuate LV remodeling 7 days post-IR injury. In our study, therapeutic benefit with Cmpd43 was achieved in scar structure and cardiac function endpoints in mouse and rat models of MI. However, distinct differences between these 2 studies are worth highlighting. In our present study: 1) treatment was 10 mg/kg given orally by gavage versus 50 mg/kg via intraperitoneal administration; 2) treatment was started 24 to 48 h post-ischemia versus 24 h before ischemia; 3) treatment duration lasted up to 28 days post-MI versus 7 days; and 4) mouse MI models were different (IR vs. permanent coronary artery occlusion). As stated earlier, the interventional approaches used in the present study to respond to acute MI could be applicable to the clinical setting. Qin et al. (10) showed that an alternate FPR1/2 dual agonist (Cmpd17B) (10) improved systolic function and reduced proinflammatory gene expression profiles in the infarct zone 28 days post-MI, which aligned with Cmpd43 activity described in this study. Cmpd17B results coupled with data from this report support the concept that FPR1/2 dual agonism improves LV structure and function post-MI.

The present findings also point to a process of early changes in cardiac macrophage phenotype, whereby FPR1/2 dual agonism evokes a more "resolution competent" cell type. This process is suggested to increase macrophage phagocytic activity within and vicinal to the MI to enhance clearance of necrotic debris. The enhanced clearance of necrotic material could enable wound healing and productive scar formation post-MI. In addition, an enhancement in homing of monocyte macrophages to the site of injury would also likely serve to increase the pool of proresolution macrophages for tissue repair. The early changes in the macrophage profile ultimately led to improvements in scar maturation and overall outcome. A recent study by Heo et al. (43) also revealed a role for FPR2 activation in recruitment of circulating proangiogenic cells into the infarcted myocardium that led to myocardial protection post-MI. These findings indicate a beneficial, yet more complex, role of FPRs in myocardial wound healing.

CONCLUSIONS

In these studies, we demonstrate that FPR1/2 dual agonism using Cmpd43 stimulates prophagocytic and prochemotactic cellular responses essential for proresolution function. As a result, Cmpd43 favorably mitigates adverse LV remodeling and promotes optimal myocardial healing in mouse and rat models of MI, leading to favorable changes in chamber function. Direct therapeutic targeting of FPRs, and in particular, FPR2, may thus represent a viable strategy to prevent HF development in patients following an MI. Clinical studies with FPR agonists will help to address this exciting potential.

ACKNOWLEDGMENTS Editorial support was provided by Geraint Owens, PhD, of Chameleon Communications International Ltd, with funding from Bristol-Myers Squibb.

ADDRESS FOR CORRESPONDENCE: Dr. Ricardo A. Garcia, Bristol-Myers Squibb Company, 311 Pennington-Rocky Hill Road, Pennington, New Jersey 08534. E-mail: Ricardo.Garcia@bms.com.

PERSPECTIVES

COMPETENCY IN MEDICAL KNOWLEDGE: Our studies demonstrated the beneficial effects of long-term FPR activation with Cmpd43 in the setting of post-MI injury. Treatment resulted in the promotion of a proresolution macrophage profile (cellular function, cytokine responses, and gene signatures) and an enhanced understanding of the signaling profile in model cell culture systems. Importantly, treatment improved LV structure and function relationships in rodent MI models (permanent coronary artery occlusion and IR injury), highlighting the importance of the resolution process in post-MI healing.

TRANSLATIONAL OUTLOOK: Demonstration of efficacy with long-term FPR agonist treatment in animal models of MI provides fundamental and essential proof of principle for future evaluation of this mechanism in the post-MI patient population.

REFERENCES

1. Writing Group Members, Mozaffarian D, Benjamin EJ, et al. Heart disease and stroke statistics-2016 update: a report from the American Heart Association. Circulation 2016;133:e38–360.

2. Serhan CN, Chiang N, Dalli J. The resolution code of acute inflammation: novel pro-resolving lipid mediators in resolution. Semin Immunol 2015;27:200–15.

3. Hammerman H, Kloner RA, Hale S, Schoen FJ, Braunwald E. Dose-dependent effects of short-term methylprednisolone on myocardial infarct extent, scar formation, and ventricular function. Circulation 1983;68:446–52.

4. Roberts R, DeMello V, Sobel BE. Deleterious effects of methylprednisolone in patients with myocardial infarction. Circulation 1976;53:I204–6.

5. Saito T, Rodger IW, Hu F, Robinson R, Huynh T, Giaid A. Inhibition of COX pathway in experimental myocardial infarction. J Mol Cell Cardiol 2004;37:71–7.

6. Kimmel SE, Berlin JA, Reilly M, et al. Patients exposed to rofecoxib and celecoxib have different odds of nonfatal myocardial infarction. Ann Intern Med 2005;142:157–64.

7. Serhan CN, Krishnamoorthy S, Recchiuti A, Chiang N. Novel anti-inflammatory-pro-resolving mediators and their receptors. Curr Top Med Chem 2011;11:629–47.

8. Kain V, Ingle KA, Colas RA, et al. Resolvin D1 activates the inflammation resolving response at splenic and ventricular site following myocardial infarction leading to improved ventricular function. J Mol Cell Cardiol 2015;84:24–35.

9. Kain V, Liu F, Kozlovskaya V, et al. Resolution agonist 15-epi-lipoxin A4 programs early activation of resolving phase in post-myocardial infarction healing. Sci Rep 2017;7:9999.

10. Qin CX, May LT, Li R, et al. Small-molecule-biased formyl peptide receptor agonist compound 17b protects against myocardial ischaemia-reperfusion injury in mice. Nat Commun 2017;8:14232.

11. Burli RW, Xu H, Zou X, et al. Potent hFPRL1 (ALXR) agonists as potential anti-inflammatory agents. Bioorg Med Chem Lett 2006;16:3713–8.

12. Sogawa Y, Shimizugawa A, Ohyama T, Maeda H, Hirahara K. The pyrazolone originally reported to be a formyl peptide receptor (FPR) 2/ALX-selective agonist is instead an FPR1 and FPR2/ALX dual agonist. J Pharmacol Sci 2009;111:317–21.

13. Forsman H, Onnheim K, Andreasson E, Dahlgren C. What formyl peptide receptors, if any, are triggered by compound 43 and lipoxin A4? Scand J Immunol 2011;74:227–34.

14. Salahpour A, Espinoza S, Masri B, Lam V, Barak LS, Gainetdinov RR. BRET biosensors to study GPCR biology, pharmacology, and signal transduction. Front Endocrinol (Lausanne) 2012;3:105.

15. Dufton N, Hannon R, Brancaleone V, et al. Anti-inflammatory role of the murine formyl-peptide receptor 2: ligand-specific effects on leukocyte responses and experimental inflammation. J Immunol 2010;184:2611–9.

16. Liang TS, Wang JM, Murphy PM, Gao JL. Serum amyloid A is a chemotactic agonist at FPR2, a low-affinity N-formylpeptide receptor on mouse neutrophils. Biochem Biophys Res Commun 2000;270:331–5.

17. Brandenburg LO, Konrad M, Wruck C, Koch T, Pufe T, Lucius R. Involvement of formyl-peptide-receptor-like-1 and phospholipase D in the internalization and signal transduction of amyloid beta 1-42 in glial cells. Neuroscience 2008;156:266–76.

18. Planaguma A, Domenech T, Jover I, et al. Lack of activity of 15-epi-lipoxin A(4) on FPR2/ALX and CysLT1 receptors in interleukin-8-driven human neutrophil function. Clin Exp Immunol 2013;173:298–309.

19. Forman HJ, Torres M. Reactive oxygen species and cell signaling: respiratory burst in macrophage signaling. Am J Respir Crit Care Med 2002;166:S4–8.

20. Gallagher R, Collins S, Trujillo J, et al. Characterization of the continuous, differentiating myeloid cell line (HL-60) from a patient with acute promyelocytic leukemia. Blood 1979;54:713–33.

21. Bartekova M, Radosinska J, Jelemensky M, Dhalla NS. Role of cytokines and inflammation in heart function during health and disease. Heart Fail Rev 2018;23:733–58.

22. ter Horst EN, Hakimzadeh N, van der Laan AM, Krijnen PA, Niessen HW, Piek JJ. Modulators of macrophage polarization influence healing of the infarcted myocardium. Int J Mol Sci 2015;16:29583–91.

23. Lambert JM, Lopez EF, Lindsey ML. Macrophage roles following myocardial infarction. Int J Cardiol 2008;130:147–58.

24. Wan E, Yeap XY, Dehn S, et al. Enhanced efferocytosis of apoptotic cardiomyocytes through myeloid-epithelial-reproductive tyrosine kinase links acute inflammation resolution to cardiac repair after infarction. Circ Res 2013;113:1004–12.

25. Gobbetti T, Coldewey SM, Chen J, et al. Nonredundant protective properties of FPR2/ALX in polymicrobial murine sepsis. Proc Natl Acad Sci U S A 2014;111:18685–90.

26. Dalli J, Montero-Melendez T, McArthur S, Perretti M. Annexin A1 N-terminal derived peptide ac2-26 exerts chemokinetic effects on human neutrophils. Front Pharmacol 2012;3:28.

27. Liu M, Chen K, Yoshimura T, et al. Formylpeptide receptors are critical for rapid neutrophil mobilization in host defense against Listeria monocytogenes. Sci Rep 2012;2:786.

28. Le Y, Murphy PM, Wang JM. Formyl-peptide receptors revisited. Trends Immunol 2002;23:541–8.

29. Harada M, Habata Y, Hosoya M, et al. N-Formylated humanin activates both formyl peptide receptor-like 1 and 2. Biochemi Biophys Res Commun 2004;324:255–61.

30. Rabiet MJ, Huet E, Boulay F. The N-formyl peptide receptors and the anaphylatoxin C5a receptors: an overview. Biochimie 2007;89:1089–106.

31. Ye RD, Boulay F, Wang JM, et al. International Union of Basic and Clinical Pharmacology. LXXIII. Nomenclature for the formyl peptide receptor (FPR) family. Pharmacol Rev 2009;61:119–61.

32. Xu J, Wang F, Van Keymeulen A, et al. Divergent signals and cytoskeletal assemblies regulate

self-organizing polarity in neutrophils. Cell 2003;114:201–14.

33. Krishnamoorthy S, Recchiuti A, Chiang N, et al. Resolvin D1 binds human phagocytes with evidence for proresolving receptors. Proc Natl Acad Sci U S A 2010;107:1660–5.

34. Sharma D, Parameswaran N. Multifaceted role of beta-arrestins in inflammation and disease. Genes Immun 2015;16:499–513.

35. Gabl M, Holdfeldt A, Sundqvist M, Lomei J, Dahlgren C, Forsman H. FPR2 signaling without beta-arrestin recruitment alters the functional repertoire of neutrophils. Biochem Pharmacol 2017;145:114–22.

36. Gera N, Swanson KD, Jin T. β-Arrestin 1-dependent regulation of Rap2 is required for fMLP-stimulated chemotaxis in neutrophil-like HL-60 cells. J Leukoc Biol 2017;101:239–51.

37. Jung M, Ma Y, Iyer RP, et al. IL-10 improves cardiac remodeling after myocardial infarction by stimulating M2 macrophage polarization and fibroblast activation. Basic Res Cardiol 2017;112:33.

38. Krishnamurthy P, Rajasingh J, Lambers E, Qin G, Losordo DW, Kishore R. IL-10 inhibits inflammation and attenuates left ventricular remodeling after myocardial infarction via activation of STAT3 and suppression of HuR. Circ Res 2009;104:e9–18.

39. Halade GV, Kain V, Serhan CN. Immune responsive resolvin D1 programs myocardial infarction-induced cardiorenal syndrome in heart failure. FASEB J 2018;32:3717–29.

40. Nahrendorf M, Pittet MJ, Swirski FK. Monocytes: protagonists of infarct inflammation and repair after myocardial infarction. Circulation 2010;121:2437–45.

41. D'Amico M, Di Filippo C, La M, et al. Lipocortin 1 reduces myocardial ischemia-reperfusion injury by affecting local leukocyte recruitment. FASEB J 2000;14:1867–9.

42. Dalli J, Consalvo AP, Ray V, et al. Proresolving and tissue-protective actions of annexin A1-based cleavage-resistant peptides are mediated by formyl peptide receptor 2/lipoxin A4 receptor. J Immunol 2013;190:6478–87.

43. Heo SC, Kwon YW, Jang IH, et al. Formyl peptide receptor 2 is involved in cardiac repair after myocardial infarction through mobilization of circulating angiogenic cells. Stem Cells 2017;35:654–65.

KEY WORDS agonist, Compound 43, formyl peptide receptor, heart failure, myocardial infarction

APPENDIX For an expanded Methods section and supplemental figures, please see the online version of this paper.

JACC: BASIC TO TRANSLATIONAL SCIENCE VOL. 4, NO. 8, 2019

EDITORIAL COMMENT

Therapeutic Treatment Approaches Post–Myocardial Infarction

A Bias Toward Formyl Peptide Receptor Agonists*

Rysa Zaman, BSc,[a,b] Slava Epelman, MD, PhD[a,b,c,d]

Myocardial infarction (MI) is the leading cause of heart failure globally. Current treatment options consist of thrombolytic agents and interventional procedures to restore blood flow to the ischemic tissue to prevent tissue necrosis. Despite these strategies, death from resultant heart failure remains high, highlighting an unmet need for new therapeutic modalities. Post MI, inflammatory neutrophils and monocytes both enter the ischemic zone. Neutrophils have been traditionally known to add further insult to injury; although emerging reparative functions have been documented (1). Monocyte function is more complex, as they possess both pathological and protective functions that are temporally regulated and associated with differentiation into macrophages. These functions include extracellular matrix degradation, debris clearance, and angiogenesis (1). Inflammatory tissue damage post-MI contributes to adverse left ventricular (LV) remodeling and eventual heart failure development, making it an attractive therapeutic target. In this issue of *JACC: Basic to Translational Science*, García et al. (2) explore the use of formyl peptide receptor (FPR) agonist, Compound 43 (Cmpd43), as a therapeutic agent that targets pattern recognition receptors to promote a more favorable immunological response and improve infarct healing.

SEE PAGE 905

FPRs are G protein–coupled receptors primarily expressed on leukocytes and have been shown to regulate both the initiation and resolution of inflammation post-MI (1). FPRs have unusual biology. For example, FPRs bind to a wide array of ligands and elicit different cellular responses specific to the ligand and cell type, elegantly encapsulated by the concept of biased agonism (3). Biased agonism describes the ability of different FPR ligands to selectively activate only a component of the downstream signaling pathways coupled to that receptor while leaving other pathways either not activated, or potentially suppressed (**Figure 1A**).

FPR2 can be engaged by mitochondria-derived formyl peptides and activate neutrophils in a proinflammatory manner (3). Conversely, $F2Pal_{10}$ also activates neutrophils but fails to induce the characteristic chemotactic response, owing to lack of recruitment of β-arrestin in the signal transduction pathway (3). The FPRs' biased agonism effect appears to be at least partially, if not totally, driven by whether β-arrestin is recruited to the receptor. As opposed to these roles in response to synthetic and self-derived molecules, the earliest descriptions of FPRs were in response to bacterial products, as FPR1 is the well-known receptor for fMLP, a bacterial peptide that is highly chemotactic for neutrophils and induces proinflammatory cytokine production and organ damage (3). Thus, biased agonism can tailor the functional repertoire of FPR-expressing cells such

*Editorials published in *JACC: Basic to Translational Science* reflect the views of the authors and do not necessarily represent the views of *JACC: Basic to Translational Science* or the American College of Cardiology.

From the [a]Department of Medicine, Toronto General Hospital Research Institute, University Health Network, Toronto, Ontario, Canada; [b]Department of Immunology, Faculty of Medicine, University of Toronto, Toronto, Ontario, Canada; [c]Ted Rogers Centre for Heart Research, Toronto, Ontario, Canada; and the [d]Peter Munk Cardiac Centre, Toronto General Hospital, Toronto, Ontario, Canada. This work was supported by the Canadian Institutes of Health Research (PJT364831) (to Dr. Epelman), Heart and Stroke Foundation (to Dr. Epelman), Ted Rogers Centre for Heart Research (to Dr. Epelman), and the Peter Munk Cardiac Centre (to Dr. Epelman). Both authors have reported that they have no relationships relevant to the contents of this paper to disclose.

The authors attest they are in compliance with human studies committees and animal welfare regulations of the authors' institutions and Food and Drug Administration guidelines, including patient consent where appropriate. For more information, visit the *JACC: Basic to Translational Science* author instructions page.

ISSN 2452-302X https://doi.org/10.1016/j.jacbts.2019.11.008

FIGURE 1 Biased Agonism in FPR Signaling During Post-Myocardial Infarction

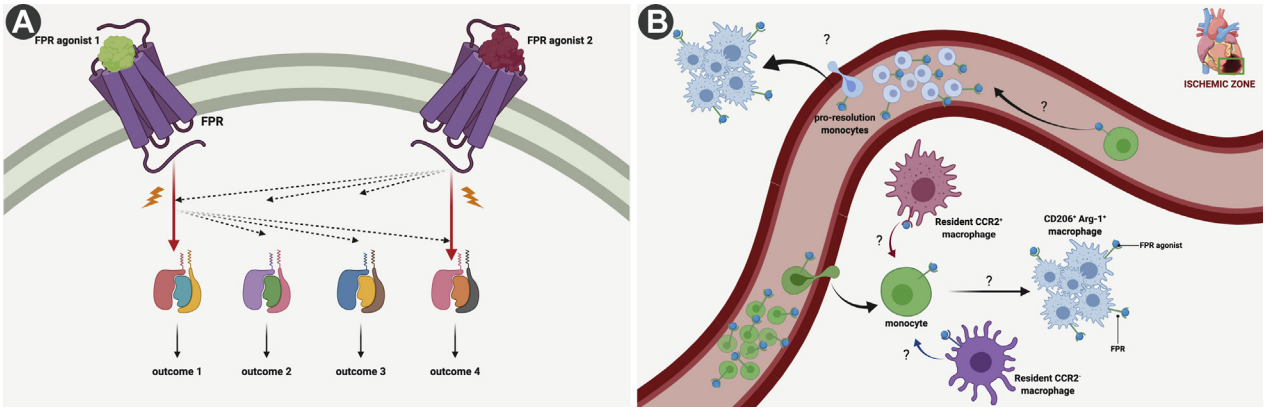

(A) Different formyl peptide receptor (FPR) ligands can activate the same FPR for a diverse array of possible outcomes depending on the ligand itself. FPR agonist 1 activates a subset of signal transduction pathways for outcome 1 while not activating or suppressing the other outcomes, whereas FPR agonist 2 activates only the pathway leading to outcome 4, which highlight multiple possible combinations. **(B)** Schematic representation of potential mechanisms behind the observation of increased $CD206^{+}$/arginase-1 $(Arg\text{-}1)^{+}$ macrophages in the heart following treatment with FPR agonists. One scenario is that upon engagement with FPR agonists, monocytes are prespecified to a proreparative fate from the systemic effects of the FPR agonist. Thus, after entering the tissue, irrespective of the cardiac microenvironment, the monocytes differentiate into $CD206^{+}/Arg\text{-}1^{+}$ macrophages. Another possibility is that monocytes in circulation, despite engagement with FPR agonists at this stage, are conditioned by the tissue microenvironment, and not FPR stimulation, to adopt a $CD206^{+}/Arg\text{-}1^{+}$ fate within the heart (Created with BioRender).

that the same receptor can be engaged for proinflammatory or anti-inflammatory effects by different ligands. Therapeutic implications of biased FPR signaling have been exploited in clinical trials with pharmaceuticals that activate proinflammatory pathways lacking in immunocompromised patients, and blunt excessive eczematous lesion formation in infants. Thus, the careful selection of agents that can activate only a single component of biased signaling receptors is essential for therapeutic success and limiting off target effects.

García et al. (2) focus on modulating recruited monocytes toward a proresolution phenotype to expedite tissue healing with Cmpd43—a dual FPR1/FPR2 agonist (4). Using in vitro assays, the authors first determined the role of FPR agonism by Cmpd43 on key macrophage functions of chemotaxis, phagocytosis, and cytokine release via receptors FPR1 and FPR2 separately. Despite conservation of signal transduction profiles between FPR1 and FPR2, the receptors appear to have variable influence on different aspects of macrophage function. Peritoneal macrophages from mice deficient of FPR2 displayed defective internalization of zymosan particles, while FPR1-deficient mice were only modestly affected. Absence of both FPR1 and FPR2 inhibited macrophage chemotaxis and oxidative burst, suggesting that both isoforms are involved in these aspects. Treatment of peritoneal macrophages with Cmpd43 in the presence of serum amyloid A triggered FPR2-dependent release of the anti-inflammatory cytokine interleukin-10, which was negated in FPR2-deficient mice. Cmpd43 also was able to partially block interleukin-6 production; however, this response was both dose and receptor dependent. This may be in part related with the ability of these G protein-coupled receptors to either homo- or heterodimerize. Thus, the effects of Cmpd43 are complex, and not yet entirely understood. The studies of García et al. (2) shed light on how macrophages respond to FPR1/FPR2 signaling in vitro. Future work on neutrophils, which both express FPR1 and FPR2, and are recruited in large numbers to the heart post-MI, would be equally valuable.

To assess the in vivo relevance of Cmpd43 treatment, García et al. (2) harvested mouse cardiac tissue 3 days post-MI. Although the total number of macrophages remained unchanged by Cmpd43 treatment, the percentage of macrophages that express arginase-1 (Arg-1) and CD206 increased. Arg-1 and CD206 are markers of resident cardiac macrophages, and also markers of macrophages that adopt a more reparative functional state. These data bring up the classic argument, which happened first? Did Cpmd43 act systemically on recruited monocytes (and other myeloid cells) and prespecify their fate to that of a $CD206^{+}$ macrophage after entry into ischemic tissue? Or did the agonist act locally on the myocardium,

reducing the damage in early phases post-MI? Was altered macrophage composition a result of different environmental signals owing to myocardial effects, or a direct effect on recruited monocytes (**Figure 1B**)? Perhaps it was a combination of both. The long-term effects of Cmpd43 treatment post-MI included an increased LV ejection fraction, reduced LV chamber dilatation, reduced LV wall thinning, and scarring compared with those treated with vehicle in both mouse and rat models. The translational potential of these findings is exciting given that the drug is orally deliverable.

It is interesting to speculate on the role of FPR agonism in the context of cardiac macrophage heterogeneity. Genetic fate mapping in mice has demonstrated that at steady state, cardiac macrophages are composed of heterogeneous populations of embryonic-derived self-renewing macrophages (expressing the receptors TIMD4/LYVE1), and a numerically smaller population of adult bone marrow-derived $CCR2^{+}$ macrophages maintained through monocyte input (5). It may be the case that $CD206^{+}$ cells in the study of García et al. (2) represent the embryonic-derived macrophages that have survived the infarct. Equally interesting would be the idea that recruited monocytes could differentiate into resident macrophage-like cells—an observation previously seen at the single cell level (5).

The work of Garcia et al. (2) adds to the growing body of knowledge, which highlights that modulating individual cell-surface receptors with FPR agonists expedites tissue healing post-MI (1,4). Among these studies, key similarities involve decreased neutrophil accumulation, expedited and increased expression of CD206 and Arg-1 in the ischemic zone, improved infarct healing, and improved cardiac function relative to vehicle-treated control subjects. Future studies using tissue specific or inducible deletion models will help answer the question of which FPR receptor(s) are involved in the beneficial effects of Cmpd43.

ADDRESS FOR CORRESPONDENCE: Dr. Slava Epelman, Toronto Medical Discovery Tower, MaRS Building, 101 College Street, 3rd Floor, Room TMDT 3-903, Toronto, Ontario M5G 1L7, Canada. E-mail: slava.epelman@uhn.ca; Twitter: @EpelmanLab.

REFERENCES

1. de Jong R, Leoni G, Drechsler M, Soehnlein O. The advantageous role of annexin A1 in cardiovascular disease. Cell Adh Migr 2017;11:261–74.

2. García RA, Ito BR, Lupisella JA, et al. Preservation of post-infarction cardiac structure and function via long-term oral formyl peptide receptor agonist treatment. J Am Coll Cardiol Basic Trans Sci 2019;4:905–20.

3. He HQ, Ye R. The formyl peptide receptors: diversity of ligands and mechanism for recognition. Molecules 2017;22:E455.

4. Qin CX, May LT, Li R, et al. Small-molecule-biased formyl peptide receptor agonist compound 17b protects against myocardial ischaemia-reperfusion injury in mice. Nat Commun 2017;8:14232.

5. Dick SA, Macklin JA, Nejat S, et al. Self-renewing resident cardiac macrophages limit adverse remodeling following myocardial infarction. Nat Immunol 2019;20:29–39.

KEY WORDS formyl peptide receptor, macrophages, monocytes, myocardial infarction

JACC: BASIC TO TRANSLATIONAL SCIENCE VOL. 4, NO. 8, 2019

PRECLINICAL RESEARCH

Seipin Knockout Mice Develop Heart Failure With Preserved Ejection Fraction

Bo Bai, PhD,[a,b] Wulin Yang, PhD,[c,d] Yanyun Fu, PhD,[a] Hannah Lee Foon, SWA, PhD,[e] Wan Ting Tay, MAppStat,[f] Kangmin Yang, PhD,[b] Cuiting Luo, BS,[b] Jayantha Gunaratne, PhD,[e] Philip Lee, PhD,[a] Michael R. Zile, MD,[g,h] Aimin Xu, PhD,[b,i] Calvin W.L. Chin, MD, PhD,[f] Carolyn S.P. Lam, MD, PhD,[f] Weiping Han, PhD,[a] Yu Wang, PhD[b]

VISUAL ABSTRACT

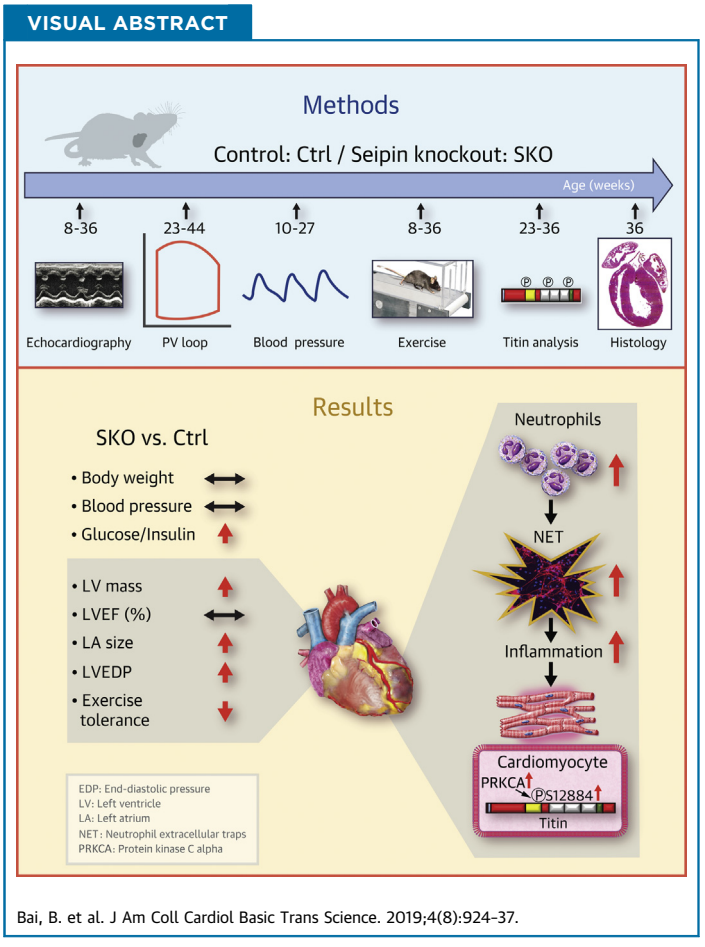

Bai, B. et al. J Am Coll Cardiol Basic Trans Science. 2019;4(8):924–37.

HIGHLIGHTS

- **The lean diabetic SKO mouse represents a novel and validated murine model of HFpEF.**
- **The SKO HFpEF mouse model recapitulates the cardiac structure and function abnormalities in lean diabetic HFpEF patients in Asia.**
- **Altered cellular titin phosphorylation and increased extracellular interstitial fibrosis associated with neutrophil extracellular traps contribute to the left ventricular stiffness.**
- **Metabolic disturbances arising from insulin resistance and diabetes in the absence of hypertension or obesity may lead to HFpEF.**

ISSN 2452-302X https://doi.org/10.1016/j.jacbts.2019.07.008

SUMMARY

The lean diabetic patients with heart failure with preserved ejection fraction (HFpEF) in Asia suffer from adverse clinical outcomes and poor life quality. The suitable animal models are urgently needed for mechanistic study and therapeutic innovations. Our study reports that lipodystrophic mice with seipin depletion are lean, diabetic, and recapitulate major manifestations of clinical HFpEF, thereby clarifying that lean diabetes per se may produce HFpEF characteristics. We further demonstrate that increased cardiac titin phosphorylation and reactive interstitial fibrosis associated with neutrophil extracellular traps lead to left ventricular stiffness and suggest that both pathways may be potential therapeutic targets in Asian HFpEF patients.

ABBREVIATIONS AND ACRONYMS

Ctrl = control (mice)

EDPVR = end-diastolic pressure-volume relationship

HFpEF = heart failure with preserved ejection fraction

IQR = interquartile range

LA = left atrial

LV = left ventricular

NET = neutrophil extracellular trap

PEVK = proline, glutamate, valine, and lysine

SKO = seipin knockout

Heart failure with preserved ejection fraction (HFpEF) has been described as the greatest unmet need in cardiovascular medicine today (1). It constitutes the dominant form of HF in aging societies, is the top cause of hospitalization among elderly persons worldwide, and carries a dismal prognosis with >50% 5-year mortality (2). Outcomes have not been improved over the last decades, and there is currently still no effective therapy proven to improve survival in HFpEF (2). There is an urgent need to better understand the pathophysiology of HFpEF and identify potential novel therapeutic targets (3).

HFpEF represents a broad cohort of patients with a range of comorbidities, such as hypertension, obesity, and diabetes, that requires individualized management based on biological phenotypes (4,5). However, recent epidemiologic data from Asia suggest a unique lean diabetic phenotype of HFpEF, compared with other HF phenotypes, has the worst quality of life, more severe signs and symptoms of HF, and the highest rate of adverse clinical outcomes (6–8).

SEE PAGE 938

A critical obstacle to therapeutic innovation in HFpEF has been the absence of suitable animal models that accurately recapitulate the complexities of the human disease (9,10). An ideal HFpEF animal model that captures 2 or more HFpEF features (e.g., concentric hypertrophy, diastolic dysfunction, and impaired exercise capacity) would be more helpful in providing mechanistic insights and therapeutic

From the [a]Singapore Bioimaging Consortium, Agency for Science, Technology and Research, Singapore; [b]State Key Laboratory of Pharmaceutical Biotechnology and Department of Pharmacology and Pharmacy, The University of Hong Kong, Hong Kong, China; [c]Anhui Province Key Laboratory of Medical Physics and Technology, Center of Medical Physics and Technology, Hefei Institutes of Physical Science, Chinese Academy of Sciences, Hefei, China; [d]Hefei Cancer Hospital, Chinese Academy of Sciences, Hefei, China; [e]Translational Biomedical Proteomics, Institute of Molecular and Cell Biology, Agency for Science, Technology and Research, Singapore; [f]National Heart Centre Singapore and Duke-National University of Singapore, Singapore; [g]Division of Cardiology, Department of Medicine, Medical University of South Carolina, Charleston, South Carolina; [h]Ralph H. Johnson Department of Veterans Affairs Medical Center, Charleston, South Carolina; and the [i]Department of Medicine, The University of Hong Kong, Hong Kong, China. This work is support by the Agency for Science, Technology and Research Biomedical Research Council, Bayer and the Asian neTwork for Translational Research and Cardiovascular Trials (ATTRaCT) Biomedical Research Council program (SPF2014/001, SPF2013/002, SPF2014/003, SPF2014/004, SPF2014/005); Research Grant Council grants (17121714) and Collaborative Research Funds (C7055-14G) of Hong Kong; the U.S. National Institutes of Health grants (1R01HL123478-01A1, NIH-NHLBI); and the Asian Sudden Cardiac Death in Heart Failure (ASIAN-HF) study is further supported by grants from Boston Scientific Investigator Sponsored Research Program, National Medical Research Council Singapore (R-172-003-219-511), and Bayer. Dr. Lam is supported by a Clinician Scientist Award from the National Medical Research Council of Singapore; has received research support from Boston Scientific, Bayer, Roche Diagnostics, AstraZeneca, Medtronic, and Vifor Pharma; has served as consultant or on the Advisory Board/Steering Committee/Executive Committee for Boston Scientific, Bayer, Roche Diagnostics, AstraZeneca, Medtronic, Vifor Pharma, Novartis, Amgen, Merck, Janssen Research & Development LLC, Menarini, Boehringer Ingelheim, Novo Nordisk, Abbott Diagnostics, Corvia, Stealth BioTherapeutics, JanaCare, Biofourmis, Darma, Applied Therapeutics, MyoKardia, WebMD Global LLC, Radcliffe Group Ltd and Corpus;and participated on behalf of the ASIAN-HF investigators. All other authors have reported that they have no relationships relevant to the contents of this paper to disclose. Membership of ASIAN-HF authors is provided in the Supplemental Appendix.

The authors attest they are in compliance with human studies committees and animal welfare regulations of the authors' institutions and Food and Drug Administration guidelines, including patient consent where appropriate. For more information, visit the *JACC: Basic to Translational Science* author instructions page.

Manuscript received May 27, 2019; revised manuscript received July 15, 2019, accepted July 16, 2019.

FIGURE 1 The Development of Cardiomegaly in the Lean Diabetic SKO Mice

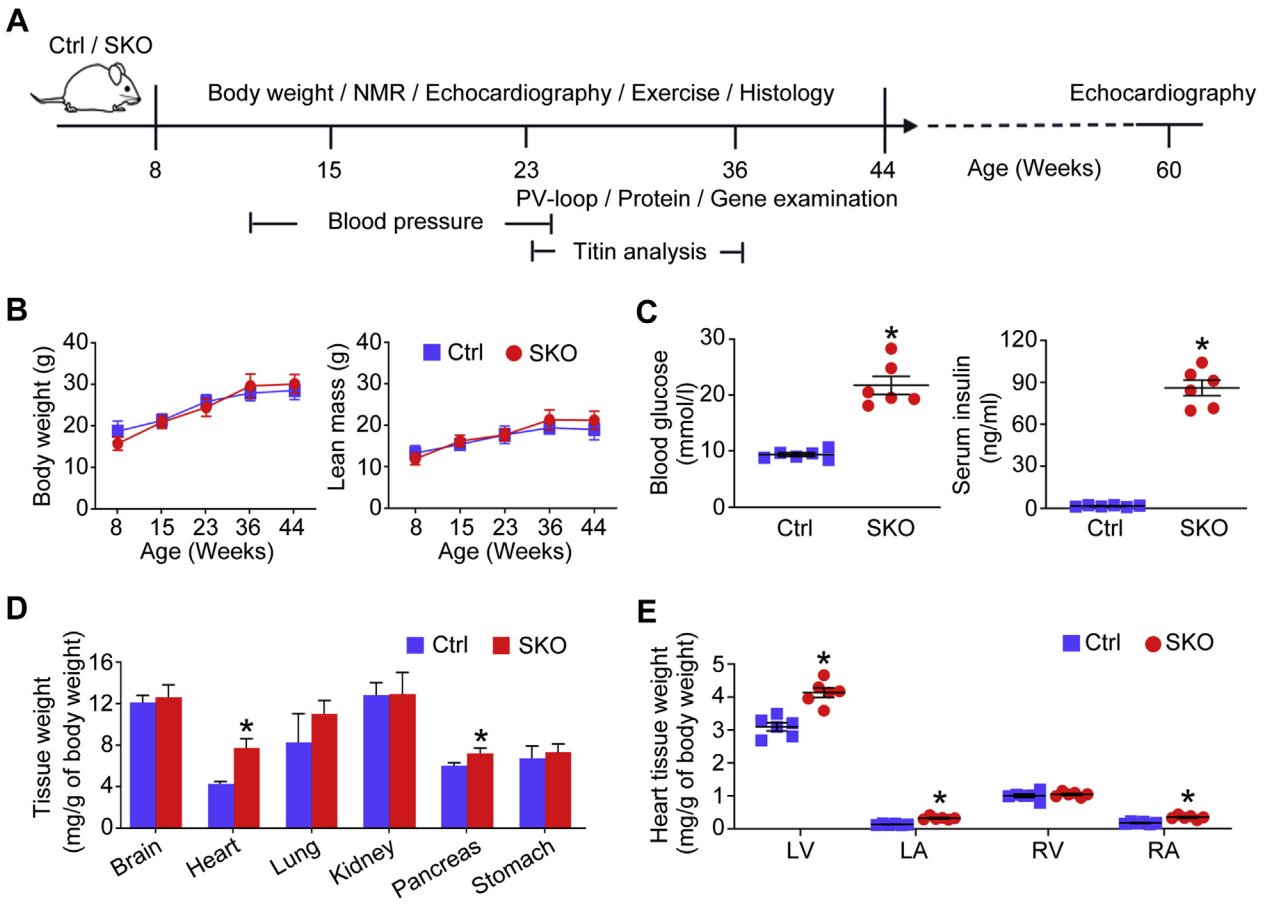

Mice were subjected to phenotypic characterizations according to the protocol **(A)** and nuclear magnetic resonance (NMR) **(B)** to measure body weight and lean mass. **(C)** Blood glucose and serum insulin of mice (18 to 24 weeks old) under basal feeding; **(D)** the ratio between tissue weight and body weight of mice (~24 weeks old); and **(E)** the ratio of left ventricular (LV), left atrial (LA), right ventricular (RV), and right atrial (RA) weight to body weight of mice (41 to 46 weeks old) were analyzed. *$p < 0.05$, compared with control (Ctrl) mice ($n = 6$). PV = pressure-volume; SKO = seipin knockout.

innovations (9,10). So far, such ideal animal models, which show the effect of lean diabetes on the onset of HFpEF, remain absent.

Lipodystrophies are clinical disorders characterized by the selective loss of adipose tissue and severe insulin resistance, leading to diabetes (11,12). Notably, the common cardiac abnormality, hypertrophic cardiomyopathy, occurs with considerable frequency in cohort patients with lipodystrophy caused by different genetic defects (13-15). Patients carrying Berardinelli-Seip congenital lipodystrophy-2 (BSCL2)/seipin mutation exhibit the most severe lipodystrophic phenotype (11,16), and they are lean, diabetic, and exhibit left ventricular (LV) hypertrophy without reduction of EF (13,15). The mechanisms underlying these cardiac manifestations remain poorly understood.

In the current study, we aimed to study whether aged seipin knockout (SKO) mice may serve as a validated model of lean diabetic HFpEF and to investigate potential pathophysiologic pathways underlying LV structural-functional abnormalities in the model.

METHODS

MICE AND STUDY DESIGN. The generation of SKO and littermate control (Ctrl) mice was described previously (17). The timeline to investigate the metabolic, cardiac, and exercise characteristics of male mice is shown in **Figure 1A**. All animal care and experimental procedures were approved by the Committee on the Use of Live Animals for Teaching and Research of the University of Hong Kong and the

Institutional Animal Care and Use Committee of the Agency for Science, Technology, and Research and were carried out in accordance with the *Guide for the Care and Use of Laboratory Animals, Eighth Edition*, published by the U.S. National Institutes of Health. The Supplemental Appendix contains additional Methods and Materials.

HUMAN STUDY POPULATION AND DESIGN. The human data were collected from the ASIAN-HF (Asian Sudden Cardiac Death in Heart Failure) registry. The prospective study design of the ASIAN-HF registry was published previously (8,18,19). The ethics approvals, study definitions, clinical outcomes, echocardiography, and imaging collection were described in detail (8). In the current study, we further analyzed and compared data from lean diabetic HFpEF patients and age-matched control subjects without HF from the community.

STATISTICAL ANALYSIS. For animal studies, all calculations were performed using SPSS software (version 19.0; IBM Corporation, Armonk, New York). Results are presented as mean ± SEM. Student's *t*-test for unpaired observations or one-way analysis of variance with Bonferroni correction for multiple comparisons was performed to analyze the statistical differences between different groups. For all statistical comparisons, p values < 0.05 indicated statistical significance. For the human cohort study, data are given as means ± SD, medians and interquartile ranges (IQR) (25th and 75th percentiles), or numbers and proportions, as appropriate. Depending on the types of data, Student's *t*-test, Wilcoxon rank sum test, or chi-square test for unpaired observations was applied and p values < 0.05 indicated statistical significance. In addition, lean diabetic HFpEF patients were matched to community control subjects without HF with the same age where possible. Otherwise, the next closest age was used.

RESULTS

LEAN AND DIABETIC SKO MICE DEVELOP CARDIOMEGALY. SKO mice developed lipodystrophy after birth (17), but had similar body weight and lean mass as the Ctrl mice (**Figure 1B**). The adult SKO mice (18 to 24 weeks old) showed significantly elevated blood glucose and serum insulin levels under basal feeding (**Figure 1C**), which also displayed glucose intolerance and reduced insulin sensitivity (17). Moreover, we observed cardiomegaly in adult SKO mice (7.7 vs. 4.3 mg/g of body weight for SKO vs. Ctrl mice, ~24 weeks old) (**Figure 1D**). The ratios of LV, left atrial (LA), and right atrial weight to body weight were significantly higher in SKO mice ages 41 to 46 weeks than in Ctrl mice of similar ages (**Figure 1E**). To clarify whether cardiomegaly was caused by the seipin mutation in mouse heart tissues, we first profiled *Bscl2* messenger ribonucleic acid level in mouse tissues. In Ctrl mice, the *Bscl2* gene was abundantly expressed in adipose tissues. By contrast, its expression level was the lowest in mouse hearts and muscles (Supplemental Figure 1A). As expected, *Bscl2* expression was not detectable in SKO mouse tissues (Supplemental Figure 1A). We then established cardiomyocyte-specific SKO. We did not observe any difference in terms of ratios between heart tissue weight and tibia length, including LV, LA, right ventricular, and right atrial tissues, between cardiomyocyte-specific SKO mice ages 55 to 60 weeks and corresponding Ctrl mice of similar ages (Supplemental Figure 1B). These data suggest that cardiac abnormalities of SKO mice were unlikely to be the result of seipin mutation in mouse hearts, but were more likely due to systematic factors (e.g., hyperglycemia).

SKO MICE EXHIBIT LV CONCENTRIC HYPERTROPHY WITHOUT HYPERTENSION. We performed echocardiography in the SKO and Ctrl mice and found thickened LV walls and increased LV mass, that is, cardiac hypertrophy in the SKO mice. These differences became even more prominent with aging (**Figure 2A**). By contrast, the LV internal diameter was comparable between the 2 groups of mice (**Figure 2A** and Supplemental Figure 2A). In addition, adult SKO mice (~36 weeks old), compared with their Ctrl mice, had higher heart weight to tibia length ratio, greater whole heart cross-sectional area as well as cardiomyocyte enlargement (**Figure 2B**). Notably, SKO mice exhibited preserved LVEF and fractional shortening (**Figure 2A**), even in mice ~60 weeks old (Supplemental Figure 2B). We next examined gene expression of cardiac hypertrophy markers, including alpha-skeletal actin (*Acta1*) and atrial natriuretic peptide (*Nppa*) (20). Both *Acta1* and *Nppa* were significantly up-regulated in heart tissues of adult SKO mice (~36 weeks old). Induction of *Nppa* and *Acta1* genes is dependent on the activation of signal transducer and activator of transcription 3 (STAT3) (21–23). Consistently, we found hyperphosphorylation of STAT3 and its upstream Janus kinase 2 (JAK2) in heart tissues of SKO mice (**Figures 2C and 2D**). Although SKO mice developed LV concentric hypertrophy with aging, the systolic and diastolic arterial blood pressure collected during the dark cycle (from 7 PM to 7 AM) was comparable between SKO and their Ctrl mice (**Figure 2E**).

SKO MICE EXHIBIT LV DIASTOLIC DYSFUNCTION, EXERCISE INTOLERANCE, AND LA ENLARGEMENT. We assessed both components of LV diastolic

FIGURE 2 The Concentric LV Hypertrophy in the Absence of Hypertension in the SKO Mice

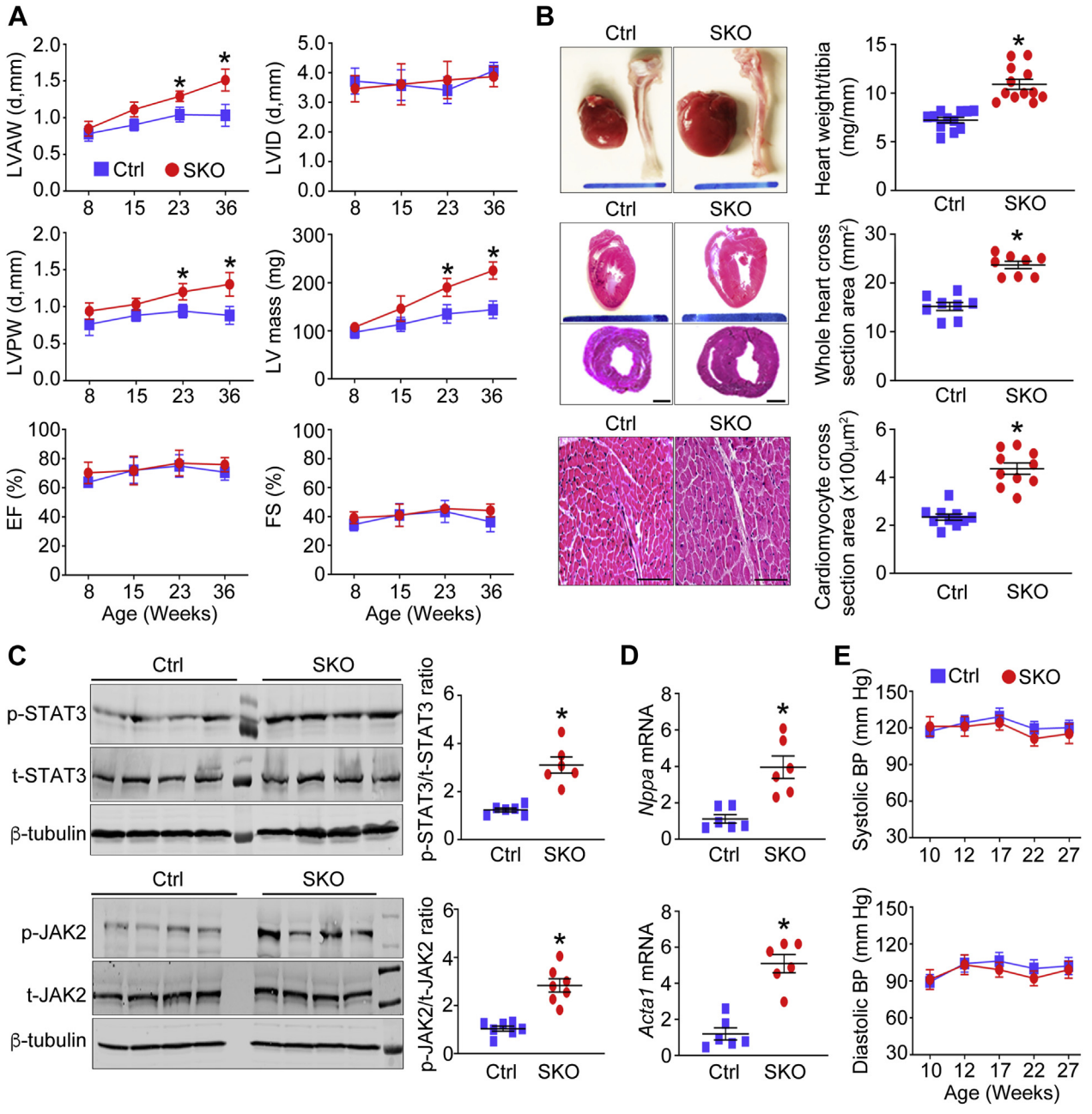

(A) At 8, 15, 23, and 36 weeks of age, mice were subjected to echocardiography to measure the thickness of the left ventricle anterior wall (LVAW) and left ventricle posterior wall (LVPW), left ventricle internal diameter (LVID) in diastole (d), LV mass, ejection fraction (EF), and fractional shortening (FS) (n = 8 to 10). **(B)** The heart tissues of adult mice (36 weeks old) were subjected to examine the ratio of heart weight to tibia length (scale bar = 10 mm, n = 12). Representative images of hematoxylin and eosin-stained heart sections (**top,** longitudinal section, scale bar = 10 mm; **bottom,** horizontal section, scale bar = 1 mm) were shown. The cross-sectional area of whole heart tissues (n = 8) and cardiomyocytes (scale bar = 100 μm, n = 10) was quantified in each group of mice. **(C)** The total (t) and phosphorylated **(p)** signal transducer and activator of transcription 3 (STAT3) and Janus kinase 2 (JAK2) were examined by Western blotting (n = 6), and **(D)** the gene expression of hypertrophic markers, including atrial natriuretic peptide (*Nppa*) and alpha-skeletal actin (*Acta1*), were detected using mouse heart tissues (n = 6). Fold change was calculated for comparison. **(E)** Blood pressure (BP) of mice was collected by telemetry system during the dark cycle (from 7 PM to 7 AM, n = 3). *$p < 0.05$, compared with Ctrl mice. mRNA = messenger ribonucleic acid; other abbreviations as in Figure 1.

FIGURE 3 LV Diastolic Dysfunction, Exercise Intolerance, and LA Enlargement in the SKO Mice

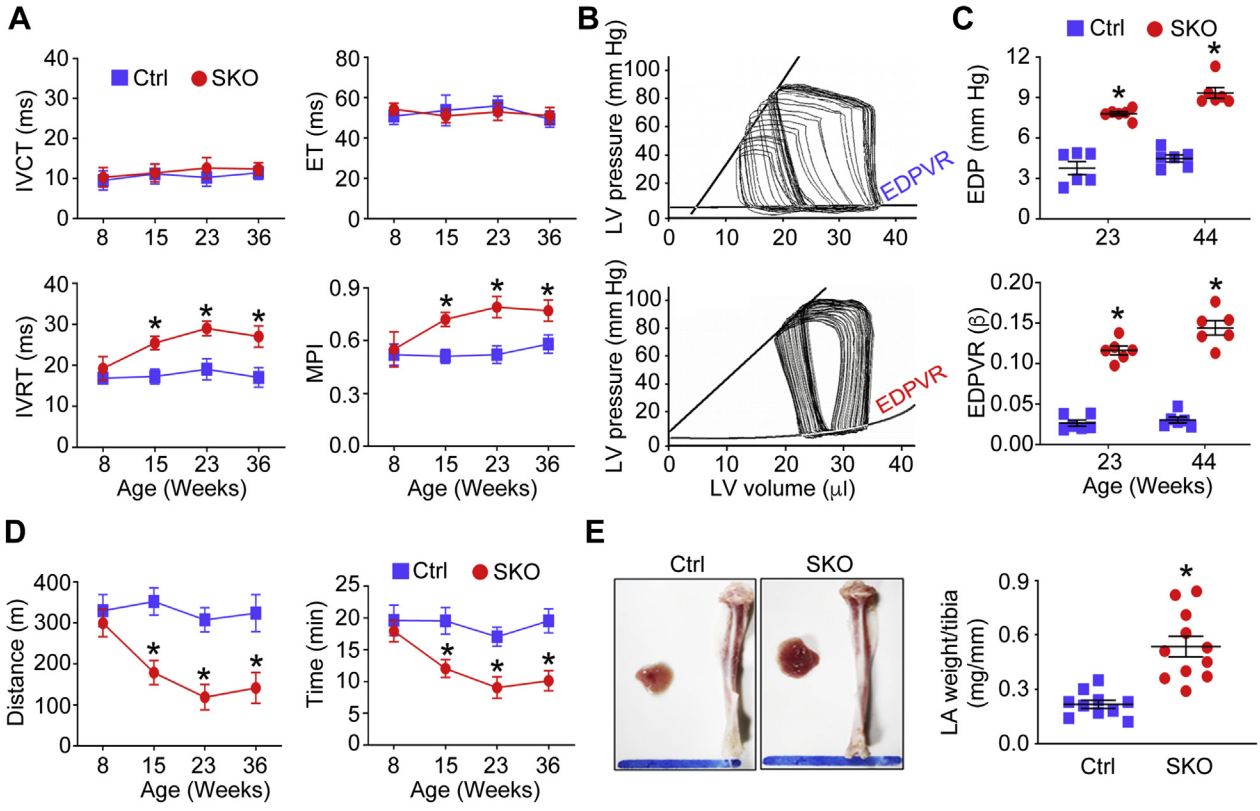

(A) The Doppler echocardiography was used to examine LV isovolumic contraction time (IVCT) and isovolumic relaxation time (IVRT), ejection time (ET), and myocardial performance index (MPI) (n = 8 to 10). The LV pressure-volume loops were analyzed to show representative examples of pressure-volume loops of mice (23 weeks old) **(B)** and measure LV end-diastolic pressure (EDP) and diastolic stiffness coefficient β derived from the end-diastolic pressure-volume relationship (EDPVR) of mice (n = 6) **(C). (D)** Mouse running distance and time via treadmill running test (n = 6); **(E)** the histology of LA tissues and ratio of LA weight to tibia length of mice (36 weeks old) were examined (scale bar = 10 mm, n = 10 to 11). *p < 0.05, compared to Ctrl mice. Abbreviations as in Figure 1.

function as mice aged: 1) active LV relaxation (isovolumic relaxation time); and 2) passive LV diastolic stiffness (end-diastolic pressure-volume relationship [EDPVR]). There was no difference in isovolumic contraction time or ejection time between SKO and Ctrl mice. In contrast, prolonged isovolumic relaxation time, indicative of impaired LV relaxation, was developed in SKO mice, compared with the Ctrl mice, beginning in young adulthood (~15 weeks old). The difference became more apparent with aging (Figure 3A). Moreover, prolonged isovolumic relaxation time contributed to worsening myocardial performance index (higher values indicating worse performance) with age in SKO mice (Figure 3A) (24). LV PV loop analysis showed steeper EDPVR in adult SKO mice compared with in Ctrl mice (23 weeks old) (Figure 3B). Accordingly, LVEDP was significantly increased in adult SKO mice (23 weeks old), and the differences became more prominent in older mice (44 weeks old) (Figure 3C). Meanwhile, the diastolic stiffness coefficient β derived from EDPVR was steadily higher in SKO mice (Figure 3C). Similar to Asian HFpEF patients that exhibited reduced exercise tolerance (6), when compared with the Ctrl group, SKO mice displayed exercise intolerance (reduced running distance and running time) beginning in young adulthood (~15 weeks old)(Figure 3D). Consistent with compromised diastolic function, the LA size and weight of SKO mice (~36 weeks old) were significantly increased (Figure 3E).

CARDIAC TITIN PHOSPHORYLATION IS ALTERED IN SKO MYOCARDIUM. To explore the underlying mechanisms for increased LV diastolic stiffness in SKO mice, we first investigated the total expression and phosphorylation of titin in LV tissues of adult mice (23 to 36 weeks old). Using agarose gel electrophoresis, we found no significant changes of total titin expression relative to myosin heavy chain in LV

FIGURE 4 Altered Cardiac Titin Phosphorylation in the SKO Mice

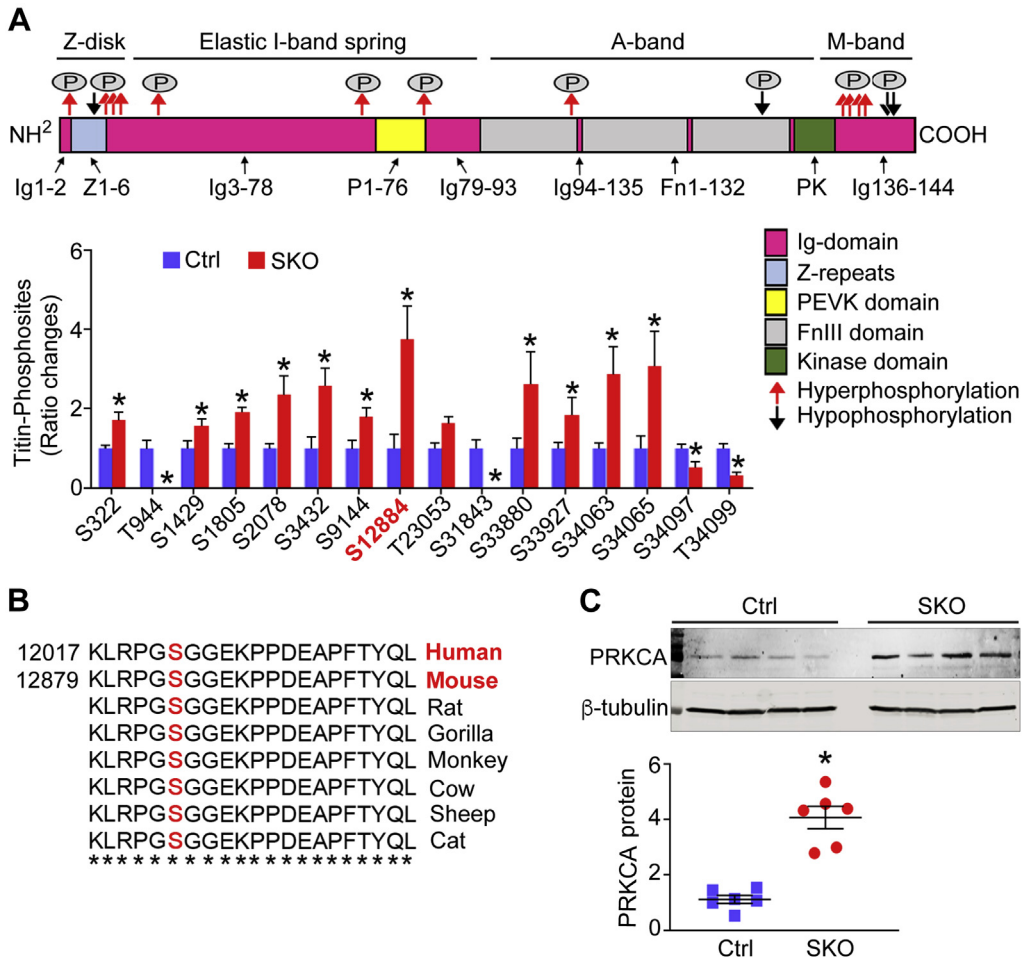

(A) The quantitative mass spectrometry was used to measure ratio changes of titin phosphosites of mouse LV tissues (23 to 36 weeks old, n = 6). The **bold line arrows (red and black)** indicate localization of changed phosphosites in the canonical sequence of mouse titin (UniProtKB entry A2ASS6). **(B)** Multiple sequence alignments showed serine (S) 12884 of murine cardiac titin was a conserved residue. **(C)** Protein expression of protein kinase C alpha (PRKCA) was examined in mouse heart tissues (23 to 36 weeks old, n = 6). Fold change was calculated for comparison. *p < 0.05, compared with Ctrl mice FnIII = fibronectin type III domain; Ig = immunoglobulin-like; PEVK = proline, glutamate, valine, and lysine; T = threonine. Abbreviations as in Figure 1.

myocardium, comparing between SKO and Ctrl mice (Supplemental Figure 3). We then examined titin phosphorylation—a crucial mechanism responsible for increased myocardial stiffness in clinical HFpEF (25). We used quantitative mass spectrometry to detect titin phosphorylation. A total of 238 titin phosphosites was quantified (localization probability *í* > 0.9). An intensity ratio of SKO versus Ctrl phosphorylation was obtained for 46 titin phosphosites, among which 30 were similar, but 16 were differentially phosphorylated between the 2 groups, with the SKO-Ctrl ratio ≤0.5 or ≥1.5 indicating as hypo phosphorylated or hyperphosphorylated residues in SKO mice compared with Ctrl mice. These sites were marked in the canonical domain sequence of mouse titin according to UniProtKB entry A2ASS6 (UniProt Consortium, Hinxton, Cambridge, United Kingdom) (**Figure 4A**). Most of the sites shared similar amino acid sequences with human titin (entry Q8WZ42) (Supplemental Figure 4). Two phosphosites were undetectable in SKO hearts: 1) threonine 944 between Z-repeat 6 and immunoglobulin-like domain 3 of the Z-disk region; and 2) serine 31843 at the fibronectin type-III domain 126 of the A-band region. Phosphorylation of serine 34097 and threonine 34099 in the M-band region was significantly down-regulated in the

SKO mouse hearts (Figure 4A). By comparison, 12 titin phosphosites were hyperphosphorylated in the SKO myocardium from Z-disk and E-, A-, and M-band regions. We found 2 hyperphosphorylated serine 322 and serine 1429 located within ZIS1 and ZIS5 regions of the Z-disk band, which contained multiple SPXR consensus motif repeats. Importantly, when focusing on the elastic I-band spring element, striking hyperphosphorylation of titin at serine 12884 (SKO-Ctrl ratio >3.5) was identified in SKO myocardium (Figure 4A). This phosphosite localized at the COOH-terminus of the titin region rich in proline, glutamate, valine, and lysine (PEVK domain) and was evolutionarily conserved across species (orthologous residue of serine 12022 of human titin at PEVK31) (Figure 4B). Hyperphosphorylation of titin at serine 12022 (serine 12884 in mouse) was previously identified in human failing hearts (26) and reported to increase myocardial stiffness in mouse and pig hearts (27,28). SKO hearts had elevated protein expression of protein kinase C alpha (PRKCA) (Figure 4C), an upstream kinase responsible for the phosphorylation of titin at serine 12884 (27,28). Conversely, we did not detect any difference in protein levels of cyclic guanosine monophosphate-dependent protein kinase (PRKG), cyclic adenosine monophosphate-dependent protein kinase catalytic, alpha (PRKACA), or extracellular signal-regulated protein kinases 1 and 2 (Erk1/2) in heart tissues of the 2 groups of mice (Supplemental Figure 5). Consistently, the cyclic adenosine monophosphate-dependent protein kinase, PRKG, or Erk1/2-dependent phosphorylation at the titin transcript variant N2-B (N2B) unique sequence of titin (N2-Bus) was not changed in LV tissues of the 2 groups of mice (Figure 4A).

SKO MOUSE MYOCARDIUM EXHIBITS REACTIVE INTERSTITIAL FIBROSIS ASSOCIATED WITH INFLAMMATION AND MASSIVE NEUTROPHIL INFILTRATION. Next, we investigated cardiac interstitial fibrosis, another hallmark seen in HFpEF patients that independently predicts intrinsic LV stiffness (25,29). The cardiac fibrosis was increased in SKO mice, compared with Ctrl mice, from young adulthood (~15 weeks old) and progressed with age (Figure 5A). Progression of cardiac fibrosis also coincided with increased gene expression of collagen 1 (*Col1a1*), interleukin 6 (*Il6*), and intercellular adhesion molecule 1 (*Icam1*), as well as augmented protein levels of tumor necrosis factor (TNF) in whole heart tissues of SKO mice (~24 weeks old) (Figures 5A and 5B). Meanwhile, several key markers reflecting activation of quiescent fibroblasts such as alpha-smooth muscle actin (ACTA2) (30) and transforming growth factor beta family (TGFB) (31) were significantly increased in hearts of adult SKO mice (~24 weeks old) (Figure 5B). The cardiac inflammation and interstitial fibrosis were associated with massive neutrophil infiltration in SKO myocardium, which also started from young ages (Figure 5C). To address the implication of infiltrated neutrophils in cardiac damage, we examined whether neutrophil extracellular traps (NET) were formed in SKO mouse hearts. The presence of NET was shown as intact neutrophils with condensed nuclei in SKO mouse hearts from a young age (15 weeks old) and persisted as large amorphous extracellular structures, released deoxyribonucleic acid fibers decorated with myeloperoxidase and citrullinated histone (32), in hearts of adult SKO mice (32 weeks old) (Figure 5D). Consistent with the formation of NET, the protein level of citrullinated histone 3, a well-recognized NET marker (33), was significantly elevated in SKO mouse hearts (24 to 30 weeks old) (Figure 5E).

SKO MICE SHARE MAJOR HFpEF CHARACTERISTICS WITH LEAN DIABETIC PATIENTS. The pan-Asian HF prospective study identified distinct lean diabetic HFpEF patients who had a strikingly high prevalence of diabetes (8). Compared with age-matched non-HF control subjects from the community, lean diabetic HFpEF patients were older, but had the comparable systolic blood pressure and body mass index. Among echocardiographic variables, lean diabetic HFpEF patients displayed nondilated concentric hypertrophy, which was evidenced by increased LV mass but normal LV volume. Despite the preserved LVEF, HFpEF patients showed apparent diastolic dysfunction, LA dilatation, as well as significantly reduced exercise tolerance (Table 1). Moreover, cardiovascular cardiac magnetic resonance in a subset of 54 lean diabetic HFpEF patients showed increased extracellular volume (median [IQR]: 30% [28, 33]), compared with healthy control subjects with normal values (median: 25% to 26%) regardless of age and sex, indicating the presence of LV fibrosis (34,35). Taken together, the major clinical characteristics of lean diabetic HFpEF patients were captured by the SKO mice.

DISCUSSION

We provide detailed cardiac phenotypic characterizations of SKO mice. The results demonstrate that lean diabetic SKO mice recapitulate multiple clinical characteristics of HFpEF, particularly those observed in lean diabetic Asian patients (Table 1). Both altered cardiac titin phosphorylation and increased LV

FIGURE 5 LV Reactive Interstitial Fibrosis and Neutrophil Infiltration in the SKO Mouse Myocardium

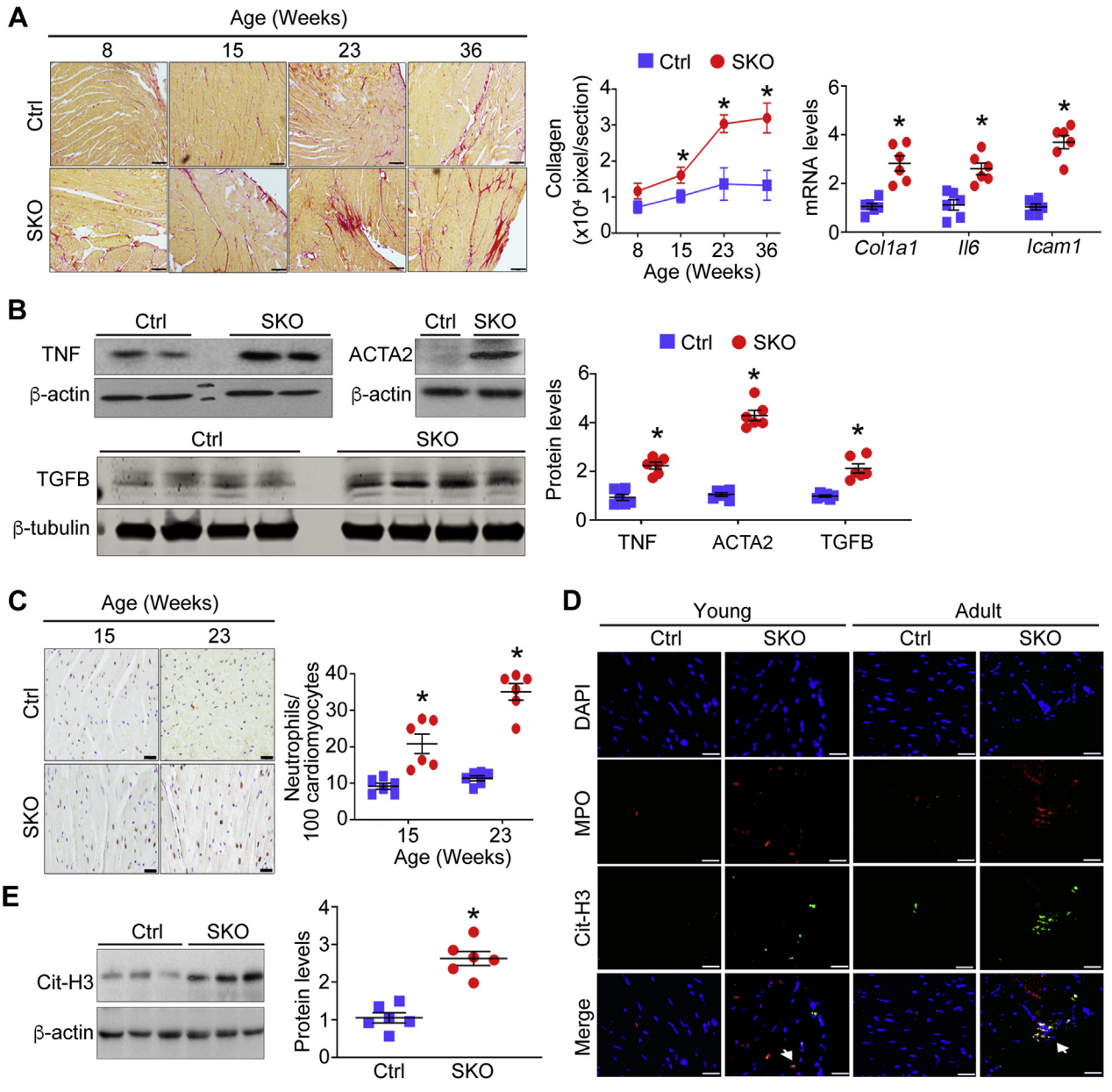

(A) Representative photomicrographs of picrosirius red staining of mouse heart tissues (scale bar = 100 μm). The pixel area of fibrosis was quantified in each group (n = 6). Gene expression of collagen 1 (*Col1a1*), interleukin 6 (*Il6*), and intercellular adhesion molecule 1 (*Icam1*), and **(B)** protein levels of alpha-smooth muscle actin (ACTA2), transforming growth factor beta family (TGFB), and tumor necrosis factor (TNF) were examined in mouse hearts (~24 weeks old, n = 6). Fold change was calculated for comparison. **(C)** Infiltrated neutrophils with positive immunohistochemical staining of antineutrophil-specific elastase were counted in mouse heart sections (scale bar = 20 μm, n = 6). **(D)** Representative images of in situ neutrophil extracellular traps in mouse hearts were indicated by **arrows** to show colocalization of deoxyribonucleic acid (4′,6-diamidino-2-phenylindole [DAPI], **blue**), myeloperoxidase ([MPO], **red**), and citrullinated histone 3 ([Cit-H3], **green**) (scale bar = 20 μm). **(E)** The protein level of Cit-H3 was examined in mouse heart tissues (24 to 30 weeks old, n = 6). Fold change was calculated for comparison. *$p < 0.05$, compared with Ctrl mice. Abbreviations as in Figure 1.

interstitial fibrosis may lead to intrinsic LV stiffness (Figure 6). Our murine HFpEF model is unique and significant with the following features: 1) diabetic animal without excessive weight gain; 2) concentric LV hypertrophy, LV diastolic dysfunction, and LA dilatation, associated with exercise intolerance and raised natriuretic peptides, recapitulating human HFpEF; 3) the LV hypertrophy occurred without an increase in blood pressure; 4) the intrinsic HFpEF features are advantageous for its utility as a preclinical model, in that the model overcomes problems of acute surgery insult, sudden onset of HF, deterioration of the LV systolic function, as well as the oncogenic response of existing animal models (9,10). As such, aged mice represent an ideal model of lean diabetic HFpEF, which allows us to continue mechanistic investigations through the multiorgan system and test novel therapeutic interventions, which are difficult to be carried out in human patients.

TITIN HYPERPHOSPHORYLATION AND INTERSTITIAL FIBROSIS CONTRIBUTE TO DIASTOLIC STIFFNESS IN THE SKO MICE. We unraveled that the post-translational modification of titin and increased interstitial fibrosis contributed to the diastolic stiffness of SKO mice, both of which are likely driven by the hyperglycemia. First, evidence linking altered titin phosphorylation with HF has been proposed in HFpEF patients (25). Recent studies have highlighted the importance of residues within the PEVK domain and N2-Bus as key targets of protein kinases in the regulation of titin mechanical function (36). Of note, hyperphosphorylation of human cardiac titin at serine 12022 (serine 12884 in mice) has been identified in the human failing hearts (26). The PEVK spring element is the critical site of PRKCA's involvement in passive myocardial stiffness. PRKCA-mediated phosphorylation at serine decreases persistence length of the PEVK spring element, thus increasing the passive tension of skinned myocytes from mouse and pig hearts (27,28). Importantly, hyperglycemia can increase the gene and protein level of PRKCA in experimental diabetic pig and rat hearts (37,38), which is in line with the increased cardiac PRKCA in diabetic SKO mice. Second, changes in collagen content, geometry, and composition are associated with abnormal diastolic function and frequently seen in human HFpEF myocardium (25,29). The cardiac collagen deposition was elevated in SKO mice from a young age and increased with aging, in association with progressive diastolic dysfunction. In SKO myocardium, interstitial fibrosis was accompanied by activation of cardiac fibroblasts, consistent with human patients. In HFpEF patients, fibroblasts are presumed to convert to collagen-producing myofibroblasts because of exposure to TGF beta family and myocardial inflammation (39), both of which were elevated in SKO myocardium. Subsequently, we sought the underlying basis for increased inflammatory and fibrotic damage in the SKO mouse hearts. We observed massive neutrophil infiltration as well as NET formation in SKO myocardium. Hyperglycemia triggers oxidative stress of neutrophils and directly primes neutrophils to undergo NET and thereby contributes to diabetic retinopathy (40) and impaired wound healing (41). NET-derived components stimulate human pulmonary fibroblasts to myofibroblasts with elevated ACTA2 expression (42). The cytotoxic histone and deoxyribonucleic acid bound to NET induces organ fibrosis in aged mice (43). In addition, NET license macrophages to turn on transcriptional

TABLE 1 The Clinical Characteristics of Patients With Lean Diabetic HFpEF and Age-Matched Control Subjects Without HF

	Control Subjects (n = 291)	Lean Diabetic HFpEF (n = 291)	p Value
Demographics			
Age, years	67.2 ± 7.2	71.3 ± 10.4	<0.001
Women	133 (46)	137 (47)	0.740
NYHA functional class			<0.001
I	283 (98)	43 (16)	
II	7 (2)	160 (58)	
III	0 (0)	64 (23)	
IV	0 (0)	7 (3)	
Reduction in exercise tolerance	8 (3)	195 (67)	<0.001
Systolic BP, mm Hg	138 ± 20	134 ± 24	0.042
Body mass index, kg/m^2	24 ± 3.8	25 ± 3.0	0.020
Diabetes	33 (12)	291 (100)	<0.001
LV dimensions			
LVEDV, ml	83 (70, 101)	86 (66, 116)	0.27
IVSD, mm	9.0 (8.0, 10.0)	11.0 (9.0, 12.0)	<0.001
PWTD, mm	9.0 (8.0, 10.0)	10.0 (9.0, 12.0)	<0.001
LVMASS, g	142 (117, 170)	182 (141, 216)	<0.001
LVMASSi, g/m^2	85 (74, 101)	105 (88, 131)	<0.001
RWT	0.37 (0.33, 0.43)	0.44 (0.38, 0.52)	<0.001
LAVi, ml/m^2	28 (24, 32)	34 (25, 46)	<0.001
LVEF, %	64 (62, 67)	60 (55, 65)	<0.001
Diastolic function			
E wave, cm/s	66 (56, 77)	83 (66, 107)	<0.001
A wave, cm/s	75 (61, 85)	85 (69, 99)	<0.001
E medial, cm/s	6.0 (5.0, 7.1)	5.0 (4.0, 6.0)	<0.001
E/e′ medial	11 (8.8, 13)	17 (13, 22)	<0.001
E/e′ lateral	8.5 (6.8, 11)	12 (9.1, 16)	<0.001

Values are mean ± SD, median (interquartile range), or n (%). Depending on the types of data, Student's *t*-test, Wilcoxon rank sum test, or chi-square test for unpaired observations was applied and p values < 0.05 indicate statistical significance.

BP = blood pressure; HFpEF = heart failure with preserved ejection fraction; IVSD = interventricular septal thickness in diastole; LAVi = left atrial volume indexed to body surface area; LVEDV = left ventricular end-diastolic volume; LVEF = left ventricular ejection fraction; LVMASS = left ventricular mass; LVMASSi = LV mass indexed to body surface area; NYHA = New York Heart Association; PWTD = posterior wall thickness in diastole; RWT = relative wall thickness.

FIGURE 6 The SKO Mouse Is a Lean Diabetic Murine Model of HFpEF

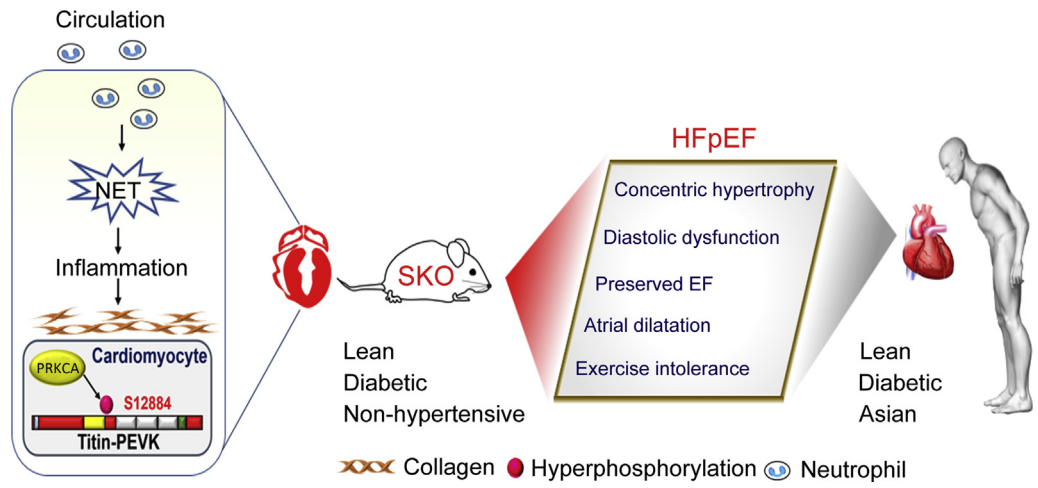

The lean diabetic SKO mice recapitulate major clinical manifestations of heart failure with preserved ejection fraction (HFpEF), resembling those observed in Asian populations, including LV concentric hypertrophy with preserved EF, increased left ventricular stiffness, and LA dilatation associated with exercise intolerance. Both cellular (PRKCA-mediated hyperphosphorylation of titin at the PEVK spring elements) and extracellular (reactive interstitial fibrosis) changes lead to left ventricular stiffness, and the latter is associated with massive neutrophil infiltration and neutrophil extracellular traps (NET) in mouse heart tissues. The NET, cellular titin changes, and extracellular interstitial fibrosis could be suggested as potential therapeutic targets in Asian HFpEF patients. Abbreviations as in **Figures 1, 2, and 4**.

regulation of *Il6* via toll-like receptor 2/4 in atherosclerosis (44). In the myocardium, the cytokines further amplify their actions primarily through the activation of JAK-STAT3 signaling. STAT3 is a ubiquitous stress-activated transcription factor that regulates gene programs important for hypertrophy, fibrosis, and inflammation (45). On cytokine binding to the specific receptors, STAT3 is phosphorylated and activated by JAK2 and then plays a crucial role in the induction of hypertrophic genes (21,22,46). Our findings show that SKO mice have cardiac inflammation, along with activated STAT3 signaling and induction of *Nppa* and *Acta1*, thus supporting the current recognition that comorbidity-driven inflammation contributes to the cardiac hypertrophy and adverse outcomes (47). As such, we suggest that NET may be a potential therapeutic target to intervene in inflammatory and fibrotic damage of SKO hearts. The activated peptidyl arginine deiminase 4 (PADI4) promotes citrullination of histone and allows decondensation of chromatin, a critical step for NET formation (33). PADI4 inhibitor (Cl-amidine) blocks NET formation and is successfully used to reduce atherosclerosis burden (48) and rescue wound healing in diabetic mice (49). It is of significant interest to examine whether Cl-amidine treatment produces beneficial effects on our HFpEF mice in a future study.

SKO MOUSE IS A UNIQUE LEAN DIABETIC HFpEF MODEL. An important benefit of preclinical animal models is the possibility to examine the contribution of single comorbidity in isolation without confounding risk factors, unlike clinical HFpEF patients frequently bound with multiple comorbidities. In terms of diabetic HFpEF models, so far, *db/db* mice with leptin receptor deficiency have been proposed to recapitulate multiple characteristics of clinical HFpEF (10,50). However, some phenotypic differences between obese diabetic *db/db* mice and lean diabetic SKO mice exist. Despite the presence of diastolic dysfunction, adult *db/db* mice develop mild LV hypertrophy, with only ~15% higher LV mass than in wild-type mice. Of note, adult *db/db* mice have apparent LV dilatation, distinct from SKO mice. The *db/db* mice also show evidence of cardiac fibrosis, but cardiac fibroblast of *db/db* mice does not undergo myofibroblast conversion (50). Another lean diabetic, nonhypertensive rat model induced by streptozotocin also shows diastolic dysfunction with increased ventricular stiffness as well as cardiac fibrosis. However, the LV eccentric hypertrophy and impaired contractile performance represent the major disadvantages

of this animal model for lean diabetic HFpEF study (51). Goto-Kakizaki rats display type 2 diabetes, salt-sensitive hypertension, hypertrophic cardiomyopathy, and cardiac fibrosis (52). However, there is little evidence that Goto-Kakizaki rat may be a lean diabetic HFpEF model. It is likely that the etiological and pathophysiological pathways are diverse among these preclinical models, despite some common clinical HFpEF features shared by animals. Thus, the specific animal model may only resemble a certain proportion of HFpEF patients. It is therefore important to carefully select suitable preclinical models for mechanistic investigation and therapeutic validation.

SKO MODEL IS CLINICALLY RELEVANT TO LEAN DIABETIC HFpEF PATIENTS IN ASIA. We believe that the current study is of particular relevance to Asian populations, in that "pure" metabolic disturbances of diabetes, without hypertension or obesity, may produce the HFpEF characteristics. The pan-Asian prospective study demonstrates that lean diabetic HFpEF patients, compared with other HF groups, have the worst quality of life, more severe signs and symptoms of HF, and the highest rate of the primary combined outcome of death and HF hospitalization (8). We further found that of 2,051 Asian patients with both body mass index and waist measurements, there was an inverse relationship between body mass index and risk of the composite outcome ("obesity paradox"); in contrast there was a direct relationship between waist-to-height ratio and risk of the composite outcome, suggesting that visceral adiposity plays an important role. The lean-fat (low body mass index but high waist-to-height ratio) patients had the highest proportion of diabetes associated with greater truncal obesity with overall sarcopenia (unpublished data presented at the ESC Heart failure Congress 2018), reminiscent of our lipodystrophic diabetic mouse model.

Moreover, the SKO model with uncontrolled hyperglycemia is clinically relevant, and appropriately represents the true natural history of diabetic HFpEF patients. Diabetic cardiomyopathy can manifest itself either as a restrictive phenotype with HFpEF or as a dilated phenotype with HF with reduced EF. The HFpEF phenotype is very common and usually occurs in patients with type 2 diabetes mellitus, whereas dilated cardiomyopathy is rare, is mainly observed in patients with type 1 diabetes mellitus. Accordingly, hyperglycemia, hyperinsulinemia, and lipotoxicity may predispose more to the HFpEF characteristics, while autoimmune processes rather lead to the HF with reduced EF features (53,54). In clinical HFpEF patients, the prevailing hypothesis is that hyperglycemia triggers a systemic inflammatory state that results in coronary microvascular endothelial dysfunction, which alters paracrine signaling between endothelial cells and cardiomyocytes and allows leukocytes to infiltrate the myocardium (5), contributing to cardiomyocyte stiffness and hypertrophy. Leukocyte infiltration leads to activation of myofibroblasts and interstitial collagen deposition. This is particularly so in the presence of hyperglycemia because cardiac PRKC activity is specifically augmented with hyperglycemia, thus promoting collagen production and deposition (55). These characteristics are clearly evident in the current SKO mice. Taken together, our SKO model represents a novel and validated murine model with lean diabetic HFpEF, which will bridge the large translation gap between preclinical and clinical studies and help to provide the more insightful understanding of the pathogenesis of the disease.

STUDY LIMITATIONS. This study provides a validated murine model of lean diabetic HFpEF and identifies underlying mechanisms. However, there remain several limitations. The inherent lipodystrophic phenotype of animals does not completely mimic the full spectrum of Asian patients' characteristics. The functional consequences of multiple titin phosphosites in the HFpEF mouse hearts remain unknown, and these consequences will likely be the subject of future studies. Moreover, despite the evidence supporting NET with pleiotropic effects to induce inflammation and tissue fibrosis, it remains to be conclusively demonstrated that NET are the primary mechanism by which diabetic conditions cause cardiac inflammation and fibrosis.

CONCLUSIONS

The lean diabetic SKO mice recapitulate major clinical manifestations of Asian HFpEF patients. Our findings help to clarify that diabetes, in the absence of obesity or hypertension, produces multiple HFpEF characteristics. Both cellular (PRKCA-mediated hyperphosphorylation of titin at the PEVK spring elements) and extracellular (reactive interstitial fibrosis) changes may lead to left ventricular stiffness, and the latter is associated with massive neutrophil infiltration and NET. The NET, cellular titin changes, and extracellular interstitial fibrosis may be potential therapeutic targets in Asian HFpEF patients.

ACKNOWLEDGMENTS The authors are grateful to their laboratory members and acknowledge the support from Singapore Bioimaging Consortium; Agency for Science, Technology and Research; and State Key Laboratory of Pharmaceutical Biotechnology and

Department of Pharmacology and Pharmacy, The University of Hong Kong. The authors also thank the Singapore Bioimaging Consortium-Nikon Imaging Center for support on microscopy. The contribution of all the site investigators and clinical coordinators of ASIAN-HF and ATTRaCT are acknowledged.

ADDRESS FOR CORRESPONDENCE: Dr. Yu Wang, Department of Pharmacology and Pharmacy, The University of Hong Kong, Sassoon Road 21, Hong Kong, China. E-mail: yuwanghk@hku.hk. OR Dr. Weiping Han, Singapore Bioimaging Consortium, Agency for Science, Technology and Research, 11 Biopolis Way, Singapore. E-mail: wh10@cornell.edu. OR Dr. Carolyn S.P. Lam, National Heart Centre Singapore and Duke-National University of Singapore, 5 Hospital Drive, Singapore. E-mail: carolyn.lam@duke-nus.edu.sg.

PERSPECTIVES

COMPETENCY IN MEDICAL KNOWLEDGE: Lean diabetes can produce the HFpEF characteristics, which is likely dependent on changed titin homeostasis and extracellular matrix fibrillar collagen. Both mechanisms are commonly identified in HFpEF animals and patients, suggesting that these could be potential therapeutic targets for HFpEF, despite the clinical etiologic heterogeneity.

TRANSLATIONAL OUTLOOK: Future research should test whether inhibition of neutrophil-induced myocardial inflammation and structural derangements can achieve therapeutic improvement for lean diabetic HFpEF in preclinical models and cohort studies.

REFERENCES

1. Lam CS, Pieske B. Heart failure with preserved ejection fraction (HFPEF) currently represents one of the greatest unmet needs in cardiology: introduction. Heart Fail Clin 2014;10:xv.

2. Owan TE, Hodge DO, Herges RM, Jacobsen SJ, Roger VL, Redfield MM. Trends in prevalence and outcome of heart failure with preserved ejection fraction. N Engl J Med 2006;355:251–9.

3. Yancy CW, Jessup M, Bozkurt B, et al. 2013 ACCF/AHA guideline for the management of heart failure: a report of the American College of Cardiology Foundation/American Heart Association Task Force on Practice Guidelines. J Am Coll Cardiol 2013;62:e147–239.

4. Shah SJ, Kitzman DW, Borlaug BA, et al. Phenotype-specific treatment of heart failure with preserved ejection fraction: a multiorgan roadmap. Circulation 2016;134:73–90.

5. Paulus WJ, Tschope C. A novel paradigm for heart failure with preserved ejection fraction: comorbidities drive myocardial dysfunction and remodeling through coronary microvascular endothelial inflammation. J Am Coll Cardiol 2013;62:263–71.

6. Tromp J, Teng TH, Tay WT, et al. Heart failure with preserved ejection fraction in Asia. Eur J Heart Fail 2018:1–14.

7. Bank IEM, Gijsberts CM, Teng THK, et al. Prevalence and clinical significance of diabetes in Asian versus white patients with heart failure. J Am Coll Cardiol HF 2017;5:14–24.

8. Tromp J, Tay WT, Ouwerkerk W, et al. Multimorbidity in patients with heart failure from 11 Asian regions: a prospective cohort study using the ASIAN-HF registry. PLoS Med 2018;15:e1002541.

9. Roh J, Houstis N, Rosenzweig A. Why don't we have proven treatments for HFpEF? Circ Res 2017;120:1243–5.

10. Valero-Munoz M, Backman W, Sam F. Murine models of heart failure with preserved ejection fraction: a "fishing expedition". J Am Coll Cardiol Basic Trans Science 2017;2:770–89.

11. Garg A. Acquired and inherited lipodystrophies. N Engl J Med 2004;350:1220–34.

12. Joffe BI, Panz VR, Raal FJ. From lipodystrophy syndromes to diabetes mellitus. Lancet 2001;357:1379–81.

13. Lupsa BC, Sachdev V, Lungu AO, Rosing DR, Gorden P. Cardiomyopathy in congenital and acquired generalized lipodystrophy: a clinical assessment. Medicine (Baltimore) 2010;89:245–50.

14. Sanon VP, Handelsman Y, Pham SV, Chilton R. Cardiac manifestations of congenital generalized lipodystrophy. Clin Diabetes 2016;34:181–6.

15. Nelson MD, Victor RG, Szczepaniak EW, Simha V, Garg A, Szczepaniak LS. Cardiac steatosis and left ventricular hypertrophy in patients with generalized lipodystrophy as determined by magnetic resonance spectroscopy and imaging. Am J Cardiol 2013;112:1019–24.

16. Wee K, Yang W, Sugii S, Han W. Towards a mechanistic understanding of lipodystrophy and seipin functions. Biosci Rep 2014;34:e00141.

17. McIlroy GD, Suchacki K, Roelofs AJ, et al. Adipose specific disruption of seipin causes early-onset generalised lipodystrophy and altered fuel utilisation without severe metabolic disease. Mol Metab 2018;10:55–65.

18. Lam CS, Anand I, Zhang S, et al. Asian Sudden Cardiac Death in Heart Failure (ASIAN-HF) registry. Eur J Heart Fail 2013;15:928–36.

19. Lam CS, Teng TK, Tay WT, et al. Regional and ethnic differences among patients with heart failure in Asia: the Asian sudden cardiac death in heart failure registry. Eur Heart J 2016;37:3141–53.

20. Heymans S, Corsten MF, Verhesen W, et al. Macrophage microRNA-155 promotes cardiac hypertrophy and failure. Circulation 2013;128:1420–32.

21. Kunisada K, Negoro S, Tone E, et al. Signal transducer and activator of transcription 3 in the heart transduces not only a hypertrophic signal but a protective signal against doxorubicin-induced cardiomyopathy. Proc Natl Acad Sci U S A 2000;97:315–9.

22. Kunisada K, Tone E, Fujio Y, Matsui H, Yamauchi-Takihara K, Kishimoto T. Activation of gp130 transduces hypertrophic signals via STAT3 in cardiac myocytes. Circulation 1998;98:346–52.

23. Yue H, Li W, Desnoyer R, Karnik SS. Role of nuclear unphosphorylated STAT3 in angiotensin II type 1 receptor-induced cardiac hypertrophy. Cardiovasc Res 2010;85:90–9.

24. Arnlov J, Ingelsson E, Riserus U, Andren B, Lind L. Myocardial performance index, a Doppler-derived index of global left ventricular function, predicts congestive heart failure in elderly men. Eur Heart J 2004;25:2220–5.

25. Zile MR, Baicu CF, Ikonomidis JS, et al. Myocardial stiffness in patients with heart failure and a preserved ejection fraction: contributions of collagen and titin. Circulation 2015;131:1247–59.

26. Hamdani N, Krysiak J, Kreusser MM, et al. Crucial role for Ca2(+)/calmodulin-dependent protein kinase-II in regulating diastolic stress of normal and failing hearts via titin phosphorylation. Circ Res 2013;112:664–74.

27. Hidalgo C, Hudson B, Bogomolovas J, et al. PKC phosphorylation of titin's PEVK element: a novel and conserved pathway for modulating myocardial stiffness. Circ Res 2009;105:631–8.

28. Hudson BD, Hidalgo CG, Gotthardt M, Granzier HL. Excision of titin's cardiac PEVK spring element abolishes PKC alpha-induced increases in

myocardial stiffness. J Mol Cell Cardiol 2010;48:972–8.

29. Rommel KP, von Roeder M, Latuscynski K, et al. Extracellular volume fraction for characterization of patients with heart failure and preserved ejection fraction. J Am Coll Cardiol 2016;67:1815–25.

30. Arora PD, McCulloch CA. Dependence of collagen remodelling on alpha-smooth muscle actin expression by fibroblasts. J Cell Physiol 1994;159:161–75.

31. Zeisberg EM, Kalluri R. Origins of cardiac fibroblasts. Circ Res 2010;107:1304–12.

32. Brinkmann V, Reichard U, Goosmann C, et al. Neutrophil extracellular traps kill bacteria. Science 2004;303:1532–5.

33. Lewis HD, Liddle J, Coote JE, et al. Inhibition of PAD4 activity is sufficient to disrupt mouse and human NET formation. Nat Chem Biol 2015;11:189–91.

34. Chin CW, Semple S, Malley T, et al. Optimization and comparison of myocardial T1 techniques at 3T in patients with aortic stenosis. Eur Heart J Cardiovasc Imaging 2014;15:556–65.

35. Dabir D, Child N, Kalra A, et al. Reference values for healthy human myocardium using a T1 mapping methodology: results from the International T1 Multicenter cardiovascular magnetic resonance study. J Cardiovasc Magn Reson 2014;16:69.

36. Linke WA, Hamdani N. Gigantic business: titin properties and function through thick and thin. Circ Res 2014;114:1052–68.

37. Guo M, Wu MH, Korompai F, Yuan SY. Upregulation of PKC genes and isozymes in cardiovascular tissues during early stages of experimental diabetes. Physiol Genomics 2003;12:139–46.

38. Giles TD, Ouyang J, Kerut EK, et al. Changes in protein kinase C in early cardiomyopathy and in gracilis muscle in the BB/Wor diabetic rat. Am J Physiol 1998;274:H295–307.

39. Westermann D, Lindner D, Kasner M, et al. Cardiac inflammation contributes to changes in the extracellular matrix in patients with heart failure and normal ejection fraction. Circ Heart Fail 2011;4:44–52.

40. Wang L, Zhou X, Yin Y, Mai Y, Wang D, Zhang X. Hyperglycemia induces neutrophil extracellular traps formation through an NADPH oxidase-dependent pathway in diabetic retinopathy. Front Immunol 2018;9:3076.

41. Wong SL, Demers M, Martinod K, et al. Diabetes primes neutrophils to undergo NETosis, which impairs wound healing. Nat Med 2015;21:815–9.

42. Chrysanthopoulou A, Mitroulis I, Apostolidou E, et al. Neutrophil extracellular traps promote differentiation and function of fibroblasts. J Pathol 2014;233:294–307.

43. Martinod K, Witsch T, Erpenbeck L, et al. Peptidylarginine deiminase 4 promotes age-related organ fibrosis. J Exp Med 2017;214:439–58.

44. Warnatsch A, Ioannou M, Wang Q, Papayannopoulos V. Inflammation: neutrophil extracellular traps license macrophages for cytokine production in atherosclerosis. Science 2015;349:316–20.

45. Haghikia A, Ricke-Hoch M, Stapel B, Gorst I, Hilfiker-Kleiner D. STAT3, a key regulator of cell-to-cell communication in the heart. Cardiovasc Res 2014;102:281–9.

46. Mir SA, Chatterjee A, Mitra A, Pathak K, Mahata SK, Sarkar S. Inhibition of signal transducer and activator of transcription 3 (STAT3) attenuates interleukin-6 (IL-6)-induced collagen synthesis and resultant hypertrophy in rat heart. J Biol Chem 2012;287:2666–77.

47. Borlaug BA. The pathophysiology of heart failure with preserved ejection fraction. Nat Rev Cardiol 2014;11:507–15.

48. Knight JS, Luo W, O'Dell AA, et al. Peptidylarginine deiminase inhibition reduces vascular damage and modulates innate immune responses in murine models of atherosclerosis. Circ Res 2014;114:947–56.

49. Fadini GP, Menegazzo L, Rigato M, et al. NETosis delays diabetic wound healing in mice and humans. Diabetes 2016;65:1061–71.

50. Alex L, Russo I, Holoborodko V, Frangogiannis NG. Characterization of a mouse model of obesity-related fibrotic cardiomyopathy that recapitulates features of human heart failure with preserved ejection fraction. Am J Physiol Heart Circ Physiol 2018;315:H934–49.

51. Akula A, Kota MK, Gopisetty SG, et al. Biochemical, histological and echocardiographic changes during experimental cardiomyopathy in STZ-induced diabetic rats. Pharmacol Res 2003;48:429–35.

52. D'Souza A, Howarth FC, Yanni J, et al. Chronic effects of mild hyperglycemia on left ventricle transcriptional profile and structural remodelling in the spontaneously type 2 diabetic Goto-Kakizaki rat. Heart Fail Rev 2014;19:65–74.

53. Paulus WJ, Dal Canto E. Distinct myocardial targets for diabetes therapy in heart failure with preserved or reduced ejection fraction. J Am Coll Cardiol HF 2018;6:1–7.

54. Maack C, Lehrke M, Backs J, et al. Heart failure and diabetes: metabolic alterations and therapeutic interventions: a state-of-the-art review from the Translational Research Committee of the Heart Failure Association-European Society of Cardiology. Eur Heart J 2018;39:4243–54.

55. Asbun J, Villarreal FJ. The pathogenesis of myocardial fibrosis in the setting of diabetic cardiomyopathy. J Am Coll Cardiol 2006;47:693–700.

KEY WORDS fibrosis, heart failure with preserved ejection fraction, neutrophil, seipin, titin

APPENDIX For supplemental material, please see the online version of this paper.

JACC: BASIC TO TRANSLATIONAL SCIENCE VOL. 4, NO. 8, 2019

EDITORIAL COMMENT

The *Bslc2*$^{-/-}$ Mouse

Adding a Missing Phenotype to the Repertoire of HFpEF Animal Models*

Fadi N. Salloum, PhD, Stefano Toldo, PhD

The quest to find a treatment for heart failure with preserved ejection fraction (HFpEF) remains 1 of the biggest challenges in modern medicine. This is mainly due to the poor understanding of the disease pathophysiology and the lack of comprehensive animal models, as well as the absence of a general consensus on the characteristics of the disease itself. Over the past few years, however, a shared belief has emerged in the scientific community: HFpEF, just like heart failure in general, may not be a singular disease but rather a syndrome with its own subtypes and phenotypes (1). HFpEF is associated with several co-morbidities such as hypertension, coronary artery disease, arrhythmias, chronic kidney disease, aging, obesity, and diabetes, which are believed to be the substrates for the development of HFpEF. Therefore, patients with HFpEF have different phenotypes, leading to a vast heterogeneity that has largely affected the outcomes of clinical trials aimed at testing therapies to effectively treat this clinical syndrome (1,2). The recognition of this heterogeneity has led the research community to identify major phenotypes in which patients present a reduced heterogeneity, with the aim of developing more targeted therapies that are better suited for the selected phenotype (2).

The use of animal models is a pivotal part of the quest to discover a new treatment because it provides an opportunity to test original hypotheses and find new and/or more effective therapies to combat clinical challenges (3). The basic research field of HFpEF has suffered considerably from the lack of adequate models that could recapitulate the complexity of this syndrome in humans. Although the development of a model that reproduces the broad spectrum of phenotypes seen in HFpEF remains the ultimate goal, adoption of simpler models of disease that develop diastolic dysfunction and signs of HFpEF seems like a closer reach for translational research. Animal models of obesity or hypertension, based on genetic, hormonal, or dietary interventions, have been developed and adopted to recapitulate some of the HFpEF phenotypes.

SEE PAGE 924

Recent epidemiological studies have shown that patients with HFpEF and diabetes in Asia are more likely to be lean compared with North European white patients with diabetes and HFpEF, who are prevalently obese (4,5). This patient population seems different from other patients usually seen in the clinics in the Western countries. The study by Bai et al. (5) in this issue of *JACC: Basic to Translational Science* explored the effect of *Bslc2* (seipin) deletion in mice to reproduce the diabetic lean phenotype while aiming to recapitulate some of the characteristics of the Asian diabetic patient population with HFpEF. The Berardinelli-Seip congenital lipodystrophy-2 (*Bslc2*)/seipin mutation in human patients induces a lipodystrophic phenotype (leanness, diabetes) with left ventricular hypertrophy and normal ejection fraction. The *Bslc2*$^{-/-}$ mice had a

*Editorials published in *JACC: Basic to Translational Science* reflect the views of the authors and do not necessarily represent the views of *JACC: Basic to Translational Science* or the American College of Cardiology.

From the Pauley Heart Center, Division of Cardiology, Department of Internal Medicine, Virginia Commonwealth University, Richmond, Virginia. Dr. Salloum is funded by grants from the National Institutes of Health (HL133167 and HL142281). Both authors have reported that they have no relationships relevant to the contents of this paper to disclose. The authors attest they are in compliance with human studies committees and animal welfare regulations of the authors' institutions and Food and Drug Administration guidelines, including patient consent where appropriate. For more information, visit the *JACC: Basic to Translational Science* author instructions page.

ISSN 2452-302X https://doi.org/10.1016/j.jacbts.2019.11.004

growth curve similar to that of the wild-type (*Bslc2*$^{+/+}$) mice, with a similar amount of lean mass and systolic blood pressure, but they developed severe hyperglycemia and cardiac hypertrophy compared with the *Bslc2*$^{+/+}$ mice. The *Bslc2*$^{-/-}$ mice also displayed an increased end-diastolic pressure/volume relationship, increased end-diastolic pressure, and enlargement of the left atrium. It is interesting to note that cardiac hypertrophy developed at 23 weeks of age, after the appearance of diastolic dysfunction (i.e., increase in isovolumetric relaxation time) and exercise intolerance, which were significantly impaired earlier in the rodent life (15 weeks). At 15 weeks, myocardial collagen deposition and neutrophil infiltration were already significantly increased in the *Bslc2*$^{-/-}$ mice. Together with the histological and physiological changes, titin phosphorylation and increased protein kinase C-α expression accompanied the development of HFpEF in the *Bslc2*$^{-/-}$ mice.

Intriguingly, all the reported changes were independent from direct effects due to the BSLC2 deletion in cardiomyocytes (5). In fact, Bscl2 messenger ribonucleic acid was barely expressed in the muscle tissue and in the heart of *Bslc2*$^{+/+}$ mice, whereas it was mostly expressed in the white and brown adipose tissues. In addition, the selective deletion of *Bslc2* in cardiomyocytes did not affect cardiac mass and function, and therefore Bai et al. suggested that systemic effects secondary to *Bslc2* deletion, such as hyperglycemia, were the culprit for the development of the HFpEF phenotype in *Bslc2*$^{-/-}$ mice. The authors also proposed, based on their findings, that neutrophil extracellular traps, cellular alterations in titin, and interstitial fibrosis may represent promising therapeutic targets in Asian patients with HFpEF.

Overall, the *Bslc2*$^{-/-}$ mouse displayed features of diastolic dysfunction and failure and recapitulated several characteristics of the lean diabetic patient with HFpEF (5). However, it is noteworthy that the glycemic levels of the *Bslc2*$^{-/-}$ mice were extremely high (>20 mM or >360 mg/dl) in the absence of any type of glycemic control, which is expected to be better managed in patients undergoing clinical assessment, treatment, and follow-up. Moreover, the relevance of the deletion/mutation of *Bslc2* for the lean diabetic patients with HFpEF in Asia or elsewhere remains unclear. Despite this lack of evidence, the *Bslc2* deletion seems to affect the heart through an extracardiac mechanism, and thus this model may prove to be useful for testing new hypotheses in this HFpEF category. The *Bslc2*$^{-/-}$ mouse, therefore, represents a new tool to be added to the existing animal models of HFpEF that can be particularly useful for studying more closely the lean diabetic phenotype of HFpEF.

ADDRESS FOR CORRESPONDENCE: Dr. Fadi N. Salloum, Division of Cardiology, Virginia Commonwealth University, 1101 East Marshall Street, Room 7-070, Box 980204, Richmond, Virginia 23298. E-mail: fadi.salloum@vcuhealth.org.

REFERENCES

1. Pfeffer MA, Shah AM, Borlaug BA. Heart failure with preserved ejection fraction in perspective. Circ Res 2019;124:1598–617.

2. Del Buono MG, Arena R, Borlaug BA, et al. Exercise intolerance in patients with heart failure: JACC State-of-the-Art Review. J Am Coll Cardiol 2019;73:2209–25.

3. Valero-Muñoz M, Backman W, Sam F. Murine models of heart failure with preserved ejection fraction: a "fishing expedition." J Am Coll Cardiol Basic Trans Science 2017;2:770–89.

4. Bank IEM, Gijsberts CM, Teng TK, et al. Prevalence and clinical significance of diabetes in Asian versus white patients with heart failure. J Am Coll Cardiol HF 2017;5:14–24.

5. Bai B, Yang W, Fu Y, et al. Seipin knockout mice develop heart failure with preserved ejection fraction. J Am Coll Cardiol Basic Trans Science 2019;4:924–37.

KEY WORDS HFpEF, lean diabetic, seipin

JACC: BASIC TO TRANSLATIONAL SCIENCE VOL. 4, NO. 8, 2019

PRECLINICAL RESEARCH

CFTR Therapeutics Normalize Cerebral Perfusion Deficits in Mouse Models of Heart Failure and Subarachnoid Hemorrhage

Darcy Lidington, PhD,[a,b,*] Jessica C. Fares, MSc,[a,b,*] Franziska E. Uhl, PhD,[c] Danny D. Dinh, MSc,[a,b] Jeffrey T. Kroetsch, PhD,[a,b] Meghan Sauvé, PhD,[a,b] Firhan A. Malik, PhD,[a] Frank Matthes, PhD,[c] Lotte Vanherle, MSc,[c] Arman Adel, BSc,[a] Abdul Momen, MD, PhD,[d] Hangjun Zhang, MD,[a,b] Roozbeh Aschar-Sobbi, PhD,[e] Warren D. Foltz, PhD,[f] Hoyee Wan, BSc,[g,h,i] Manabu Sumiyoshi, MD,[h,j] R. Loch Macdonald, MD, PhD,[g,h] Mansoor Husain, MD,[a,d,k,l] Peter H. Backx, PhD, DVM,[e,m] Scott P. Heximer, PhD,[a,k] Anja Meissner, PhD,[a,c,†] Steffen-Sebastian Bolz, MD, PhD[a,b,k,†]

VISUAL ABSTRACT

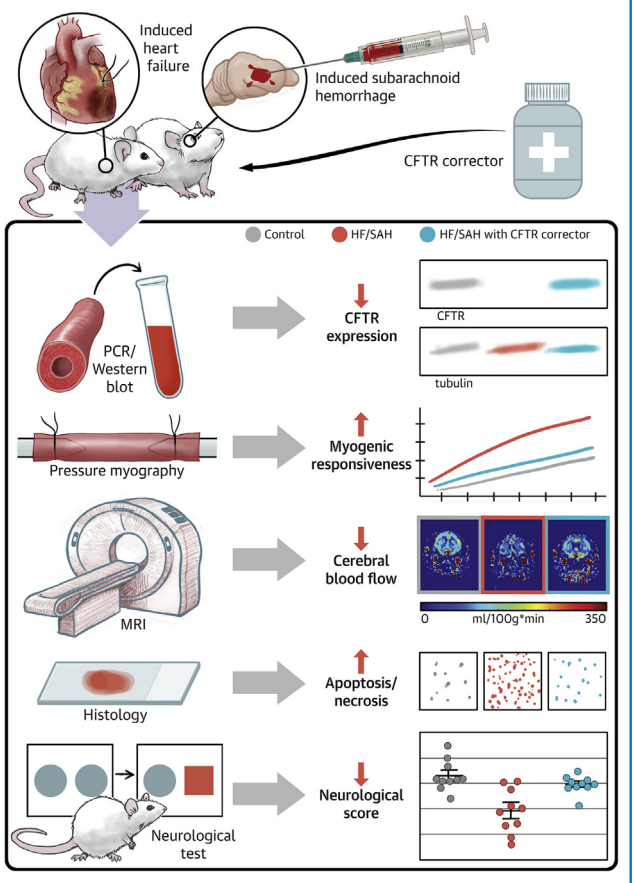

Lidington, D. et al. J Am Coll Cardiol Basic Trans Science. 2019;4(8):940-58.

ISSN 2452-302X https://doi.org/10.1016/j.jacbts.2019.07.004

HIGHLIGHTS

- **The cystic fibrosis transmembrane conductance regulator (CFTR) is a significant modulator of cerebrovascular reactivity; the loss of CFTR function enhances myogenic vasoconstriction.**
- **Heart failure and subarachnoid hemorrhage downregulate cerebrovascular CFTR protein expression; this leads to enhanced cerebral artery vasoconstriction, reduced cerebral perfusion, neuronal injury, and ultimately, neurologic deficits.**
- **CFTR therapeutics that maintain CFTR expression normalize the perfusion deficits, reduce neuronal injury, and improve neurologic function in these pathological settings.**

SUMMARY

Heart failure (HF) and subarachnoid hemorrhage (SAH) chronically reduce cerebral perfusion, which negatively affects clinical outcome. This work demonstrates a strong relationship between cerebral artery cystic fibrosis transmembrane conductance regulator (CFTR) expression and altered cerebrovascular reactivity in HF and SAH. In HF and SAH, CFTR corrector compounds (C18 or lumacaftor) normalize pathological alterations in cerebral artery CFTR expression, vascular reactivity, and cerebral perfusion, without affecting systemic hemodynamic parameters. This normalization correlates with reduced neuronal injury. Therefore, CFTR therapeutics have emerged as valuable clinical tools to manage cerebrovascular dysfunction, impaired cerebral perfusion, and neuronal injury. (J Am Coll Cardiol Basic Trans Science 2019;4:940–58)

ABBREVIATIONS AND ACRONYMS

CBF = cerebral blood flow

CFTR = cystic fibrosis transmembrane conductance regulator

HF = heart failure

MAP = mean arterial pressure

MOPS = 3-morpholinopropanesulfonic acid

MRI = magnetic resonance imaging

NIH = National Institutes of Health

PCA = posterior cerebral artery

SAH = subarachnoid hemorrhage

S1P = sphingosine-1-phosphate

TNF = tumor necrosis factor

TPR = total peripheral resistance

Survival rates for heart attack and stroke victims have significantly improved over the last 40 years. However, the extended longevity is frequently accompanied by cognitive decline. Cognitive impairment accelerates disease progression, reduces treatment compliance, progressively limits therapeutic treatment options, and imposes a substantial socioeconomic burden (1). Thus, cognitive

From the [a]Department of Physiology, University of Toronto, Toronto, Ontario, Canada; [b]Toronto Centre for Microvascular Medicine at The Ted Rogers Centre for Heart Research Translational Biology and Engineering Program, University of Toronto, Ontario, Canada; [c]Wallenberg Center for Molecular Medicine and Department of Experimental Medical Science, Lund University, Lund, Sweden; [d]Division of Cell & Molecular Biology, Toronto General Hospital Research Institute, Toronto, Ontario, Canada; [e]Division of Cardiology, University Health Network, Toronto, Ontario, Canada; [f]STTARR Innovation Centre, Department of Radiation Oncology, Princess Margaret Hospital, Toronto, Ontario, Canada; [g]Labatt Family Centre of Excellence in Brain Injury and Trauma Research, Keenan Research Centre for Biomedical Research and Li Ka Shing Knowledge Institute, St. Michael's Hospital, Toronto, Ontario, Canada; [h]Division of Neurosurgery, St. Michael's Hospital, and Department of Surgery, University of Toronto, Toronto, Ontario, Canada; [i]Sunnybrook Research Institute, Physical Sciences Platform and Department of Medical Biophysics, University of Toronto, Toronto, Ontario, Canada; [j]Institute of Health Biosciences, Department of Neurosurgery, University of Tokushima Graduate School, Tokushima, Japan; [k]Heart & Stroke/Richard Lewar Centre of Excellence for Cardiovascular Research, University of Toronto, Toronto, Ontario, Canada; [l]Department of Medicine, University of Toronto, Toronto, Ontario, Canada; and the [m]Department of Biology, York University, Toronto, Ontario, Canada. *Dr. Lidington and Ms. Fares contributed equally to this work and are joint first authors. †Drs. Meissner and Bolz contributed equally to this work and are joint senior authors. Dr. Kroetsch was supported by a Queen Elizabeth II/Heart & Stroke Foundation of Ontario Graduate Scholarship in Science and Technology. Dr. Sauvé was supported by Canadian Institutes of Health Research (CIHR) Doctoral Research Award and by Natural Sciences and Engineering Research Council (NSERC) of Canada. Dr. Dinh was supported by a NSERC MATCH scholarship. Dr. Malik was supported by a PGS-D doctoral scholarship. Dr. Backx was supported by the Canadian Institutes of Health Research (CIHR) (PJT 153159). Dr. Heximer was supported by CIHR (MOP-106670). Dr. Meissner was supported by the Swedish Science Council (VR 2017-01243), the Åke Wibergs Stiftelse (M17-0031), the Knut & Alice Wallenberg Foundation (2015.0030), and Lund University. Dr. Bolz was supported by the Operating and Infrastructure Grants from the Heart and Stroke Foundation of Ontario (HFSO) (G13-0002610 and G16-00014175) and CIHR (PJT 153269); a HSFO Career Investigator Award (CI-7432) and Mid-Career Investigator Award; the Brain Aneurysm Foundation (Northwell Health - North Shore University Hospital Brain Aneurysm Centre Chair of Research Award); the Canadian Foundation for Innovation and Ontario Research Fund (11810); and research support from the University of Toronto. Dr. Macdonald is chief scientific officer of Edge Therapeutics, Inc. All other authors have reported that they have no relationships relevant to the contents of this paper to disclose.

The authors attest they are in compliance with human studies committees and animal welfare regulations of the authors' institutions and Food and Drug Administration guidelines, including patient consent where appropriate. For more information, visit the *JACC: Basic to Translational Science* author instructions page.

Manuscript received April 29, 2019; revised manuscript received July 15, 2019, accepted July 16, 2019.

decline has emerged as a major clinical concern for patients with heart failure (HF) and stroke. Therefore, improving cognitive function will positively affect the primary disease, in addition to yielding both personal and socioeconomic benefits.

Our recent work focused on 2 etiologically distinct pathologies that are strongly associated with cognitive impairment: heart failure (HF) and subarachnoid hemorrhage (SAH). Clinically, the prevalence of early-onset cognitive impairment in patients with HF ranges from 25% to 75% (2); the prevalence in SAH is estimated to be 73% (3). Experimental mouse models emulate several key features of these diseases, including reduced cerebral blood flow (CBF) and compromised neurologic function (2,4-7). Despite their distinct etiologies, a common microvascular mechanism contributes to the reduced cerebral perfusion observed in experimental HF and SAH: an increase in cerebral artery myogenic reactivity, and hence, resistance to blood flow (5,6,8).

At the molecular level, both pathologies induce robust tumor necrosis factor (TNF) expression within the cerebral artery wall; this smooth muscle cell–localized TNF acts by an autocrine and/or paracrine mechanism to increase the bioavailability of sphingosine-1-phosphate (S1P), a pro-constrictive mediator that augments myogenic reactivity (4,6,8). Specifically, TNF signaling in cerebral arteries stimulates S1P production and concomitantly downregulates a critical negative regulator of S1P signaling, the cystic fibrosis transmembrane conductance regulator (CFTR) (8-10). CFTR acts as a negative regulator, because it sequesters S1P from its receptors and transports it across the plasma membrane for intracellular degradation (8). Therefore, reduced CFTR activity increases S1P bioavailability and represents a key component of the pathological augmentation of cerebral artery myogenic tone in HF and SAH (4,6,8).

SEE PAGE 959

Antagonizing TNF signaling with etanercept successfully abolishes the pathological augmentation of cerebrovascular vasoconstriction in HF and SAH, and thus, improves cerebral perfusion (4,6,8). This intervention also reduces neuronal injury and improves neuro-functional outcome (5,6), which strongly suggests that cerebral hypoperfusion contributes to the neurologic injury observed in these 2 models. However, as a clinical intervention, etanercept carries significant adverse effect risks stemming from immunosuppression (11) and potential effects on blood pressure control (12).

Based on our previous observations that 1) cerebral artery CFTR expression is reduced in HF and SAH (6,8); and 2) antagonizing TNF signaling in these pathologies normalizes CFTR expression concomitantly with vascular reactivity (6,8), we propose that CFTR represents a good therapeutic target for improving perturbed microvascular reactivity in HF and SAH and hence, CBF and cognitive decline. Food and Drug Administration–approved medications that increase CFTR expression and/or activity are available (13), and they are not generally associated with adverse side effects.

METHODS

The present investigation acquired the CFTR corrector therapeutic "C18" and the anti-human CFTR antibody (designated "596") through the Cystic Fibrosis Foundation Therapeutics Chemical and Antibody Distribution Programs. All other reagents used in this investigation are commercially available and are listed in the Supplemental Appendix.

ANIMALS. The Institutional Animal Care and Use Committees at the University of Toronto and the University Health Network approved all animal care and experimental protocols. Commercially available male wild-type mice (2 to 3 months; C57BL/6N) were purchased from Charles River Laboratories (Montreal, Quebec, Canada). Male mice homozygous for the ΔF508 CFTR mutation ($CFTR^{tm1EUR}$; designated "ΔF508" in the present study) (14), CFTR gene deletion ($CFTR^{tm1Unc}$; designated $CFTR^{-/-}$) and the complimentary wild-type control littermates were obtained from an established colony at the Hospital for Sick Children (Toronto, Ontario, Canada) (all $CFTR^{-/-}$, $CFTR^{\Delta F508}$, and wild-type littermates are mixed strains). Phenotype details for these CFTR mutant mice can be found in the Supplemental Appendix. All mice were housed under a standard 14 h/10 h light–dark cycle, fed normal chow, and had access to water *ad libitum*.

MYOCARDIAL INFARCTION. HF was induced by surgical ligation of the left anterior descending coronary artery (4). Briefly, mice were anesthetized with isoflurane, intubated with a 20-gauge angiocatheter, and ventilated with room air. Under sterile conditions, the thorax and pericardium were opened, and the left anterior descending coronary artery was permanently ligated with 7-0 silk suture (Deknatel; Fall River, Massachusetts). In sham-operated control mice, the thorax and pericardium were opened, but the left anterior descending coronary artery was not ligated. Following the procedure, the chest was

closed, and the mice were extubated upon spontaneous respiration. All experimental measurements in the HF model were conducted at or after 6 weeks post-infarction. Our previous work demonstrated that the cardiac injury is stable after 6 weeks, and thus, treatments do not alter and/or improve cardiac function (4). This allowed us to unambiguously attribute improvements in CBF in this model to a cerebrovascular mechanism.

INDUCTION OF SAH. We used a well-characterized model of experimental SAH (6). Briefly, each mouse was anesthetized (isoflurane), and its head was fixed in a stereotactic frame; a 7-mm incision was made along the midline of the anterior scalp and a 0.9-mm hole drilled into the skull 4.5-mm anterior to the bregma. A spinal needle was advanced to the chiasmatic cistern; 80 μl of arterial blood was injected into the intracranial space over 10 s. The injected blood was obtained from a separate wild-type donor mouse (via cardiac puncture) immediately before injection and did not contain anticoagulants. Following injection, the scalp incision was closed. Buprenorphine (0.05 mg/kg; 0.5 to 1.0 ml volume) was administered twice a day for 2 days (initiated immediately following the SAH surgical procedure). Sham-operated animals underwent an identical surgical procedure, with sterile saline injected instead of blood. All experimental measurements in the SAH model were conducted at 2 days post-SAH induction. Our previous work demonstrated that SAH maximally augments myogenic tone at this time point; reductions in CBF, neuronal injury, and compromised neurologic function are also evident at this time (6).

ISOLATION AND FUNCTIONAL ASSESSMENT OF RESISTANCE ARTERIES. Mouse olfactory (a first branch of the anterior cerebral artery) and posterior cerebral arteries (PCAs) were carefully dissected, cannulated onto micropipettes, stretched to their in vivo lengths, and pressurized to 45 mm Hg, as previously described (4,6). Mouse skeletal muscle resistance arteries were dissected from the cremaster muscle, cannulated, and pressurized to 60 mm Hg. All functional experiments were conducted in 3-morpholinopropanesulfonic acid (MOPS) buffered saline at 37°C with no perfusion. Vasomotor responses to phenylephrine (5 μmol/l for PCAs, 10 μmol/l for cremaster skeletal muscle arteries) provided an assessment of vessel viability at the beginning and end of each experiment. Arteries that failed to show ≥25% constriction to phenylephrine were excluded.

Myogenic responses were elicited by stepwise 20 mm Hg increases in transmural pressure from 20 to 80 mm Hg (olfactory arteries) or 100 mm Hg (PCAs and cremaster skeletal muscle resistance arteries). At each pressure step, vessel diameter (dia_{active}) was measured once a steady state was reached (5 min). Vessels that required treatment [e.g., $CFTR_{(inh)}$-172] were incubated with the reagent in MOPS for 30 min, and myogenic responses were then assessed in the presence of that reagent. Following completion of all dia_{active} measurements, MOPS buffer was replaced with a calcium-free version and maximal passive diameter (dia_{max}) was recorded at each pressure step.

Myogenic tone was calculated as the percent constriction in relation to the maximal diameter at each respective transmural pressure: tone (% of dia_{max}) = $[(dia_{max} - dia_{active})/dia_{max}] \times 100$, where dia_{active} was the vessel diameter in MOPS containing calcium and dia_{max} was the diameter in calcium-free MOPS. Analyses of vasomotor responses to phenylephrine used the same calculation, only in this case, dia_{active} represented the vessel diameter at steady state following application of the given agent and dia_{max} represented the maximal diameter measured under calcium-free conditions.

GLOBAL HEMODYNAMIC PARAMETERS. Echocardiographic measurements were collected with a 30-MHz mechanical sector transducer (Vevo 770; Visual Sonics, Toronto, Ontario, Canada) in conjunction with the mean arterial pressure (MAP) measurements (SPR-671 micro-tip mouse pressure catheter; Millar Inc., Houston, Texas) as previously described (4,8). Measurements and calculations are described in the Supplemental Appendix.

MAGNETIC RESONANCE IMAGING–BASED CEREBRAL BLOOD FLOW MEASUREMENTS. We used a noninvasive cardiac magnetic resonance imaging (MRI) approach (Flow-sensitive Alternating Inversion Recovery [FAIR] technique) to evaluate cerebral perfusion, as previously described (6). Briefly, the FAIR technique isolates perfusion as an accelerated T_1 signal relaxation. MRI signals (Biospec 70/30 USR; Bruker Corporation, Ettlingen, Germany) were acquired from vertical sections of the fore-, mid-, and hind-brain, which correspond to the anterior, mixed, and posterior circulations. FAIR images were evaluated for designated regions of interest (region placement is displayed in Supplemental Figure 1) using standardized algorithms and image processing procedures (MIPAV; National Institutes of Health [NIH], Bethesda, Maryland; http://mipav.cit.nih.gov). The procedures are described in detail in the Supplemental Appendix.

FIGURE 1 CBF Is Reduced in CFTRΔF508 Mice

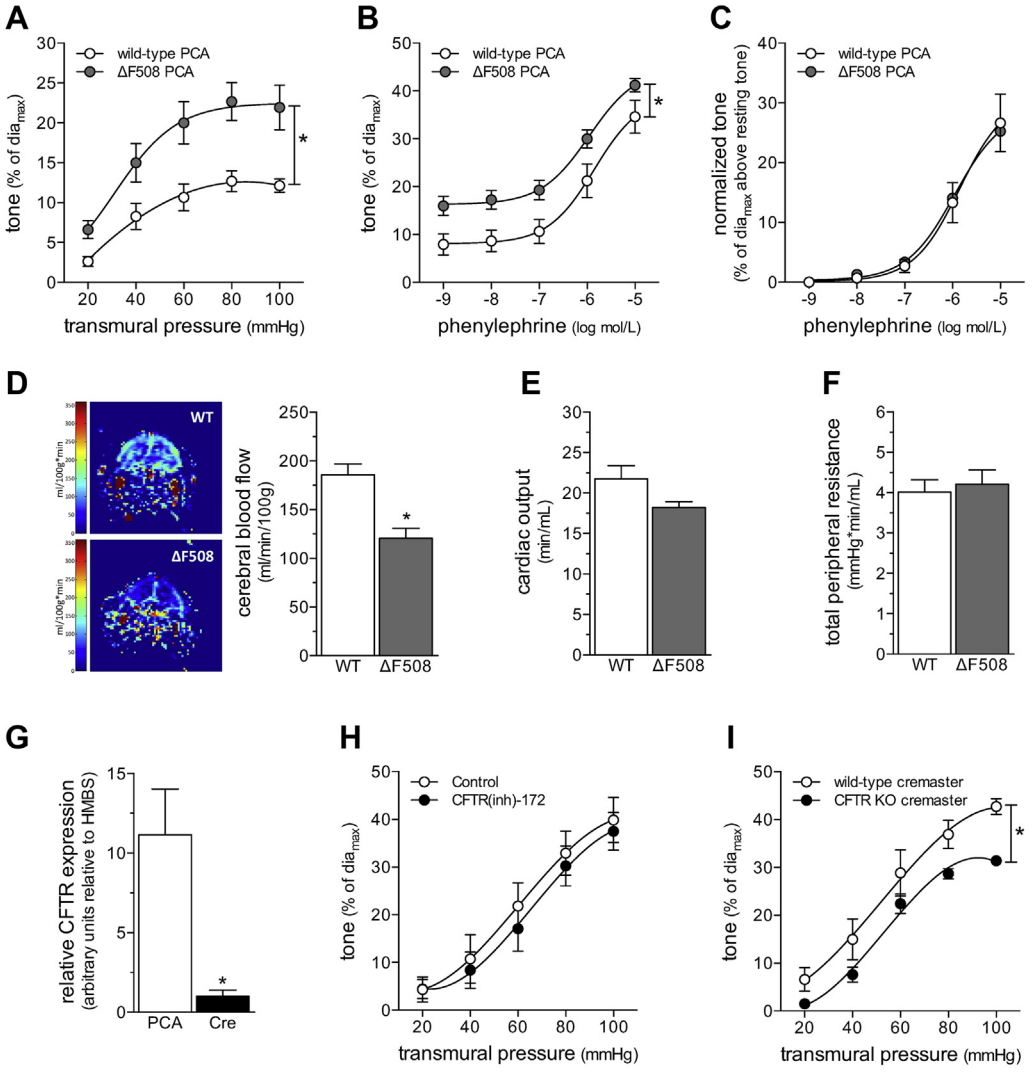

(A) Myogenic vasoconstriction is stronger in posterior cerebral arteries (PCAs) isolated from cystic fibrosis transmembrane conductance regulator (CFTR) ΔF508 mutant mice, relative to wild-type (WT) littermate control mice. **(B)** PCAs isolated from $CFTR^{\Delta F508}$ mice display an upward shift in their phenylephrine dose–response relationship. **(C)** However, once the phenylephrine responses are normalized to basal tone ($tone_{active} - tone_{rest}$, where $tone_{active}$ is the tone at given phenylephrine concentration and $tone_{rest}$ is the tone immediately before stimulation), the WT and $CFTR^{\Delta F508}$ phenylephrine dose–response relationships are virtually identical. Mean maximal vessel diameters at 45 mm Hg (dia_{max}) are: $CFTR^{\Delta F508}$: 186 ± 2 μm; n = 6 from 4 mice, and WT: 169 ± 8 μm; n = 5 from 3 mice (*t*-test: p = NS for dia_{max}). **(D)** Magnetic resonance imaging was used to measure cerebral blood flow in predefined forebrain cortical regions. Representative perfusion maps from WT and $CFTR^{\Delta F508}$ mouse forebrains are shown. Cerebral blood flow (CBF) is significantly lower in $CFTR^{\Delta F508}$ mice (n = 10), relative to WT littermates (n = 11); however, neither **(E)** cardiac output (n = 5 for both groups) nor **(F)** total peripheral resistance (n = 5 for both groups) differed between the 2 genotypes. **(G)** In WT mice, CFTR mRNA expression is significantly higher in PCAs (n = 5), relative to cremaster skeletal muscle arteries (Cre) (n = 6). **(H)** Cre myogenic tone is not altered by CFTR inhibition in vitro (100 nmol/l $CFTR_{(inh)}$-172 for 30 min). **(I)** However, CFTR gene deletion (CFTR KO) induces a modest, but significant attenuation of myogenic tone. Mean maximal vessel diameters at 60 mm Hg (dia_{max}) are **(G)** WT: 72 ± 3 μm, n = 5 from 4 mice; **(H)** CFTR knock out (KO): 88 ± 4 μm, n = 6 from 4 mice; and **(H)** WT littermates: 78 ± 4 μm, n = 5 from 2 mice. All data are mean ± SEM. In **(A to C, H, and I)**, *p < 0.05 for unpaired comparisons with a 2-way analysis of variance; in **(D to G)**, *p < 0.05 for unpaired comparisons with a *t*-test.

FIGURE 2 **C18 increases WT CFTR Protein Expression and Function by a Proteostatic Mechanism**

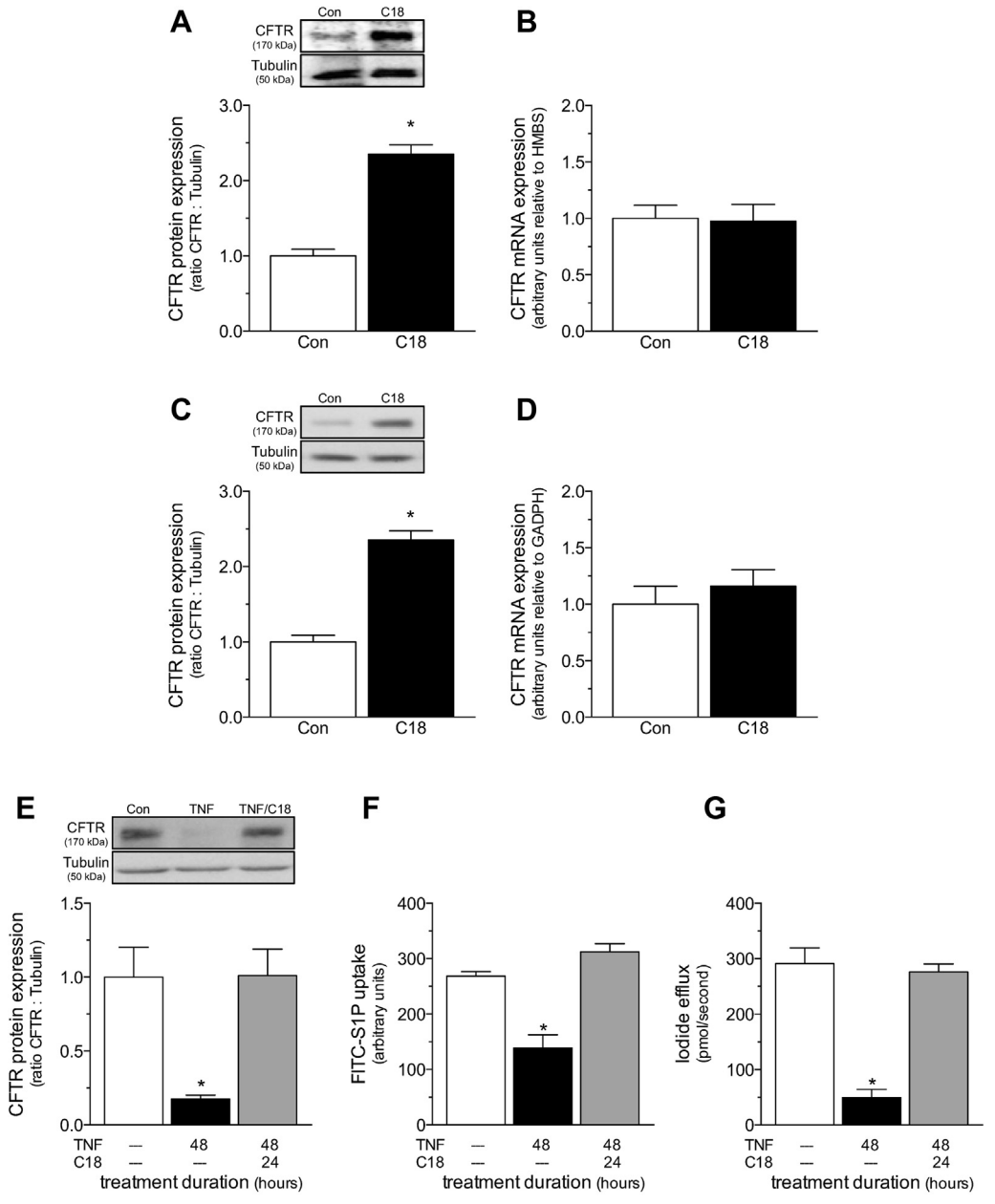

(A) Cerebral arteries isolated from naïve mice treated with C18 (3 mg/kg intraperitoneally daily for 2 days; n = 5) have higher CFTR protein expression than arteries collected from vehicle control (Con) mice (n = 5). **(B)** C18 does not influence cerebral artery CFTR mRNA expression (Con: n = 6; C18: n = 5). **(C)** C18 (6 μmol/l; 24 h) increases CFTR protein expression in baby hamster kidney fibroblast cells stably expressing human CFTR (n = 12 for both groups). **(D)** C18 does not influence CFTR mRNA expression in this system (n = 6 for both groups). **(E)** Tumor necrosis factor (TNF) (10 ng/ml for 48 h) downregulates CFTR protein expression in mesenteric artery primary vascular smooth muscle cells (Con: n = 8; TNF: n = 8); co-incubating TNF with C18 (6 μmol/l; 24 h) following 24 h TNF incubation (i.e., 48 h TNF + 24 h C18) fully restores CFTR protein expression (n = 7). The restoration of CFTR protein expression in vascular smooth muscle cells correlates with the normalization of attenuated **(F)** Fluorescein isothiocyanate-labeled sphingosine-1-phosphate (FITC-S1P) uptake (measured as an increase in fluorescence intensity at 525 nm by a standard fluorescence-activated cell sorting analysis technique; Con: n = 7; TNF: n = 10; TNF+C18: n = 6) and **(G)** forskolin-stimulated iodide efflux (Con: n = 7; TNF: n = 6; TNF+C18: n = 6). All data are mean ± SEM. In **(A to D)**, *p < 0.05 for an unpaired comparison with a *t*-test; in **(E to G)**, *p < 0.05 for unpaired comparisons to the Con mice with a 1-way analysis of variance and Tukey's post hoc test. Other abbreviation as in Figure 1.

FIGURE 3 C18 Restores Cerebral Perfusion in HF

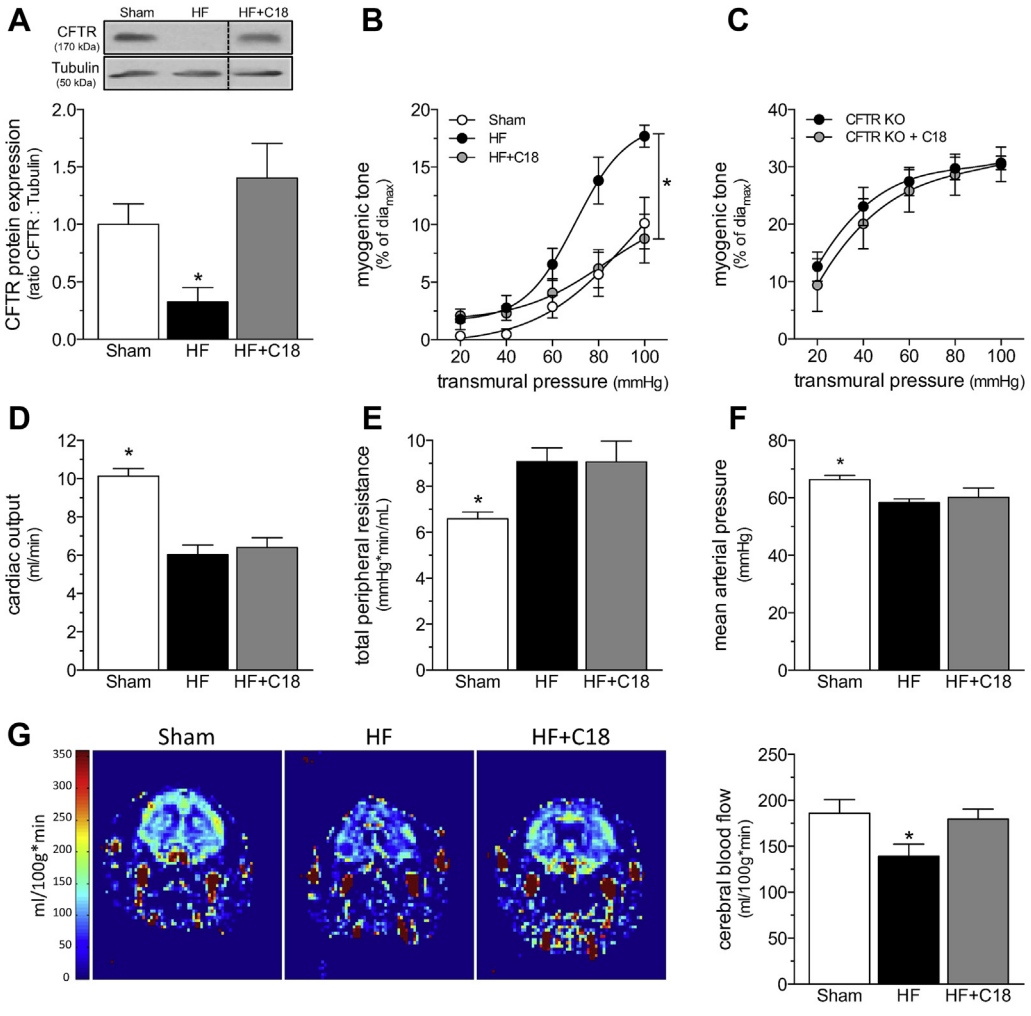

(A) Cerebral arteries isolated from mice with HF (6 weeks post-left anterior descending coronary artery ligation) have reduced CFTR protein expression (n = 5) relative to arteries isolated from sham-operated controls (n = 6). C18 treatment in vivo (3 mg/kg intraperitoneally daily for 2 days) eliminates this reduction in cerebral artery CFTR protein expression (n = 8). **(B)** C18 treatment in vivo reduces myogenic tone in PCAs isolated from HF mice, an effect **(C)** not observed in PCAs isolated from CFTR KO mice. Mean maximal vessel diameters at 45 mm Hg (dia_{max}) are sham: 146 ± 9 μm; n = 5 from 3 mice; HF: 149 ± 8 μm; n = 6 from 4 mice; HF+C18: 155 ± 8 μm; n = 8 from 6 mice (1-way analysis of variance: p = NS); and CFTR KO: 142 ± 5 μm; n = 6 from 3 mice; CFTR KO+C18: 145 ± 5 μm; n = 6 from 3 mice (Student's *t*-test: p = NS). Relative to sham-operated control mice, mice with HF have **(D)** reduced cardiac output (sham: n = 6; HF: n = 8; HF+C18: n = 8), **(E)** elevated total peripheral resistance (n = 6 for all groups), and **(F)** reduced mean arterial pressure (n = 6 for all groups); C18 treatment did not affect these parameters in mice with HF. **(G)** Representative magnetic resonance perfusion maps that were used to determine forebrain cortical cerebral blood flow. HF stimulated a reduction in cerebral perfusion, and C18 treatment significantly improved cerebral perfusion in mice with HF (sham: n = 6; HF: n = 8; HF+C18: n = 8). All data are mean ± SEM. For **(A and G)**, *p < 0.05 for unpaired comparisons to the sham with a 1-way analysis of variance and Dunnett's post hoc test; for **(B)**, *p < 0.05 for unpaired comparisons to sham with a 2-way analysis of variance and Tukey's post hoc test; in **(C)**, groups were statistically compared with a 2-way analysis of variance (p = NS); and in **(D to F)**, *p < 0.05 for unpaired comparisons to HF with a 1-way analysis of variance and Dunnett's post hoc test. All samples in the representative Western blot image displayed in **(A)** originated from the same film, but the HF+C18 sample was not adjacently positioned on this film, as shown in this Figure. Abbreviations as in Figures 1 and 3.

MRI-BASED EDEMA MEASUREMENT. Edema was assessed by quantitative T_2 mapping (15), using a 7-T micro-MRI system (Biospec 70/30 USR; Bruker Corporation). The T_2 mapping acquisition generated quantitative T_2 maps in 9 contiguous 2-dimensional axial slices, with 1 mm thickness, covering the volume from the fore-brain through to the hind-brain. T_2 maps were generated from

FIGURE 4 **C18 Does Not Induce Cerebral Edema**

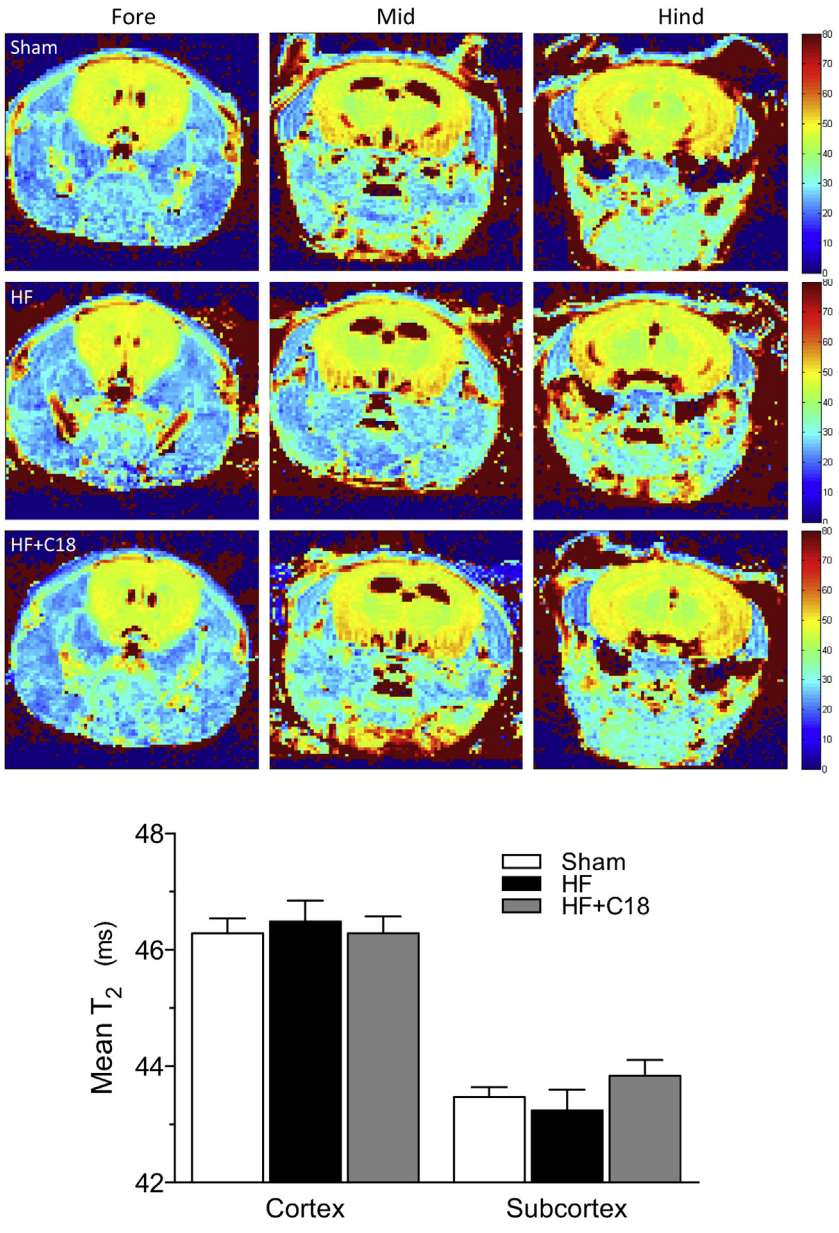

Representative quantitative T_2 maps that assess brain water content as T_2 relaxation times in magnetic resonance images. A total of 9 T_2 maps were assessed per mouse, which cover the fore-, mid-, and hind-brain regions. The representative images display slices from the **(left)** fore-, **(center)** mid-, and **(right)** hind-brain regions of **(top)** sham, **(middle)** HF, and **(bottom)** C18-treated (3 mg/kg intraperitoneally daily for 2 days) HF mice. Neither HF nor C18 treatment in HF mice induced an alteration in the T_2 relaxation times in any region of interest within any of the slices assessed. The data were therefore pooled to yield a mean T_2 relaxation time for the cortical and subcortical region and graphically presented (sham: n = 7; HF: n = 7; HF+C18: n = 6). All data are mean ± SEM. Groups were statistically compared with a 1-way analysis of variance test (p = NS among the sham, HF, and HF+C18 groups in the cortical and subcortical regions, respectively). Abbreviations as in Figure 1.

T_2-weighted images at echo times from 12 to 384 ms, using inline Bruker software, via linear regression of the logarithmically transformed signal magnitudes and the echo times on a per voxel basis. The T_2 values were extracted using MIPAV software, using manually drawn regions of interest placed within the fore-, middle- and hind-brain T_2 maps.

FIGURE 5 C18 Improves Neuronal Morphology and Neuronal Function in HF

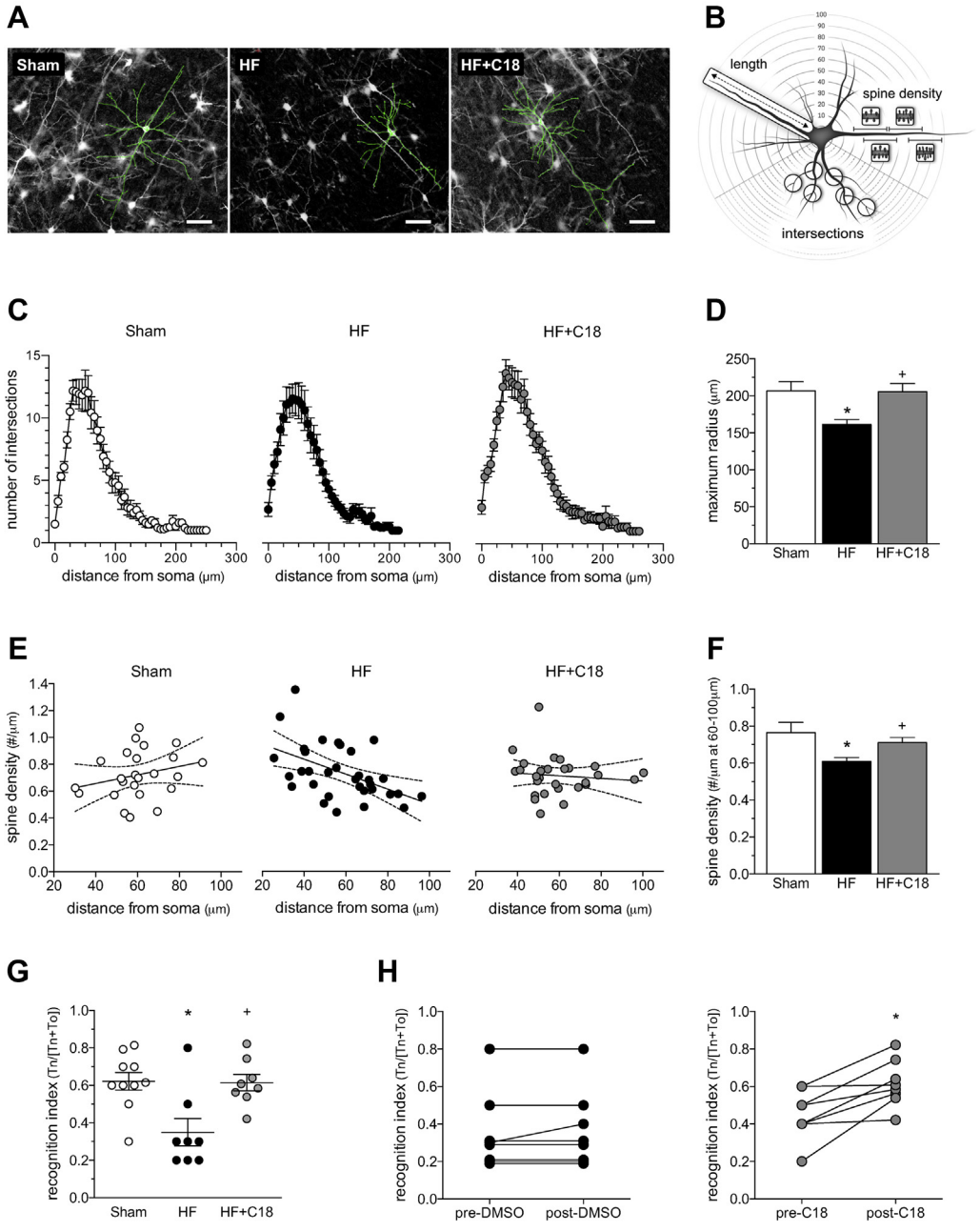

Continued on the next page

CELL CULTURE AND MOLECULAR AND/OR BIOCHEMICAL ASSESSMENTS. We previously described the mesenteric artery smooth muscle and baby hamster kidney fibroblast cell systems and their culture conditions (8,16). Standard procedures were used for Western blots, real-time polymerase chain reaction, Fluorescein isothiocyanate labeled S1P (FITC-S1P) uptake, and iodide efflux measurements (6,8,16). Specific details are provided in the Supplemental Appendix.

FLUORESCENT IMMUNOHISTOCHEMISTRY AND FLUORO-JADE STAINING. Brains were cleared of blood and fixed via aortic perfusion with 4% paraformaldehyde; the brains were then dissected, and

coronal sections 1 mm posterior to the bregma were cut. We used standard procedures to prepare slides with 5-μm-thick cryostat slices and to complete the assessments of cleaved caspase-3 and Fluoro-Jade staining (6). Caspase-3 and Fluoro-Jade–positive cells were counted in the cortical region of coronal sections that included the left and right temporal and parietal lobes at 200× magnification (1 slice assessed per mouse). The procedures are described in detail in the Supplemental Appendix.

HISTOLOGICAL ANALYSIS OF DENDRITE MORPHOLOGY. Brains were cleared of blood and processed with a commercially available Rapid GolgiStain kit (FD NeuroTechnologies Inc.; Columbia, Maryland, USA), as previously described (5). Neurons and their dendritic networks were imaged using stereology-based NIS Elements AR software (Nikon Instruments Europe; Amsterdam, the Netherlands) and analyzed using Image J (NIH). The dendrite networks of single cortical pyramidal neurons from the frontal cortex were identified and digitally isolated from hyperstack images using the semi-automated Simple Neurite Tracer plugin for Image J; the traced images were subsequently analyzed by Sholl analysis (https://imagej.net/Sholl_Analysis, version 3.7.4). The procedures are described in greater detail in the Supplemental Appendix.

NEUROLOGIC FUNCTION IN SAH MICE. Neurologic function was assessed using the modified Garcia score, as previously described (6). The neurologic assessment consists of 6 domains: spontaneous activity, spontaneous movement of all 4 limbs, forepaw outstretching, climbing, body proprioception, and response to vibrissae touch. Two blinded observers conducted the neurologic assessment 2 days after SAH. The maximum score is 18, indicative of normal neurologic function.

COGNITIVE FUNCTION IN HF MICE. We used a well-established novel object recognition task to evaluate rhino-cortical nonspatial memory, as previously described (5,17). Briefly, habituated mice were exposed to 2 identical objects for 5 min. After a 5-min delay, 1 of the original objects was replaced with a novel object, and the mice were retested. The mice were video-tracked with AnyMaze software (Stoelting; Dublin, Ireland) that recorded the time spent interacting with the novel (Tn) and original (To) objects. A recognition index was calculated as the time spent interacting with the novel object versus the total time spent interacting with either object (Tn/[Tn+To]). The objects and arena were thoroughly cleaned with 70% ethanol between each test, to eliminate potential odor cues.

STATISTICAL ANALYSIS. All data are expressed as means ± SEM, where n is the number of independent measures (i.e., samples, vessels assessments, or experimental subjects). Data were statistically analyzed using Graphpad Prism 6 software (San Diego, California). For statistical comparisons, a Student's *t*-test was used for the comparison of 2 independent groups. For comparison of multiple independent groups, 1-way analysis of variance was used, followed by a Tukey's or Dunnett's post hoc test, as appropriate. For the assessment of myogenic responses and dose–response relationships, data were analyzed with a 2-way analysis of variance, followed by a Tukey's post hoc test. Differences were considered significant at $p < 0.05$. All histological and

FIGURE 5 Continued

(A) Representative images of Golgi-stained pyramidal neurons from sham mice, mice with heart failure (HF), and C18-treated HF mice (3 mg/kg intraperitoneally daily for 2 weeks; treatment initiated at 10 weeks post-infarction). The morphology of both the basal and apical dendrites is highlighted with traces superimposed onto the images. **(B)** The images displayed in **(A)** are quantitatively assessed by Sholl analysis, which characterizes the dendritic network at 5-μm intervals to a maximal radius of 300 μm away from soma. **(C)** Sholl analysis histograms plotting the number of dendrite intersections (i.e., dendritic branching) versus dendrite length (i.e., distance from neuronal soma) show no differences in branching morphology across the sham (n = 12 neurons from N = 4 mice), HF (n = 12; N = 4), and HF+C18 (n = 11; N = 4) groups. However, dendritic length is shorter in HF mice, relative to the sham and HF+C18 groups. Accordingly, **(D)** the mean dendrite length (i.e., maximum radius) is significantly reduced in HF mice relative to sham mice, an effect that is normalized by C18 treatment. **(E)** In sham mice (n = 11; N = 4), the spine density of basal dendrites is relatively consistent over the length of the dendrite, yielding a slope that is not statistically different from zero. In HF mice (n = 13; N = 4), a statistically significant ($p < 0.05$) negative slope is observed, indicating a loss of spine density within the distal regions of the dendrite; HF mice treated with C18 (n = 12; N = 4) do not possess the negative slope observed for HF mice. Consequently, **(F)** mean basal dendrite spine density 60 to 100 μm from soma is significantly reduced in HF mice relative to sham controls; this morphological difference is normalized by C18 treatment. **(G)** Relative to sham mice (N = 10), HF (N = 8) attenuates rhino-cortical–dependent, short-term retention of object familiarity in a nonspatial novel object recognition task, with a 5-min delay interval; the attenuation is not present in C18-treated HF mice (N = 8). **(H)** Longitudinal pre-/post-treatment analyses of the same vehicle- and C18- treated HF mice confirm a statistically significant C18 treatment effect on rhino-cortical, short-term retention memory. In **(D, F, and G),** *$p < 0.05$ for unpaired comparisons to the sham and +$p < 0.05$ for an unpaired comparison between the HF and HF+C18 groups with a 1-way analysis of variance and Tukey's post hoc test. In **(H)** *$p < 0.05$ for a comparison with a paired *t*-test. Tn = time spent interacting with novel object; To = time spent interacting with original object.

neurological/cognitive function data were collected under blinded conditions; all other data presented in this study did not require blinding and were not collected under blinded conditions.

RESULTS

DEFICIENT CFTR FUNCTION DRIVES REDUCED CEREBRAL PERFUSION. Our previous work demonstrated that CFTR prominently regulates cerebral artery myogenic tone and identified a strong correlation between cerebral artery CFTR protein expression and cerebral perfusion (6,8). Therefore, our mechanistic concept proposes that correcting deficient cerebrovascular CFTR activity (i.e., reduced S1P transport due to decreased CFTR expression at the cell surface) is a viable therapeutic strategy for normalizing compromised cerebral myogenic responsiveness, and hence, CBF (8).

To establish the causative link between cerebral artery CFTR activity and cerebral perfusion, we used CFTR mutant mice (described in detail in the Supplemental Appendix). Although CFTR mutant mice are smaller in size and have a strong propensity for bowel obstruction, they possess a relatively mild cystic fibrosis phenotype compared with humans: most organs, including the lower respiratory tract, appear histologically normal in the absence of challenge (18,19). Nevertheless, CFTR mutant mice in general, and $CFTR^{-/-}$ mice in particular, are known to adversely react to stress (18). In our hands, $CFTR^{-/-}$ mice were extremely sensitive to experimental stressors, which did not permit accurate and reproducible echocardiography and/or CBF measurements. $CFTR^{\Delta F508}$ mice, which have minimal cell surface CFTR expression and activity (14), were more stable. This underpinned our strategic decision to use $CFTR^{\Delta F508}$ mice for relating cerebral artery myogenic tone to hemodynamic parameters in a loss of function phenotype.

We assessed vasomotor reactivity in PCAs to directly compare the $CFTR^{\Delta F508}$ phenotype to our previously published characterization of PCA responses from CFTR knockout mice (8). As expected, PCAs from $CFTR^{\Delta F508}$ mice displayed augmented myogenic tone, relative to wild-type littermates (**Figure 1A**); the magnitude of the augmentation was qualitatively similar to that found for $CFTR^{-/-}$ mice (8). Phenylephrine responses displayed an upward shift due to the enhanced myogenic tone (**Figure 1B**); however, the EC_{50} values were not different (log EC_{50} wild type: -5.83 ± 0.21; $n = 5$ from 3 mice; log EC_{50} $CFTR^{\Delta F508}$: -6.00 ± 0.04; $n = 6$ from 4 mice; Student's *t*-test: $p = NS$), and the difference between the curves was eliminated by correcting for the difference in basal tone (i.e., myogenic tone at 45 mm Hg) (**Figure 1C**). Therefore, the ΔF508 mutation augmented myogenic responsiveness, but did not alter general contractility. CBF was significantly lower in $CFTR^{\Delta F508}$ mice (**Figure 1D**); however, neither cardiac output (**Figure 1E**) nor total peripheral resistance (TPR) (**Figure 1F**) were affected by the mutation (additional hemodynamic parameters are listed in Supplemental Table 1). Based on these observations, the cerebral perfusion deficit was clearly vascular in origin.

The $CFTR^{\Delta F508}$ mutation did not change TPR, indicating that not all vascular beds were subject to CFTR-dependent regulation. Because TPR is primarily generated and regulated by skeletal muscle resistance arteries (20), we assessed whether CFTR influenced myogenic tone in mouse cremaster skeletal muscle resistance arteries. CFTR mRNA expression was approximately 10-fold lower in wild-type mouse cremaster skeletal muscle resistance arteries, relative to cerebral arteries (**Figure 1G**). Inhibiting CFTR activity in vitro (100 nmol/; $CFTR_{(inh)}$-172, 30 min) did not affect wild-type cremaster artery myogenic tone (**Figure 1H**), which was in contrast to our recent observations that $CFTR_{(inh)}$-172 augmented olfactory cerebral artery myogenic tone (6). Unlike PCAs (8), CFTR gene deletion did not augment myogenic tone in cremaster skeletal muscle resistance arteries (**Figure 1I**); myogenic tone was mildly attenuated and corresponded to lower MAP (Supplemental Figure 2). Phenylephrine dose–response relationships were not altered by either CFTR inhibition in vitro or CFTR gene deletion (Supplemental Figure 3).

In summary, our $CFTR^{\Delta F508}$ experiments established: 1) a causative link between CFTR expression, PCA myogenic responsiveness, and CBF; 2) that CFTR modulates myogenic tone in specific vascular beds; and 3) that CFTR does not modulate skeletal muscle resistance artery tone, which was notable, because these arteries prominently contribute to TPR. Because HF and SAH downregulate cerebral artery CFTR expression concomitant with microvascular dysfunction (6,8), these data provide a strong mechanistic foundation for using CFTR-modulating medications to specifically correct cerebrovascular dysfunction and CBF deficits in this pathological setting.

C18 INCREASES CFTR ACTIVITY FOLLOWING TNF-DEPENDENT DOWN-REGULATION. Current CFTR-modulating medications, identified via high-throughput drug screens, are experimentally and clinically used to mitigate the effects of cystic fibrosis. CFTR therapeutics are broadly segregated

FIGURE 6 C18 Restores Cerebral Perfusion In SAH

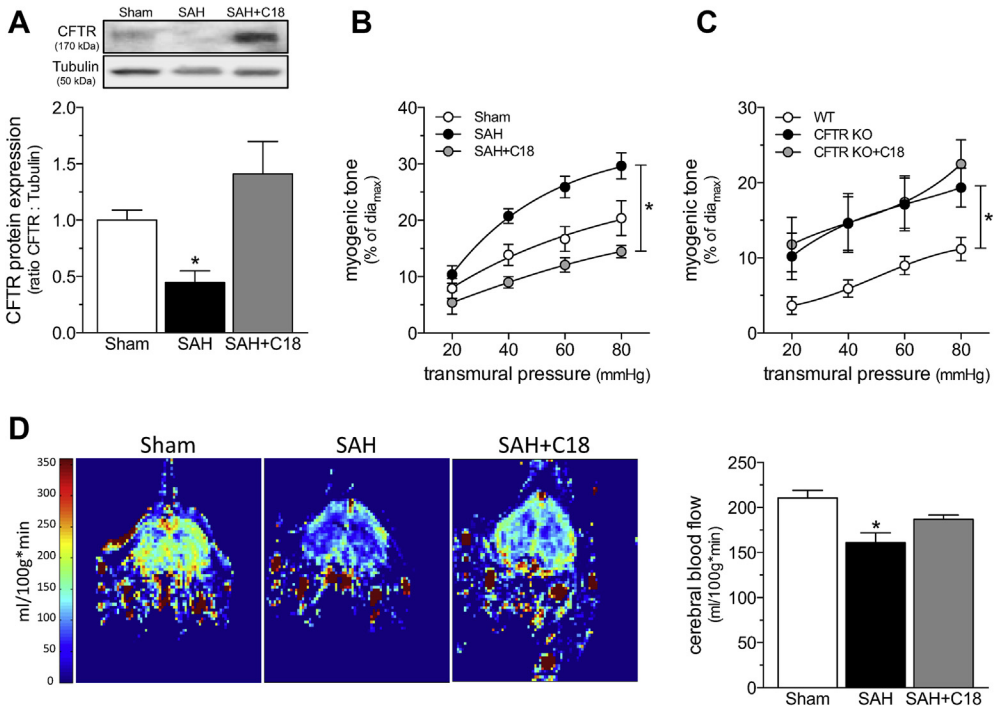

(A) Cerebral arteries isolated from mice with SAH (2 days post-SAH induction) have reduced CFTR protein expression (n = 6), relative to arteries isolated from sham-operated controls (n = 6). C18 treatment in vivo (3 mg/kg intraperitoneally daily for 2 days) eliminated this reduction in artery CFTR protein expression (n = 6). **(B)** C18 treatment in vivo reduced myogenic tone in olfactory arteries isolated from mice with SAH, an effect **(C)** not observed in olfactory arteries isolated from CFTR KO mice. Mean maximal vessel diameters at 45 mmHg (dia_{max}) are sham: 113 ± 3 μm; n = 5 from 3 mice; SAH: 109 ± 6 μm; n = 6 from 6 mice; SAH+C18:104 ± 12 μm; n = 5 from 4 mice (1-way analysis of variance: p = NS); and CFTR WT: 98 ± 6 μm; n = 8 from 4 mice; CFTR KO: 110 ± 8 μm; n = 5 from 4 mice; CFTR KO+C18: 96 ± 6 μm; n = 6 from 3 mice (1-way analysis of variance: p = NS). **(D)** Representative magnetic resonance perfusion maps that were used to determine forebrain cortical CBF. SAH stimulated a reduction in cerebral perfusion; C18 treatment significantly improved cerebral perfusion in mice with SAH (sham: n = 10; SAH: n = 5; SAH+C18: n = 9). All data are mean ± SEM. In **(A and D)**, *p < 0.05 for unpaired comparisons to the sham with a 1-way analysis of variance and Dunnett's post hoc test. In **(B)**, *p < 0.05 for unpaired comparisons to SAH with a 2-way analysis of variance and Tukey's post hoc test. In **(C)**, *p < 0.05 for unpaired comparisons to WT with a 2-way analysis of variance and Tukey's post hoc test. Abbreviations as in Figures 1, 3, and 4.

into 2 distinct classes: CFTR potentiators (which increase CFTR channel activity) and CFTR correctors (which increase CFTR cell surface expression). Because CFTR potentiators (e.g., ivacaftor) display limited efficacy when CFTR abundance is low, we selected a CFTR corrector for our intervention. In this regard, we used the experimental CFTR corrector C18 based on the previous demonstration that it directly interacts with and stabilizes wild-type CFTR, thereby increasing CFTR expression at the plasma membrane (21).

We first confirmed that C18 is capable of increasing both mouse and human CFTR expression. Cerebral arteries isolated from naïve mice injected with C18 (3 mg/kg intraperioneally daily for 2 days) displayed higher CFTR protein expression levels, relative to vehicle-treated control mice (Figure 2A); CFTR mRNA expression was not affected by C18 (Figure 2B). To confirm C18's effect on human CFTR, we used a heterologous expression system of baby hamster kidney fibroblast cells that stably expressed a human CFTR construct. C18 treatment (6 μmol/l; 24 h) more than doubled CFTR protein expression in baby hamster kidney fibroblast cells (Figure 2C), but had no effect on CFTR mRNA expression in this system (Figure 2D). Collectively, the data are consistent with previous observations that C18 exerts direct stabilizing effects on CFTR protein expression (21) and demonstrates its efficacy against both murine and human CFTR.

We next assessed whether C18 treatment increases CFTR abundance in a cell culture setting that modeled the relevant pathophysiological mechanisms and cellular environment. As we previously

FIGURE 7 Lum Increases WT CFTR Protein Expression by a Proteostatic Mechanism and Restores Cerebral Perfusion in SAH

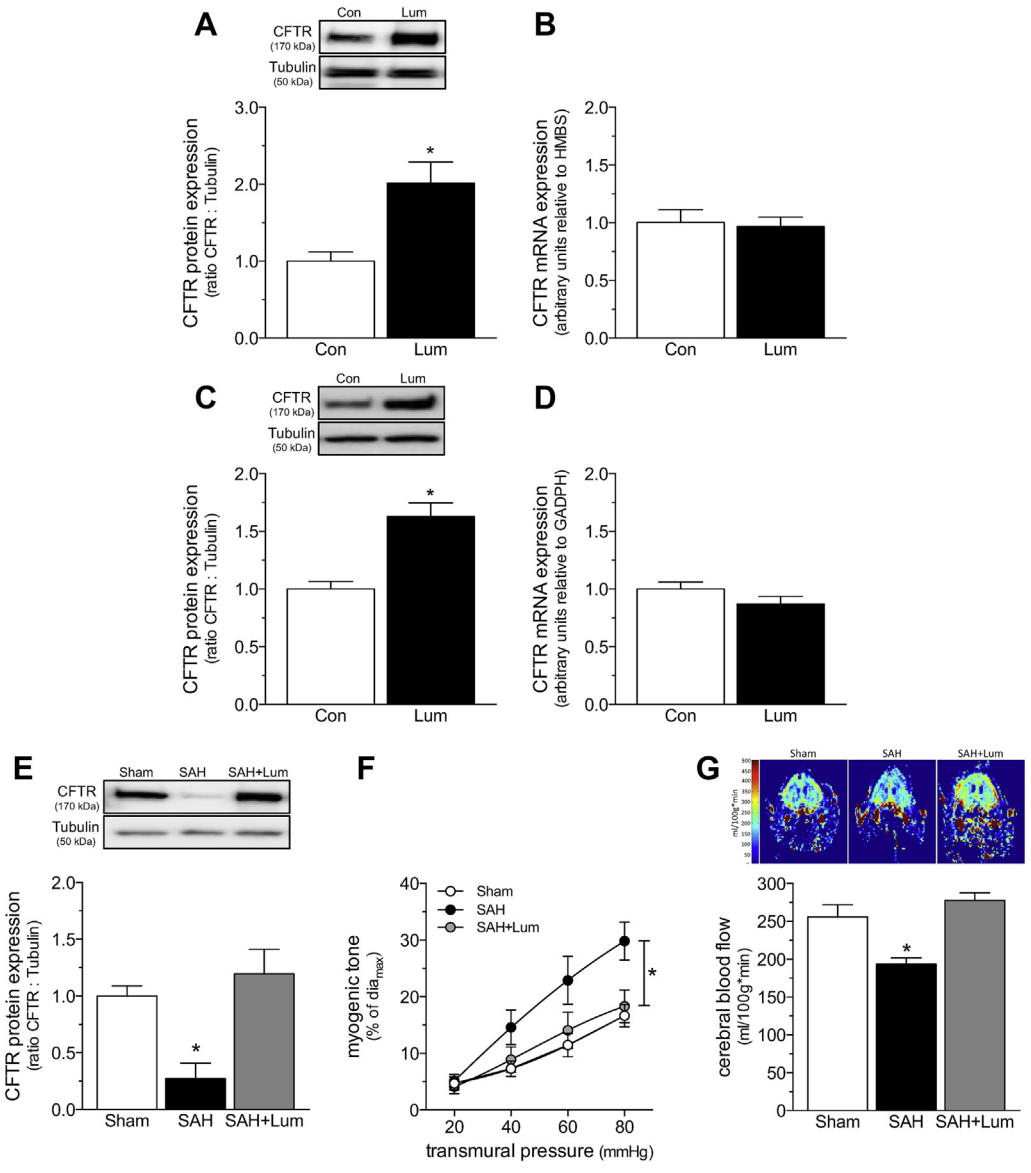

(A) Cerebral arteries isolated from naïve mice treated with Lum (3 mg/kg intraperitoneally daily for 2 days; n = 6) have higher CFTR protein expression than arteries collected from vehicle controls (n = 7). **(B)** Lum does not influence cerebral artery CFTR mRNA expression (n = 5 for both groups). **(C)** Lum (6 μmol/l; 24 h) increases CFTR protein expression in baby hamster kidney fibroblast cells stably expressing human CFTR (n = 13 for both groups). **(D)** Lum does not influence CFTR mRNA expression in this system (n = 6 for both groups). **(E)** Cerebral arteries isolated from mice with SAH (2 days post-SAH induction) have reduced CFTR protein expression (n = 5) relative to arteries isolated from sham-operated controls (n = 6). Lum treatment in vivo (3 mg/kg intraperitoneally daily for 2 days) eliminates this reduction in cerebral artery CFTR protein expression (n = 6). **(F)** Lum treatment in vivo reduces myogenic tone in olfactory arteries isolated from mice with SAH. Mean maximal vessel diameters at 45 mm Hg (dia_{max}) are sham: 91 ± 3 μm; n = 7 from 4 mice; SAH: 86 ± 2 μm; n = 6 from 3 mice; SAH+Lum: 87 ± 4 μm; n = 7 from 4 mice (1-way analysis of variance: p = NS). **(G)** Representative magnetic resonance perfusion maps that were used to determine CBF. SAH stimulated a reduction in cerebral perfusion; Lum treatment significantly improved cerebral perfusion in mice with SAH (sham: n = 6; SAH: n = 5; SAH+Lum: n = 6). All data are mean ± SEM. In **(A to D)**, * $p < 0.05$ for an unpaired comparison with a *t*-test; in **(E and G)**, *$p < 0.05$ for unpaired comparisons to sham with a 1-way analysis of variance test and Dunnett's post hoc test. In **(F)**, *$p < 0.05$ for unpaired comparisons to sham with a 2-way analysis of variance and Tukey's post hoc test. Abbreviations as Figures 1 to 3.

FIGURE 8 CFTR Correction Reduces Neuronal Injury in SAH

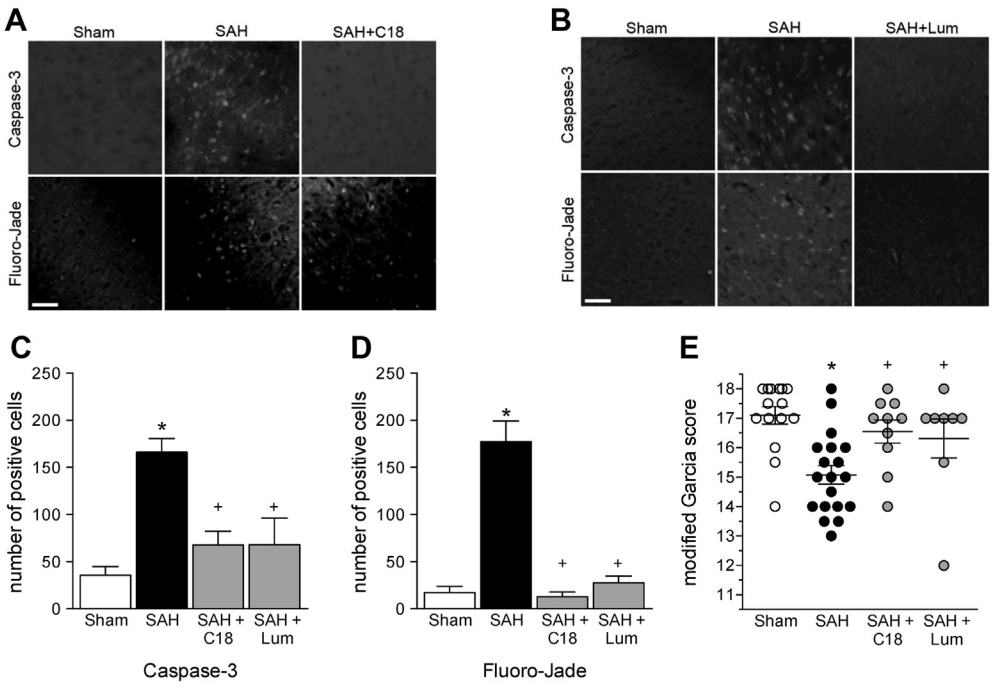

(Top) Representative images of cortical cells stained for cleaved caspase-3 expression and **(bottom)** with Fluoro-Jade for cohorts involving **(A)** C18 (3 mg/kg intraperitoneally daily for 2 days) and **(B)** lumacaftor (Lum) (3 mg/kg intraperitoneally daily for 2 days) treatment regimens. Subarachnoid hemorrhage (SAH) (n = 13 mice) increases the number of **(C)** caspase-3 and **(D)** Fluoro-Jade positive cells relative to sham-operated control mice (n = 12); both C18 (n = 6) and lumacaftor (n = 5) abolished the increase in caspase-3 and Fluoro-Jade staining. **(E)** Mice with SAH (n = 19) have a lower modified Garcia score (maximum score = 18; blinded assessments made 2 days post-SAH) compared with sham-operated mice (n = 15); both C18 (n = 10) and Lum (n = 8) treatment restored the neurological score to the sham level. All data are mean ± SEM; *p < 0.05 for unpaired comparisons to sham and +p < 0.05 compared with untreated SAH with a 1-way analysis of variance and Tukey's post hoc test.

demonstrated (8), TNF (10 ng/ml) reduced CFTR protein expression in primary vascular smooth muscle cells, and thus, simulated the TNF-dependent CFTR down-regulation observed in HF (8) and SAH (6) (**Figure 2E**). As expected, the decline in CFTR expression correlated with attenuated FITC-S1P uptake [i.e., a CFTR-dependent process (8)] (**Figure 2F**) and forskolin-stimulated iodide efflux [i.e., a classical measure of CFTR activity (16)] (**Figure 2G**). C18 treatment (6 μmol/l; 24 h co-incubation with 10 ng/ml TNF following 24-h incubation with 10 ng/ml TNF) reversed the decline in CFTR expression (**Figure 2E**) and fully restored FITC-S1P uptake (**Figure 2F**) and iodide efflux (**Figure 2G**). These results aligned with our prediction that under conditions in which CFTR is downregulated, C18's proteostatic effect increases total CFTR expression and restores its activity.

C18 TREATMENT RECTIFIES DEFICIENT CBF IN HF.

As previously documented by Meissner et al. (8), the induction of HF stimulated a significant reduction in cerebral artery CFTR protein expression (**Figure 3A**) that coincided with a marked augmentation in PCA myogenic tone (**Figure 3B**). As predicted by the data in **Figure 2**, C18 treatment in vivo (3 mg/kg intraperioneally daily for 2 days) restored CFTR expression in cerebral arteries isolated from mice with HF (**Figure 3A**) and concomitantly normalized PCA myogenic tone (**Figure 3B**). The attenuation of myogenic tone was associated with an expected shift in phenylephrine responsiveness, due to the reduction in basal tone; however, the EC_{50} values were not different (log EC_{50} sham: −6.30 ± 0.14; n = 6 from 4 mice; log EC_{50} HF: −6.25 ± 0.07; n = 5 from 3 mice; log EC_{50} HF+C18: −5.94 ± 0.21; n = 5 from 4 mice; 1-way analysis of variance: p = NS), and the curves overlapped after correction for the difference in basal tone (Supplemental Figure 4). C18 treatment did not affect PCA myogenic tone or phenylephrine responses in sham-operated mice (Supplemental Figure 5). Using PCAs isolated from CFTR knockout mice, we confirmed that C18 mediates its attenuating

effect on myogenic tone by targeting CFTR. As expected, PCAs from CFTR knockout mice displayed augmented myogenic tone that was not susceptible to in vivo C18 treatment (**Figure 3C**); phenylephrine responses were not affected by C18 treatment (Supplemental Figure 6).

At the systemic level, the induction of HF significantly reduced cardiac output relative to sham-operated control mice (**Figure 3D**; measured at 6 weeks post-infarction). TPR increased as a compensatory response (**Figure 3E**) to prevent a large reduction in MAP (**Figure 3F**) (4,8). Despite the relatively small reduction in MAP, CBF was markedly reduced (**Figure 3G**). C18 treatment in vivo restored CBF in mice with HF (**Figure 3G**), correlating to the normalization of PCA myogenic tone (**Figure 3B**). C18 did not ameliorate the cardiac injury induced by the left anterior descending coronary artery ligation procedure (Supplemental Table 2). Therefore, the improvement in CBF can be unambiguously attributed to a vascular mechanism. Furthermore, because C18 had no effect on TPR or MAP (**Figure 3**), the C18-mediated restoration of CBF had to be a localized microvascular effect that was independent of changes to systemic hemodynamic parameters. This therapeutic profile aligns well with our previously described etanercept intervention (4).

In addition to maintaining constant perfusion when systemic pressure fluctuates, the myogenic response also protects fragile capillary beds from damaging pressure levels (22) and maintains capillary hydrostatic pressure at levels that minimize edema formation (23). In this context, therapeutically reducing cerebral artery myogenic tone, even from the augmented level that occurs in HF, could potentially cause the counter-productive side effect of cerebral edema formation. Therefore, we used noninvasive imaging for edema to confirm that neither HF nor C18 treatment in the context of HF induced evident edema in any region of the brain (**Figure 4**).

C18 TREATMENT NORMALIZES HF-INDUCED CHANGES IN NEURONAL STRUCTURE AND MEMORY DEFICITS. Consistent with our previous histological analyses (5), HF significantly altered the morphology of pyramidal neurons in the frontal cortex. Specifically, HF (at 12 weeks post-infarction) induced 2 significant alterations: dendritic atrophy and a reduction in basal dendrite spine density (**Figure 5** and Supplemental Table 3). As shown in **Figure 5C** and summarized in Supplemental Table 3, HF did not affect the number of dendrite intersections. Because apical and basal dendrites can be differentially affected by stressors (24), we conducted a subanalysis to confirm that neither apical nor basal dendrite intersection morphology was affected (Supplemental Figure 7; Supplemental Table 3). However, our analysis demonstrated the presence of dendrite atrophy (i.e., a 22% reduction in dendrite length (**Figures 5C and 5D**) that was present in both apical (24% reduction) and basal (20% reduction) dendrites (Supplemental Figure 7). HF also reduced basal dendritic spine density in the distal regions of the dendrite (60 to 100 μm from the soma) (**Figure 5E and 5F**); apical dendritic spine density was not significantly altered (Supplemental Figure 8). C18-treated HF mice (3 mg/kg intraperioneally daily for 2 weeks) did not display dendrite atrophy or a reduction in dendritic spine density (**Figure 5**, Supplemental Figure 8, Supplemental Table 3).

The altered cortical neuron morphology in HF mice correlated with impaired rhino-cortical–dependent, short-term retention of object familiarity (**Figure 5G**); this impairment was not present in C18-treated HF mice. Longitudinal pre-treatment (i.e., at 10 weeks post-infarction) and post-treatment analyses of the same vehicle- and C18- treated HF mice confirmed that C18 reversed the impairment caused by HF (**Figure 5H**).

Importantly, the C18-mediated normalization of histological and cognitive parameters is not attributable to improved cardiac function because the ejection fraction did not change following C18 treatment (3 mg/kg intraperioneally daily for 2 weeks; pre-C18 ejection fraction: 47 ± 3%; post-C18 ejection fraction: 46 ± 3%; n = 8; paired *t* test: p = NS). We also confirmed that the vehicle- and C18-treated groups possessed comparable reductions in ejection fraction at the 2 weeks post-treatment time point (sham: 64 ± 2%, n = 8; HF: 46 ± 4% *; n = 7; HF+C18: 46 ± 3% *; n = 8; * denotes $p < 0.05$ for both HF and HF+C18 relative to sham; p = NS for HF relative to HF+C18 following unpaired comparisons with a 1-way analysis of variance and Tukey's post hoc test).

C18 TREATMENT RECTIFIES DEFICIENT CBF IN SAH. Our previous work demonstrated that SAH has a similar cerebrovascular phenotype as HF, in that 1) cerebral artery CFTR protein expression is reduced; 2) cerebral artery myogenic tone is augmented; and 3) cerebral perfusion is reduced (6). As in HF (**Figure 3**), C18 treatment in vivo (3 mg/kg intraperioneally daily for 2 days) restored CFTR expression in cerebral arteries from mice with SAH (**Figure 6A**) and

concomitantly normalized olfactory cerebral artery myogenic tone (**Figure 6B**). The attenuation of myogenic tone was associated with an expected baseline shift in phenylephrine responsiveness, due to the reduction in basal tone; however, the EC_{50} values were not different (log EC_{50} sham: -5.52 ± 0.23; $n = 5$ from 3 mice; log EC_{50} SAH: -6.01 ± 0.16; $n = 6$ from 6 mice; log EC_{50} SAH+C18: -6.01 ± 0.31; $n = 5$ from 4 mice; 1-way analysis of variance: $p = NS$), and the curves overlapped after correction for the difference in basal tone (Supplemental Figure 9). C18 treatment did not affect olfactory cerebral myogenic tone or phenylephrine responses in sham-operated mice (Supplemental Figure 10). Using olfactory cerebral arteries isolated from CFTR knockout mice, we confirmed that C18 mediated its attenuating effect on myogenic tone by targeting CFTR. As expected, olfactory cerebral arteries from CFTR knockout mice displayed augmented myogenic tone that was not susceptible to in vivo C18 treatment (**Figure 6C**); phenylephrine responsiveness in these arteries was not affected by C18 treatment (Supplemental Figure 11). Importantly, in vivo C18 treatment restored CBF (**Figure 6D**), once again correlating with the normalization of olfactory cerebral artery myogenic tone (**Figure 6B**).

LUMACAFTOR TREATMENT RECTIFIES DEFICIENT CBF IN SAH. We complemented our C18 data with interventions that used the CFTR corrector lumacaftor, a clinically relevant C18 analogue that is approved by the Food and Drug Administration for treating cystic fibrosis, in combination with the CFTR potentiator ivacaftor (i.e., Orkambi; Vertex, Boston, Massachusetts). We first confirmed that lumacaftor was capable of increasing both mouse and human CFTR expression. As observed for C18 (**Figure 2**), lumacaftor increased CFTR protein expression in mouse cerebral arteries (mice injected with 3 mg/kg intraperitoneally daily for 2 days) and baby hamster kidney fibroblast cells that stably expressed human CFTR (**Figure 7**). In both settings, CFTR mRNA expression was unaffected, indicating a nontranscriptional mechanism (**Figure 7**). Consistent with our C18 data in SAH (**Figure 6**), lumacaftor treatment in vivo (3 mg/kg intraperitoneally daily for 2 days) restored CFTR expression in cerebral arteries from SAH mice (**Figure 7**) and concomitantly normalized olfactory cerebral artery myogenic tone and cerebral perfusion (**Figure 7**). Lumacaftor did not affect phenylephrine responsiveness (Supplemental Figure 12) and consequently, the EC_{50} values were not different (log EC_{50} sham: -5.79 ± 0.09; $n = 7$ from 4 mice; log EC_{50} SAH: -5.93 ± 0.19; $n = 6$ from 3 mice; log EC_{50} SAH+Lum: -5.90 ± 0.18; $n = 7$ from 4 mice; 1-way analysis of variance: $p = NS$).

C18 AND LUMACAFTOR REDUCE NEURONAL INJURY IN SAH. The neuronal injury induced by SAH can be easily characterized with standard histological techniques (Fluoro-Jade and activated caspase-3 staining) and simple neurologic testing (Modified Garcia Score) (6); we used these methods to determine whether the restoration of normal myogenic responsiveness and CBF correlated with improved neurologic function in the delayed ischemia phase of the SAH disease. Both C18 and lumacaftor significantly attenuated neuronal injury at 2 days post-SAH, as assessed by activated caspase-3 and Fluoro-Jade staining (**Figure 8**); these neuronal injury reductions correlated with improved neurologic function (**Figure 8E**). Specifically, SAH mice scored lower than sham-operated mice on the modified Garcia neurologic function test. However, C18- and lumacaftor-treated SAH mice had neurologic function scores comparable to sham-operated mice.

DISCUSSION

This investigation demonstrated that CFTR is a prominent regulator of cerebral perfusion, and consequently, is a therapeutic target. In experimental models of HF and SAH, cerebral artery CFTR expression was downregulated; the loss of CFTR activity augmented myogenic vasoconstriction, thereby increasing vascular resistance, and consequently, reducing cerebral perfusion. Therapeutic agents that restored CFTR expression in these pathological settings normalized cerebrovascular reactivity and perfusion. These improvements correlated with improved neurologic injury and function. Therefore, CFTR therapeutics may represent an untapped resource for clinically managing injurious cerebral perfusion deficits, and hence, neurologic outcome in patients with HF and SAH.

The CFTR corrector compounds C18 and lumacaftor were originally developed to chaperone misfolded mutant CFTR proteins to the plasma membrane. This indication does not apply to patients with HF and SAH, because 1) most patients possess wild-type CFTR; and 2) the pathological reduction in CFTR activity is due to a transcription-based mechanism, not a trafficking defect. Thus, it was necessary to confirm that C18 and lumacaftor increased wild-type CFTR abundance. Our data showed that C18 and lumacaftor increased wild-type CFTR abundance by a nontranscriptional, proteostatic mechanism.

This is consistent with a separate study that demonstrated the stabilization of cell surface–localized CFTR against internalization and subsequent degradation (21). Over time, stabilizing cell surface CFTR elevates overall CFTR expression levels because less cell surface CFTR was internalized and routed to degradation mechanisms.

We strategically selected proximal PCAs for our HF studies and olfactory cerebral arteries for our SAH studies to directly compare the CFTR-targeted interventions to our previous work (4,6,8). Although PCAs and olfactory arteries originate from distinct regions of the cerebral microcirculation (i.e., posterior and anterior, respectively) and display differences in their baseline myogenic tone curves, they behave similarly in terms of the pathological signaling mechanisms that augment myogenic responsiveness (4,6,8). The comparable success of the CFTR-targeted interventions in PCAs and olfactory arteries suggests that CFTR regulates vascular reactivity broadly throughout the cerebral microcirculation.

To increase brain perfusion, cerebrovascular resistance must decrease in relation to TPR. We therefore compared the role that CFTR plays in cerebral arteries to skeletal muscle resistance arteries. We selected skeletal muscle resistance arteries for this comparison, because this vascular bed forms the body's largest circulatory network (40% of body mass is skeletal muscle); therefore, it is a prominent determinant of TPR. Our comparisons of 1) CFTR inhibition in cerebral and skeletal muscle resistance arteries, and 2) TPR measurements in CFTR mutant and wild-type mice indicated that CFTR's vascular effects do not appreciably influence MAP. This is presumably explained by the observed differences in CFTR expression across these vascular beds: skeletal muscle resistance arteries have 10-fold lower CFTR expression than do cerebral arteries. Therefore, CFTR therapeutics should exhibit similarly restricted effects. CFTR corrector treatment increases cerebral perfusion without affecting TPR. This specific effect is highly advantageous because the lack of a direct effect on peripheral resistance increases the likelihood that the intervention can be added to prescribed blood pressure management practices that would already be in place.

The myogenic response, which continuously matches vascular resistance to the prevalent transmural pressure (25,26), is the functional basis of CBF autoregulation. In addition to dictating cerebral perfusion through its autoregulatory function, the myogenic response also maintains capillary pressures at levels that minimize damage and edema formation (22,23). Therefore, reducing myogenic reactivity has the potential to induce edema formation by permitting additional pressure to enter the capillary beds. On a related aspect, because S1P prominently regulates blood–brain barrier permeability (27), CFTR-dependent changes in S1P signaling could cause edema through alterations in barrier function. Thus, it was crucial to exclude edema as a negative effect of our intervention. CFTR corrector treatment (C18) did not induce edema in mice with HF. This confirmed that: 1) hydrostatic pressure in the cerebral microcirculation remained within tolerable limits (this would be expected because the CBF and MAP measures were comparable to sham animals); and 2) blood–brain barrier function was preserved during treatment.

A key translational question is whether CFTR regulates vasoconstriction in the human cerebrovascular microcirculation. To our knowledge, cerebrovascular CFTR expression has never been assessed in human cerebral arteries, nor has cerebral perfusion been systematically assessed in patients with cystic fibrosis. Our previous translational work that compared human and/or mouse mesenteric and skeletal muscle artery CFTR expression and function (28) provides a decent hint. As observed in the mouse, human mesenteric arteries both express CFTR and display functional sensitivity to CFTR inhibition, whereas human skeletal muscle resistance arteries possess no detectable CFTR protein and are consequently insensitive to CFTR inhibition (28). Thus, the functional profile for mesenteric and skeletal muscle resistance arteries overlapped in mice and humans, providing reasonable grounds to speculate that CFTR's functional role in the mouse cerebral microcirculation will also translate to the human setting.

We previously showed that HF downregulates CFTR expression in lung terminal bronchiolar epithelial cells (8), and thus, reductions in CFTR expression were not restricted to the vascular system. It is therefore tempting to speculate that CFTR therapeutics could provide other substantive benefits beyond the improvement of cerebral perfusion. In contrast, it is not known whether the HF and SAH pathologies ubiquitously downregulate CFTR expression in all tissues, meaning that CFTR therapeutics could also have unanticipated, nonbeneficial effects in other tissues by increasing CFTR expression above normal levels. At present, clinical trial data for lumacaftor and lumacaftor/ivacaftor in healthy subjects are proprietary, and therefore, are not publicly available. However, NIH clinical trial records indicate that several safety studies in healthy subjects have

been completed and more are ongoing. The consecutive initiation of clinical trials in healthy patients is a strong, yet indirect indication that no serious adverse events have been encountered to date. As a Food and Drug Administration–approved medication in combination with ivacaftor, lumacaftor has already cleared rigorous standards for safety and toxicity (13,29).

HF and SAH are fundamentally different pathologies that share a common aspect of downregulated cerebral artery CFTR expression (6,8). One key strength of the present investigation was that we demonstrated therapeutic efficacy in 2 distinct injury processes with markedly different severities. The "delayed cerebral ischemia" that occurrs at 2 days post-SAH causes acute, irrevocable neuronal injury. Thus, we targeted CFTR as a preventative intervention against a severe insult. The cerebral effects of HF were not nearly as overt, largely because the primary injury occurred at the heart rather than in the brain. Chronic malperfusion induced reversible neurologic deficits via dendritic atrophy and reduced synaptic strength [i.e., reduced spine density (30)]. In this context, we delayed treatment in HF until cognitive impairment was evident and then targeted CFTR as a means of restoring normal neuronal function. Therefore, our investigation demonstrated that therapeutically targeting CFTR can 1) improve outcomes in multiple, etiologically distinct pathologies; 2) prevent acute, irreversible neuronal injury; and 3) reverse deleterious alterations in neuronal connectivity. In addition to establishing the broad usefulness of targeting CFTR as an intervention, the fact that therapeutic success was observed across the 2 etiologically distinct disease models argues against a nonspecific or off-target effect of the intervention.

As a caveat, the SAH vasculopathy is not solely defined by a functional abnormality in myogenic reactivity and autoregulation. As demonstrated by Sabri et al. (31), an SAH model similar to ours elicited marked morphological changes to microvascular structure, including increased wall thickness and a convoluted and/or irregular luminal surface. Although Sabri et al. also demonstrated reduced luminal diameter in microvessels, the relative contributions of aberrant vasoconstriction (e.g., augmented myogenic tone) and structural changes to this deficit could not be discerned (31). In the present investigation, SAH had no effect on maximal luminal diameter, which was determined under calcium-free conditions to yield maximal dilation. Thus, we have no evidence that structural changes contributed to the perfusion deficits we observed. Nevertheless, pathological changes to cerebrovascular structure have the potential to significantly alter vascular reactivity and cerebral perfusion and warrant further investigation.

CONCLUSIONS

The present investigation provides direct evidence that CFTR regulates cerebrovascular reactivity and validates CFTR as a therapeutic target for normalizing cerebral perfusion deficits in HF and SAH. Both HF and SAH reduced cerebral perfusion by downregulating cerebral artery CFTR protein expression, thereby compromising autoregulatory control. This study demonstrated that clinically available CFTR therapeutics can restore cerebral artery CFTR expression, vascular reactivity, and cerebral perfusion. Remarkably, this therapeutic effect appears to be primarily localized to the cerebral microcirculation because CFTR does not modulate the reactivity of peripheral arteries involved in blood pressure control. Therefore, CFTR therapeutics could emerge as valuable clinical tools to manage cerebrovascular dysfunction, impaired cerebral perfusion, and neuronal injury. The observations presented herein encourage an immediate clinical assessment of CFTR therapeutics for the prevention and improvement of cerebral perfusion deficits in HF and SAH.

ACKNOWLEDGMENTS The authors gratefully acknowledge the Lund University Bioimaging Center for providing access to the Nikon Eclipse T*i*2 microscope system.

ADDRESS FOR CORRESPONDENCE: Dr. Steffen-Sebastian Bolz, Toronto Centre for Microvascular Medicine at TBEP, University of Toronto, 661 University Avenue, 14th Floor, Toronto, Ontario, Canada, M5G 1M1. E-mail: sts.bolz@utoronto.ca.

PERSPECTIVES

COMPETENCY IN MEDICAL KNOWLEDGE: Both HF and SAH reduce cerebral perfusion by altering autoregulatory control mechanisms. Because current medical interventions do not target these causal mechanisms, they display limited efficacy. Restoring normal myogenic reactivity in cerebral arteries represents a significant advantage over current strategies.

TRANSLATIONAL OUTLOOK: These data provide strong proof of principle for clinically assessing whether CFTR therapeutics improve cerebral perfusion in patients with HF and SAH.

REFERENCES

1. Román GC. Brain hypoperfusion: a critical factor in vascular dementia. Neurol Res 2004;26:454–8.

2. Doehner W, Ural D, Haeusler KG, et al. Heart and brain interaction in patients with heart failure: overview and proposal for a taxonomy. A position paper from the Study Group on Heart and Brain Interaction of the Heart Failure Association. Eur J Heart Fail 2018;20:199–215.

3. Wong GK, Lam S, Ngai K, et al. Evaluation of cognitive impairment by the Montreal cognitive assessment in patients with aneurysmal subarachnoid haemorrhage: prevalence, risk factors and correlations with 3 month outcomes. J Neurol Neurosurg Psychiatry 2012;83:1112–7.

4. Yang J, Hossein Noyan-Ashraf M, Meissner A, et al. Proximal cerebral arteries develop myogenic responsiveness in heart failure via tumor necrosis factor-α-dependent activation of sphingosine-1-phosphate signaling. Circulation 2012;126:196–206.

5. Meissner A, Visanji NP, Momen MA, et al. Tumor necrosis factor-α underlies loss of cortical dendritic spine density in a mouse model of congestive heart failure. J Am Heart Assoc 2015;4:e001920.

6. Yagi K, Lidington D, Wan H, et al. Therapeutically targeting tumor necrosis factor-α/sphingosine-1-phosphate signaling corrects myogenic reactivity in subarachnoid hemorrhage. Stroke 2015;46:2260–70.

7. Xiao M, Li Q, Feng H, Zhang L, Chen Y. Neural vascular mechanism for the cerebral blood flow autoregulation after hemorrhagic stroke. Neural Plast 2017;2017:5819514.

8. Meissner A, Yang J, Kroetsch JT, et al. Tumor necrosis factor-α-mediated downregulation of the cystic fibrosis transmembrane conductance regulator drives pathological sphingosine-1-phosphate signaling in a mouse model of heart failure. Circulation 2012;125:2739–50.

9. Nakamura H, Yoshimura K, Bajocchi G, Trapnell BC, Pavirani A, Crystal RG. Tumor necrosis factor modulation of expression of the cystic fibrosis transmembrane conductance regulator gene. FEBS Lett 1992;314:366–70.

10. Besançon F, Przewlocki G, Baró I, Hongre AS, Escande D, Edelman A. Interferon-gamma downregulates CFTR gene expression in epithelial cells. Am J Physiol 1994;267:C1398–404.

11. Murdaca G, Spanò F, Contatore M, et al. Infection risk associated with anti-TNF-α agents: a review. Expert Opin Drug Saf 2015;14:571–82.

12. Kroetsch JT, Levy AS, Zhang H, et al. Constitutive smooth muscle tumour necrosis factor regulates microvascular myogenic responsiveness and systemic blood pressure. Nat Commun 2017;8:14805.

13. Boyle MP, Bell SC, Konstan MW, et al. A CFTR corrector (lumacaftor) and a CFTR potentiator (ivacaftor) for treatment of patients with cystic fibrosis who have a phe508del CFTR mutation: a phase 2 randomised controlled trial. Lancet Respir Med 2014;2:527–38.

14. van Doorninck JH, French PJ, Verbeek E, et al. A mouse model for the cystic fibrosis delta F508 mutation. EMBO J 1995;14:4403–11.

15. Loubinoux I, Volk A, Borredon J, et al. Spreading of vasogenic edema and cytotoxic edema assessed by quantitative diffusion and T2 magnetic resonance imaging. Stroke 1997;28:419–26.

16. Malik FA, Meissner A, Semenkov I, et al. Sphingosine-1-phosphate is a novel regulator of cystic fibrosis transmembrane conductance regulator (CFTR) activity. PLoS One 2015;10:e0130313.

17. Lueptow LM. Novel object recognition test for the investigation of learning and memory in mice. J Vis Exp 2017;126:e55718.

18. Wilke M, Buijs-Offerman RM, Aarbiou J, et al. Mouse models of cystic fibrosis: phenotypic analysis and research applications. J Cyst Fibros 2011;10 Suppl 2:S152–71.

19. Lavelle GM, White MM, Browne N, McElvaney NG, Reeves EP. Animal models of cystic fibrosis pathology: phenotypic parallels and divergences. Biomed Res Int 2016;2016:5258727.

20. Korthuis RJ. Regulation of vascular tone in skeletal muscle. In: Granger DN, Granger J, editors. Skeletal Muscle Circulation. San Rafael, CA: Morgan & Claypool Life Sciences, 2011:7–34.

21. Okiyoneda T, Veit G, Dekkers JF, et al. Mechanism-based corrector combination restores ΔF508-CFTR folding and function. Nat Chem Biol 2013;9:444–54.

22. Bidani AK, Griffin KA, Williamson G, Wang X, Loutzenhiser R. Protective importance of the myogenic response in the renal circulation. Hypertension 2009;54:393–8.

23. Moien-Afshari F, Skarsgard PL, McManus BM, Laher I. Cardiac transplantation and resistance artery myogenic tone. Can J Physiol Pharmacol 2004;82:840–8.

24. Cook SC, Wellman CL. Chronic stress alters dendritic morphology in rat medial prefrontal cortex. J Neurobiol 2004;60:236–48.

25. Paulson OB, Strandgaard S, Edvinsson L. Cerebral autoregulation. Cerebrovasc Brain Metab Rev 1990;2:161–92.

26. Toth P, Tarantini S, Csiszar A, Ungvari Z. Functional vascular contributions to cognitive impairment and dementia: mechanisms and consequences of cerebral autoregulatory dysfunction, endothelial impairment, and neurovascular uncoupling in aging. Am J Physiol Heart Circ Physiol 2017;312:H1–20.

27. Prager B, Spampinato SF, Ransohoff RM. Sphingosine 1-phosphate signaling at the blood-brain barrier. Trends Mol Med 2015;21:354–63.

28. Hui S, Levy AS, Slack DL, et al. Sphingosine-1-phosphate signaling regulates myogenic responsiveness in human resistance arteries. PLoS One 2015;10:e0138142.

29. Wainwright CE, Elborn JS, Ramsey BW, et al. Lumacaftor-ivacaftor in patients with cystic fibrosis homozygous for Phe508del CFTR. N Engl J Med 2015;373:220–31.

30. Nimchinsky EA, Sabatini BL, Svoboda K. Structure and function of dendritic spines. Annu Rev Physiol 2002;64:313–53.

31. Sabri M, Ai J, Lakovic K, D'abbondanza J, Ilodigwe D, Macdonald RL. Mechanisms of microthrombi formation after experimental subarachnoid hemorrhage. Neuroscience 2012;224:26–37.

KEY WORDS cognitive impairment, corrector compounds, cystic fibrosis transmembrane conductance regulator (CFTR), myogenic vasoconstriction, sphingosine-1-phosphate, tumor necrosis factor, vascular smooth muscle cells

APPENDIX For an expanded Methods section and supplemental figures and tables, please see the online version of this paper.

JACC: BASIC TO TRANSLATIONAL SCIENCE VOL. 4, NO. 8, 2019

EDITORIAL COMMENT

Targeting Muscles in the Brain to Enhance Cerebral Perfusion*

Jin-Moo Lee, MD, PhD,[a] Abhinav Diwan, MD,[b] Gregory J. Zipfel, MD[c]

Pound for pound, the brain is the most energy-consuming organ in the human body, requiring 20% of cardiac output but only weighing in at 3% of body weight. The energy demands of brain metabolism combined with its low intrinsic energy reserves impose a requirement of steady and constant blood supply to the brain as a whole, regardless of natural variations in arterial blood pressure. The homeostatic process by which arterioles dilate or constrict to maintain constant cerebral blood flow (CBF) over a large range of blood pressures is termed cerebral autoregulation. When this process is impaired, consequences can be dire (e.g., brain perfusion rises or falls at the mercy of systemic blood pressure fluctuations), leading to cerebral ischemia under conditions of relative hypotension, or blood-brain barrier breakthrough and cerebral edema under conditions of relative hypertension.

Cerebral autoregulation is regulated in part by passive mechanisms involving intrinsic responses of the smooth muscle cells (SMCs) to changes in transmural pressure in brain arterioles, termed the "myogenic response." Cerebral arterioles constrict by way of SMC contraction to increases in transmural pressure or dilate by way of SMC relaxation in response to decreases in transmural pressure. They are regulated by a variety of molecular signaling pathways, including cellular mechanosensors sensitive to stretch, intracellular ion levels, and second messenger systems.

Scores of disorders can impair cerebral autoregulation, leading to reduced CBF and varying degrees of brain injury. One such condition of immense public health significance is chronic heart failure (HF), the most common cardiovascular disease in the elderly, which results in decreases in cardiac output affecting all organs in advanced stages. The brain is particularly vulnerable for reasons discussed earlier but also because autoregulatory mechanisms may be affected by chronic HF. HF is associated with increases in cerebrovascular myogenic tone, resulting in decreased global CBF (1). This pathophysiological mechanism may in part explain the increasingly recognized complication of neurocognitive impairment in patients with HF (2).

Rodent models of ischemic HF have revealed some clues regarding the cellular and molecular mechanisms involved in this autoregulatory disruption. HF results in increased circulating levels of tumor necrosis factor (TNF), an inflammatory cytokine, with a strong inverse correlation with survival. Moreover, TNF expression is also increased in SMCs within the cerebral vasculature. TNF, in turn, triggers a cascade of signaling, including increased local bioavailability of sphingosine-1-phosphate (S1P), which signals via G-protein-coupled S1P receptors to release calcium from the sarcoplasmic reticulum and increase sensitivity to calcium signaling via RhoA/Rho kinase activation. These cascades augment myogenic response to a given transmural pressure, leading to an

*Editorials published in *JACC: Basic to Translational Science* reflect the views of the authors and do not necessarily represent the views of *JACC: Basic to Translational Science* or the American College of Cardiology.

From the [a]Department of Neurology and the Hope Center for Neurological Disorders, Washington University School of Medicine, St. Louis, Missouri; [b]Division of Cardiology, Department of Internal Medicine, Washington University School of Medicine and John Cochran Veterans Affairs Medical Center, St. Louis, Missouri; and the [c]Department of Neurosurgery and the Hope Center for Neurological Disorders, Washington University School of Medicine, St. Louis, Missouri. Dr. Lee has received research grants from Biogen; and is a consultant for Regenera. Dr. Diwan consults for ERT (Clinical Trails Technology Solutions) for interpretations of echocardiograms. Dr. Zipfel has reported that he has no relationships relevant to the contents of this paper to disclose.

The authors attest they are in compliance with human studies committees and animal welfare regulations of the authors' institutions and Food and Drug Administration guidelines, including patient consent where appropriate. For more information, visit the *JACC: Basic to Translational Science* author instructions page.

ISSN 2452-302X https://doi.org/10.1016/j.jacbts.2019.11.003

exaggerated autoregulatory curve and potentially compromised CBF. An important regulator of S1P metabolism in the cerebral vasculature is the cystic fibrosis transmembrane regulator (CFTR), better known for its role in chloride secretion in lung epithelium, which enhances S1P transport across the plasma membrane leading to its intracellular degradation and prevents it from engaging S1P receptor signaling (3). Indeed, down-regulation of CFTR has been identified as a critical mediator of TNF-α–induced increases in cerebrovascular myogenic tone in animal models of chronic HF.

SEE PAGE 940

It is difficult to conceive that chronic HF has common pathobiology with acute subarachnoid hemorrhage (SAH). However, in this issue of *JACC: Basic to Translational Science*, Lidington et al. (4) report not only a common pathobiology but a novel therapeutic target to treat cerebrovascular complications of these 2 very different diseases. In contrast to chronic HF, SAH is an acute emergency resulting from the rupture of a cerebral aneurysm and bleeding into the subarachnoid space surrounding the brain. This uncommon cause of stroke has a mortality rate of 30%, and 50% of survivors have long-term cognitive deficits. The largest treatable cause of poor SAH outcome is delayed cerebral ischemia (DCI), the development of new focal neurological deficits or deterioration in level of consciousness that results from a variety of causes, including vasospasm, microthrombi, and autoregulatory failure.

Previous work from Lidington et al. (5) has shown a remarkable similarity between cerebrovascular mechanisms leading to DCI after SAH and that observed after chronic HF in rodent experimental models. These studies have shown enhanced cerebrovascular myogenic response due to decreased CFTR expression, reversible by blocking TNF-α signaling. However, to avoid the wide-ranging side effects of TNF-α blockade, the authors (4) chose to target CFTR for several reasons: 1) its selective expression in cerebrovascular SMCs, making it a specific target for cerebrovascular myogenic tone; and 2) the availability of numerous drugs approved by the US Food and Drug Administration (FDA) that increase CFTR expression/activity with a favorable side-effect profile.

To demonstrate a causal link between CFTR activity and cerebrovascular myogenic tone, Lidington et al. (4) compared ex vivo posterior cerebral artery (PCA) myogenic tone between CFTR mutant mice ($CFTR^{\Delta f508}$) and wild-type mice. As expected, they found that PCAs in the mutant mice had augmented myogenic tone compared with PCAs in wild-type mice. In contrast, arteries derived from cremasteric muscles were unaffected by the CFTR mutation, suggesting that cerebrovascular arteries were selectively regulated by CFTR. Bulk blood flow measures confirmed this result in vivo: CBF was significantly reduced in CFTR mutant mice, whereas total peripheral resistance (mainly mediated by skeletal muscle vascular tone) and cardiac output were unchanged. These data suggest that CFTR activity is a selective driver of cerebrovascular myogenic tone, without apparent effect on other vascular beds.

To examine the efficacy of CFTR-targeted therapies on preclinical models of HF and SAH, the authors used 2 different small molecule CFTR interventions: 1) C18, a "CFTR corrector" that increases CFTR cell surface expression; and 2) lumacaftor, a C18 analogue that is FDA approved for the treatment of cystic fibrosis (4). After inducing ischemic cardiomyopathy and HF with permanent left anterior descending coronary artery occlusion resulting in myocardial infarction in mice, CFTR expression was decreased in the PCAs; this outcome was in parallel with augmentation in ex vivo PCA myogenic tone. In HF mice treated with C18, CFTR expression in PCAs was restored, as was ex vivo PCA myogenic tone. C18 had no effect on PCAs derived from CFTR knockout mice, confirming that CFTR was the target for the effect of C18. In vivo hemodynamic assessment showed a decrease in cardiac output and a small drop in arterial pressure following HF induction, as well as a marked reduction in CBF. C18 treatment increased CBF to levels comparable to those of sham-operated control mice. Again, this effect was exclusive of any effect on cardiac output or total peripheral resistance. Consistent with the salutary effects of C18 on CBF, mice also exhibited improvement in neurobehavioral tests; in particular, their performance on a novel object recognition task was restored to a level similar to that of sham-operated control mice. Morphometry of pyramidal neurons in the frontal cortex revealed that C18 attenuated dendritic atrophy and reduced dendritic spine density in the HF mice, providing histopathological correlates of the improved neurobehavioral tests.

A similar benefit was seen in a mouse model of SAH, induced by arterial blood injected into the chiasmatic cistern (4). In this model, cerebral artery myogenic tone increases and is maximal 2 days after ictus, mimicking the DCI observed in human SAH (albeit on a different time scale). Post-SAH reduction in CFTR protein expression in cerebral arteries was attenuated by C18 and lumacaftor treatment, as was ex vivo cerebral artery–augmented myogenic tone.

Post-SAH reductions in CBF also normalized after treatment with C18 and lumacaftor. C18 and lumacaftor reduced selective neuronal death (assessed by caspase-3 and Fluoro-Jade staining) in cortical regions and improved the modified Garcia neurological function scores comparable to those of sham-operated control mice.

Collectively, these studies show that CFTR is an important regulator of cerebral perfusion, acting by modulating cerebral myogenic tone. Importantly, its effects appear to be relatively selective for the cerebral vasculature, as CFTR-specific interventions did not alter myogenic tone in skeletal muscle or total peripheral resistance. This makes it an attractive target for a diverse array of disorders that disrupt cerebral autoregulation. Indeed, the authors show convincingly that CFTR corrector compounds C18 and lumacaftor normalize cerebrovascular reactivity, CBF, and neurobehavioral deficits in preclinical models of both HF and SAH (4). These are 2 very different diseases but with apparent overlap in vascular pathobiology. Lumacaftor is an especially attractive candidate drug because it is already FDA-approved and ripe for drug repurposing. But alas, cautious optimism is recommended, as the field of neurovascular protection is littered with numerous failed drugs and clinical trials. Thus, more rigorous preclinical testing is warranted using the STAIR (Stroke Therapy Academic Industry Roundtable Preclinical Recommendations) criteria (6) before engaging in clinical trials.

ADDRESS FOR CORRESPONDENCE: Dr. Jin-Moo Lee, Department of Neurology, Washington University School of Medicine, 660 South Euclid Avenue, Campus Box 8111, St. Louis, Missouri 63110. E-mail: leejm@wustl.edu.

REFERENCES

1. Havakuk O, King KS, Grazette L, et al. Heart failure-induced brain injury. J Am Coll Cardiol 2017;69:1609–16.

2. Toledo C, Andrade DC, Diaz HS, Inestrosa NC, Del Rio R. Neurocognitive disorders in heart failure: novel pathophysiological mechanisms underpinning memory loss and learning impairment. Mol Neurobiol 2019;56:8035–51.

3. Meissner A, Yang J, Kroetsch JT, et al. Tumor necrosis factor-alpha-mediated down-regulation of the cystic fibrosis transmembrane conductance regulator drives pathological sphingosine-1-phosphate signaling in a mouse model of heart failure. Circulation 2012;125:2739–50.

4. Lidington D, Fares JC, Uhl FE, et al. CFTR therapeutics normalize cerebral perfusion deficits in mouse models of heart failure and subarachnoid hemorrhage. J Am Coll Cardiol Basic Trans Science 2019;4:940–58.

5. Lidington D, Kroetsch JT, Bolz SS. Cerebral artery myogenic reactivity: the next frontier in developing effective interventions for subarachnoid hemorrhage. J Cereb Blood Flow Metab 2018;38:17–37.

6. Fisher M, Feuerstein G, Howells DW, et al. Update of the stroke therapy academic industry roundtable preclinical recommendations. Stroke 2009;40:2244–50.

KEY WORDS cerebral autoregulation, chronic heart failure, cystic fibrosis transmembrane regulator, subarachnoid hemorrhage

JACC: BASIC TO TRANSLATIONAL SCIENCE VOL. 4, NO. 8, 2019

PRECLINICAL RESEARCH

Cardiac Versus Renal Response to Volume Expansion in Preclinical Systolic Dysfunction With PDEV Inhibition and BNP

Siu-Hin Wan, MD,[a,b] Isabel Torres-Courchoud, MD, PhD,[c] Paul M. McKie, MD,[a,b] Joshua P. Slusser, BSc,[d] Margaret M. Redfield, MD,[a,b] John C. Burnett, Jr, MD,[a,b] David O. Hodge, MS,[d] Horng H. Chen, MBBCh[a,b]

VISUAL ABSTRACT

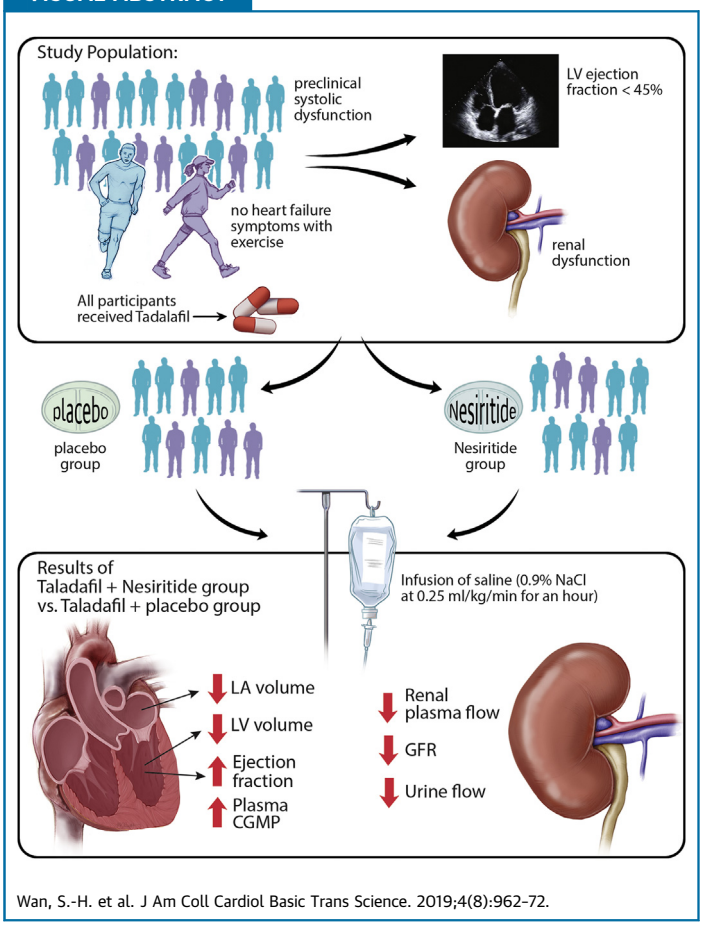

Wan, S.-H. et al. J Am Coll Cardiol Basic Trans Science. 2019;4(8):962-72.

HIGHLIGHTS

- **In preclinical systolic dysfunction, defined as left ventricular systolic dysfunction with no heart failure signs or symptoms, impairment in cardiorenal response to volume expansion may lead to symptomatic heart failure. Rescue of this impaired process in preclinical disease may prevent development of symptomatic heart failure.**
- **In preclinical systolic dysfunction, inhibition of phosphodiesterase-V in combination with exogenous B-type natriuretic peptide administration results in improved cardiac function but worsened renal function in response to acute volume expansion.**

ISSN 2452-302X https://doi.org/10.1016/j.jacbts.2019.08.008

- **Future studies are needed to further define the physiological effects and long-term outcomes of phosphodiesterase-V inhibition and exogenous BNP administration. Understanding the cardiorenal effects and outcomes of combination phosphodiesterase-V with exogenous B-type natriuretic peptide may affect the clinical management of patients with preclinical systolic dysfunction and renal dysfunction.**

SUMMARY

Impaired cardiorenal response to acute saline volume expansion in preclinical systolic dysfunction (PSD) may lead to symptomatic heart failure. The objective was to determine if combination phosphodiesterase-V inhibition and exogenous B-type natriuretic peptide (BNP) administration may enhance cardiorenal response. A randomized double-blinded, placebo-controlled study was conducted in 21 subjects with PSD and renal dysfunction. Pre-treatment with tadalafil and subcutaneous BNP resulted in improved cardiac function, as evidenced by improvement in ejection fraction, left atrial volume index, and left ventricular end-diastolic volume. However, there was reduced renal response with reduction in renal plasma flow, glomerular filtration rate, and urine flow. (Tadalafil and Nesiritide as Therapy in Pre-clinical Heart Failure; NCT01544998) (J Am Coll Cardiol Basic Trans Science 2019;4:962–72) © 2019 The Authors. Published by Elsevier on behalf of the American College of Cardiology Foundation. This is an open access article under the CC BY-NC-ND license (http://creativecommons.org/licenses/by-nc-nd/4.0/).

ABBREVIATIONS AND ACRONYMS

ACC = American College of Cardiology

AHA = American Heart Association

ANP = atrial natriuretic peptide

BNP = B-type natriuretic peptide

cGMP = cyclic guanosine monophosphate

GFR = glomerular filtration rate

HF = heart failure

LAVI = left atrial volume index

LVEF = left ventricular ejection fraction

LVEDV = left ventricular end-diastolic volume

LVESV = left ventricular end-systolic volume

NP = natriuretic peptide

PDEV = type V phosphodiesterase

PSD = preclinical systolic dysfunction

RPF = renal plasma flow

SC = subcutaneous

VE = acute saline volume expansion

Heart failure (HF) remains a major cause of morbidity and mortality worldwide, with >1 million hospitalizations and >$30 billion in health-related costs in the United States annually (1). Preclinical systolic dysfunction (PSD) represents a continuum in the spectrum of HF with reduced ejection fraction and is characterized by systolic dysfunction with absence of signs and symptoms of HF (American College of Cardiology/American Heart Association [ACC/AHA] stage B HF). It is increasingly recognized that PSD is common in the general population and associated with cardiorenal dysfunction and progression to symptomatic HF and mortality (2,3). The St Vincent's Screening To Prevent Heart Failure (STOP-HF) trial demonstrated that early screening and identification is important among those with stage B HF to prevent progression to symptomatic HF and improve outcomes (4).

Natriuretic peptides (NPs) have important physiological functions. Deficiency is associated with HF and fluid retention, and therapies with natriuretic-based therapies may be important in preventing progression along the HF spectrum (5). Cyclic 3′-5′-guanosine monophosphate (cGMP) is the second messenger of the NP system, is metabolized by type V phosphodiesterase (PDEV), and plays an important role in the preservation of myocardial, vascular, and renal function in PSD and HF (6). Previous animal studies have supported the therapeutic role of PDEV inhibitors in cardiac dysfunction (7).

We recently reported that the cGMP signaling pathway is impaired in subjects with PSD, characterized by decreased glomerular filtration rate (GFR) and renal blood flow (RBF), with an attenuated renal

From the [a]Department of Cardiovascular Diseases, Mayo Clinic and Foundation, Rochester, Minnesota; [b]Cardiorenal Research Laboratory, Division of Cardiovascular Diseases, Mayo Clinic and Foundation, Rochester, Minnesota; [c]Hospital Reina Sofía, Tudela, Navarra, Spain; and [d]Department of Health Sciences Research, Mayo Clinic and Foundation, Rochester, Minnesota. This research was supported by grants from the National Institutes of Health (PO1 HL 76611, R01 HL 84155, HL136440) and NIH/NCRR Center for Translational Science Activities (grant number UL1 RR024150). Drs. Wan and Torres-Courchoud contributed equally to this work and are joint first authors. Drs. Chen and Burnett hold patents and licensed designer natriuretic peptides; and are co-founders of Zumbro Discovery. All other authors have reported that they have no relationships relevant to the contents of this paper to disclose.

The authors attest they are in compliance with human studies committees and animal welfare regulations of the authors' institutions and Food and Drug Administration guidelines, including patient consent where appropriate. For more information, visit the *JACC: Basic to Translational Science* author instructions page.

Manuscript received April 15, 2019; revised manuscript received August 28, 2019, accepted August 29, 2019.

cGMP response to acute volume expansion (VE) (8). Attenuation of renal cGMP generation may be secondary to renal PDEV upregulation, as observed in experimental HF. Furthermore, renal PDEV upregulation may lead to the attenuation of renal cGMP generation in response to both endogenous and exogenous NP. Experimental animal studies have shown that long-term PDEV inhibition enhances cardiorenal response to exogenous B-type natriuretic peptide (BNP) by inhibiting cGMP degradation (9,10). Furthermore, animal studies have demonstrated synergistic effects of combination therapy with PDEV inhibition and exogenous BNP administration. Although PDEV inhibitors are clinically approved for erectile dysfunction and pulmonary hypertension, and nesiritide (recombinant human BNP) is approved for acute decompensated HF, the cardiorenal effects of combining PDEV inhibitors and BNP in humans have not been tested.

SEE PAGE 973

The objective of our study was to assess, for the first time in subjects with PSD and renal dysfunction, whether combination tadalafil (a long-acting PDEV inhibitor) and BNP, in response to acute VE, will enhance cardiorenal response compared with tadalafil alone. Combination therapy with tadalafil and BNP may have potential for rescuing cardiorenal impairment and preventing progression to symptomatic HF.

METHODS

STUDY DESIGN. We used a double-blinded, placebo-controlled, crossover study protocol to compare cardiorenal responses to acute saline VE after tadalafil and subcutaneous (SC) placebo versus tadalafil and SC BNP administration in subjects with PSD and renal dysfunction. This study was approved by the Mayo Foundation Institutional Review Board and was performed at the Clinical Research Unit at Saint Mary's Hospital, Mayo Clinic (Rochester, Minnesota). Written informed consent was obtained from all participants.

STUDY POPULATION. Twenty-five patients who met criteria for PSD (AHA stage B HF) and renal dysfunction (estimated GFR between 30 and 90 ml/min) were enrolled. Four subjects were excluded: 1 participant had GFR <30 ml/min on renal function reassessment; 1 participant withdrew consent before the study; 2 participants were unable to participate due to difficulty in obtaining venous and bladder access (**Figure 1**). Twenty-one subjects were randomized to receive tadalafil and SC placebo or tadalafil and SC BNP before VE. Cardiac and renal assessment, including transthoracic echocardiogram, urine, and plasma analysis, was performed at baseline and 60 min after VE. All patients returned for a second visit and underwent the crossover arm of the study. Sample size calculation is shown in Supplemental Table 1.

INCLUSION CRITERIA. Inclusion criteria were the following: ejection fraction <45%; no current or previous diagnosis of HF; not on loop diuretics; renal dysfunction (creatinine clearance between 30 and 90 ml/min using the Modification of Diet in Renal Disease formula); and minimal distance >450 m on 6-min walk test in the absence of mechanical limitations. Cardiovascular medications were at stable doses for at least 2 weeks before study entry.

ECHOCARDIOGRAPHIC ASSESSMENT. Echocardiographic images were obtained from standard acoustic windows according to the recommendations of the American Society of Echocardiography (11). Ventricular volumes were assessed by biplane Simpsons method of discs, and a 2-dimensional ejection fraction was obtained. Left ventricular (LV) diastolic function filling pressures were assessed by mitral inflow pulsed-wave Doppler examination and tissue Doppler imaging of the mitral annulus. All echocardiographic data were obtained by a certified sonographer and interpreted by H.H.C., who was blinded to the assigned treatment.

STUDY PROTOCOL. Before study initiation, subjects were stabilized for 1 week on a low-salt diet (120 mEq sodium/day). Baseline hematology and biochemistry laboratory tests, 6-min walking test, vital signs, and a physical examination were obtained. Subjects who met inclusion criteria were recruited and admitted to the Clinic Research Unit at St. Mary's Hospital, Mayo Clinic Center for Translational Science Activities (CTSA), Rochester, Minnesota, 1 day before the study date (**Figure 1**).

On the study day, subjects received their regular medications, except for diabetic therapies that were postponed until the first meal after the last renal clearance measurement. Subjects were orally hydrated with 10 ml/kg of water to ensure sufficient urinary flow.

Subjects were placed into a supine position for 1 h. During the first 15 min, 2 standard intravenous catheters were placed, 1 in each arm, for infusion and blood sampling. Iothalamate and para-aminohippurate were administered, followed by urinary and blood measurements, including urinary flow

FIGURE 1 **Study Design**

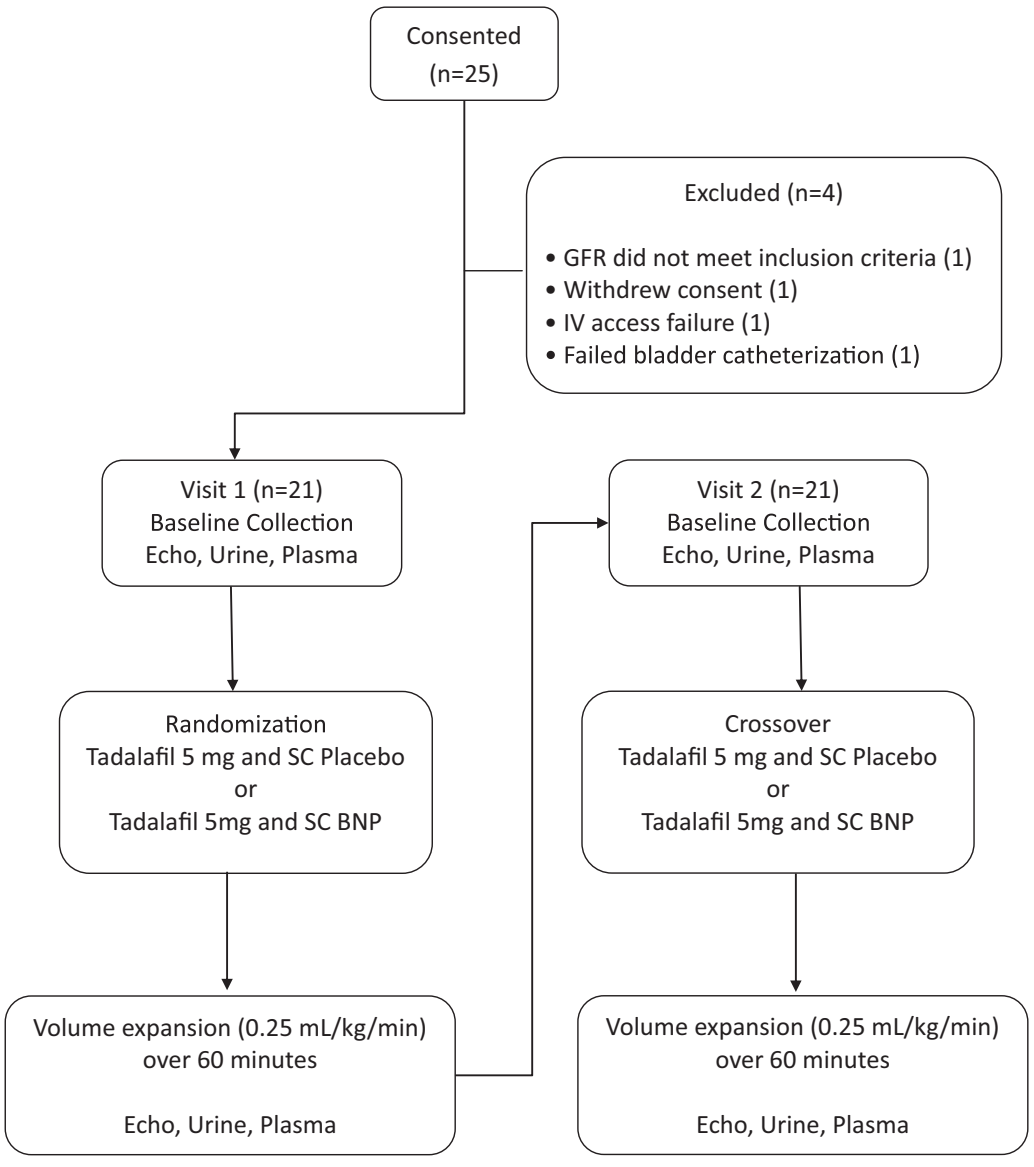

BNP = B-type natriuretic peptide; GFR = glomerular filtration rate; SC = subcutaneous.

(ml), urinary sodium excretion (mEq/min), urinary cGMP excretion (pmol/min), blood sodium (mEq/l), and cGMP (pmol/ml). Renal clearances and venous blood samples were obtained at 30 and 60 min, respectively. Subjects were monitored by electrocardiography, and blood pressures were obtained. An echocardiogram was obtained for left atrial (LA) and LV volumes, as well as systolic and diastolic function.

Subjects were then randomized to receive oral tadalafil 5 mg + SC placebo or tadalafil 5 mg + SC BNP 10 microgram/kg (Scios, Mountain View, California). After a 15-min lead-in period, a 30-min renal clearance and blood sample were repeated. An acute saline load was administered (0.9% sodium chloride at 0.25 ml/kg/min for 1 h), and every 30 min, renal and blood samples were obtained. Immediately after the end of the acute volume expansion, an echocardiogram was performed. Subjects returned at least 1 week later for the crossover portion of the study.

TABLE 1 Baseline Characteristics of the Study Population

	Subjects (n = 21)
Age (yrs)	67.5 ± 14.3
Female	4 (19)
Heart rate (beats/min)	62.7 ± 5.9
Blood pressure (mm Hg)	
Systolic	124.7 ± 16.6
Diastolic	71.6 ± 9.3
Body weight (kg)	87.5 ± 14.7
Body mass index (kg/m^2)	29.1 ± 5.0
GFR (ml/min)	66.4 ± 12.0
Diabetes mellitus	3 (14)
Coronary artery disease	14 (67)
Myocardial infarction	7 (33)
Hypertension	9 (43)
ACEI or ARB	18 (86)
Beta-blocker	19 (90)
Thiazide diuretic agents	7 (33)
LV ejection fraction (%)	40.3 ± 8.9
LV end-systolic volume (ml)	122.4 ± 42.2
LV end-diastolic volume (ml)	199.7 ± 48.4
LV end-systolic diameter (cm)	4.4 ± 0.5
LV end-diastolic diameter (cm)	5.7 ± 0.4
LA volume index (ml/m^2)	82.1 ± 21.1
RV systolic pressure (mm Hg)	28.0 ± 5.4
E/e′ (medial)	14.7 ± 9.1
ANP (pg/ml)	71.4 ± 45.4
BNP (pg/ml)	146.5 ± 107.1
Aldosterone (ng/dl)	3.7 ± 2.7
Angiotensin II (pg/ml)	3.3 ± 2.3

Values are mean ± SD or n (%).

ACEI = angiotensin-converting enzyme inhibitor; ANP = atrial natriuretic peptide; ARB = angiotensin receptor blocker; BNP = B-type natriuretic peptide; cGMP = cyclic guanosine monophosphate; E/e′ = E velocity/e′ velocity; GFR = glomerular filtration rate; LA = left atrium; LV = left ventricular; RV = right ventricular.

NEUROHORMONAL, ELECTROLYTE, AND RENAL ASSESSMENT. Plasma atrial natriuretic peptide (ANP), BNP, aldosterone, angiotensin II, and urine cGMP were measured by radioimmunoassay as previously described (8). Plasma and urine concentration of iothalamate and para-amino-hippurate, as well as creatinine, were measured by the Mayo Core Renal laboratory.

STATISTICAL METHODS. Continuous variables are presented as mean ± SD and discrete variables as frequency (proportion). Comparisons between the 2 treatment groups (tadalafil and SC placebo, and tadalafil and SC BNP) were made using the Student's *t*-test for normally distributed continuous variables, the rank-sum test for continuous variables with a skewed distribution, and the Pearson chi-square test for independence of categorical variables. Comparisons within groups (between visit 1 and visit 2) were made using a paired Student's t-test. The relationship between continuous variables was assessed using Pearson correlation coefficients. For all analyses, statistical significance was accepted as $p < 0.05$. Statistical analyses were completed with SAS 9.4 (SAS Institute Inc, Cary, North Carolina).

RESULTS

Baseline characteristics of the study population before acute VE are shown in Table 1. The proportion of women in the study population was 19%, and the average body mass index was 29.1 ± 5.0 kg/m^2. The prevalence of known coronary artery disease and previous myocardial infarction were 67% and 33%, respectively. Hypertension was present in 43% of subjects, and 86% were taking an angiotensin-converting enzyme inhibitor or angiotensin receptor blocker, 90% a beta blocker, and 33% a thiazide diuretic. Echocardiographic parameters showed that the average LV ejection fraction (LVEF) was 40.3 ± 8.9%, LV end-diastolic volume (LVEDV) was 199.7 ± 48.4 ml, medial E/e′ was 14.7 ± 9.1, and right ventricular systolic pressure was 28.0 ± 5.4 mmHg. Although plasma ANP and BNP were mildly elevated, plasma aldosterone and angiotensin II levels were within the normal range, which is consistent with PSD (12).

RESPONSE TO ACUTE VOLUME EXPANSION. Tadalafil and SC placebo. Subjects randomized to receive tadalafil and SC placebo had no significant change in systolic blood pressure or heart rate with acute saline VE compared with baseline (Table 2). In response to VE, pre-treatment with tadalafil and SC placebo resulted in increased LVEDV (209.8 ml vs. 196.1 ml; $p = 0.006$) and right ventricular systolic pressure (30.6 mm Hg vs. 28.1 mm Hg; $p = 0.037$), with no change in LVEF (39.4% vs. 38.9%; $p = 0.551$). With VE, ANP and plasma cGMP increased, aldosterone decreased, whereas BNP and angiotensin II remained unchanged. Renal response to VE, as assessed by renal plasma flow (RPF) (364.1 ml/min vs. 302.6 ml/min; $p = 0.023$), urine flow (7.1 vs. 4.4 ml/min; $p < 0.001$), and sodium excretion (245.1 mEq/min vs. 159.0 mEq/min; $p < 0.001$), was higher than baseline in the subjects pre-treated with tadalafil and SC placebo. GFR tended to be higher (82.6 ml/min vs. 72.7 ml/min; $p = 0.081$) in response to VE.

Tadalafil and SC BNP. Subjects treated with tadalafil and SC BNP had lower systolic blood pressure (112.4 mm Hg vs. 124.7 mm Hg; $p < 0.001$) and higher heart rate (62.4 beats/min vs. 58.9 beats/min;

TABLE 2 Clinical Outcomes in Tadalafil and SC Placebo Versus Tadalafil and SC BNP at Baseline and After Normal Saline VE

	Tadalafil and SC Placebo			Tadalafil and SC BNP		
Variable	Baseline (n = 21)	VE (n = 21)	p Value (baseline vs. VE)	Baseline (n = 21)	VE (n = 21)	p Value (baseline vs. VE)
Systolic BP (mm Hg)	120.9 ± 18.3	118.3 ± 14.4	0.248	124.7 ± 14.2	112.4 ± 13.7	<0.001
Diastolic BP (mm Hg)	68.4 ± 10.0	62.9 ± 8.6	0.007	69.3 ± 8.9	60.3 ± 8.3	<0.001
Heart rate (beats/min)	59.6 ± 8.6	61.4 ± 9.0	0.235	58.9 ± 8.4	62.4 ± 9.2	0.018
GFR (ml/min)	72.7 ± 33.6	82.6 ± 24.2	0.081	79.2 ± 38.3	67.9 ± 32.8	0.015
Renal plasma flow (ml/min)	302.6 ± 152.3	364.1 ± 122.8	0.023	333.9 ± 158.7	258.9 ± 133.2	0.022
Urine flow (ml/min)	4.4 ± 2.7	7.1 ± 2.8	<0.001	5.5 ± 3.3	5.3 ± 4.0	0.842
Sodium excretion (mEq/min)′	159.0 ±78.8	245.1 ± 112.7	<0.001	204.4 ± 134.2	246.2 ± 130.5	0.250
Urinary cGMP excretion (pmol/min)	796.4 ± 428.9	824.9 ± 506.2	0.671	852.9 ± 481.7	3,419.8 ± 1,993.9	<0.001
LVEF (%)	38.9 ± 7.7	39.4 ± 7.6	0.551	38.8 ± 9.0	43.1 ± 7.8	<0.001
LV end-diastolic volume (ml)	196.1 ± 46.3	209.8 ± 49.0	0.006	199.1 ± 47.0	177.2 ± 46.1	0.005
LV end-systolic volume (ml)	119.7 ± 37.5	122.3 ± 39.1	0.625	127.6 ± 39.7	101.1 ± 37.0	<0.001
Cardiac output (l/min)	4.6 ± 0.8	5.1 ± 0.8	<0.001	4.6 ± 1.0	5.0 ± 1.0	0.095
E/e′	15.0 ± 7.7	14.3 ± 6.7	0.144	14.5 ± 8.6	12.8 ± 5.6	0.275
RVSP (mm Hg)	28.1 ± 7.9	30.6 ± 7.0	0.037	27.8 ± 5.7	26.8 ± 9.8	0.546
LAVI (ml/m^2)	85.8 ± 26.6	92.2 ± 23.6	0.112	86.2 ± 14.7	76.4 ± 16.9	0.017
ANP (pg/ml)	92.9 ± 81.5	113.1 ± 100.7	0.044	71.4 ± 45.4	56.0 ± 38.5	0.079
BNP (pg/ml)	144.5 ± 97.5	151.8 ± 112.5	0.208	146.5 ± 107.1	1297.5 ± 1380.9	<0.001
cGMP (pmol/ml)	4.0 ± 2.1	5.4 ± 3.3	0.014	3.9 ± 2.0	18.9 ± 13.6	<0.001
Aldosterone (ng/dl)	4.6 ± 3.3	2.7 ± 1.0	0.005	3.7 ± 2.7	3.5 ± 1.8	0.850
Angiotensin II (pg/ml)	3.8 ± 3.8	3.3 ± 2.4	0.528	3.3 ± 2.3	3.8 ± 2.3	0.248

Values are mean ± SD.

BP = blood pressure; LAVI = left atrial volume index; LVEF = left ventricular ejection fraction; RVSP = right ventricular systolic pressure; SC = subcutaneous; VE = volume expansion; other abbreviations as in Table 1.

p = 0.018) with VE compared with baseline (Table 2). Pre-treatment with tadalafil and SC BNP resulted in increased LVEF (43.1% vs. 38.8%; p < 0.001) and decreased LVEDV (177.2 ml vs. 199.1 ml; p = 0.005), left ventricular end-systolic volume (LVESV) (101.1 ml vs. 127.6 ml; p < 0.001), and left atrial volume index (LAVI) (76.4 ml/m^2 vs. 86.2 ml/m^2; p = 0.017). Plasma cGMP increased with VE (18.9 pmol/ml vs. 3.9 pmol/ml; p < 0.001), whereas ANP, aldosterone, and angiotensin II remained unchanged. There was a decrease in RPF (258.9 ml/min vs. 333.9 ml/min; p = 0.022) and GFR (67.9 ml/min vs. 79.2 ml/min; p = 0.015) with VE. Pre-treatment with tadalafil and SC BNP resulted in no change in urine flow or sodium excretion in response to VE.

TADALAFIL AND SC BNP VERSUS TADALAFIL AND SC PLACEBO. Hemodynamic parameters. Pre-treatment with tadalafil and SC BNP resulted in a greater reduction in systolic blood pressure from baseline to VE (−12.3 ± 9.0 mm Hg vs. −2.5 ± 9.7 mm Hg; p = 0.002), with trends for greater reduction in diastolic pressure (−9.0 ± 9.4 mm Hg vs. −5.5 ± 8.3 mm Hg; p = 0.207) and a greater increase in heart rate (3.3 ± 5.8 mm Hg vs. 1.8 ± 6.8 mm Hg; p = 0.155) compared with tadalafil and SC placebo (Figure 2).

Echocardiographic parameters. Changes in echocardiographic parameters and pre-treatment with tadalafil and SC BNP versus tadalafil and SC placebo with VE response are shown in Figure 3. With VE, subjects randomized to tadalafil and SC BNP versus tadalafil and SC placebo had a greater increase in LVEF (5.8 ± 4.7% vs. 0.6 ± 4.3%; p = 0.002), with decreases in LAVI (−8.1 ± 12.1 ml/m^2 vs. 5.8 ± 14.1 ml/m^2; p = 0.005), LVEDV (−19.9 ± 24.5 ml vs. 12.5 ± 17.4 ml; p < 0.001), and LV end-systolic volume (LVESV) (−24.6 ± 21.1 ml vs. 1.4 ± 12.5 ml; p < 0.001). With VE, subjects randomized to tadalafil and SC BNP had a reduction in right ventricular systolic pressure (−1.3 ± 6.8 mm Hg vs. 2.3 ± 3.1 mm Hg; p = 0.130) compared with tadalafil and SC placebo, but this did not reach statistical significance.

Renal neurohormonal and physiological parameters. Tadalafil and SC BNP, compared with tadalafil and SC placebo, resulted in a decrease in urine flow with VE (−0.2 ± 4.6 ml/min vs. 2.6 ± 1.8 ml/min; p = 0.015), GFR (−12.7 ± 21.2 ml/min/1.73 m^2 vs. 9.4 ± 22.7 ml/min/1.73 m^2; p = 0.003), and RPF (−69.1 ± 124 ml/min vs. 54.5 ± 98.3 ml/min; p = 0.001). A higher urinary cGMP excretion response to VE was observed in the tadalafil and SC BNP versus tadalafil

FIGURE 2 Blood Pressure and Heart Rate Response to VE in Tadalafil and SC Placebo Versus Tadalafil and SC BNP

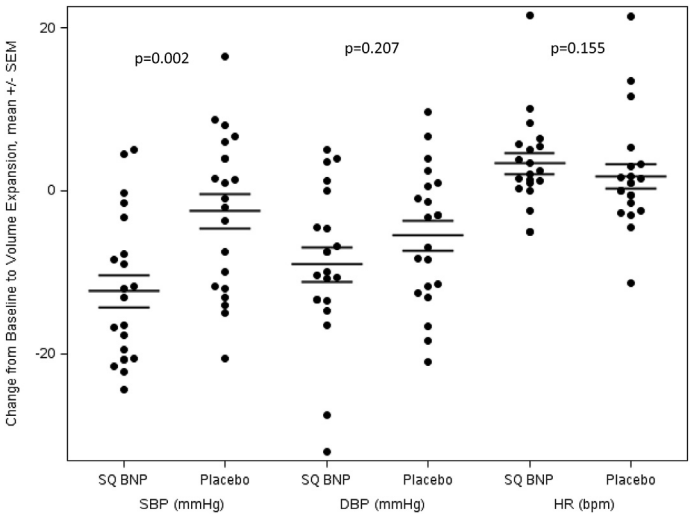

DBP = diastolic blood pressure; HR = heart rate; SBP = systolic blood pressure; VE = volume expansion; other abbreviations as in Figure 1.

and SC placebo group (2,567 ± 1,888 ml/min vs. 34 ± 355 ml/min; p < 0.001) (Figure 4).

With VE, higher plasma cGMP levels were observed with tadalafil and SC BNP versus tadalafil and SC placebo groups (15.3 ± 13.2 pmol/ml vs. 1.4 ± 2.4 pmol/ml; p < 0.001) (Table 3). ANP was decreased in the tadalafil and SC BNP versus tadalafil and SC placebo group (−15.1 ± 35.3 pg/ml vs. 20.3 ± 40.8 pg/ml; p = 0.007). There was no significant change in aldosterone and angiotensin II levels in response to VE in both groups (Table 3).

FIGURE 3 Echocardiographic Parameters and Response to VE in Tadalafil and SC Placebo Versus Tadalafil and SC BNP

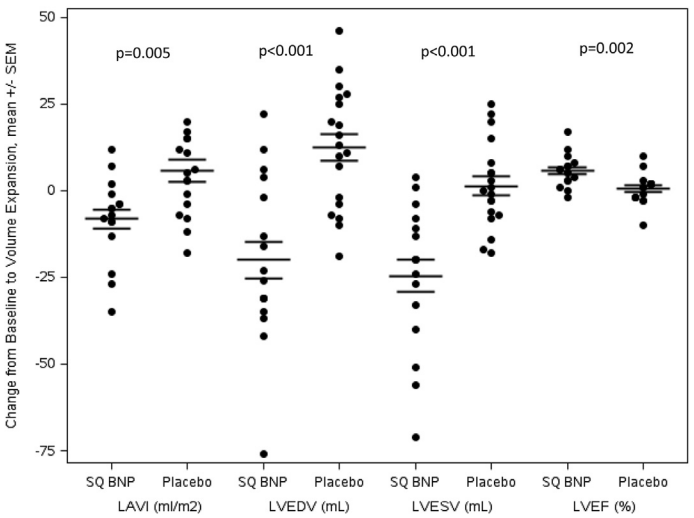

LAVI = left atrial volume index; LVEDV = left ventricular end-diastolic volume; LVESV = left ventricular end-systolic volume; LVEF = left ventricular ejection fraction; other abbreviations as in Figure 2.

Subgroup analysis (eGFR < 60 ml/min vs. eGFR ≥ 60 ml/min). We performed subgroup analyses for estimated GFR <60 ml/min versus estimated GFR ≥60 ml/min for blood pressure, echocardiographic parameters (including LAVI, LVEDV, LVESV, and EF), and renal parameters (including urine flow, RPF, and urinary cGMP). The results compared the tadalafil and SC placebo versus tadalafil and SC BNP subgroups. The additional analyses demonstrated that those with estimated GFR ≥60 ml/min had statistically worsened renal outcomes (urine flow, GFR, RPF) in the BNP versus placebo groups. Among those with an estimated GFR <60 ml/min, there was no statistically significant difference. However, because the sample size in this subgroup was small (n = 4 in each group) and there did appear to be a trend for worsened renal outcomes in the BNP versus placebo groups, as demonstrated by GFR and RPF, we could not exclude the possibility of an association between BNP and worsened renal outcomes among those with a reduced estimated GFR. Further investigation with a larger population is necessary to determine susceptibility to deterioration of renal function when BNP is combined with tadalafil (Supplemental Table 2).

We also evaluated for a correlation between baseline GFR and outcomes. There was a negative correlation between baseline GFR and RPF, and a trend toward negative correlation for urine flow and GFR (p = 0.05 as cutoff for statistical significance) (Supplemental Table 3).

Correlation between change in blood pressure and renal outcomes. We conducted additional analyses in which the change in BP was plotted against the renal parameters (including urine flow, GFR, RPF, and urinary cGMP) in each treatment group to determine the degree with which BP reduction contributed to the results. In both the placebo and BNP groups, there was no significant association between change in blood pressure and renal outcomes. However, this was likely due to the small sample size, and therefore, further investigation with a larger population is needed to determine if greater reduction in blood pressure from a combination of BNP and PDEV inhibition may be related to worse renal outcomes (Supplemental Figure 1).

FIGURE 4 Renal Parameters and Response to VE in Tadalafil and SC Placebo Versus Tadalafil and SC BNP

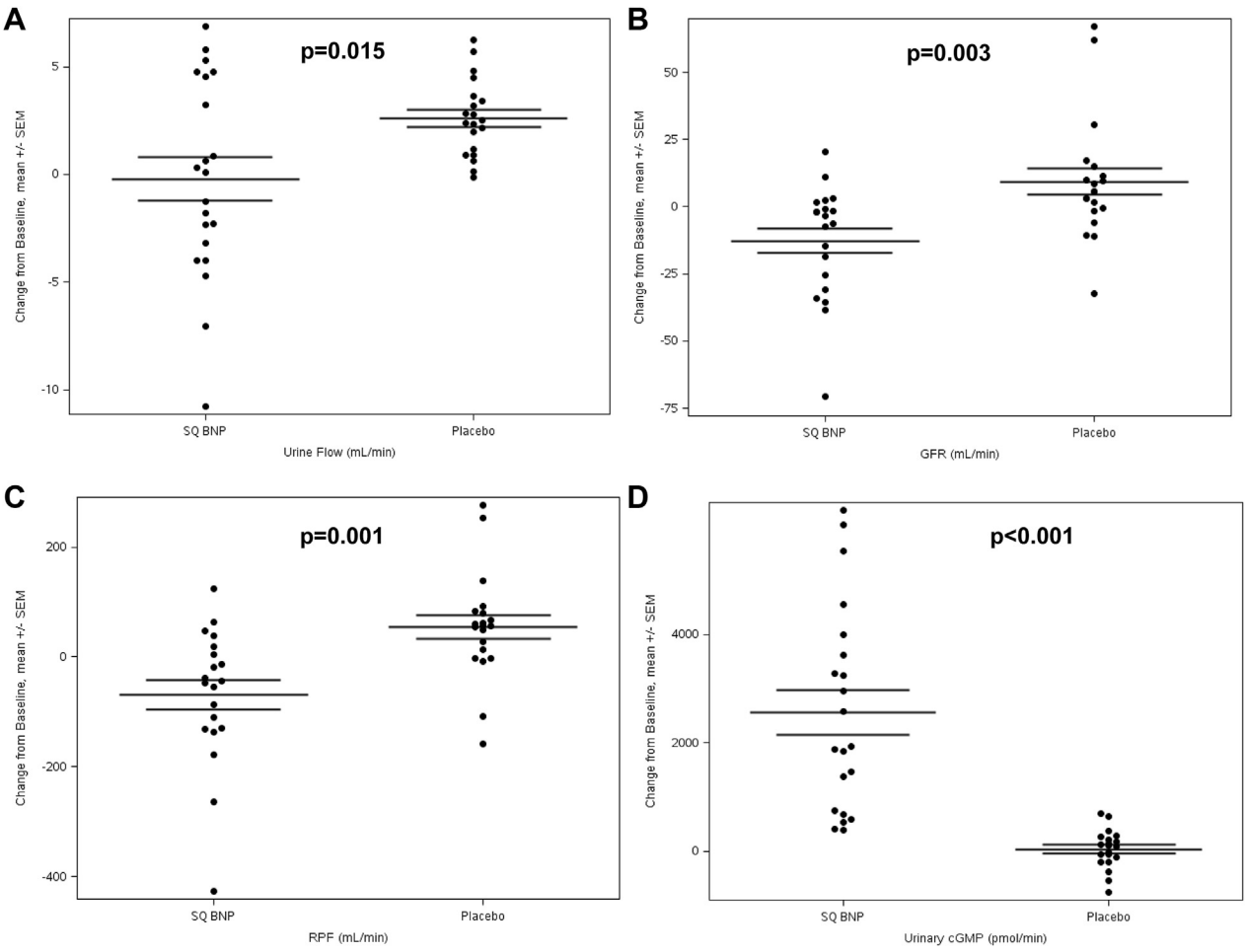

(A) Urine flow. **(B)** GFR. **(C)** Renal plasma flow (RPF). **(D)** Urinary cyclic guanosine monophosphate (cGMP). Other abbreviations as in Figures 1 and 2.

ADVERSE EVENTS. None of the subjects who received tadalafil and SC placebo had adverse events. In the treatment group, after administration of tadalafil and SC BNP, 2 subjects (10%) experienced nausea and/or vomiting on the first morning of the study, 1 (5%) had transient chest discomfort that resolved spontaneously, and 1 (5%) had hypotension that subsequently resolved with saline infusion.

DISCUSSION

The present study was the first-in-human study to define the acute cardiorenal effects of combination tadalafil and SC BNP in response to VE in subjects with PSD and renal dysfunction. Based on our preclinical studies, we hypothesized that the combination of tadalafil and SC BNP would enhance the cardiorenal response to VE in subjects with PSD with renal dysfunction versus tadalafil alone. In this cohort of subjects with PSD and renal dysfunction, pre-treatment with tadalafil and SC BNP before VE resulted in improved cardiac function compared

TABLE 3 Humoral Outcomes in Tadalafil and SC Placebo Versus Tadalafil and SC BNP, Change From Baseline to After Normal Saline VE

Variable	Tadalafil and SC Placebo (n = 21)	Tadalafil and SC BNP (n = 21)	p Value
ANP (pg/ml)	20.3 ± 40.8	−15.1 ± 35.3	0.007
BNP (pg/ml)	7.3 ± 25.1	1,201.7 ± 1,382.1	<0.001
cGMP (pmol/ml)	1.4 ± 2.4	15.3 ± 13.2	<0.001
Aldosterone (ng/dl)	−1.8 ± 2.7	−0.1 ± 3.2	0.073
Angiotensin II (pg/ml)	−0.5 ± 3.7	0.6 ± 2.0	0.108

Values are mean ± SD.
Abbreviations as in Tables 1 and 2.

with tadalafil and SC placebo, as evidenced by a greater increase in LVEF and reduction in LAVI, LVESV, and LVEDV. Plasma ANP was decreased in the tadalafil and SC BNP versus tadalafil and SC placebo group, which suggested a decrease in cardiac filling pressure in response to VE in the tadalafil and SC BNP group. Pre-treatment with tadalafil and SC BNP before acute VE resulted in increased cGMP levels. However, the favorable cardiac response to VE with tadalafil and SC BNP was associated with an attenuated renal response. Specifically, renal responses to acute VE after pre-treatment with tadalafil and SC BNP, including RPF, GFR, and urine flow, were reduced compared with tadalafil and SC placebo.

PSD, or asymptomatic LV dysfunction, is considered ACC/AHA stage B HF (13). Although the exact definition of LV systolic dysfunction varies in different trials, it is generally defined as LVEF <40% to 50%. It is a common entity that affects approximately 3% to 6% of the general adult population of the United States, and it is more common among men and those with cardiovascular comorbidities (e.g., coronary artery disease and hypertension) (2,14). PSD is associated with increased mortality and cardiovascular events, and the annual incidence of progression from PSD to symptomatic HF is approximately 5% to 20% (14–16). Neurohormonal activation plays an important role in the progression along the HF spectrum. The neurohumoral substudy of the SOLVD (Studies of Left Ventricular Dysfunction) cohort demonstrated a significant increase in neurohumoral activation in the symptomatic cohort compared with the prevention cohort (i.e., PSD) (12). The neurohumoral profile of the present cohort was similar to those in the SOLVD prevention cohort, with a mild activation of the NP system without activation of the renin angiotensin aldosterone system.

Impaired sodium excretion to sodium load is a pathognomonic feature of clinical congestive HF (17). With normal physiology, when renal perfusion and sodium delivery to the kidneys is reduced, renin is released, which eventually stimulates aldosterone, which results in sodium retention. Those with symptomatic HF have excessive renin-angiotensin-aldosterone activation, and subsequent salt retention and inability to excrete sodium load, which leads to increased intra- and extravascular volume (18). This leads to typical HF symptoms, including dyspnea and edema. We previously reported that there is impaired renal response to VE in patients with PSD compared with normal subjects (8). Renal cGMP activation was paradoxically decreased with attenuated urinary sodium excretion in subjects with PSD when exposed to acute VE compared with normal subjects. However, when exogenous SC BNP was administered before acute VE, the patients with PSD experienced an increase in urinary cGMP and natriuresis similar to subjects without underlying cardiac or renal dysfunction (19,20). Potential mechanisms for impaired renal response to acute VE in patients with PSD include decreased plasma ANP levels, upregulation of PDEV that leads to greater degradation of cGMP, down-regulation of NPs in the kidney, and upregulation of neutral endopeptidases, which leads to disruption of the homeostasis of NPs with downstream effects on the renal system.

Phosphodiesterase-5 is ubiquitous in the body, and PDEV inhibitors are currently approved by the Food and Drug Administration (FDA) for the management of erectile dysfunction and pulmonary hypertension. PDEV metabolizes cGMP, a second messenger that leads to vascular smooth muscle relaxation and subsequent vasodilatation. Renal cGMP plays an important role in modulating GFR and natriuresis. The effects of long-term PDEV inhibition in experimental HF and its influence on enhancing the renal actions of exogenous BNP with maximizing the cGMP system in an animal model have been previously described (9). The renal effect of BNP and PDEV inhibition were synergistic compared with BNP monotherapy, which suggested that PDEV upregulation might contribute to NP desensitization. Thus, there might be a role for combined treatment with PDEV inhibitors and BNP to maximize the benefits of endogenous and exogenous NPs.

The present study was the first-in-human study to define the acute biological effects of combination tadalafil and BNP on the cardiorenal response to VE in PSD. There was a significant improvement in cardiac function in response to acute VE with combination tadalafil and BNP administration in subjects with PSD and renal dysfunction. However, there was a worsening of renal function that might have been due to the decrease in blood pressure and RPF observed with combination tadalafil with BNP. With decreases in renal perfusion pressure, sodium delivery in the descending loop of Henle decreases, which results in greater sodium reabsorption and reduced sodium excretion (21). Although autoregulatory mechanisms in the kidney attempts to maintain a relatively constant GFR with higher renal artery blood pressures, GFR reduces when the renal vasodilatory and vasoconstrictive homeostatic mechanisms are overwhelmed (22).

Clinical and therapeutic implications include modulation of the NP system and its potential beneficial cardiac and renal effects. Sacubitril/valsartan, which has been approved for the treatment of HF with reduced EF, exerts its action in part via neprilysin inhibition and potentiation of the NP pathway (23). By decreasing NP degradation, there are important outcome benefits for patients with systolic dysfunction and HF. In addition, different patient populations may have different endogenous levels of NPs; therefore, therapeutic options should focus on both inhibition of NP degradation and exogenous administration of NPs (24,25).

Given the findings of this study regarding blood pressure reduction and effects on renal parameters, we believe further investigation is necessary with different doses of PDEV inhibitors and subcutaneous BNP to determine if there may be beneficial cardiac and renal effects at different doses. Furthermore, additional investigation is necessary in unique populations, such as the hypertensive population, to see if there may be a clinical benefit.

In summary, the results demonstrated that in human subjects with PSD and renal dysfunction, combination tadalafil and BNP compared with tadalafil alone resulted in cardiac function improvement but reduced renal function with acute VE.

STUDY LIMITATIONS. A limitation of this study was that only 1 dose of tadalafil and SC BNP was tested. Future studies are needed to further evaluate the effects of lower, non-hypotensive doses of tadalafil and SC BNP. The study also assessed acute physiological derangements, and hence, it might not reflect the long-term effects of tadalafil and SC BNP on cardiorenal function and the neurohormonal effects in PSD.

CONCLUSIONS

In this first-in-human study of subjects with PSD and renal dysfunction, pre-treatment with tadalafil and BNP compared with tadalafil alone resulted in improved cardiac function but worsened renal function with VE. Combination tadalafil and BNP demonstrated potentiation of the cGMP pathway, with increased plasma and urinary cGMP levels. However, combination tadalafil and BNP also led to decreased blood pressures and reduced renal perfusion, which might explain why there was worsened renal function. There was a differential cardiac versus renal response to VE with combination of tadalafil and BNP in subjects with PSD and renal dysfunction.

ADDRESS FOR CORRESPONDENCE: Dr. Horng H. Chen, Department of Cardiovascular Diseases, Mayo Clinic, 200 First Street Southwest, Rochester, Minnesota 55905. E-mail: chen.horng@mayo.edu.

PERSPECTIVES

COMPETENCY IN MEDICAL KNOWLEDGE: In PSD, which is defined as systolic dysfunction in the absence of signs and symptoms of HF, inhibition of PDEV in combination with exogenous BNP administration resulted in improved cardiac function but worsened renal function in response to acute VE.

TRANSLATIONAL OUTLOOK: Understanding the cardiorenal effects and outcomes of combination PDEV with exogenous BNP may impact the clinical management of patients with PSD and renal dysfunction.

REFERENCES

1. Benjamin EJ, Virani SS, Callaway CW, et al. Heart disease and stroke statistics-2018 update: a report from the American Heart Association. Circulation 2018;137:e67–492.

2. Wang TJ, Evans JC, Benjamin EJ, Levy D, LeRoy EC, Vasan RS. Natural history of asymptomatic left ventricular systolic dysfunction in the community. Circulation 2003;108:977–82.

3. Volpe M, Tritto C, DeLuca N, et al. Abnormalities of sodium handling and of cardiovascular adaptations during high salt diet in patients with mild heart failure. Circulation 1993;88:1620–7.

4. Ledwidge M, Gallagher J, Conlon C, et al. Natriuretic peptide-based screening and collaborative care for heart failure: the STOP-HF randomized trial. JAMA 2013;310:66–74.

5. Wang TJ. Natriuretic peptide deficiency-when there is too little of a good thing. JAMA Cardiol 2018;3:7–9.

6. Stevens TL, Burnett JC Jr., Kinoshita M, Matsuda Y, Redfield MM. A functional role for endogenous atrial natriuretic peptide in a canine model of early left ventricular dysfunction. J Clin Invest 1995;95:1101–8.

7. Takimoto E, Koitabashi N, Hsu S, et al. Regulator of G protein signaling 2 mediates cardiac compensation to pressure overload and antihypertrophic effects of PDE5 inhibition in mice. J Clin Invest 2009;119:408–20.

8. McKie PM, Schirger JA, Costello-Boerrigter LC, et al. Impaired natriuretic and renal endocrine response to acute volume expansion in pre-clinical systolic and diastolic dysfunction. J Am Coll Cardiol 2011;58:2095–103.

9. Chen HH, Huntley BK, Schirger JA, Cataliotti A, Burnett JC Jr. Maximizing the renal cyclic 3′-5′-guanosine monophosphate system with type V phosphodiesterase inhibition and exogenous natriuretic peptide: a novel strategy to improve renal function in experimental overt heart failure. J Am Soc Nephrol 2006;17:2742–7.

10. Forfia PR, Lee M, Tunin RS, Mahmud M, Champion HC, Kass DA. Acute phosphodiesterase 5 inhibition mimics hemodynamic effects of B-type natriuretic peptide and potentiates B-type natriuretic peptide effects in failing but not normal canine heart. J Am Coll Cardiol 2007;49:1079–88.

11. Lang RM, Badano LP, Mor-Avi V, et al. Recommendations for cardiac chamber quantification by echocardiography in adults: an update from the American Society of Echocardiography and the European Association of Cardiovascular Imaging. J Am Soc Echocardiogr 2015;28:1–39 e14.

12. Francis GS, Benedict C, Johnstone DE, et al. Comparison of neuroendocrine activation in patients with left ventricular dysfunction with and

without congestive heart failure. A substudy of the Studies of Left Ventricular Dysfunction (SOLVD). Circulation 1990;82:1724–9.

13. Yancy CW, Jessup M, Bozkurt B, et al. 2017 ACC/AHA/HFSA focused update of the 2013 ACCF/AHA guideline for the management of heart failure: a report of the American College of Cardiology/American Heart Association Task Force on Clinical Practice Guidelines and the Heart Failure Society of America. J Am Coll Cardiol 2017;70:776–803.

14. Wang TJ, Levy D, Benjamin EJ, Vasan RS. The epidemiology of "asymptomatic" left ventricular systolic dysfunction: implications for screening. Ann Intern Med 2003;138:907–16.

15. SOLVD Investigators, Yusuf S, Pitt B, Davis CE, Hood WB Jr., Cohn JN. Effect of enalapril on mortality and the development of heart failure in asymptomatic patients with reduced left ventricular ejection fractions. N Engl J Med 1992;327:685–91.

16. Lauer MS, Evans JC, Levy D. Prognostic implications of subclinical left ventricular dilatation and systolic dysfunction in men free of overt cardiovascular disease (the Framingham Heart Study). Am J Cardiol 1992;70:1180–4.

17. Braunwald E, Plauth WH Jr., Morrow AG. A Method for the detection and quantification of impaired sodium excretion. Results of an oral sodium tolerance test in normal subjects and in patients with heart disease. Circulation 1965;32:223–31.

18. Selektor Y, Weber KT. The salt-avid state of congestive heart failure revisited. Am J Med Sci 2008;335:209–18.

19. Wan SH, McKie PM, Schirger JA, et al. Chronic peptide therapy with B-type natriuretic peptide in patients with pre-clinical diastolic dysfunction (stage B heart failure). J Am Coll Cardiol HF 2016;4:539–47.

20. Zhao W, Katzmarzyk PT, Horswell R, Wang Y, Johnson J, Hu G. HbA1c and heart failure risk among diabetic patients. J Clin Endocrinol Metab 2014;99:E263–7.

21. Haas JA, Granger JP, Knox FG. Effect of renal perfusion pressure on sodium reabsorption from proximal tubules of superficial and deep nephrons. Am J Physiol 1986;250:F425–9.

22. Shipley RE, Study RS. Changes in renal blood flow, extraction of inulin, glomerular filtration rate, tissue pressure and urine flow with acute alterations of renal artery blood pressure. Am J Physiol 1951;167:676–88.

23. McMurray JJ, Packer M, Desai AS, et al. Angiotensin-neprilysin inhibition versus enalapril in heart failure. N Engl J Med 2014;371:993–1004.

24. Raymond I, Groenning BA, Hildebrandt PR, et al. The influence of age, sex and other variables on the plasma level of N-terminal pro brain natriuretic peptide in a large sample of the general population. Heart 2003;89:745–51.

25. Lam CS, Burnett JC Jr., Costello-Boerrigter L, Rodeheffer RJ, Redfield MM. Alternate circulating pro-B-type natriuretic peptide and B-type natriuretic peptide forms in the general population. J Am Coll Cardiol 2007;49:1193–202.

KEY WORDS B-type natriuretic peptide, cardiorenal, heart failure, nesiritide, phosphodiesterase inhibition, systolic dysfunction

APPENDIX For supplemental figures and tables, please see the online version of this paper.

JACC: BASIC TO TRANSLATIONAL SCIENCE VOL. 4, NO. 8, 2019

EDITORIAL COMMENT

Paradoxical Cardiorenal Responses Following Acute Vasodilator/Natriuretic Treatment in Presystolic Heart Failure

Should We Be Surprised?*

Tamar S. Polonsky, MD, MSCI,[a] George L. Bakris, MD[b]

The kidney is a regulatory organ and is focused on maintenance of fluid and pressure homeostasis. The kidney is equipped with many mechanisms by which to maintain volume homeostasis; it takes its cues, however, from its "marital partner," the heart, in many circumstances and especially when the heart is failing (1). The heart and the kidney communicate through hormonal and neural systems to maintain life and organ function. The kidney is especially sensitive to changes in sodium delivery and sudden blood pressure reductions, and thus 1 needs to distinguish between immediate and long-term responses to hemodynamic changes of the kidney. What is perceived as an adverse response initially may be a beneficial response chronically, especially if the cardiovascular response is positive.

SEE PAGE 962

The current study by Wan et al. (2) in this issue of *JACC: Basic to Translational Science* describes the acute cardiorenal effects of combining tadalafil, a phosphodiesterase-5 inhibitor (PDE5i), with nesiritide, a recombinant human B-type natriuretic peptide (BNP), in response to acute saline volume expansion in participants with preclinical systolic dysfunction (PSD) and stages 2 and 3A chronic kidney disease (CKD). The authors hypothesized that this combination would enhance the cardiorenal response to volume expansion in PSD compared with a PDE5i alone. Unfortunately, this was not the case. All variables reflecting cardiac performance and related compensatory hormonal changes were favorable; renal response was not. Pre-treatment with tadalafil alone increased renal plasma, urine flow, and sodium excretion. In contrast, pre-treatment with tadalafil plus nesiritide decreased renal plasma flow, glomerular filtration rate, and urine flow. Hence, addition of human BNP altered the predicted renal response. Before discussing the reasons for this paradox, it is important to note that the participants received only 1 dose of tadalafil plus nesiritide or placebo before the acute saline volume expansion.

What are possible reasons for this response? First, we need to understand the neurohormonal changes that affect the heart and the kidney at this stage of heart failure in the presence of CKD. As the authors note (2), the neurohumoral profile of their cohort is reminiscent of those in the SOLVD (Studies of Left Ventricular Dysfunction) Prevention cohort; that is, mild activation of the natriuretic peptide system and no activation of the renin-angiotensin-aldosterone system. An impaired renal response to acute volume expansion in the patients with PSD compared with normal subjects is known. In addition, patients with left ventricular dysfunction who are asymptomatic or have Class II heart failure symptoms already have a decreased ability to augment plasma atrial natriuretic

*Editorials published in *JACC: Basic to Translational Science* reflect the views of the authors and do not necessarily represent the views of *JACC: Basic to Translational Science* or the American College of Cardiology.

From the [a]Department of Medicine, Section of Cardiology, University of Chicago Medicine, Chicago, Illinois; and the [b]American Heart Association Comprehensive Hypertension Center, Section of Endocrinology, Diabetes and Metabolism, University of Chicago Medicine, Chicago, Illinois. Both authors have reported that they have no relationships relevant to the contents of this paper to disclose.

The authors attest they are in compliance with human studies committees and animal welfare regulations of the authors' institutions and Food and Drug Administration guidelines, including patient consent where appropriate. For more information, visit the *JACC: Basic to Translational Science* author instructions page.

ISSN 2452-302X https://doi.org/10.1016/j.jacbts.2019.11.002

peptide in response to sodium loading and thus may retain sodium.

The importance of the natriuretic peptide system in response to volume expansion in PSD is further underscored by data from animal studies showing significant urinary retention when the natriuretic peptide receptor-A is blocked (3). In contrast, a study randomized 36 adults with preclinical diastolic dysfunction to receive subcutaneous BNP for 12 weeks versus placebo (4). This study reported an increase in urinary cyclic guanosine monophosphate (cGMP) and natriuresis at 12 weeks with volume expansion, an effect similar to that in subjects without underlying cardiac or kidney dysfunction.

Given the data from the current study (2), potential mechanisms for impaired renal response to acute volume expansion in patients with PSD include decreased plasma atrial natriuretic peptide levels, up-regulation of PDE5 leading to greater degradation of cGMP, down-regulation of natriuretic peptides in the kidney, and up-regulation of neutral endopeptidases leading to disruption of the homeostasis of natriuretic peptides with downstream effects within the nephron. This latter hypothesis seems most plausible based on data regarding cGMP levels in the combination group.

As the authors speculate (2), PDE5 metabolizes cGMP, a second messenger that leads to vascular smooth muscle relaxation and subsequent vasodilation. Renal cGMP plays an important role in modulating glomerular filtration rate (GFR) and natriuresis. Chronic PDE5 inhibition for 10 days in dogs with experimental heart failure accentuated the renal actions of exogenous BNP by maximizing the cGMP system (5). The renal effect of BNP and PDE5i were synergistic compared with BNP monotherapy. This suggests that PDE5 up-regulation may contribute to natriuretic peptide desensitization. Thus, there may be a role for combined chronic treatment using both PDE5i and BNP to maximize the benefits of endogenous and exogenous natriuretic peptides.

The divergent responses between the heart and the kidney in the study by Wan et al. (2) may also relate to acute hemodynamic accommodation to changes in blood pressure. Specifically, there was a large drop in systolic blood pressure within the normal range from 125 to 112 mm Hg that was not seen in the placebo group. This would have an acute effect of reducing the GFR and, to a lesser extent, reducing renal plasma flow, especially in the presence of CKD. This would contribute to decreased sodium delivery to the descending loop of Henle, and result in greater sodium reabsorption and thus less sodium excretion. Moreover, 1 should also note that although autoregulatory mechanisms in the kidney attempt to maintain a relatively constant GFR within the normal pressure range, acute reductions even within this range result in these homeostatic mechanisms being transiently overwhelmed until they re-establish homeostasis.

Taken together with previous data, this study (2) helps in understanding the acute changes imposed by modifying the natriuretic peptide system in the early stage of heart failure and has clinical and therapeutic implications. Use of sacubitril/valsartan, currently approved for the treatment of advanced heart failure with reduced ejection fraction, resulted in positive renal benefits when used chronically (6). However, it should be assessed in this earlier setting of heart failure because of its potentiating effects on the natriuretic peptide pathway.

Finally, these results should remind us not to make decisions about long-term outcomes from acute changes in kidney function, especially if they are understandable based on hemodynamic and neurohumoral changes. This is exemplified by the original reports 20 years ago of nephrotoxicity from angiotensin-converting enzyme inhibitors because there were acute increases of 20% to 30% in serum creatinine (1). Publication of the early reports resulted in a major hesitancy to use this class of medication in heart failure and CKD. However, use over the last 20 years has taught us that up to a 30% increase in serum creatinine translates into equal or better cardiovascular and renal outcomes. Thus, it must be remembered that the current study (2) of acute findings in the kidney may translate to beneficial long-term outcomes.

ADDRESS FOR CORRESPONDENCE: Dr. George L. Bakris, American Heart Association Comprehensive Hypertension Center, University of Chicago Medicine, 5841 South Maryland Avenue, MC 1027, Chicago, Illinois 60637. E-mail: gbakris@uchicago.edu.

REFERENCES

1. Polonsky TS, Bakris GL. Heart failure and changes in kidney function: focus on understanding, not reacting. Heart Fail Clin 2019;15:455–61.

2. Wan S-H, Torres-Courchoud I, McKie PM, et al. Cardiac versus renal response to volume expansion in preclinical systolic dysfunction with PDEV inhibition and BNP. J Am Coll Cardiol Basic Trans Science 2019;4:962–72.

3. Forfia PR, Lee M, Tunin RS, Mahmud M, Champion HC, Kass DA. Acute phosphodiesterase

5 inhibition mimics hemodynamic effects of B-type natriuretic peptide and potentiates B-type natriuretic peptide effects in failing but not normal canine heart. J Am Coll Cardiol 2007;49:1079–88.

4. Wan SH, McKie PM, Schirger JA, et al. Chronic peptide therapy with B-type natriuretic peptide in patients with preclinical diastolic dysfunction (stage B heart failure). J Am Coll Cardiol HF 2016;4:539–47.

5. Chen HH, Huntley BK, Schirger JA, Cataliotti A, Burnett JC Jr. Maximizing the renal cyclic 3′-5′-guanosine monophosphate system with type V phosphodiesterase inhibition and exogenous natriuretic peptide: a novel strategy to improve renal function in experimental overt heart failure. J Am Soc Nephrol 2006;17:2742–7.

6. Haynes R, Judge PK, Staplin N, et al. Effects of sacubitril/valsartan versus irbesartan in patients with chronic kidney disease. Circulation 2018;138:1505–14.

KEY WORDS glomerular filtration rate, natriuresis, nesiritide, systolic heart failure

JACC: BASIC TO TRANSLATIONAL SCIENCE VOL. 4, NO. 8, 2019

STATE-OF-THE-ART REVIEW

Epigenetics in Cardiac Hypertrophy and Heart Failure

Chia-Feng Liu, PhD,[a] W.H. Wilson Tang, MD[a,b]

JACC: BASIC TO TRANSLATIONAL SCIENCE CME/MOC/ECME

This article has been selected as this month's *JACC: Basic to Translational Science* CME/MOC/ECME activity, available online at http://www.acc.org/jacc-journals-cme by selecting the *JACC* Journals CME/MOC/ECME tab.

Accreditation and Designation Statement

The American College of Cardiology Foundation (ACCF) is accredited by the Accreditation Council for Continuing Medical Education (ACCME) and the European Board for Accreditation in Cardiology (EBAC) to provide continuing medical education for physicians.

The ACCF designates this Journal-based CME/MOC/ECME activity for a maximum of 1 AMAPRA Category 1 Credit or 1 EBAC Credit. Physicians should only claim credit commensurate with the extent of their participation in the activity.

Successful completion of this CME activity, which includes participation in the evaluation component, enables the participant to earn up to 1 Medical Knowledge MOC point in the American Board of Internal Medicine's (ABIM) Maintenance of Certification (MOC) program. Participants will earn MOC points equivalent to the amount of CME credits claimed for the activity. It is the CME activity provider's responsibility to submit participant completion information to ACCME for the purpose of granting ABIM MOC credit.

Epigenetics in Cardiac Hypertrophy and Heart Failure will be accredited by the European Board for Accreditation in Cardiology (EBAC) for 1 hour of External CME credits. Each participant should claim only those hours of credit that have actually been spent in the educational activity. The Accreditation Council for Continuing Medical Education (ACCME) and the European Board for Accreditation in Cardiology (EBAC) have recognized each other's accreditation systems as substantially equivalent. Apply for credit through the post-course evaluation.

Method of Participation and Receipt of CME/MOC/ECME Certificate

To obtain credit for *JACC: Basic to Translational Science* CME/MOC/ECME, you must:

1. Be an ACC member or JACBTS subscriber.
2. Carefully read the CME/MOC/ECME-designated article available online and in this issue of the *journal*.
3. Answer the post-test questions. At least 2 questions provided must be answered correctly to obtain credit.
4. Complete a brief evaluation.
5. Claim your CME/MOC/ECME credit and receive your certificate electronically by following the instructions given at the conclusion of the activity.

CME/MOC/ECME Objective for This Article: Upon completion of this activity, the learner should be able to: 1) identify the inheritance pattern of hypertrophic cardiomyopathy; 2) discuss the recommendations for screening first degree family members of patients with inherited cardiomyopathies (such as hypertrophic cardiomyopathy); and 3) compare the molecular mechanisms for epigenetic gene regulation.

CME/MOC/ECME Editor Disclosure: CME/MOC/ECME Editor L. Kristin Newby, MD, is supported by research grants from Amylin, Bristol-Myers Squibb Company, GlaxoSmithKline, Sanofi, Verily Life Sciences (formerly Google Life Sciences), the MURDOCK Study, NIH, and PCORI; receives consultant fees/honoraria from BioKier, DemeRx, MedScape/TheHeart.org, Metanomics, Philips Healthcare, Roche Diagnostics, CMAC Health Education & Research Institute; serves as an Officer, Director, Trustee, or other fiduciary role for the AstraZeneca HealthCare Foundation and the Society of Chest Pain Centers (now part of ACC); and serves in another role for the American Heart Association and is the Deputy Editor of *JACC: Basic to Translational Science*.

Author Disclosures: Dr. Tang is supported by grants from the National Institutes of Health (NIH) and the Office of Dietary Supplements (R01DK106000, R01HL126827), Collins Family Fund, and Wortzman Family Fund. The content is solely the responsibility of the authors and does not necessarily represent the official views of the NIH. Dr. Tang has a financial relationship with Sequana Medical Inc. and MyoKardis Inc. Dr. Liu has reported that she does not have any relationships relevant to the contents of this paper to disclose.

Medium of Participation: Online (article and quiz).

CME/MOC/ECME Term of Approval

Issue Date: December 2019
Expiration Date: November 30, 2020

From the [a]Department of Cardiovascular and Metabolic Sciences, Lerner Research Institute, Cleveland Clinic, Cleveland, Ohio; and the [b]Department of Cardiovascular Medicine, Heart and Vascular Institute, Cleveland Clinic, Cleveland, Ohio. Dr. Tang is supported by grants from the National Institutes of Health (NIH) and the Office of Dietary Supplements (R01DK106000, R01HL126827), Collins Family Fund, and Wortzman Family Fund. The content is solely the responsibility of the authors and does

ISSN 2452-302X https://doi.org/10.1016/j.jacbts.2019.05.011

Epigenetics in Cardiac Hypertrophy and Heart Failure

Chia-Feng Liu, PhD,[a] W.H. Wilson Tang, MD[a,b]

HIGHLIGHTS

- **Epigenetic mechanisms associated with the pathological process of cardiac hypertrophy and failure include DNA methylation, post-modification of histones, ATP-dependent chromatin conformation and remodeling, and non-coding RNAs.**
- **Systemic- and cardiac-epigenetic mechanisms may both influence the disease processes of cardiac hypertrophy and failure.**
- **Identifying vital epigenetic machinery in cardiac diseases may facilitate developing personalized therapy for HF.**

SUMMARY

Heart failure (HF) is a complex syndrome affecting millions of people around the world. Over the past decade, the therapeutic potential of targeting epigenetic regulators in HF has been discussed extensively. Recent advances in next-generation sequencing techniques have contributed substantial progress in our understanding of the role of DNA methylation, post-translational modifications of histones, adenosine triphosphate (ATP)-dependent chromatin conformation and remodeling, and non-coding RNAs in HF pathophysiology. In this review, we summarize epigenomic studies on human and animal models in HF. (J Am Coll Cardiol Basic Trans Science 2019;4:976–93)

The word "epigenetics" is composed of a Greek prefix, "epi," meaning "upon," "on," or "around" and the word "genetics." Therefore, epigenetics can be defined as the mechanism that affects heritable changes in gene expression and function without alternating the sequence of the genome. It plays fundamental roles in regulating the architecture of chromatins and gene expression at various molecular levels for maintaining cell identity and controlling cell differentiation, which are critically important for normal development and diseases. Changes of the epigenome are hallmarks of various cancers and several potentially molecules have been identified as potential new drug therapies.

The study of epigenetics in cardiovascular diseases is a relatively new field. Heart failure (HF), being the leading cause of death worldwide, occurs when the myocardium has long been recognized to undergo structural and functional remodeling. Such processes may be the cause and/or consequence of various genomic and transcriptional reprogramming of the cardiomyocytes and other nearby cells. Hence, better understanding of how epigenetic regulations are involved in HF may open a new perspective for translational research into new diagnostic tools as well as novel strategies in drug design and discovery.

Epigenetic regulation can be classified at 4 different molecular levels: 1) DNA methylation, 2) post-translational modifications of histones, 3) adenoisine triphosphate (ATP)-dependent chromatin conformation and remodeling, and 4) non-coding RNAs. In this review, we will summarize the recent advances and provide an overview of the epigenomics studies focusing on HF in humans and animal models.

DNA METHYLATION: A POTENTIAL BIOMARKER FOR HF

The methylation of DNA in eukaryotes predominantly occurs at the fifth carbon of the pyrimidine ring of the

not necessarily represent the official views of the NIH. Dr. Tang has a financial relationship with Sequana Medical Inc. and MyoKardis Inc. Dr. Liu has reported that she does not have any relationships relevant to the contents of this paper to disclose. The authors attest they are in compliance with human studies committees and animal welfare regulations of the authors' institutions and Food and Drug Administration guidelines, including patient consent where appropriate. For more information, visit the *JACC: Basic to Translational Science* author instructions page.

Manuscript received February 26, 2019; revised manuscript received May 29, 2019, accepted May 30, 2019.

JACC: BASIC TO TRANSLATIONAL SCIENCE VOL. 4, NO. 8, 2019
DECEMBER 2019:976–93

ABBREVIATIONS AND ACRONYMS

BET = bromodomain

EZH2 = Enhancer of zeste homolog 2

HAT = histone acetyltransferase

HDAC = histone deacetylase

HDM = histone demethylase

HF = heart failure

HMT = histone methyltransferase

lnc-RNAs = long ncRNAs

PRC2 = polycomb repressor complex 2

PTMs = post-translational modifications

TAD = topologically associating domains

TMAO = trimethylamine *N*-oxide

cytosine (5mC) and followed by a guanine dinucleotide where cytosine and guanine are separated by a phosphate (CpG). DNA methylation plays a crucial role in gene regulation, particularly on transcriptional repression that depends on where methylation is located. Increased methylation of CpG-enriched regions, known as CpG islands (CGI) at the promoter region of genes, is often associated with gene silencing, whereas methylated CpG found in the gene body is usually related to gene activation (1). In many pathological conditions, particularly in the cancer genome, alteration of DNA methylation of genes is the first epigenetic hallmark associated with the disease process (2). For example, a typical signature in many types of cancer cells is the hypermethylation at CGI of tumor suppressor genes causing transcriptional silencing of these genes. The silencing of these tumor suppressor genes affects the progression of the tumorigenesis (3).

The pioneering genome-wide studies on DNA methylation in the failing human myocardium were performed a decade ago (4,5). Movassagh et al. first demonstrated that a large population of CGI and promoters were hypomethylated in the end-stage failing heart, and such differential DNA methylation patterns correlated with differential expression of angiogenic factors (4). Using methylated DNA immunoprecipitation followed by sequencing, they determined that the differential DNA methylation between non-failing and end-stage failing hearts did not occur evenly across the genome, but concentrated at promoter CGIs, intragenic CGIs, and gene bodies (5). In 2013, Haas et al. identified a set of candidate genes with altered DNA methylation status that may be involved in HF by using a lower-resolution method (6). Among these candidate genes, 2 genes displayed differential gene expression in dilated cardiomyopathy (DCM): adenosine receptor A2A (*Adora2A*) and lymphocyte antigen 75 (*Ly75*). Interestingly, when they validated these 2 genes by knockdown either *Ly75* or *Adora2A* using morpholino in zebrafish, both morphants (zebrafish mutants) developed severe HF similar to that observed in humans (6).

A more extensive human study on DNA methylation in HF was published recently. Meder et al. generated a genome-wide DNA methylation profile in patients with DCM and in donor left-ventricular biopsies and whole peripheral blood using a high-resolution epigenomic-wide method with a large cohort (7). They identified 59 CpG loci with significant changes in DNA methylation in the myocardium of patients with DCM compared with clinical controls. Among these CpG loci, 29 and 30 were hypomethylated and hypermethylated in DCM, respectively. Using multi-omics approaches, they linked a subset of 517 epigenetic loci with DCM and cardiac gene expression. By further examining the methylome of peripheral blood cells, a differential display of 217 methylation sites between controls and patients with DCM was observed. Moreover, when they compared methylome between myocardium and peripheral blood cells, they identified distinct epigenetic methylation patterns that are conserved between 2 tissues. For example, the *NPPA* (natriuretic peptide A, also known as ANP) and *NPPB* (natriuretic peptide B, also known as BNP) loci were demethylated in DNA in heart tissues and peripheral blood cells from patients with DCM (7).

Using a cell-sorting technique coupled with a whole-genome bisulfite sequencing approach, Gilsbach et al. showed that only a few genomic regions within gene body of 6 genes exhibited differential DNA methylation between non-failing and failing human cardiomyocytes (8). However, those genes did not express differentially between the 2 groups. Additionally, the global DNA methylation patterns are not significantly different between non-failing and failing cardiomyocytes. Therefore, the authors concluded that methylated CpG is relatively stable in chronic HF (8). However, this observation differs from other studies in which more differential DNA methylated regions and gene loci were identified. In fact, Meder et al. found 59 differential CpG regions in DCM comparing to non-failing hearts from a total of 72 left ventricular biopsies. Moreover, a recent study by Glezeva et al. using capture-based bisulfite sequencing method also identified 151 differential methylation regions in DCM in comparison with non-failing hearts (9). Such discrepant findings in DNA methylation patterns in the failing heart could be due to the different technologies for DNA methylation that were used in studies (whole genome bisulfite sequencing [WGBS] vs. bead array vs. capture-based bisulfite sequencing). Another reason could be that the study by Gilsbach et al. (8) used sorted cardiomyocytes whereas other studies used bulk left ventricle tissues (4,5,7,9), and Gilsbach's study only used 5 pairs of samples using WGBS method and the pooled biological replicates for DNA methylation analysis.

Taken together, all the published studies to date have demonstrated that alternation of DNA methylation is highly associated with DCM. Recently, coupling RNA-seq and genome-wide DNA methylation approaches, Pepin et al. linked DNA methylation to metabolic reprogramming in men with

end-stage ischemic cardiomyopathy (ICM). They also identified the differential DNA methylation between ICM and non-ischemic cardiomyopathy (NICM) (10). Specifically, the authors observed that 12.6% of CpG sites were differentially methylated between ICM and NICM, and that hypermethylation within promoter-associated CpG islands was observed in ICM samples. These hypermethylated gene loci are involved in oxidative metabolism and are downstream of an epigenetic repressor Enhancer of zeste homolog 2 (EZH2, a component of the polycomb repressive complex 2 and a histone methyltransferase) as well as Kuppel like factor 15 (KLF15), which is also an EZH2 target. These observations implied that human ischemic HF may display a distinctive DNA methylation signature associated with oxidative metabolism and anaerobic glycolysis. Furthermore, differential DNA methylation is likely mediated by EZH2-DNA methyltransferase complex to affect its downstream gene targets that are involved in metabolic reprogramming, such as KLF15.

Different etiologies of HF may generate different DNA methylation patterns. Using a targeted bisulfite sequence approach for patients with HF with various etiologies, Glezeva et al. identified 5 unique differentially methylated regions (DMR) in hypertrophic obstructive cardiomyopathy (HOCM), 151 DMRs in DCM and 55 DMRs in ICM and a total of the 209 genes were associated with these DMRs (9). Further validation for the genes associated with these DMRs confirmed that 6 protein-coding genes and 2 microRNA (miRNA) displayed significantly altered gene expression in at least 1 of the disease groups comparing with the control group. Among them, 2 novel HOCM-related genes were identified from this study, namely *HEY2* and *MSR1*. Both gene loci were hypermethylated in patients with HOCM, and their gene expression level was reduced. In addition, 2 genes involved in the regulation of the extracellular matrix, *CTGF* and *MMP2*, were found to be hypomethylated with increased gene expression level in DCM. Moreover, *COX17*, *MYMO3,* and miR24-1 were found to be hypermethylated with reduced gene expression, whereas *CTGF* miR155 was hypomethylated with elevated gene expression in ICM (9).

POST-TRANSLATIONAL MODIFICATIONS OF HISTONES: DYNAMIC PROCESSES ACCOMPLISHED BY WRITERS AND READERS ENZYMATICALLY

Histone proteins are the component of the chromatin complex that forms chromosomes. The histone octamer contains 2 copies of H2A, H2B, H3, and H4 proteins and forms the core of a nucleosome, wrapped 1.67 times by approximately 147 base pair (bp) of DNA. This conserved core complex is linked with a short linker DNA in a range between 20 and 80 bp and assembling into higher-order structures. The structures are stabilized by the linker histone H1, which usually binds to the entry/exit site of DNA on the surface of the nucleosomal core and wraps another 20 bp of DNA (11).

Unlike DNA methylation, in which the location of the methylation in the genome has a big impact on its functions, the regulatory function of the epigenetic modifications on histones are more delicate. The functions of histone modification are influenced not only by the location of these modifications (i.e., which amino acid residue and of genomic regions), but also by the type and the number of modifications on histones. The post-translational modifications (PTMs) of histones include acetylation, methylation, phosphorylation, ubiquitylation, and sumoylation at different amino acid residues of the canonical histone proteins as well as variant histones such as H3.1,H3.3, H2A.Z, and macroH2A (12,13). These modifications affect the gene expression by changing chromatin structure to influence DNA accessibility or by recruiting various regulatory molecules such as histone modifiers, chromatin regulators, DNA repair molecules, and transcription factors. Studies from the past 2 decades have established a series of epigenetic codes for various histone modifications associated with the transcriptional status of genes. For example, acetylation of histone H3 at lysine 27 (K) residue marks active enhancers and promoter regions, whereas tri-methylation of histone H3 at K4 residues (H3K4me3) is associated with the active promoter region of genes. The comprehensive details of the histone codes associated with the regulation of gene expression have been reviewed elsewhere (12).

The PTMs of histones and their roles during cardiomyocyte differentiation and heart development for tissue regeneration have been studied extensively (14–18). However, our understanding of these regulations in HF remains unclear. The PTMs of histones is achieved by the actions of histone “writers” and “erasers.” They are enzymes that either add (write) PTM to histones or remove (erase) PTM from the histone proteins. Currently, the best understood the regulation of PTM on histones is on acetylation, methylation, phosphorylation (19). In this review, we will focus on 2 major PTMs to histone proteins - methylation and acetylation.

JACC: BASIC TO TRANSLATIONAL SCIENCE VOL. 4, NO. 8, 2019
DECEMBER 2019:976–93

HISTONE ACETYLATION AND DEACETYLATION. Acetylation commonly occurs on the lysine residues of the histone, which neutralizes the positive charge of the lysine and reduces the ionic interaction between histone proteins and DNA. This increases the DNA accessibility to transcription factors, chromatin remodelers, and modifiers and is frequently associated with transcription activation (20). Histone acetylation is controlled by histone acetyltransferase (HAT [writer]) and deacetylase (HDAC [eraser]). HATs can be divided into 2 different classes based on their localization in the cell (21). Type A HATs are in the nucleus playing an essential role in activation of gene transcription, whereas type B HATs are located in the cytoplasm mainly involved in the acetylation of newly synthesized histone. There are 4 major classes of HDAC classified by their catalytic domain (20,22). Class I HDACs, HDAC1, 2, 3, and 8, are widely expressed, whereas Class II (HDAC4, 5, 7, and 9 belong to the IIa group, and HDAC6 and 10 belong to the IIb group) are cell-type restricted. Class III HDACs are sirtuins 1-7 and they are NAD(+) dependent (20,22).

Evidence from animal models shows that HAT and HDAC are highly linked to cardiac hypertrophy. When CREB-binding protein/p300, a well-known HAT, was overexpressed in mouse myocardium, the mouse developed left ventricular myocyte hypertrophy, dilatation, and dysfunction (23). Cardiac-overexpression of p300 in mouse also acetylated GATA4, a zinc finger transcription factor known for mediating myocyte hypertrophy and increased DNA binding activity of GATA4 to its downstream target. This stimulated the expression of the GATA4-dependent hypertrophy-responsive genes including *Nppa*, prepro-endothelin-1, and β-myosin heavy chain (*Myh7*). In contrast, in inhibition of p300 activity with curcumin (a p300-specific HAT inhibitor) in a phenylephrine-induced hypertrophy rat model, it was observed that cardiomyocytes decreased acetylation of histone 3 and histone 4 as well as GATA4 DNA binding activity. In a hypertension salt-sensitive Dahl rat model as well as a surgically induced myocardial infarction (MI) rat model, oral curcumin administration prevented deterioration of systolic function and HF (24). Therefore, deacetylation or inhibition of HAT may play a role in HF.

Consistent with this notion, several studies have manipulated the expression of histone deacetylase in mouse hearts and in primary cardiomyocytes. Single knockout for deacetylase class II members (HDAC II) *Hdac*5 or 9 in mice were sensitive to cardiac stress signals, such as pressure overload and calcineurin stimulation, and developed age-dependent cardiac hypertrophy (25,26). Moreover, expression of cardiac hypertrophic genes (such as *Nppa* and *Myh7*) was enhanced in response to the stress signals in *Hdac5*- or *Hdac9*-null mice. This cardiac phenotype was caused by the activation of a prohypertrophic transcription factor, myocyte enhancer factor-2 (MEF2C), which can be inhibited by HDAC II (27). When infecting with a mutant form of *Hdac9* or *Hdac5* with more potent repressive activity on gene expression in phenylephrine-induced hypertrophic cardiomyocytes, it was demonstrated using chromatin immunoprecipitation coupled with quantitative PCR (ChIP-qPCR) assay that the acetylation state of histone 3 was significantly reduced at promoter regions of *Nppa* and *Myh7*. However, the gene loci that were not regulated during hypertrophy (e.g., *Gapdh*) were not affected. Furthermore, reduction of the acetylation on histone 3 correlated with the gene expression of *Nppa* and *Myh7* but not *Gapdh* (25). The results indicated that HDAC II has an inhibition role for cardiac hypertrophy.

Interestingly, when the activity of HDAC class I (HDAC I) was abolished, it had effects opposite to that of HDAC II. The inactivation for HDAC I member, *Hdac2,* in mice genetically or chemically, resulted in less sensitivity to hypertrophic stimuli, whereas the mice with *Hdac2* overexpression developed cardiac hypertrophy (28). The expression of cardiac hypertrophy genes, namely, *Nppa*, *Mhy7*, and *Acta1*, was not significantly different between control littermate and *Hdac2*$^{-/-}$ mice following transverse aortic constriction (TAC) or isoproterenol infusion (28). However, the state of histone acetylation was not investigated in this study. Cardiac-specific inactivation of *Hdac3*, another member of HDAC I, in mice caused cardiac hypertrophy as well as affected the genes associated with the fatty acid metabolism. Although there are no global changes of histone acetylation in *Hdac3* conditional knockout (cKO) hearts, histone acetylation was found to be increased at the promoter region of myocardial energetic genes and glucose use such as *Ucp2 and 3* (uncoupling protein 2 and 3)*, fatty acyl-CoA synthetase, fatty acid transport protein,* and *Pyruvate dehydrogenase kinase 4* (29). These data suggested that HDAC3 may have a complementary role in regulating cardiac growth and myocardial energy metabolism (29).

HISTONE METHYLATION AND DEMETHYLATION. Histone methylations can be associated with gene activation or repression, depending on which residue on histone the modification occurred. For example, the H3K4me3 is usually associated with active promoter activity whereas the tri-methylation of histone 3 lysine 9 (H3K9me3) is usually linked to

transcriptional repression (12,14). Methylation of histones also plays a critical role in the progress of HF as evidenced by the different effects in modulating of histone demethylase (HDM,[eraser]), co-factor or histone methyltransferase (HMT,[writer]) in cardiomyopathy mouse models. Zhang et al. demonstrated that JMJD2A, a HDM, promotes cardiac hypertrophy in TAC mice (30). Inactivation of *Jmjd2a* in the mouse myocardium resulted in an attenuated hypertrophic phenotype after the TAC procedure, whereas the overexpression of *Jmjd2a* increased the hypertrophic response to TAC-induced hypertrophy. This increasing development of hypertrophy is due to the activation of four-and-a-half LIM domain1 (FHL1), which is a key molecule in developing hypertrophy in the TAC mouse model (31). It was found that JMJD2A binds to the promoter region of FHL1 and reduced the level of H3K9me3 in the heart after the TAC procedure. Interestingly, JMJD2A was significantly up-regulated in patients with HOCM (30).

Another example of histone methylation can be found in disruption of dystrophin-glycoprotein complex in DCM. When a disruptor of telomeric silencing (*DOT1l*), the H3K79 methyltransferase, was specifically deleted in the mouse heart, mutant mice developed various abnormalities leading to cardiac remodeling and increased cardiomyocyte cell death (32). Further analysis of these mice found that the cardiac abnormalities were due to dysregulation of dystrophin (*Dmd*) in hearts. Consistent with its methyltransferase function, DOT1L was found to be directly bound to the *Dmd* gene locus in the postnatal mouse heart. This binding correlated positively with the enrichment of H3K79me2/3 in the *Dmd* gene body, whereas such enrichment was abolished in the *Dot1l* cKO mouse hearts (32).

Moreover, a recent study showed that G9a/EHMT2, another HMT, was found to be required for cardiomyocyte homeostasis to silence the fetal gene program in the adult heart (33). Conditional aberration of *G9a* in 2-month-old mouse myocardia caused various cardiac dysfunctions within the first 4 weeks of knockout induction. The results indicate that G9a is required for the proper cardiac function in normal mouse hearts. Further investigation of *G9a*-KO mice in comparison with control showed that G9a suppresses the key cardiac regulatory genes via H3K9me2. G9a also interacts with EZH2 (an HMT) and forms a complex with MEF2C to regulate MEF2C-dependent gene expression. Interestingly, *G9a* was found to be up-regulated during the initial stages of cardiac hypertrophy. Furthermore, chemical inactivation of *G9a* in TAC mice improved cardiac function and prevented the development of hypertrophy suppressing the expression of anti-hypertrophy genes in cardiomyocytes (33). Taken together, G9a functions as an anti-hypertrophic regulator in healthy hearts, while serving as a hypertrophy activator in stressed hearts to promote cardiac hypertrophy.

Finally, the misregulation of the cofactor of histone methylation also showed effects on the regulation of HF. In vivo cardiac-specific deletion of the PAX transcription activation domain interacting protein (PTIP), a cofactor of H3K4 methylation, in adult mice caused the reduction of H3K4me3 (34). Using RNA microarray analysis, it was shown that a total of 221 genes were significantly altered in the *Ptip* cKO mouse hearts. The altered genes include Kv channel-interacting protein 2 (*Kcnip2*), a regulator for cardiac repolarization current that was previously shown to be down-regulated in a failing heart. Further analysis using ChIP-qPCR to detect H3K4me3 enrichment at 5' regulatory region of *Kcnip2* in control and *Ptip* cKO mouse hearts confirmed that the *Ptip* deletion directly affects the reduction of H3K4me3 at *Kcnip2* gene region (34). These findings support the notion that the methylation of histones plays a crucial role in modulating cardiac hypertrophy and HF.

One interesting study done by Hohl et al. showed that, although HDAC4 belongs to histone deacetylase, HDAC4 may play a central role for rapid modifications of H3K9 methylation in response to cardiac load. Using human left ventricular tissues in ChIP-qPCR assays, Hohl et al. found that the promoter regions of *Nppa* and *Nppb,* 2 hallmark genes for maladaptive remodeling of the left ventricle, displayed a higher level of activation marks for H3K9ac and H3K27ac in failing hearts, whereas the repressive marks, H3K9me3 and H3K9me2, were substantially reduced (35). Using a similar method, the authors also observed that heterochromatin protein 1 (HP1), a transcriptional repressor and H3K9me3 binding protein, was dissociated from the promoter regions, which may activate both *Nppa* and *Nppb* gene expression. The H3K9 demethylation and up-regulation of *NPPA* and *NPPB* in human failing myocardium correlated with the nuclear export of phosphorylated HDAC4. Inactivation of HDAC4 in the mouse hearts resulted in a reversal of these events in cardiomyocytes (35). How does a histone deacetylase "promote" demethylation of histone? Apparently 2 HMTs, JMJD1A and 2A, were up-regulated in failing human hearts. The up-regulation of *JMJD1A* was positively correlated with the increased *NPPA* and *NPPB* expression. In addition, both demethylases bind to the promoter region of *NPPA*. HDAC4 is associated with the transcriptional repression complex with the H3K9me3 binding protein, HP1, and the

JACC: BASIC TO TRANSLATIONAL SCIENCE VOL. 4, NO. 8, 2019
DECEMBER 2019:976–93

histone methyltransferase, SUV39H. This complex is dissociated in response to the stress condition by the calmodulin-dependent protein kinase II δB-induced phosphorylation and nuclear export of HDCA4. Therefore, it is conceivable that the dissociation of the HDAC4-HP1-SUV39H complex opens up space at the promoter region of *Nppa* and *Nppb*, allowing the entry of the HMTs, JMJD1 and 2, to achieve the demethylation machinery in failing myocardium (35).

GENOME-WIDE STUDIES ON PTMs OF HISTONES. Several genome-wide studies on PTMs of histone in myocardium have been conducted in animal models and humans. The first genome-wide study on methylation of histone in both human and rodent myocardium was published in 2009. Using a chromatin immunoprecipitates using genomic tiling arrays (ChIP-on-ChIP) technique, Kaneda et al. showed that the distribution patterns of H3K4me3 and H3K9me3 were significantly different between healthy and failing hearts (36). The differential distribution patterns of the 2 histone marks were found mainly at the gene loci involved in calcium signaling and cardiac contractility during the development of HF. In 2011, Movassagh et al. demonstrated that H3K36me3, a histone marker for active transcription, exhibited a differential methylation pattern and enrichment in cardiomyopathic and normal human hearts. The differential displays of H3K36me3 were mainly found in non-coding RNA loci, suggesting the involvement of the non-coding RNA in cardiomyopathy (4).

The most comprehensive genome-wide studies on PTMs of histones in cardiac hypertrophy and HF in an animal model was published in 2013 by Papait et al. Using ChIP followed by sequencing analysis for mouse cardiomyocytes isolated from sham and TAC mice for 7 histone epigenetic marks, Papait et al. identified that the level of histone acetylations (e.g., H3K9ac and H3K27ac) was decreased around the gene loci whose expression was down-regulated in TAC mice (37). In addition, there was a correlation between the gene expression level for those differentially expressed in TAC mice and the enrichment of histone methylation repression marks (e.g., H3K27me3, H3K9me2, and H3K9me3). The more active the transcription, the less enrichment for histone repression marks they observed (37). The authors also identified 9,207 cardiac-hypertrophy-specific-active enhancers that have DNA-binding motifs for MEF2C and its closely related family member, MEF2A. These results were validated using ChIP-qPCR analysis. The data suggested that MEF2A and 2C stimulate the cardiac hypertrophy gene expression via enhancers (37).

Although several genome-wide studies in the myocardium in both animals and humans have been published, their measurements were performed in bulk tissue specimens rather than in microdissected cells. Therefore, the data interpretation was based on several mixed-cell populations. Because epigenetic regulation is critical for cell-fate specification and differentiation, the effect of such regulation is highly cell-type–specific. Thus, it is necessary to determine the epigenetic signatures in a specific cell type. Recently, Gilsbach et al. used a nuclear staining with fluorescence-assisted sorting method to specifically isolate human cardiomyocytes from normal fetal, infant, and adult hearts as well as failing ones for a genome-wide epigenetic study (8). They showed that the whole-transcriptome regulation for normal cardiomyocytes during normal development is established by dynamic methylated CpG and common histone signatures at distal *cis*-acting elements of genes and gene bodies. One interesting finding from this study is that the expression of failing myocardium-related genes is modulated by active enhancer histone marks but not by DNA methylation. This observation is different from what was previously reported, and needs to be validated in a larger cohort study. Furthermore, because a heart is made up of other cell types besides cardiomyocytes (such as cardiac fibroblasts), it is necessary to generate epigenetic maps for other heart cell types.

In summary, our understanding of histone modifications on adult and failing hearts may have improved compared with a decade ago. However, we still lack systematic studies for normal and failing hearts in humans. Moreover, the currently published histone modification human studies have focused mainly on DCM and predominantly in males. Different types of cardiomyopathy may have their own distinct regulatory mechanisms. Sexual dimorphism can also link to different genetic and epigenetic regulations (38).

ATP-DEPENDENT CHROMATIN CONFORMATION, REMODELING, AND HF

The mammalian chromatin architecture and organization are highly regulated. The dynamic modification of the epigenome, including post-translational modification on histone tails and DNA methylation, causes chromatin remodeling and re-organization. This is an important process for controlling cell-fate determination, differentiation, and organ development (14). The chromatin regulators, such as histone modifiers, co-factors, and transcriptional regulators, can recruit or be recruited by other chromatin

regulators and transcription factors to regulate gene expression. By recruiting all necessary regulators, the distal *cis*-acting elements, such as enhancers, can form chromatin loops to interact with the proximal promoter regions of genes, and thus initiate and enhance the transcriptional activity of genes with the basal transcriptional complex (e.g., RNA polymerase II).

The histone writers and erasers achieve the PTMs on histones. These PTMs serve as "marks" to be recognized and interpreted by "readers" that carry on the action for regulating gene expression. The role of readers in HF is just emerging. Studies on modulating the function of bromodomain (BET) proteins, an acetylated-lysine binding protein and an epigenetic reader, have suggested that chromatin structure and organization are important in regulating the kinetics of gene expression in failing hearts (39,40). The BET family comprises BRD2, BRD3, BRD4, and BRDT. Among them, BRD4 protein expression was increased during cardiac hypertrophy. Inhibition of BET activity with the small molecule JQ1, either in mice or primary cell culture, suppressed phenylephrine-mediated cellular hypertrophy and pathological gene induction. Spiltoir et al. showed that the hypertrophic stimuli stimulated recruitment of BRD4 to the transcriptional start site of the gene *Nppa*. Binding of BRD4 to the ANF transcription start site was associated with increased phosphorylation of local RNA polymerase II. Recently, Duan et al. showed that administration of the JQ1 has therapeutic effects in animal HF models (41). Using an unbiased ingenuity pathway analysis, the authors showed that BET inhibition preferentially suppressed innate inflammatory and profibrotic transcriptional networks, namely, Nuclear Factor κB and Transforming Growth Factor-β signalings. Taken together, these studies suggested that BET proteins can be good pharmacological targets for treating HF.

In addition to the histone writers and readers and co-activators mentioned above, ATP-dependent chromatin remodeling complexes (ADCRs) are another group of regulators that may play a critical role in chromatin remodeling. ADCRs contain an adenosine triphosphate (ATPase) subunit that belongs to the SNF2 superfamily of proteins. The complex uses ATP hydrolysis as an energy source to alter or disrupt the histone-DNA interaction. In mammals, 4 ADCR families (the SWI/SNF, ISWS, CHD, and INO80) have been identified (42). Among these families, the roles of the SWI/SNF group in cardiac development and hypertrophy have been studied extensively during the past decade (43-48). These studies have found that BAF complex, the mammalian analog of the SWI/SNF complex, is usually abundant in the embryonic heart but down-regulated in adult myocardium. The complex modulates gene expression of an important and motor molecule of the heart, myosin heavy chain (MHC). Two isoforms of MHC, α- and β-MHC, are specifically expressed in the mammalian hearts, and they are located on the same chromosome (49). Alpha-MHC has higher ATPase activity than β-MHC. Alpha-MHC is expressed in adult cardiomyocytes primarily, whereas β-MHC is expressed in embryonic cardiomyocytes.

How does the BAF complex modulate the expression of these 2 isoforms? Using various myocardial-specific deletion of *Brg1* mouse models at different developmental stages, it was shown that BRG1, an important ATPase subunit of the BAF complex, interacts with HDACs and poly ADP-ribose polymerase (PARPs), e.g., PARP1, to suppress the adult isoform of α-MHC, encoded by *Myh6* gene, and activates the fetal isoform (β-MHC), encoded by *Myh7* gene, in the embryonic heart. Because the BAF complex was down-regulated in adult cardiomyocytes, the suppression of α-MHC is removed. Therefore, the expression of the adult isoform of MHC (α-MHC) is up-regulated (46). Interestingly, the down-regulation of *BRG1* gene expression at birth was also observed in normal human hearts. However, unlike in adult mouse hearts where the BRG1 was undetectable in cardiomyocytes, it remains detectable in human adult cardiomyocytes, suggesting the other mechanisms may be present in regulating the switch of fetal and adult MHC in humans (50). Nevertheless, in hypertrophic and failing hearts, the subunits of BAF complexes and its binding partners, HDACs and PARPs, were increased and the expression of fetal MHC was up-regulated, whereas the adult MHC was decreased (46).

Another mechanism for the inhibition of adult *Myh6* gene is that BRG1 recruited G9a, a HMT, and DNA methyltransferase (DMNT3) to the promoter region of *Myh6* in the adult hypertrophic and failing hearts. The recruitment of G9a/DMNT3 complex resulted in the deposition of the H3K9me3, a repressive chromatin mark, and CpG methylation at promoter region of *Myh6*, which may subsequently activate the inhibition machinery for *Myh6* gene (51). When *Brg1* was specifically deleted in mouse hearts, the cardiac hypertrophy was diminished in the TAC mice. Therefore, it is conceivable that the proper expression and maintenance of the state of adult MHC expression can be a promising approach for treating HF. Moreover, BRG1 can directly increase the expression of osteopontin, a pro-fibrotic factor

TABLE 1 Summary of Chromatin Regulator in Cardiomyopathy

Regulator	Action	Effect	Reference
CREB-binding protein (P300)	Acetylation of histone tails.	(1) Increasing acetylation of MEF2 and GATA4. (2) Cardiac hypertrophy regulation.	23,24
HDAC2	Deacetylation of histone tails.	(1) Overexpression of HDAC2 caused stimulation of the Akt/GlaxoSmithKline3b pathway. (2) Cardiac hypertrophy regulation.	28
HDAC3	Deacetylation of histone tails.	Regulation of cardiac growth and myocardial energy metabolism.	29
HDAC4	(1) Deacetylaion of histone tails. (2) Control H3K9 demethylation and HP1 dissociation to the *NPPA* promoter in response to elevated preload.	Mediation of H3K9 methylation and HP1 dissociation to *NPPA* promoter.	35
HDAC5 and 9	Deacetlylaion of histone tails.	Inhibit the transcriptional activity of MEF2c and act as negative regulator of cardiac hypertrophy.	25,26
DOT1L	Methylation of H3K79me.	Reduction of DOT1L activity causes DCM.	117
JMJD2A	Demethylation of H3K9me3, H3K4me3, and H3K27me3.	Activate cardiac hypertrophy and alter cardiac gene expression.	30
PTIP	(1) Co-factor of H3K4 methylation (2) Regulates the expression of *Kcnip2*.	Misregulation of PTIP cause cardiac hypertrophy and failure.	34
G9a/EHMT2	Methylation of H3K9me2 and H3K27me3 (lesser extent).	(1) Maintain cardiomocyte homeostasis and interact with MEF2C to silence the fetal gene program in the adult heart. (2) Promote cardiac hypertrophy in stressed hearts.	33
SWARCA4 (BRG1)	(1) Regulates PARP-1/HDAC. (2) Recruits G9a and DMNT3.	(1) Activation of Brg1 diminished cardiac hypertrophy in TAC mice. (2) Activates fetal MHC isoform expression and repress adult MHC isoform in the hypertrophic and failing adult heart.	46,51
CTCF	Regulating chromatin 3D structure.	Inactivation of CTCF caused HF.	60

3D = 3 dimensional; CTCF = CCCTC-binding factor; *DOT1l* = disruptor of telomeric silencing1 like histone lysine methyltransferase; H3K4me3 = tri-methylation of lysine 4 on histone 3; H3K9me3 = tri-methylation of lysine 9 on histone 3; HDAC = histone deacetylase; HF = heart failure; HP1 = heterochromatin protein 1; *Kcnip2* = Kv channel-interacting protein 2; MHC = myosin heavy chain; NPPA = natriuretic peptide A; PARP = poly ADP-ribose polymerase; PTIP = PAX transcription activation domain interacting protein; TAC = transverse aortic constriction.

induced cardiac fibrosis (52). Thus, it seems that BRG1 acts as a stress-activated chromatin remodeler that controls fetal reprogramming of cardiac genes, e.g., the switch of adult form, *Myh6*, to fetal gene, *Myh7*, and activates hypertrophy and HF (46).

Chromatin remodeling complexes can swap histone variants, such as H3.3 and H2A.Z, with the canonical histone proteins in the nucleosome. It is clear now the incorporation of histone variants is critical for regulating the chromatin structure and gene expression. For example, a SWI/SNF chromatin-remodeling complex, SWR1, can switch H2A with H2A.Z at specific genomic loci to maintain genome integrity and to facilitate initiation of transcription, whereas INO80 chromatin-remodeling enzyme can evict H2A.Z from nucleosome to stabilize the chromatin (53).

The role of histone variants in development and diseases has been described elsewhere (54–56). Nevertheless, the role of histone variants in HF remains largely unknown. It was reported that the histone variant H2A.Z is up-regulated in TAC mice hearts and knockdown H2A.Z with shRNA in cultured rat cardiomyocytes under mechanical hypertrophic growth conditions attenuated cardiac hypertrophy and downregulated growth-related genes (namely, cyclin-dependent kinase 7 and ribosomal S6) (57). When HIRA, a histone chaperone protein responsible for incorporation of histone variant H3.3, was specifically deleted in the mouse heart, the heart developed fibrosis, cardiac hypertrophy, as well as abnormal cardiac function. In addition, the sarcolemmal integrity was compromised in the *Hira*-deleted mouse (58). The histone variant H3.3 was shown to be associated with gene bodies of active genes in non-pluripotent cells and enriched at both active and silence genes in embryonic stem cell and precursor cells (59). Misregulation of incorporation of H3.3 would alter the gene expression. Indeed the cardiac transcriptome of *Hira*-cko hearts was altered in comparison with the control hearts.

Chromatin loops participated in the same regulatory territory, forming a higher order of chromatin structure known as topologically associating domains (TAD). Recently, the importance of TAD in HF has been reported (60). Rosa-Garrido et al. inspected the chromatin configuration differences among cardiomyocytes isolated from 3 different groups of mice and their correlation to the gene expression using high-resolution chromatin mapping and RNAseq approaches. These 3 groups are as follows: (1) normal adult, (2) induced-cardiac hypertrophy by TAC, and (3) cardiac-specific deletion of CCCTC-binding factor (CTCF) (*Ctcf*-KO) mice. CTCF was previously shown to regulate chromatin three-dimensional (3D) structure

TABLE 2 Potential Epigenetics Drugs for HF

Chemical	Action	Cardiac Outcome	Current Clinical Application	Ref. #'s
5-aza	DNA MTi.	Improved cardiac function partially.	ALL; AML; sickle cells disease.	113–115
Apicidin	HDACi for class I subtypes 1, 2, and 3.	Decreased myocardial hypertrophy.	NR	109
Curcumin	HATi for p300.	Prevented deterioration of systolic function and HF.	OA; RA; diabetes.	24,110–112
Givinostat (ITF2357)	Pan-HDACi.	Decreased inflammatory response and angiogenic effects. Reduced EMT and cardiac fibrosis.	Duchenne muscular dystrophy; juvenile idiopathic arthritis; polycythemia vera; myelofibrosis.	104–107
JQ1	BET bromodomain inhibitor.	Suppressed cardiac hypertrophy and pathological cardiac remodeling. Improved cardio function in TAC mice.	Variety of cancers.	39–41
SK-7041	HDACi for class I subtypes 1 and 2.	Reduced myocardial hypertrophy.	NR.	108
Trichostatin A	HDACi for class I and II.	Suppressed cardiac hypertrophy and improve survival rate.	Variety of cancers.	99
Valpronic acid	HDACi for class I and II.	Suppressed cardiac hypertrophy and improved survival rate.	Variety of cancers.	108
Vorinostat (SAHA)	HDACi for class I and II.	Reduced infarct size and improved cardiac function	Cutaneous T-cell lymphoma.	102,103

5-aza = 5-azacytidine; ALL = acute lymphoblastic leukemia; AML = acute myeloid leukemia; BET = bromodomain; EMT = epithelia-mesenchymal transition; HDACi = histone deacetylase inhibitor; HMTi = histone methyltransferase inhibitor; MTi = methylation inhibition; NR = no report; OA = osteoarthritis; RA = rheumatoid arthritis; SAHA = suberoylanilide hydroxamic acid. Other abbreviations as in Table 1.

(61,62). Interestingly, mice with the cardiac-specific deletion of *Ctcf* developed HF. Moreover, the expression of CTCF was reduced in human patients with a failing heart and was increased in patients whose hearts were assisted by a left ventricle assist device. Rosa-Garrido et al. also described the alterations of chromatin architecture in healthy and diseased cardiac myocytes in mice. Significant alternations of chromatin loops and the boundary strength of TADs were found in cardiomyocytes from both *Ctcf*-KO and TAC mice. The enhancers and promoters interaction for major cardiac-related loci was also altered in the cardiomyocytes from failing hearts. In addition, there was a positive correlation between the alteration of gene expression levels and changes in chromatin compartmentalization in *Ctcf*-KO and TAC mice. It remains unclear if the similar TADs and chromatin looping structures and alterations would exist in human patients with HF.

Using a chromosome conformation capture technique approach, Hi-C, to create the 3D map of the chromosome interaction for induced pluripotent stem cell-derived cardiomyocytes, Montefiori et al. recently linked the known cardiovascular disease-associated single nucleotide polymorphism to the target genes (63). The authors identified that the majority of non-coding regions could influence genes that are far away from them and some regions may modulate the gene expression for more than 2 genes. These findings are consistent with the notions that the long distance enhancers interact with the promoter to establish a long-range control of gene expression, and it is important to consider this aspect when interpreting functional targets of disease loci. A summary of epigenetic modifications and chromatin remodeling involved in cardiomyopathy is listed in Table 1.

LONG NON-CODING RNAs: THE NEW PLAYERS IN EPIGENETIC REGULATION FOR HF

Only <2% of transcribed RNAs translate into proteins (64,65). Recent advances in transcriptomics and bioinformatics techniques revealed that untranslated RNAs (non-coding RNA [ncRNA]) are key regulators for transcription and translation in developmental as well as disease processes. In addition to the traditional, well-known non-coding RNAs (such as transfer RNA and ribosomal RNA), the rest of the non-coding RNAs can be classified into 2 categories based on their size. One category of ncRNA is the small nc-RNA, which is <200 nucleotides long. Small nc-RNA includes miRNA, piwi-interacting RNA, short interfering RNA, small nucleolar RNAs, small nuclear RNAs, extracellular RNAs, and small Cajal body-specific RNAs. The other category of ncRNA is the long ncRNAs (lncRNAs), which are longer than 200 nucleotides. lncRNAs have been linked to playing critical roles in chromatin remodeling. The epigenetic functions of small nc-RNA (especially miRNA) are extensive and have been reviewed elsewhere (66–70). Here we will focus on the epigenetic roles of lncRNA in HF.

Like other non-coding RNA, lncRNAs do not encode any protein product but elicit their functions via diverse mechanisms (71). For example, lncRNA can interact with chromatin regulators and transcriptional modifiers to enhance or repress expression of downstream genes. lncRNAs can also regulate gene expression by interfering with miRNA pathways. They also play essential roles on post-translational regulations that involve RNA splicing, messenger RNA (mRNA) stability, and translation. Furthermore, several lncRNAs have been identified to play vital roles during heart development (72).

FIGURE 1 **The Epigenetic Mechanisms in Heart Failure**

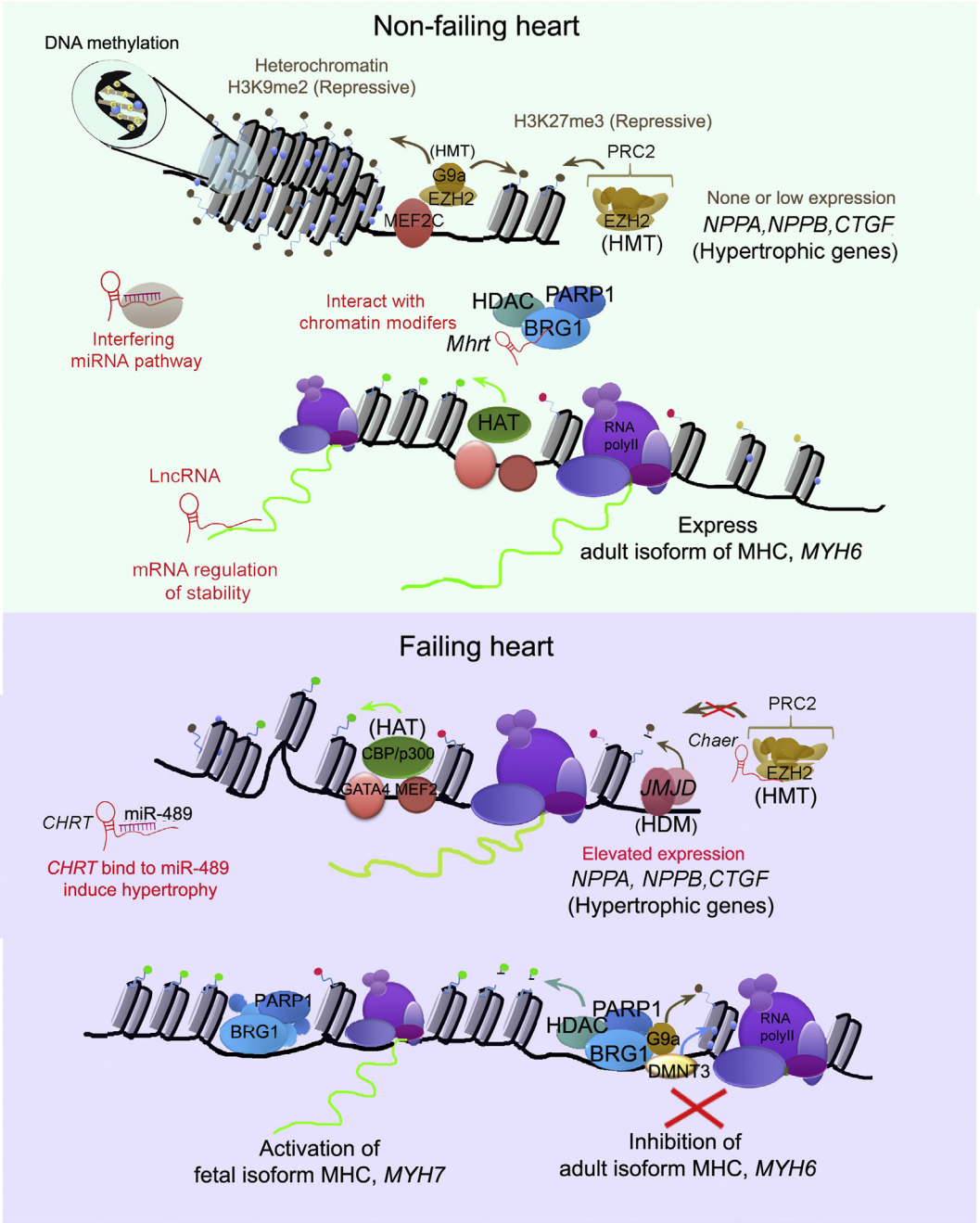

Continued on the next page

Studies suggested that lncRNA plays a vital role in myocardium remodeling and pathogenesis in failing hearts. The mitochondria-derived lncRNA long intergenic non-coding RNA predicting cardiac remodeling (*LIPCAR*) was associated with left ventricular remodeling. This assumption is based on the observation that the LIPCAR is elevated in plasma of patients with HF after MI compared with MI patients without left ventricular remodeling (73). By lncRNA array screening, Piccoli et al. identified that cardiac fibroblast-specific lncRNA, maternally expressed gene 3, was the most abundant CF-lncRNA in the mice that underwent the TAC procedure during the first 4 weeks (74). The Wang and Xiao's group together identified that 15 and 135 lncRNAs were dysregulated in cardiac hypertrophy and failing mouse hearts, respectively (75). The study used whole-transcriptome analysis for left ventricle samples collected from mice after 1 week of TAC (hypertrophic stage), and 8 weeks of TAC procedure (end-stage HF). Among these dysregulated lncRNAs, 2 of them are particularly interesting. The first 1 is H19 and is a highly abundant and conserved imprinted lncRNA. *H19* was significantly up-regulated in HF samples in comparison with control samples. Consistent with this finding, *H19* was later shown to be a negative regulator of cardiomyocyte hypertrophy (76). Another interesting lncRNA from their findings is a cardiac hypertrophy-associated epigenetic regulator (*Chaer*), which is a heart-enriched lncRNA (77). *Chaer* was shown to be involved in cardiac hypertrophy development by directly binding to the catalytic subunit of polycomb repressor complex 2 (PRC2). PRC2 is responsible for methylation of H3K27me3 for gene silencing. The interaction between *Chaer* and PRC2 decreased the level of H3K27me3 in the promoter region of cardiac hypertrophy-related genes, such as *NPPA*. Therefore, it may cause induction of these cardiac hypertrophy-related genes in hypertrophy hearts (77).

Long non-coding RNAs also regulate the chromatin-remodeling molecule to maintain cardiac functions. A cardiac-specific long-non RNA cluster, Myheart (*Mhrt*), was found to abound in the heart and have a protective role in pathological hypertrophy in heart (52). *Mhrt* is a cluster of lncRNA and was located at *myh6-myh7* gene loci. Expression of *Mhrt* was down-regulated in TAC mice hearts, in part due to the suppression by BRG1-HDAC-PARP chromatin remodeling complexes. Genetic restoration of *Mhrt779*, the most abundant *Mhrt* species, prevented the pathological hypertrophy phenotype after TAC in the heart. In fact, *Mhrt* can directly bind to the helicase domain of BRG1 that prevents the binding of BRG1 to its genomic DNA targets and thus prevents activation of downstream gene targets of BRG1, such as *Myh6* (52).

Using a global lncRNA expression profiling method, another cardio-specific enriched lncRNA, cardiac hypertrophy-associated transcript (*Chast*), was identified (78). *Chast* is specifically up-regulated in cardiomyocytes in TAC mice as well as in human patients who have aortic stenosis with hypertrophy heart phenotypes. Moreover, *Chast* seems to inhibit the expression of Pleckstrin homology domain-containing protein family member 1 (*Plekhm1*). PLEKHM1 is an autophagy regulator. Because inhibition of autophagy in cardiomyocytes was shown to cause cardiac remodeling, it was proposed that *Chast* enhances cardiac hypertrophy and myocardium remodeling by inhibiting the function of PLEKHM1 to prevent autophagy of cardiomyocytes.

FIGURE 1 Continued

Epigenetic regulations include DNA methylation, PTMs of histones, ATP-dependent chromatin conformation and remodeling, and non-coding RNA-mediated regulation. DNA methylated CpG-enriched region at the promoter region of genes is often associated with gene silencing, whereas methylated CpG found in the gene body is usually related to gene activation. Histone modifications associated with gene expression normally occur on histone 3. The histone writers (HAT and HMT) and erasers (HDAC and HMT) are responsible for PTMs of histone. The active histone mark, H3K27ac and repressive marks, H3K9me2 and H3k27me3, and promoter mark, H3K4me3, are shown. LncRNA can work with epigenetic regulators to effect activation or repression on chromosome remodeling and accessibility as well as the mRNA stability. In the non-failing heart, normal adult cardiac genes, adult isoform *MYH6*, express normally in cardiomyocyte. The cardiac hypertrophy genes, such as *NPPA* and *CTGF*, are not expressed or are at a basal level in non-failing hearts. The DNA around the promoter region of the hypertrophic-related gene loci is hypermethylated, and the chromatin state is inactive by marking H3K27me3 and/or H3K9me2. The PRC2/EZH2 and G9a-EZH2-MEF2C complexes involved in histone methylation in normal hearts are shown. It was shown that lncRNA, Mhrt, plays a critical role in maintaining *MYH6* expression in the adult heart by preventing BRG1 binding to the promoter region of *MYH6*. However, in failing hearts, in addition to normal cardiac gene expression, the hearts return to the fetal gene program and express the fetal isoform of myosin heavy chain, *MYH7*. This is likely due to the re-activation of BRG1 during heart failure. The potential mechanisms are shown. Two cardiac transcription factors, GATA4, MEF2C, and CBP/p300 (HAT), and JMJD (HMT) are involved in cardiac hypertrophy and heart failure. Two examples of the actions of lncRNAs, *CHRT* and *Chaer*, involved in cardiac hypertrophy and heart failure are presented. (Please see text for details.) ATP = adenosine triphosphate; CpG = cytosine-phosphate-guanine ; HAT = histone acetyltransferase; HDAC = histone deacetylase; HMT = histone methyltransferase; mRNA = messenger RNA; *MYH6* = myosin heavy chain; *MYH7* = myosin heavy chain beta; PTM = post-translational modifications.

CENTRAL ILLUSTRATION The Epigenetic Mechanisms in Heart Failure

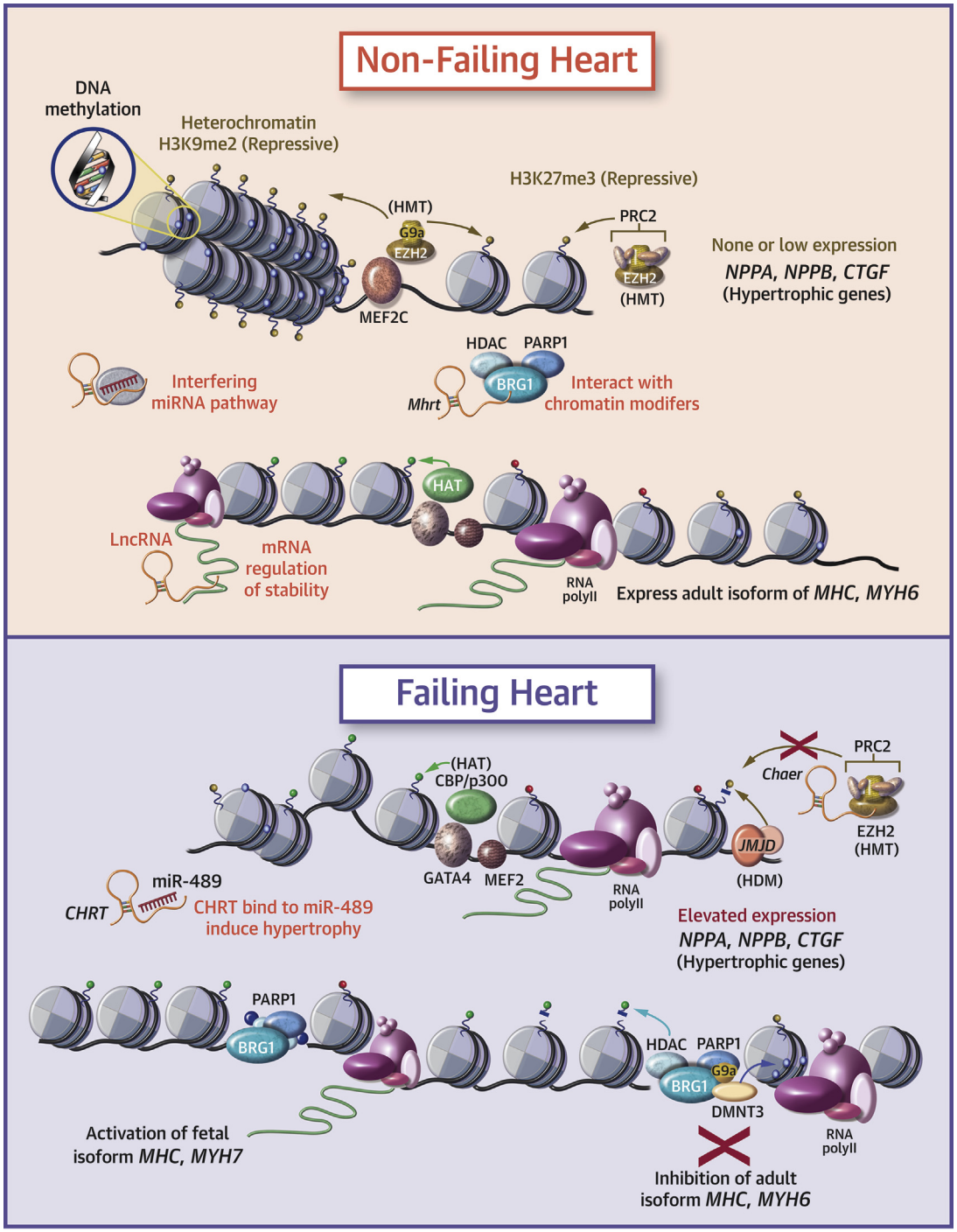

Liu, C.-F. et al. J Am Coll Cardiol Basic Trans Science. 2019;4(8):976–93.

Using a deep sequencing of the non-coding RNA transcriptome method, Yang et al. found that the expression of lncRNAs, but not miRNA, is differentially expressed between nonischemic and ischemic human failing left ventricles (79). Interestingly, 10% of the differentially expressed lncRNAs can be improved or normalized for patients whose hearts were assisted with a left ventricular assist device. A recent study evaluated the potential of circulating lncRNAs as biomarkers for HF (80). Xuan et al. assessed the circulating levels of 13 known to be relevant to cardiovascular disease lncRNAs. Plasma samples from 72 patients with HF and 60 from non-HF patients were tested using quantitative reverse transcription-PCR. They identified 2 lncRNAs, NRON and MHRT, that may serve as novel predictive biomarkers for a failing heart.

As mentioned earlier, lncRNAs can also elicit their function by interfering with the function of miRNAs. One example is the interaction between lncRNA (cardiac hypertrophy-related factor [*CHRF*]) and *mir-489* (81). CHRF was shown to act as a sponge RNA to directly bind to *mir-489*, an anti-cardiac hypertrophy miRNA. This interaction affects the inhibition of myeloid differentiation primary response gene (*myd88*) by miR-489 and, therefore, causes cardiac hypertrophy.

NUTRITION, GUT MICROBIOME, AND EPIGENETICS: INTERPLAY AMONG HOST, GUT MICROBIOTIAL METABOLITES, AND HOST CHROMATIN

In addition to the intrinsic factors, epigenetics is highly influenced by external factors, such as nutrients, toxins, stress, and other environmental factors directly or indirectly. Recently, attention has focused on how microbe diet interactions influence gene activity via epigenetic mechanisms that may affect an individual's health (82–84). Many gut metabolites, such as butyrate, acetate, and folate, may influence epigenetic processes by regulating enzyme activity that is responsible for epigenetic modifications (85). Butyrate, a short-chain fatty acid, is a potent inhibitor of HDACs and thus causes histone hyperacetylation (86). The acetylation of histone increases chromatin accessibility, which allows access of transcription factors and other critical factors to the open chromatin regions allowing for gene transcription. The presence of butyrate and its related sub-product, e.g., sodium butyrate, thus can alter the gene expression via inhibition of histone deacetylase (86–88). In colon cancer research, it was demonstrated that butyrate inhibits HDAC activity and elicits its anti-inflammatory effects via suppressing the nuclear factor κB and interferon γ production and increases the expression of peroxisome proliferator-activated receptor γ (PPARγ) (89,90). Many studies have shown that activation of the PPARγ has a beneficial role in cardiac diseases (91). Therefore, butyrate may have a direct protective role in cardiovascular disease via anti-inflammatory machinery. However, whether or not the anti-inflammatory effects of butyrate also involved epigenetic regulation in cardiovascular diseases remains elusive. In addition, Mathew et al. showed that the effect of butyrate on histone H3 modification altered the G1-specific cell cycle proteins and further resulted in the arrest of smooth muscle cell proliferation, which may provide an atheroprotective potential (92). The data suggested that butyrate may have a role in preventing cardiovascular diseases as well as in therapeutic intervention of arterial restenosis and in-stent-restenosis as a pharmacological agent, respectively (92).

Folate is a type of B vitamin that can be synthesized by gut bacteria or obtained from the diet, and is required for methionine homeostasis (85). It is a methyl donor to generate S-adenosylmethionine (SAM), which is a methyl-donating substrate for methyltransferase needed for the methylation of cytosine in DNA or lysine in histones. Folate and methionine deficiency leads to reduced SAM levels and subsequently reduces the methylation on histone 3 lysine (H3K4) in yeast and human cells as well as in an in vivo model (93,94). In addition, it was shown that the deficiency on dietary methyl-donors had a great impact on the epigenetic profile and also resulted in the development of metabolic diseases (95). However, the link between the gut microbiome-produced folate to HF remains unclear.

Choline is another methyl-group donor for epigenetic modification and is an essential nutrient. Choline is not only used by the host but also by the bacteria residing in the intestine of the host. Gut microbes used choline to produce trimethylamine (TMA), which can be further oxidized in the host's liver to generate trimethylamine *N*-oxide (TMAO), a metabolite linked to HF susceptibly, adverse prognosis, and induction of inflammation (96,97). By manipulating choline in a gnotobiotic mouse model harboring the synthetic gut bacterial community either with the 1 can consume choline and produce TMA (CC^{+}) or the 1 can not (CC^{-}), Romano et al. showed that gut bacteria compete with the host for the usage of choline. This competition caused the global reduction of DNA methylation on examined organs of the host, namely, brain, heart, liver, and colon (98). Despite, the elevated TMAO, behavior

JACC: BASIC TO TRANSLATIONAL SCIENCE VOL. 4, NO. 8, 2019
DECEMBER 2019:976–93

changes, and exacerbation of metabolic disease, no cardiac phenotype was reported. Additionally, how TMAO influences the susceptibility of the failure and if this gut metabolite has any epigenetic role in the heart remain unclear. Although the ability of the gut microbiome to influence epigenetics has been established in cell lines and lower model organisms focusing on brain development, immune system, and cancer biology (86–88,92), data supporting their contributory role in HF and cardiovascular diseases are still emerging.

THERAPEUTIC POTENTIAL OF TARGETING EPIGENETIC REGULATORS IN HF

Many drug candidates targeting epigenetic molecules have been identified for cancer therapy and other diseases. Also, several of them have been used in cardiac hypertrophy and failing heart studies in cellular and animal models (**Table 2**). Those epigenetic-candidate drugs may also be used to treat patients with cardiac hypertrophy and HF. One promising approach is targeting the BET complex. As mentioned earlier, BET proteins play roles in chromatin remodeling and establishing the basic transcriptional complex at the promoter region of genes to regulate gene expression. Several studies showed that administration of a BET inhibitor, JQ1, in vivo and in vitro could suppress pathological cardiac remodeling, suppress pathological hypertrophy, and block the innate inflammatory and profibrotic myocardial program (39,41).

Another potential target of epigenetic molecules is HDAC. There are many HDAC inhibitors (HDACi) and animal testing demonstrated the beneficial effects of HDACi treatments in preventing or improving cardiac functions. Treatment of either trichostatin A and scriptaid, 2 broad-spectrum HDACis, in a pressure-overload hypertrophy mouse model revealed that cardiac hypertrophy and fibrosis were suppressed, and the hypertrophy-associated switch of adult and fetal isoforms of myosin heavy chain expression was diminished (99). In addition, the same HDAC inhibitors were shown to reduce myocardial infarct size and to preserve systolic function in a Langendorff perfusion *in vitro* model as well as in a mouse ischemia/reperfusion model (100,101). Using mouse and rabbit ischemic/reperfusion models, Xie et al. showed that suberoylanilide hydroxamic acid (SAHA, also known as Vorinostat), a Food and Drug Administration–approved HDACi for cancer treatment (102), also can preserve the systolic function and reduce infarct size (103). Additionally, using a simulated ischemic/reperfusion neonatal rat ventricular myocyte culture system, Xie et al. further demonstrated that the cardioprotective effects are partly due to induction of cardiomyocyte autophagy (103). Givinostat, another pan-HDACi, which is used in treating Duchenne muscular dystrophy, inflammatory diseases, myelofibrosis, and blood cancers (104–106), has been shown to attenuate inflammatory response and angiogenic effects, reduce endothelial-to-mesenchymal transition, and reduce cardiac fibrosis on an acute MI mouse model (107). Moreover, when using SK-7041, a Class I HDACi, in either angiotensin II infusion or TAC cardiac hypertrophy mouse modes, Kee et al. demonstrated that myocardial hypertrophy was reduced and the survival rate was improved in mouse and rat hypertrophy models (108). Using an in vitro screening assay, Gallo et al. identified a truncated form of apicdin, another class I HDACi, and this HDACi also demonstrated similar results as what Kee et al. found (109). These results suggested that cardioprotective effects were mainly mediated by class I HDACs.

Many small molecules for inhibition of HDAC have been developed and tested to treat cardiac diseases. However, unlike HDAC, only a few inhibitors of HAT currently show a potential protective effect against cardiac disease. One of them is curcumin, which was first used as an anti-inflammatory reagent. Currently, curcumin has been suggested for treating osteoarthritis, rheumatoid arthritis, and diabetes (110–112). It is a natural compound derived from the active ingredient of turmeric (*Curcuma longa*), which can act as a p300-specific histone HAT inhibitor. Oral treatment with curcumin in a rat MI model demonstrated improvement in left ventricular function and reduction of fibrosis compared with non-treatment MI rats (24).

A DNA methylation inhibitor, 5-azacytidine (5-aza), is widely used to treat leukemia and sickle cell diseases (113,114). In a spontaneously hypertensive rat model, intraperitoneal injection of 5-aza at a dose of 10 mg/kg resulted in improvement in cardiac function as well as reduction in cardiac fibrosis (115).

Last but not least, lncRNA silencing approach using GapmeR, a type of antisense oligonucleotide, is another potential therapeutic target for HF (116). Although no clinical trials targeting lncRNAs were performed, several in vivo studies have shown that injection of lncRNA GapmeR such as GapmeR-*Chast* preserved or improved cardiac function in mice after pressure overload-induced cardiac hypertrophy and HF (74,78).

CONCLUSIONS AND FUTURE PERSPECTIVES

This review summarizes recent studies that supported key contributing roles of epigenetic mechanisms in cardiac hypertrophy and failure and may have important therapeutic implications for HF (**Figure 1, Central Illustartion**). However, the ubiquitous characteristics of epigenetic regulators have created a significant challenge to develop targeted epigenetic therapies for cardiac diseases. First, because most epigenetic regulators modulate gene expression via conventional mechanisms, the global inhibition or activation of such regulators may have pleiotropic effects with no cardiac specificity. Second, the heart is made up of several different types of cells. Each cell type may possess its own epigenetic signature in response to disease conditions. Before generalizing such a knowledge base for cardiac therapies, larger cohort studies with cell-specific epigenetic maps for various types of cardiomyopathy are necessary. Equally important is the need to identify cardiac disease-specific genes and their corresponding epigenetic regulators and to establish networks between the epigenetic alterations and the signaling transduction cascades (specifically to cardiac hypertrophy and failing hearts). Another challenge of epigenetic therapy for HF (as is true for other diseases) is to minimize the off-target effects by developing suitable and efficient methods for delivering to the specific locations within a heart. Lastly, a potential near-term application of the current knowledge base of epigenetic regulation for cardiac diseases is the development of epigenetic biomarkers for diagnosis, prognosis, and therapy optimization, especially from easily accessible tissues (such as peripheral blood or blood cells) that may reflect cardiac-specific alterations. Generating such insights into epigenetic modifications along the natural history of human HF will catalyze the development of personalized therapies for cardiomyopathy and HF.

ACKNOWLEDGMENTS We thank Dr. Kymberleigh Romano and Ms. Kirsten Bede for review of the manuscript and suggestions.

ADDRESS FOR CORRESPONDENCE: Dr. W.H. Wilson Tang, Department of Cardiovascular Medicine, Heart and Vascular Institute, Cleveland Clinic, 9500 Euclid Avenue, Desk J3-4, Cleveland, Ohio 44195. E-mail: tangw@ccf.org.

REFERENCES

1. Jones PA. Functions of DNA methylation: islands, start sites, gene bodies and beyond. Nat Rev Genet 2012;13:484–92.

2. Feinberg AP, Vogelstein B. Hypomethylation distinguishes genes of some human cancers from their normal counterparts. Nature 1983;301:89–92.

3. Esteller M. CpG island hypermethylation and tumor suppressor genes: a booming present, a brighter future. Oncogene 2002;21:5427–40.

4. Movassagh M, Choy MK, Goddard M, Bennett MR, Down TA, Foo RS. Differential DNA methylation correlates with differential expression of angiogenic factors in human heart failure. PLoS One 2010;5:e8564.

5. Movassagh M, Choy MK, Knowles DA, et al. Distinct epigenomic features in end-stage failing human hearts. Circulation 2011;124:2411–22.

6. Haas J, Frese KS, Park YJ, et al. Alterations in cardiac DNA methylation in human dilated cardiomyopathy. EMBO Mol Med 2013;5:413–29.

7. Meder B, Haas J, Sedaghat-Hamedani F, et al. Epigenome-wide association study identifies cardiac gene patterning and a novel class of biomarkers for heart failure. Circulation 2017;136:1528–44.

8. Gilsbach R, Schwaderer M, Preissl S, et al. Distinct epigenetic programs regulate cardiac myocyte development and disease in the human heart in vivo. Nat Commun 2018;9:391.

9. Glezeva N, Moran B, Collier P, et al. Targeted DNA methylation profiling of human cardiac tissue reveals novel epigenetic traits and gene deregulation across different heart failure patient subtypes. Circ Heart Fail 2019;12:e005765.

10. Pepin ME, Ha CM, Crossman DK, et al. Genome-wide DNA methylation encodes cardiac transcriptional reprogramming in human ischemic heart failure. Lab Invest 2019;99:371–86.

11. Luger K, Mader AW, Richmond RK, Sargent DF, Richmond TJ. Crystal structure of the nucleosome core particle at 2.8 A resolution. Nature 1997;389:251–60.

12. Zhao Y, Garcia BA. Comprehensive catalog of currently documented histone modifications. Cold Spring Harb Perspect Biol 2015;7:a025064.

13. Bowman GD, Poirier MG. Post-translational modifications of histones that influence nucleosome dynamics. Chem Rev 2015;115:2274–95.

14. Chen T, Dent SY. Chromatin modifiers and remodellers: regulators of cellular differentiation. Nat Rev Genet 2014;15:93–106.

15. Burridge PW, Sharma A, Wu JC. Genetic and epigenetic regulation of human cardiac reprogramming and differentiation in regenerative medicine. Annu Rev Genet 2015;49:461–84.

16. Preissl S, Schwaderer M, Raulf A, et al. Deciphering the epigenetic code of cardiac myocyte transcription. Circ Res 2015;117:413–23.

17. Schmitt AD, Hu M, Jung I, et al. A compendium of chromatin contact maps reveals spatially active regions in the human genome. Cell Reports 2016;17:2042–59.

18. Quaife-Ryan GA, Sim CB, Ziemann M, et al. Multicellular transcriptional analysis of mammalian heart regeneration. Circulation 2017;136:1123–39.

19. Rothbart SB, Strahl BD. Interpreting the language of histone and DNA modifications. Biochim Biophys Acta 2014;1839:627–43.

20. Gray SG, Teh BT. Histone acetylation/deacetylation and cancer: an "open" and "shut" case? Curr Mol Med 2001;1:401–29.

21. Lee KK, Workman JL. Histone acetyltransferase complexes: 1 size doesn't fit all. Nat Rev Mol Cell Biol 2007;8:284–95.

22. Marmorstein R. Structure of histone deacetylases: insights into substrate recognition and catalysis. Structure 2001;9:1127–33.

23. Yanazume T, Hasegawa K, Morimoto T, et al. Cardiac p300 is involved in myocyte growth with decompensated heart failure. Mol Cell Biol 2003;23:3593–606.

24. Morimoto T, Sunagawa Y, Kawamura T, et al. The dietary compound curcumin inhibits p300 histone acetyltransferase activity and prevents heart failure in rats. J Clin Invest 2008;118:868–78.

25. Zhang CL, McKinsey TA, Chang S, Antos CL, Hill JA, Olson EN. Class II histone deacetylases act

as signal-responsive repressors of cardiac hypertrophy. Cell 2002;110:479–88.

26. Chang S, McKinsey TA, Zhang CL, Richardson JA, Hill JA, Olson EN. Histone deacetylases 5 and 9 govern responsiveness of the heart to a subset of stress signals and play redundant roles in heart development. Mol Cell Biol 2004; 24:8467–76.

27. McKinsey TA, Zhang CL, Olson EN. MEF2: a calcium-dependent regulator of cell division, differentiation and death. Trends Biochem Sci 2002; 27:40–7.

28. Trivedi CM, Luo Y, Yin Z, et al. Hdac2 regulates the cardiac hypertrophic response by modulating Gsk3 beta activity. Nat Med 2007;13:324–31.

29. Montgomery RL, Potthoff MJ, Haberland M, et al. Maintenance of cardiac energy metabolism by histone deacetylase 3 in mice. J Clin Invest 2008;118:3588–97.

30. Zhang QJ, Chen HZ, Wang L, Liu DP, Hill JA, Liu ZP. The histone trimethyllysine demethylase JMJD2A promotes cardiac hypertrophy in response to hypertrophic stimuli in mice. J Clin Invest 2011;121:2447–56.

31. Sheikh F, Raskin A, Chu PH, et al. An FHL1-containing complex within the cardiomyocyte sarcomere mediates hypertrophic biomechanical stress responses in mice. J Clin Invest 2008;118:3870–80.

32. Nguyen AT, Xiao B, Neppl RL, et al. DOT1L regulates dystrophin expression and is critical for cardiac function. Genes Dev 2011;25:263–74.

33. Papait R, Serio S, Pagiatakis C, et al. Histone methyltransferase G9a is required for cardiomyocyte homeostasis and hypertrophy. Circulation 2017;136:1233–46.

34. Stein AB, Jones TA, Herron TJ, et al. Loss of H3K4 methylation destabilizes gene expression patterns and physiological functions in adult murine cardiomyocytes. J Clin Invest 2011;121:2641–50.

35. Hohl M, Wagner M, Reil JC, et al. HDAC4 controls histone methylation in response to elevated cardiac load. J Clin Invest 2013;123:1359–70.

36. Kaneda R, Takada S, Yamashita Y, et al. Genome-wide histone methylation profile for heart failure. Genes Cells 2009;14:69–77.

37. Papait R, Cattaneo P, Kunderfranco P, et al. Genome-wide analysis of histone marks identifying an epigenetic signature of promoters and enhancers underlying cardiac hypertrophy. Proc Natl Acad Sci U S A 2013;110:20164–9.

38. Ratnu VS, Emami MR, Bredy TW. Genetic and epigenetic factors underlying sex differences in the regulation of gene expression in the brain. J Neurosci Res 2017;95:301–10.

39. Anand P, Brown JD, Lin CY, et al. BET bromodomains mediate transcriptional pause release in heart failure. Cell 2013;154:569–82.

40. Spiltoir JI, Stratton MS, Cavasin MA, et al. BET acetyl-lysine binding proteins control pathological cardiac hypertrophy. J Mol Cell Cardiol 2013;63: 175–9.

41. Duan Q, McMahon S, Anand P, et al. BET bromodomain inhibition suppresses innate inflammatory and profibrotic transcriptional networks in heart failure. Sci Transl Med 2017;9: pii: eaah5084.

42. Narlikar GJ, Sundaramoorthy R, Owen-Hughes T. Mechanisms and functions of ATP-dependent chromatin-remodeling enzymes. Cell 2013;154:490–503.

43. Banerjee R, Bultman SJ, Holley D, et al. Non-targeted metabolomics of Brg1/Brm double-mutant cardiomyocytes reveals a novel role for SWI/SNF complexes in metabolic homeostasis. Metabolomics 2015;11:1287–301.

44. Bevilacqua A, Willis MS, Bultman SJ. SWI/SNF chromatin-remodeling complexes in cardiovascular development and disease. Cardiovasc Pathol 2014;23:85–91.

45. Bultman SJ, Holley DW, G GdR, et al. BRG1 and BRM SWI/SNF ATPases redundantly maintain cardiomyocyte homeostasis by regulating cardiomyocyte mitophagy and mitochondrial dynamics in vivo. Cardiovasc Pathol 2016;25: 258–69.

46. Hang CT, Yang J, Han P, et al. Chromatin regulation by Brg1 underlies heart muscle development and disease. Nature 2010;466:62–7.

47. Scott CA, Marsden AN, Rebagliati MR, et al. Nuclear/cytoplasmic transport defects in BBS6 underlie congenital heart disease through perturbation of a chromatin remodeling protein. PLoS genetics 2017;13:e1006936.

48. Vieira JM, Howard S, Villa Del Campo C, et al. BRG1-SWI/SNF-dependent regulation of the Wt1 transcriptional landscape mediates epicardial activity during heart development and disease. Nat Commun 2017;8:16034.

49. England J, Loughna S. Heavy and light roles: myosin in the morphogenesis of the heart. Cell Mol Life Sci 2013;70:1221–39.

50. Qian Y, Xiao D, Guo X, et al. Hypomethylation and decreased expression of BRG1 in the myocardium of patients with congenital heart disease. Birth Defects Res 2017;109:1183–95.

51. Han P, Li W, Yang J, et al. Epigenetic response to environmental stress: assembly of BRG1-G9a/GLP-DNMT3 repressive chromatin complex on Myh6 promoter in pathologically stressed hearts. Biochim Biophys Acta 2016;1863:1772–81.

52. Han P, Li W, Lin CH, et al. A long noncoding RNA protects the heart from pathological hypertrophy. Nature 2014;514:102–6.

53. Billon P, Cote J. Precise deposition of histone H2A.Z in chromatin for genome expression and maintenance. Biochim Biophys Acta 2013;1819: 290–302.

54. Chen P, Zhao J, Li G. Histone variants in development and diseases. J Genet Genomics 2013;40:355–65.

55. Gaume X, Torres-Padilla ME. Regulation of reprogramming and cellular plasticity through histone exchange and histone variant incorporation. Cold Spring Harb Symp Quant Biol 2015;80: 165–75.

56. Yuen BT, Knoepfler PS. Histone H3.3 mutations: a variant path to cancer. Cancer Cell 2013; 24:567–74.

57. Chen IY, Lypowy J, Pain J, et al. Histone H2A.z is essential for cardiac myocyte hypertrophy but opposed by silent information regulator 2alpha. J Biol Chem 2006;281:19369–77.

58. Valenzuela N, Fan Q, Fa'ak F, et al. Cardiomyocyte-specific conditional knockout of the histone chaperone HIRA in mice results in hypertrophy, sarcolemmal damage and focal replacement fibrosis. Dis Model Mech 2016;9:335–45.

59. Ahmad K, Henikoff S. The histone variant H3.3 marks active chromatin by replication-independent nucleosome assembly. Mol Cell 2002;9:1191–200.

60. Rosa-Garrido M, Chapski DJ, Schmitt AD, et al. High-resolution mapping of chromatin conformation in cardiac myocytes reveals structural remodeling of the epigenome in heart failure. Circulation 2017;136:1613–25.

61. Filippova GN. Genetics and epigenetics of the multifunctional protein CTCF. Curr Top Dev Biol 2008;80:337–60.

62. Garrick D, De Gobbi M, Gibbons R, Higgs DR. CTCF, cohesin and higher-order chromatin structure. Epigenomics 2009;1:232.

63. Montefiori LE, Sobreira DR, Sakabe NJ, et al. A promoter interaction map for cardiovascular disease genetics. Elife 2018;7:pii: e35788.

64. Project E. The ENCODE (ENCyclopedia Of DNA Elements) Project. Science 2004;306:636–40.

65. Hangauer MJ, Vaughn IW, McManus MT. Pervasive transcription of the human genome produces thousands of previously unidentified long intergenic noncoding RNAs. PLoS Genetics 2013;9:e1003569.

66. de Lucia C, Komici K, Borghetti G, et al. microRNA in cardiovascular aging and age-related cardiovascular diseases. Front Med 2017;4:74.

67. Shah P, Bristow MR, Port JD. MicroRNAs in heart failure, cardiac transplantation, and myocardial recovery: biomarkers with therapeutic potential. Curr Heart Failure Reports 2017;14: 454–64.

68. Wojciechowska A, Braniewska A, Kozar-Kaminska K. MicroRNA in cardiovascular biology and disease. Adv Clin Experimental Med 2017;26: 865–74.

69. Bayoumi AS, Aonuma T, Teoh JP, Tang YL, Kim IM. Circular noncoding RNAs as potential therapies and circulating biomarkers for cardiovascular diseases. Acta Pharmacologica Sinica 2018;7: 1100–9.

70. Mellis D, Caporali A. MicroRNA-based therapeutics in cardiovascular disease: screening and delivery to the target. Biochem Soc Trans 2018; 46:11–21.

71. Fatica A, Bozzoni I. Long non-coding RNAs: new players in cell differentiation and development. Nat Rev Genet 2014;15:7–21.

72. Hennessy EJ. Cardiovascular disease and long noncoding RNAs: tools for unraveling the mystery Lnc-ing RNA and phenotype. Circ Cardiovasc Genet 2017;10:e001556.

73. Kumarswamy R, Bauters C, Volkmann I, et al. Circulating long noncoding RNA, LIPCAR, predicts

survival in patients with heart failure. Circ Res 2014;114:1569–75.

74. Piccoli MT, Gupta SK, Viereck J, et al. Inhibition of the cardiac fibroblast-enriched lncRNA Meg3 prevents cardiac fibrosis and diastolic dysfunction. Circ Res 2017;121:575–83.

75. Lee JH, Gao C, Peng G, et al. Analysis of transcriptome complexity through RNA sequencing in normal and failing murine hearts. Circ Res 2011;109:1332–41.

76. Liu L, An X, Li Z, et al. The H19 long noncoding RNA is a novel negative regulator of cardiomyocyte hypertrophy. Cardiovasc Res 2016;111:56–65.

77. Wang Z, Zhang XJ, Ji YX, et al. The long noncoding RNA Chaer defines an epigenetic checkpoint in cardiac hypertrophy. Nat Med 2016;22:1131–9.

78. Viereck J, Kumarswamy R, Foinquinos A, et al. Long noncoding RNA Chast promotes cardiac remodeling. Sci Transl Med 2016;8:326ra22.

79. Yang KC, Yamada KA, Patel AY, et al. Deep RNA sequencing reveals dynamic regulation of myocardial noncoding RNAs in failing human heart and remodeling with mechanical circulatory support. Circulation 2014;129:1009–21.

80. Xuan L, Sun L, Zhang Y, et al. Circulating long non-coding RNAs NRON and MHRT as novel predictive biomarkers of heart failure. J Cell Mol Med 2017;21:1803–14.

81. Wang K, Liu F, Zhou LY, et al. The long noncoding RNA CHRF regulates cardiac hypertrophy by targeting miR-489. Circ Res 2014;114:1377–88.

82. Sanders LM, Zeisel SH. Choline: dietary requirements and role in brain development. Nutr Today 2007;42:181–6.

83. Sezgin Z, Dincer Y. Alzheimer's disease and epigenetic diet. Neurochem Int 2014;78:105–16.

84. Aleksandrova K, Romero-Mosquera B, Hernandez V. Diet, gut microbiome and epigenetics: emerging links with inflammatory bowel diseases and prospects for management and prevention. Nutrients 2017;9. pii:E962.

85. Jeffery IB, O'Toole PW. Diet-microbiota interactions and their implications for healthy living. Nutrients 2013;5:234–52.

86. Candido EP, Reeves R, Davie JR. Sodium butyrate inhibits histone deacetylation in cultured cells. Cell 1978;14:105–13.

87. Davie JR. Inhibition of histone deacetylase activity by butyrate. J Nutr 2003;133:2485S–93S.

88. Aoyama M, Kotani J, Usami M. Butyrate and propionate induced activated or non-activated neutrophil apoptosis via HDAC inhibitor activity but without activating GPR-41/GPR-43 pathways. Nutrition 2010;26:653–61.

89. Andoh A, Fujiyama Y, Hata K, et al. Counter-regulatory effect of sodium butyrate on tumour necrosis factor-alpha (TNF-alpha)-induced complement C3 and factor B biosynthesis in human intestinal epithelial cells. Clin Exp Immunol 1999;118:23–9.

90. Place RF, Noonan EJ, Giardina C. HDAC inhibition prevents NF-kappa B activation by suppressing proteasome activity: down-regulation of proteasome subunit expression stabilizes I kappa B alpha. Biochem Pharmacol 2005;70:394–406.

91. Khuchua Z, Glukhov AI, Strauss AW, Javadov S. Elucidating the beneficial role of PPAR agonists in cardiac diseases. Int J Mol Sci 2018;19(11):pii: E3464.

92. Mathew OP, Ranganna K, Yatsu FM. Butyrate, an HDAC inhibitor, stimulates interplay between different posttranslational modifications of histone H3 and differently alters G1-specific cell cycle proteins in vascular smooth muscle cells. Biomed Pharmacother 2010;64:733–40.

93. Sadhu MJ, Guan Q, Li F, et al. Nutritional control of epigenetic processes in yeast and human cells. Genetics 2013;195:831–44.

94. Mentch SJ, Mehrmohamadi M, Huang L, et al. Histone methylation dynamics and gene regulation occur through the sensing of one-carbon metabolism. Cell Metab 2015;22:861–73.

95. Obeid R. The metabolic burden of methyl donor deficiency with focus on the betaine homocysteine methyltransferase pathway. Nutrients 2013;5:3481–95.

96. Wang Z, Klipfell E, Bennett BJ, et al. Gut flora metabolism of phosphatidylcholine promotes cardiovascular disease. Nature 2011;472:57–63.

97. Organ CL, Otsuka H, Bhushan S, et al. Choline diet and its gut microbe-derived metabolite, trimethylamine N-Oxide, exacerbate pressure overload-induced heart failure. Circ Heart Fail 2016;9:e002314.

98. Romano KA, Martinez-Del Campo A, Kasahara K, et al. Metabolic, epigenetic, and transgenerational effects of gut bacterial choline consumption. Cell Host Microbe 2017;22:279–90 e7.

99. Kong Y, Tannous P, Lu G, et al. Suppression of class I and II histone deacetylases blunts pressure-overload cardiac hypertrophy. Circulation 2006;113:2579–88.

100. Granger A, Abdullah I, Huebner F, et al. Histone deacetylase inhibition reduces myocardial ischemia-reperfusion injury in mice. FASEB J 2008;22:3549–60.

101. Zhao TC, Cheng G, Zhang LX, Tseng YT, Padbury JF. Inhibition of histone deacetylases triggers pharmacologic preconditioning effects against myocardial ischemic injury. Cardiovasc Res 2007;76:473–81.

102. Bubna AK. Vorinostat-an overview. Indian J Dermatol 2015;60:419.

103. Xie M, Kong Y, Tan W, et al. Histone deacetylase inhibition blunts ischemia/reperfusion injury by inducing cardiomyocyte autophagy. Circulation 2014;129:1139–51.

104. Bose P, Verstovsek S. Developmental therapeutics in myeloproliferative neoplasms. Clin Lymphoma Myeloma Leukemia 2017;17s:S43–52.

105. Mauro A, Rigante D, Cimaz R. Investigational drugs for treatment of juvenile idiopathic arthritis. Expert Opin Invest Drugs 2017;26:381–7.

106. Shawi F, Perras C, Severn M. Emerging drugs for Duchenne Muscular Dystrophy. CADTH Issues in Emerging Health Technologies. Ottawa (ON): Canadian Agency for Drugs and Technologies in Health, CADTH 2017. , 2016:1–19.

107. Milan M, Pace V, Maiullari F, et al. Givinostat reduces adverse cardiac remodeling through regulating fibroblasts activation. Cell Death Dis 2018;9:108.

108. Kee HJ, Sohn IS, Nam KI, et al. Inhibition of histone deacetylation blocks cardiac hypertrophy induced by angiotensin II infusion and aortic banding. Circulation 2006;113:51–9.

109. Gallo P, Latronico MV, Gallo P, et al. Inhibition of class I histone deacetylase with an apicidin derivative prevents cardiac hypertrophy and failure. Cardiovasc Res 2008;80:416–24.

110. Amalraj A, Varma K, Jacob J, et al. A novel highly bioavailable curcumin formulation improves symptoms and diagnostic indicators in rheumatoid arthritis patients: a randomized, double-blind, placebo-controlled, two-dose, three-arm, and parallel-group study. J Med Food 2017;20:1022–30.

111. Haroyan A, Mukuchyan V, Mkrtchyan N, et al. Efficacy and safety of curcumin and its combination with boswellic acid in osteoarthritis: a comparative, randomized, double-blind, placebo-controlled study. Bmc Complem Altern M 2018;18(1):7.

112. Panahi Y, Khalili N, Sahebi E, et al. Curcuminoids plus piperine modulate adipokines in type 2 diabetes mellitus. Curr Clin Pharmacol 2017;12:253–8.

113. Kantarjian HM, Roboz GJ, Kropf PL, et al. Guadecitabine (SGI-110) in treatment-naive patients with acute myeloid leukaemia: phase 2 results from a multicentre, randomised, phase 1/2 trial. Lancet Oncol 2017;18:1317–26.

114. Molokie R, Lavelle D, Gowhari M, et al. Oral tetrahydrouridine and decitabine for non-cytotoxic epigenetic gene regulation in sickle cell disease: a randomized phase 1 study. PLoS Med 2017;14:e1002382.

115. Watson CJ, Horgan S, Neary R, et al. Epigenetic therapy for the treatment of hypertension-induced cardiac hypertrophy and fibrosis. J Cardiovasc Pharmacol Ther 2016;21:127–37.

116. Swayze EE, Siwkowski AM, Wancewicz EV, et al. Antisense oligonucleotides containing locked nucleic acid improve potency but cause significant hepatotoxicity in animals. Nucleic Acids Res 2007;35:687–700.

117. Nguyen AT, Taranova O, He J, Zhang Y. DOT1L, the H3K79 methyltransferase, is required for MLL-AF9-mediated leukemogenesis. Blood 2011;117:6912–22.

KEY WORDS cardiac hypertrophy, epigenetics, heart failure

JACC: BASIC TO TRANSLATIONAL SCIENCE
VOL. 4, NO. 8, 2019

ISSN 2452-302X

CORRECTION

Thompson PD, Taylor B

A Novel Mechanism to Explain Statin-Associated Skeletal Muscle Symptoms

J Am Coll Cardiol Basic Trans Science 2019;4:524-6.

The reference citation for Reference 11 as published in "A Novel Mechanism to Explain Statin-Associated Skeletal Muscle Symptoms" in the August 2019 issue of *JACC: Basic to Translational Science* is incorrect. The correct reference citation is:

11. Thompson PD, Zmuda JM, Domalik LJ, Zimet RJ, Staggers J, Guyton JR. Lovastatin increases exercise-induced skeletal muscle injury. Metabolism. 1997;46:1206-10.

The Authors regret the error.

The online version of the paper has been corrected to reflect this change.

https://doi.org/10.1016/j.jacbts.2019.11.001